7-2010

MECHANICAL TESTING DEVICE FOR VISCOELASTIC BIOMATERIALS

Jeff D. Berg
University of Nebraska at Lincoln, jberg3@unl.edu

MECHANICAL TESTING DEVICE FOR VISCOELASTIC BIOMATERIALS

by

Jeff Berg

A THESIS

Presented to the Faculty of

The Graduate College at the University of Nebraska

In Partial Fulfillment of the Requirements

For the Degree of Master of Science

MAJOR: Mechanical Engineering

Under the Supervision of Professor Carl A. Nelson

Lincoln, Nebraska

July, 2010

MECHANICAL TESTING DEVICE FOR VISCOELASTIC BIOMATERIALS

Jeff Berg, M.S.

University of Nebraska, 2010

Adviser: Carl A. Nelson

Nearly all biologic tissues exhibit viscoelastic behavior. This behavior is characterized by hysteresis in the response of the material to load or strain. This information can be utilized in extrapolation of life expectancy of vascular implant materials including native tissues and synthetic materials. This behavior is exhibited in many engineering materials as well such as the polymers PTFE, polyamide, polyethylene, etc. While procedures have been developed for evaluating the engineering polymers the techniques for biologic tissues are not as mature. There are multiple reasons for this. A major one is a cultural divide between the medical and engineering communities. Biomedical engineers are beginning to fill that void.

A digitally controlled drivetrain designed to evaluate both elastic and viscoelastic characteristics of biologic tissues has been developed. The initial impetus for the development of this device was to evaluate the potential for human umbilical tissue to serve as a vascular graft material. The consequence is that the load frame is configured for membrane type specimens with rectangular dimensions of no more than 25mm per side. The designed load capacity of the drivetrain is to impose an axial load of 40N on the specimen.

This drivetrain is capable of assessing the viscoelastic response of the specimens by four different test modes: stress relaxation, creep, harmonic induced oscillations, and controlled strain rate tests.

The fluorocarbon PTFE has mechanical properties commensurate with vascular tissue. In fact, it has been used for vascular grafts in patients who have been victims of various traumas. Hardware and software validation of the device was accomplished by testing PTFE

and comparing the results to properties that have been published by both researchers and manufacturers.

CONTENTS

LIST OF TABLES

LIST OF FIGURES

ACKNOWLEDGMENTS

The author wishes to express sincere appreciation to Professors Nelson, Barton, and Gu for their assistance in the preparation of this manuscript. In addition, special thanks to Dr. James Hammel whose vision served as the impetus to fabricate this device. Further thanks to all persons listed below whom contributed to this research as well.

Dr. Carl Nelson	Adviser
Dr. James Hammel	UNMC
Dr. John Barton	UNL Dept. of Mech. Engr.
Dr. Linxia Gu	UNL Dept. of Mech. Engr.
Dr. Mike Hoffman	UNL Dept. of Elec. Engr.
Hai Li Lang	UNMC
Dr. Mark Beatty	UNL/Dentistry/UNMC
Aaron Holmberg	Machining
Mumar Hossain	BOSE data

VARIABLES & CONSTANTS

	INDEPENDENT VARIABLES	
t	*Time* =	seconds
ω	*Angular frequency* =	Rad/sec
τ	*Dummy integration variable in convolution integral* =	seconds
i	*Complex #* =	$\sqrt{-1}$
	DEPENDENT VARIABLES	
σ	*Tensile stress* =	Force/Area
σ_{shear}	*Shear stress* =	Force/Area
ε	*Strain* =	%
$\dot{\varepsilon}$	*Strain rate*=	%/sec
f	*Cyclic rotational rate*=	Hz
	PROPERTIES	
E	*Relaxation modulus (time domain)*=	Force/Area
D	*Creep compliance (tme domain)*=	$(Force/Area)^{-1}$
E*	*Complex Relaxation modulus (complex domain)*=	Force/Area
D*	*Complex Creep compliance (complex domain)*=	$(Force/Area)^{-1}$
E'	*Relaxation "storage" modulus*=	Force/Area
D'	*Creep "storage" compliance*=	$(Force/Area)^{-1}$
E''	*Relaxation "loss" modulus*=	Force/Area
D''	*Creep "loss" compliance*=	$(Force/Area)^{-1}$
η	*Viscous damping parameter*=	$\frac{Force}{Area}_{Time}$
E_∞	*Steady-state relaxation modulus of the Weichert model*=	Force/Area
E_i	*Individual Relaxation modulus of the Maxwell elements in the Weichert model* =	Force/Area
η_i	*Individual damping parameters of either the Maxwell or Voigt elements* =	$\frac{Force}{Area}_{Time}$
η_∞	*Steady-state damping parameter of the Kelvin model*=	$\frac{Force}{Area}_{Time}$
D_i	*Individual Creep compliance of the Voigt elements in the Kelvin model* =	$(Force/Area)^{-1}$
D_0	*Initial Offset Compliance of the Kelvin model* =	$(Force/Area)^{-1}$
$G_{relaxation}$	*Impulse Response function for relaxation* =	Force/Area
G_{creep}	*Impulse Response function for creep* =	$(Force/Area)^{-1}$
	DRIVETRAIN PARAMETERS	
ϕ_{pitch}	*Ball screw pitch*=	1 mm
D_{screw}	*Ball screw diameter*=	6mm
θ	*Ball screw inclination angle*=	3^0
$\rho_{leverage}$	*Ball screw leverage coefficient*=	0.3mm
μ	*Ball screw friction coefficient (conservative assumption)*=	0.1
P_{rating}	*Power requirement of servomotors*=	28 W per axis
T_{orq}	*Servomotor torque requirement*=	11mJ per axis

	SPECIMEN PARAMETERS	
$L_{specimen}$	*Measured specimen length after pretension*=	mm
δ	*Specimen deflection*=	mm
t	*Specimen thickness*	mm
w	*Specimen width*	mm

1. Introduction

Nearly all biologic tissues exhibit viscoelastic behavior. This behavior is characterized by hysteresis in the response of the material to load. This information can be utilized in extrapolation of life expectancy of vascular implant materials including native tissues and synthetic materials. This behavior is exhibited in many engineering materials as well such as the polymers PTFE, polyamide, polyethylene, etc. While procedures have been developed for evaluating the engineering polymers the techniques for biologic tissues are not as mature. There are multiple reasons for this. A major one is a cultural divide between the medical and engineering communities. Biomedical engineers are beginning to fill that void.

The other major factor is the condition of the specimens. While it is possible to get the polymer materials in bulk form and various geometries conducive to evaluating the viscoelastic parameters, this is not the case for biologic specimens. Biologic specimens are frequently available only in small strip or membrane configurations.

This presents significant challenges in mounting the specimen. Boundary conditions can play a significant role in evaluating the viscoelastic response to the point that the response is dominated by the mounting conditions rather than the properties of the specimen itself. Another concern is the hydration factor of biologic specimens; wet and dry specimens behave very differently. This is true of polymers but not to the degree that it is for biologic specimens.

Another condition of biologic specimens is their compliance. Even compared to polymers these specimens are soft. So the load levels obtained during such tests are quite low. Most conventional test methods are not feasible due to the nature of these specimens.

A digitally controlled drivetrain designed to evaluate both elastic and viscoelastic characteristics of biologic tissues has been developed (**Figure 1-1**). The initial impetus for the development of this device was to evaluate the potential for human umbilical tissue to serve as a vascular graft material. Typically, patch material for vascular repair consists of

homograft, a non-viable processed material derived from tissue obtained from the aorta of deceased donors. Homograft is used as graft material in surgical procedures to repair cardiac congenital septal defects in infants. The use of the homograft tissue presents immune response complications and the infant requires medication with detrimental side effects. One potential solution is to substitute the infant's umbilical cord tissue as the graft material in order to eliminate immune response complications. This device was to compare the umbilical tissue to that of the homograft material to assess the elastic and viscoelastic differences.

Figure 1-1: Viscoelastic test device.

1.1. Concept Development & Evolution

As mentioned previously,, the initial impetus for the development of this device was to evaluate the potential for human umbilical tissue to serve as a vascular graft material. Since the geometric configuration of these specimens resembles a membrane the initial design proposal was to mount the specimens in a rigid frame, attach an accelerometer, and apply a harmonic stimulus via an electrodynamic vibration table. The testing procedure would comply with ASTM standards so consistency between test samples would be expected to be quantifiable.[1, 2]

The challenge would be how to mount the specimen and pretension it. **Figure 1-2** was the proposed specimen frame configuration. The brackets contain suture pins that pierce the specimen and the degrees of freedom of the four corners allow expansion of the frame to pretension the specimen as well as rotations to compensate for tension variability within the specimen. Three concerns were expressed during the first design review process:

1) fabrication cost of the specimen brackets with suture pins;
2) the mass of the accelerometer contributing to the measured response;
3) extrapolation of the response from vibration frequencies to those of physiologic conditions.

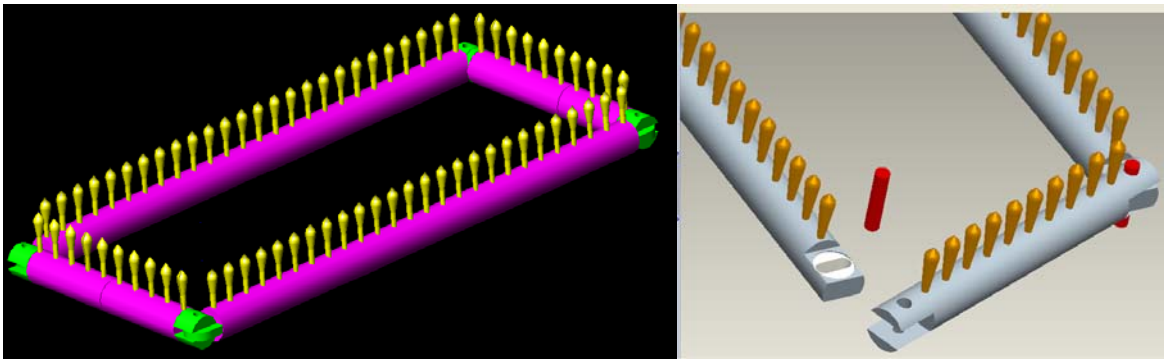

Figure 1-2: Initial design proposal.

The conclusions of the first design review were to explore creep and stress relaxation test procedures. These tests can and have been executed on conventional mechanical test platforms such as a commercial INSTRON machine. However, the test platform would require a load cell with very good resolution at very low loading conditions. An INSTRON platform with a low load capacity exists in the College of Dentistry but the pneumatic specimen grips do not represent the operational boundary conditions of a vascular graft. Moreover, the INSTRON platform is only capable of executing uniaxial tests. The additional capability of inducing shear in the specimen as described in section **3.1.1** motivated a second design proposal.

The configuration of the second design shown in **Figure 1-3** is a frame system with specimen brackets attached to the top surface via threaded connections. Linear bearings allow for extensional translations and the threaded connections allow for rotational degrees of freedom. Close inspection of the specimen brackets in **Figure 1-3** show ½ mm through-holes exist in a recessed area spaced apart by 2mm. The desire of the investigator at the time was

to manually suture the specimen to the brackets as done in the vascular graft application. The unresolved issues after the second design review concerned how to actuate the frame. The third design iteration ensued.

The third design review investigated utilizing a ball screw to actuate the frame, but as shown in **Figure 1-4** clearance prohibits rotations about the four pivot axes. The third design evolved to eliminate the linear bearings and embed the ball screws within the longitudinal axes of the frame. The ball screws are driven by attached spur gears which in turn are driven by a worm gear also shown in **Figure 1-4**.

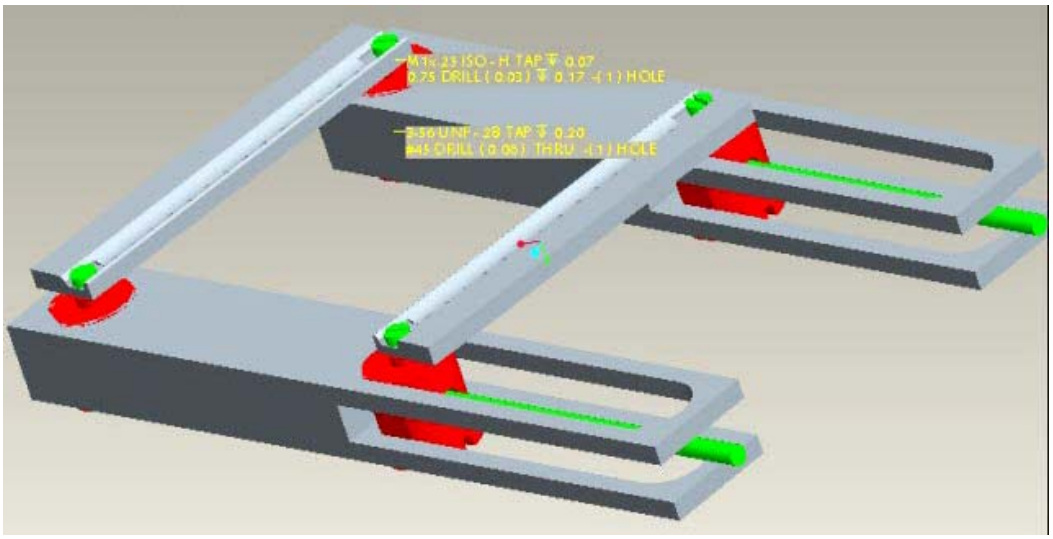

Figure 1-3: Second design proposal.

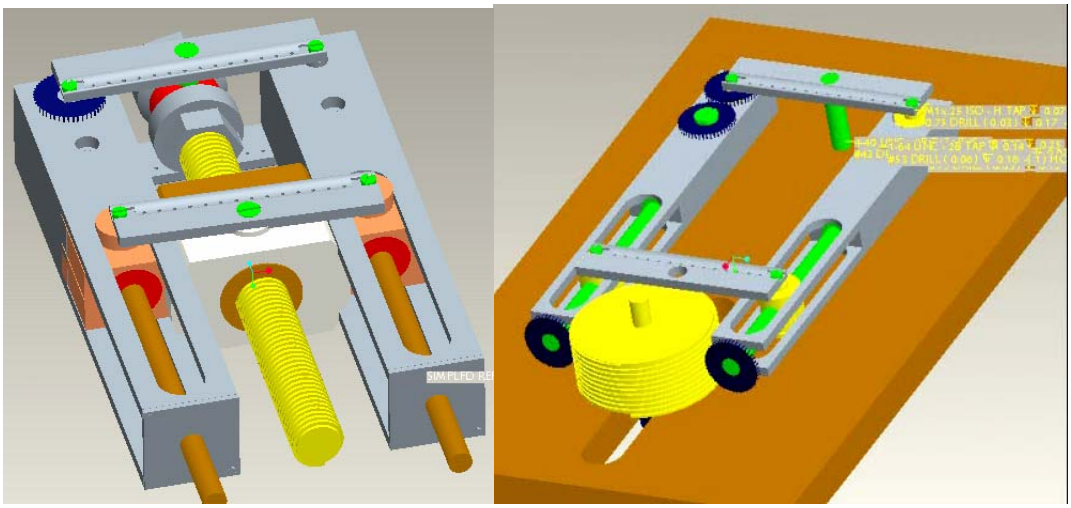

Figure 1-4: Third design iteration addressed actuation.

The third design review favored the twin ball screw frame but friction of the worm gear actuation was a concern. A consensus was attained to substitute in another spur gear to mesh with the two spur gears attached to the ball screws. This central spur gear is rotated manually with calibrated torque wrenches. Moreover, the central spur gear allows latitude to adjust the diameter to affect the gear ratio if needed to test materials of different stiffness values. The actual device is depicted in **Figure 3-11**. The frame can be articulated about the pivot axes to form a parallelogram as shown in **Figure 3-10** by simply disengaging the central spur gear.

Subsequent field tests with actual homograft tissue, proved the relaxation rates of the specimens exceeded expected values. The consequence is that maintaining torque and recording results manually cannot be accomplished precisely. At that time it was deemed necessary to automate the actuation system. An automated drivetrain gives the additional capability of testing the material dynamically. The design and validation of the load frame and the actuation system is the primary directive covered by this thesis. A secondary directive of obtaining material model parameters from empirical data is also covered.

2. Background & Theory

The engineering practice of characterizing the elastic and viscous behavior of materials is often divided generically into two disciplines: solid and fluid mechanics. The elasticity of a material relates the material deflections or distortions to the applied load or vice-versa **(Eq: 2-1)**, whereas viscosity relates the deflection or distortion rate with respect to time to the applied load or vice-versa **(Eq: 2-2)**.

Many materials exhibit the characteristics of both of these material types and are called "viscoelastic." Polymers have this behavior, and quite often so do biologic tissues. The nature of this behavior implies that these materials have strain rate dependence inherent in their stiffness or compliance. In other words, these materials can be quite rigid if the applied load or deflection is an impulse or has high slope, whereas they are quite soft if the applied stimulus is static in nature or has very small slope.

$$\sigma = E\varepsilon \qquad \textbf{(Eq: 2-1)}$$

$$\sigma_{shear} = \eta\dot{\varepsilon} \qquad \textbf{(Eq: 2-2)}$$

2.1. Linear Models

In linear theory, viscoelastic materials have two different modulus values. One is associated with the elastic behavior and is referred to as the "storage" modulus E'. The other is associated with the viscous behavior and is referred to as the "loss" modulus E" **(Eq: 2-3)**. The inverses of these two moduli are referred to as the "storage" and "loss" compliance **(Eq: 2-4)**.

$$E = E' + iE'' \qquad \textbf{(Eq: 2-3)}$$

$$D = D' + iD'' \qquad \textbf{(Eq: 2-4)}$$

Reciprocity relations between the modulus and compliance functions allow transformation between these two measures. **(Eq: 2-5)** is the reciprocity relation in the time domain, and **(Eq: 2-6)** is the reciprocity relation in the frequency domain.[3, 4]

$$\int_0^t E(t-\tau)\frac{dD(\tau)}{d\tau}d\tau = \int_0^t D(t-\tau)\frac{dE(\tau)}{d\tau}d\tau = 1 \qquad \textbf{(Eq: 2-5)}$$

$$E(i\omega)D(i\omega) = D(i\omega)E(i\omega) = 1 \qquad \textbf{(Eq: 2-6)}$$

Due to reciprocity, only two of the four parameters, E', E", D', and D", need to be determined. Nonetheless, the device described within this thesis is capable of evaluating all four independently which serves as a redundant check on the properties. The device is capable of evaluating the parameters under both static and dynamic conditions.

The materials tested are initially assumed to be linear solids such that the viscoelastic behavior can be modeled by a linear combination of springs and viscous dampers in parallel or series. If the material is nonlinear, then there will be discrepancy in results obtained from the dynamic versus the static tests. If this type of discrepancy is noticed, it is likely to be attributable to nonlinear strain rate dependence. If nonlinear behavior is due to displacement magnitudes, it will manifest itself in discrepancies between the static tests.

There are two common linear models accepted in the engineering community that represent viscoelastic behavior of real materials, **Figure 2-1** and **Figure 2-2**. Both models have similar behavior and can represent both relaxation and creep behavior, but each mathematical representation is more intuitive for one versus the other. The model of **Figure 2-1** is preferred to represent relaxation behavior, whereas **Figure 2-2** is preferred for creep behavior. More on this matter is discussed in sections **4.1** and **4.2.**

The time series expressions **(Eq: 2-7)** and **(Eq: 2-8)** for both models only represent the material response to a step input in strain for the Weichert model and stress for the Kelvin model. In the case of the Weichert model, inspection of **(Eq: 2-7)** reveals that the "relaxation modulus," E(t), is at a maximum at t = 0 and decays to its minimum value as $t \rightarrow \infty$. Hence, the stress relaxes over time even though the strain remains constant. This is the very nature of "stress relaxation." This is a phenomenon that is common and has to be accounted for in polymers that are utilized in gasket applications. This phenomenon also applies to biologic tissues.

In the case of the Kelvin model, inspection of **(Eq: 2-8)** reveals that the "creep compliance," D(t), is at a minimum at t = 0. The transient term, the time series summation, approaches a finite value as $t \rightarrow \infty$. There also exists a linear term with time which implies the

compliance can become infinite as t→∞. Hence, the strain continues to "creep" upward with time even though the stress remains constant. This is the very nature of "creep." This is a phenomenon that is common and has to be accounted for in polymers that are utilized in pressure containment applications. This phenomenon also applies to biologic tissues.

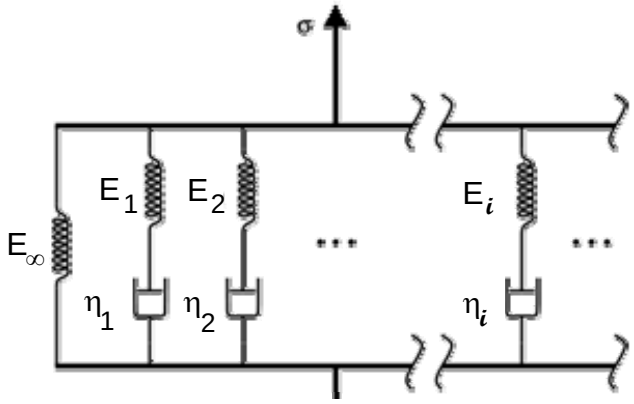

$$E(t) = E_{\infty} + \sum_{i=1}^{j} E_i e^{\frac{-E_i}{\eta_i}t} \qquad \textbf{(Eq: 2-7)}$$

Figure 2-1: Weichert model consisting of a number of Maxwell elements in parallel with a relaxation spring, E_{∞}.[5]

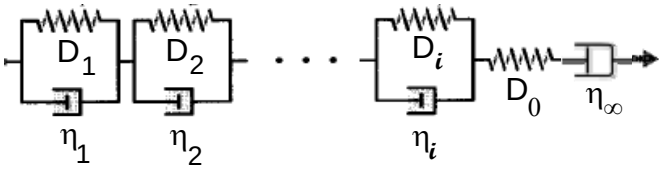

$$D(t) = D_0 + \frac{t}{\eta_{\infty}} + \sum_{i=1}^{j} D_i \left(1 - e^{\frac{-1}{D_i \eta_i}t}\right) \qquad \textbf{(Eq: 2-8)}$$

Figure 2-2: Kelvin general model consisting of a number of Voigt elements in series with a Maxwell element.[5]

2.2. Application of Fourier Transform to a Step Response

Without redundant discussion on the methodology covered in detail in sections **4.1** and **4.2**, one method to assess viscoelastic behavior is to monitor material response to a stimulus that resembles a step input in time. That stimulus could either be a force or displacement. **(Eq: 2-7)** and **(Eq: 2-8)** show that the time response of the linear viscoelastic models is a series of decaying or rising exponentials. Attempting to evaluate the individual material

parameters E_∞, E_i, η_i, D_0, D_i, η_i, and η_∞ from empirical data can become computationally intense, especially with higher-order models. There have been a number of numerical techniques practiced over the years. Moreover, once the parameters have been evaluated, there are arguments as to the relevance of inferring the complex parameters of the complex moduli of **(Eq: 2-3)** and **(Eq: 2-4)** since the conditions of these tests are considered static.

The design of this device took an alternative approach to analyzing the empirical data in the time domain. Nothing was assumed about the material dynamics, so it was not accepted a priori that a step input would not induce a dynamic response. This is a fundamental distinction in how viscoelastic practitioners define the relaxation and creep responses as discussed in sections **4.1** and **4.2**. These responses are stated to be attributed to a step input, yet in practice a ramp function stimulus is applied such that dynamic inertial effects are avoided.[3] This creates a paradox between the assumptions of the theoretical model and experimental practice since the true definition of step function is an instantaneous excitation.

For the response of the material to be truly independent of the input stimulus, the impulse response function is the ultimate objective. Since inducing a true impulse experimentally can be challenging, it is common practice to generate the impulse response function indirectly by using a step input. This is achieved by taking the derivative of the step response; the frequency domain response can then be found via the Fourier transform of that derivative.[6] This device evaluates the material parameters and complex modulus from the conversion of the empirical data in the time domain to the frequency domain, all performed in an integrated software application, National Instruments LabVIEW 8.6.1. This approach is not common among the viscoelastic practitioners but yields comparable results.

This technique is very effective if the system dynamics contain poles that are complex. It can be difficult if the poles are purely real. If the models of section **2.1** are correct for viscoelastic behavior, **(Eq: 2-7)** and **(Eq: 2-8)** indicate the poles of these materials should all be real. Indeed this appears to be the case on some analyses of data sets on various polymers presented in Chapter **5**. However, this could be an artifact of the test conditions as discussed.

In the case when all the poles are real, there is no frequency content to the system dynamics and the resulting impulse response is flat or devoid of structure. Despite the difficulties presented, if all of the poles are real the software is able to accurately evaluate the material parameters. The algorithm is based on perturbations in frequency spectrum of the material response.

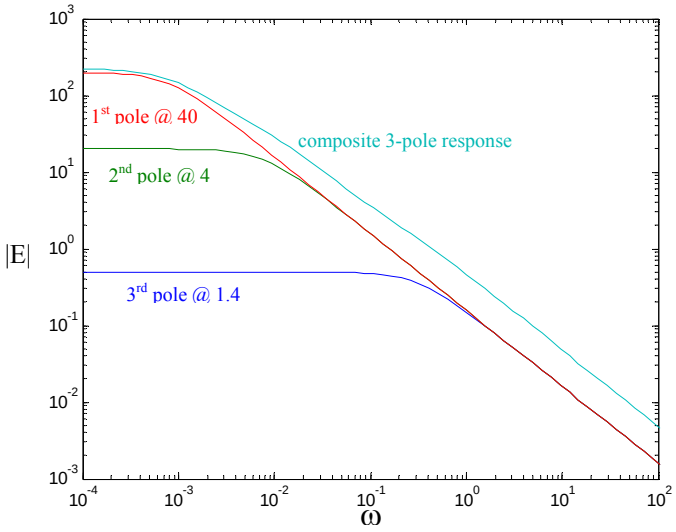

Figure 2-3: Step response frequency spectrum of multi-pole system.

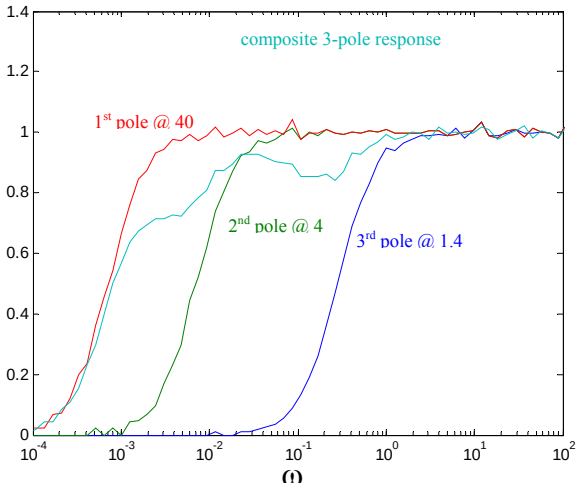

Figure 2-4: Derivative of step response frequency spectrum.

Figure 2-3 depicts a generic magnitude spectrum, synthetically generated, of a 3rd order system to a step input. Note that the decay slope at high frequencies is ultimately -1.0. **Figure 2-4** is the derivative of **Figure 2-3**. As high-order poles are encountered, perturbations in spectrum occur which serve as indicators to the locations of those poles.

Location of those poles allows the evaluation of the material and modulus parameters. This concept is proven out with analyses on PTFE in Chapter **5**.

Another potential benefit of performing the analyses in the frequency regime versus the time domain is the potential of the test apparatus to skew the response results due to some unforeseen background noise or something internal to the device. Since the impulse response spectrum should be devoid of structure for a system with all real poles, then deviations from a flat spectrum likely identify some external influence that could skew the results. In fact, that did occur in the relaxation test mode as discussed in sections **4.1.2** and **5.3**.

There is an important obstacle in accurately processing empirical data that is discrete. Due to the fact that empirical data is discrete, generating the frequency content of the material response dictates that "discrete" Fourier transform algorithms have to be employed. If the signal in the time domain is considered non-periodic, then interpretation of the transform results is not straightforward. This is attributable to the "discrete" Fourier transform inherently presumes periodicity. There are two techniques that can address this difficulty.

One is "windowing." An informal perspective of "windowing" is that it is a weighting function in the time domain. There are numerous "window" functions. The simplest are square or triangular while others are very sophisticated exponential-type functions such as the "Gaussian," "Riesz," "Riemann," "de la Vallé-Poisson," and many more.[7] LabVIEW software is utilized in this system for the servomotor control scheme, and it has integrated tools for performing the "discrete" Fourier transform. It has a number of pre-programmed windows but you can construct a custom window as well. The reciprocity relations of **(Eq: 2-5)** and **(Eq: 2-6)** are also commonly known as the convolution theorem. Convolution in the time domain results in multiplication in the frequency domain. The converse is true as well based on the fundamentals of the convolution theorem.[8] Since the "window" possesses its own Fourier transform, multiplication of two signals in the time domain, the "window" with the material step response results in convolution in the frequency domain. This fact makes the

magnitude spectrum of a non-periodic signal have some frequency content associated with that of the "window." **Figure 2-5** illustrates the effects of "windowing." What is depicted is the magnitude spectrum of the step response of a generic underdamped 2nd order system with two window types: 1) Hanning; 2) rectangle. The spectra are distinctly different. The response in the time domain is depicted in **Figure 2-6**. The Hanning window shows the expected peak at the oscillation frequency. The rectangle window contains some high-frequency peaks. Closer inspection of **Figure 2-6** shows some higher frequency oscillations on top of a base frequency just above 1 Hz. Which window is more appropriate? It takes some experience to be able to decipher the results and apply an appropriate "window" for the response signal of interest. It turns out that the rectangle window is well suited for non-periodic signals that lack frequency structure.

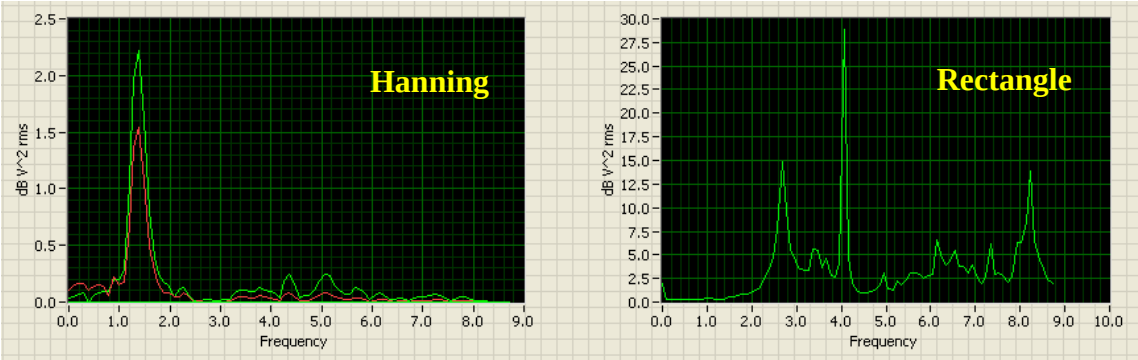

Figure 2-5: Effect of windowing.

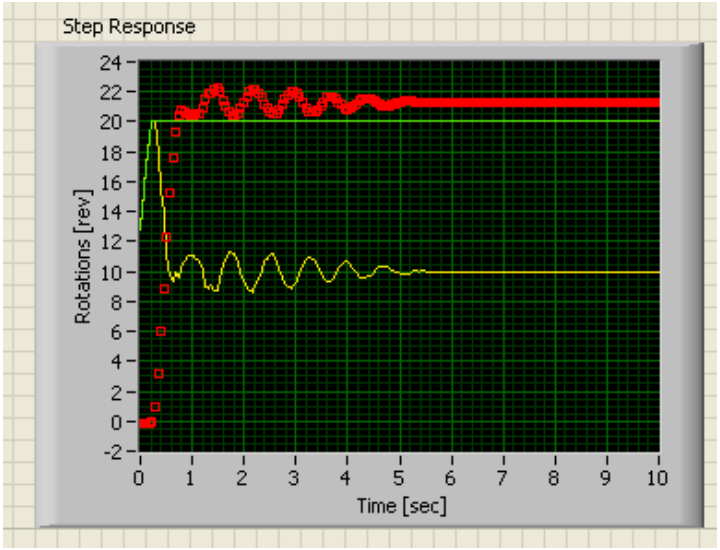

Figure 2-6: Generic underdamped step response of 2nd order system.

Another aspect to defining "windowing" is the time span. It is important that the window time span to be long relative to any transients in the response. If it is not, then those transients are essentially filtered out.

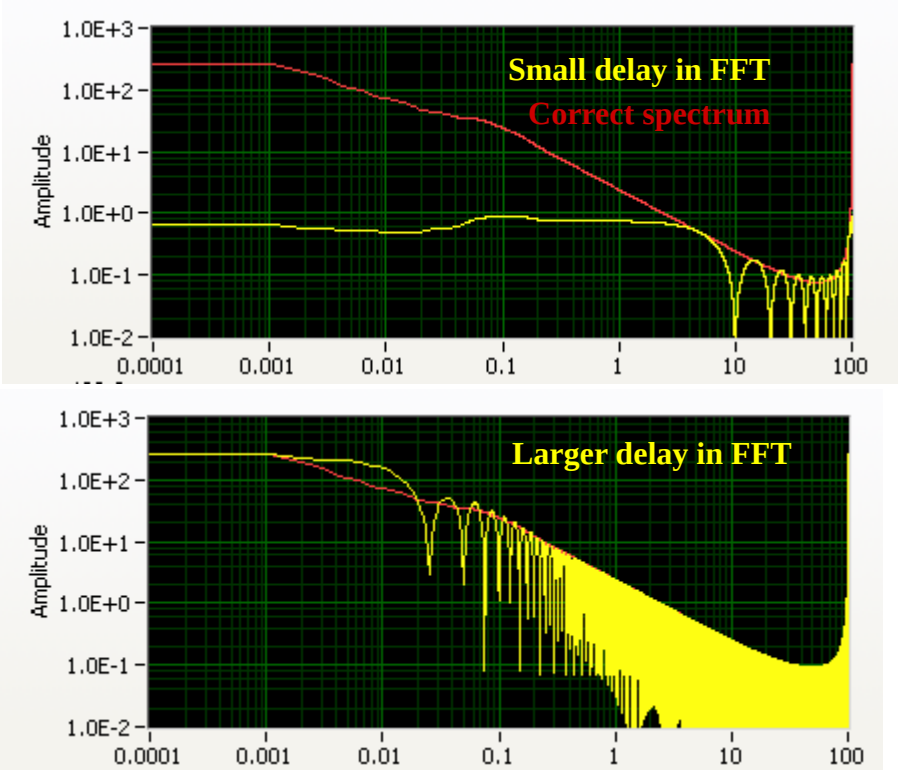

Figure 2-7: Effect of artificially induced delay of step input.

$$E(i\omega) = \frac{E_\infty}{i\omega} + \sum_{k=1}^{j} \frac{E_k \eta_k}{(i\eta_k \omega + E_k)} \qquad \textbf{(Eq: 2-9)}$$

$$D(i\omega) = \frac{D_0}{i\omega} + \frac{1}{\eta_\infty (i\omega)^2} + \sum_{k=1}^{j} D_k \left(\frac{1}{i\omega} + \frac{1}{(i\omega + D_k \eta_k)} \right) \qquad \textbf{(Eq: 2-10)}$$

The second technique aside from "windowing" to facilitate obtaining frequency spectrum of a non-periodic signal is to introduce a delay in the stimulus that is input to the "discrete" Fourier transform. This is simply done by making the step input magnitude zero for all time less than some prescribed delay. The effect of such a delay on the magnitude spectrum of actual relaxation test data is depicted in **Figure 2-7**. Without an adequate delay, the DC gain is incorrect. As it is for "windowing," determining an appropriate delay is a matter of

experience. In the particular data set of **Figure 2-7** the duration of the experiment was 1000 seconds and the induced delay was 40 seconds.

At this juncture, the material parameters can be evaluated by the software from these pseudo-static tests, and then the complex modulus can be inferred analytically via substitution of the appropriate values into **(Eq: 2-9)** and **(Eq: 2-10)**. These two equations are the Fourier transforms of the time-domain step response described by **(Eq: 2-7)** and **(Eq: 2-8)** respectively. Both **(Eq: 2-9)** and **(Eq: 2-10)** can be split into imaginary and real constituents. These constituents are grouped according to **(Eq: 2-3)** and **(Eq: 2-4)**. As discussed in section **2.1**, the real component of **(Eq: 2-3)** is associated with the elastic behavior of the material and is referred to as the "storage" modulus E'. The imaginary component is associated with the viscous behavior and is referred to as the "loss" modulus E". The inverses of these two moduli are referred to as the "storage" and "loss" compliance **(Eq: 2-4)**. Moreover, reciprocity relations between the modulus and compliance functions allow transformation between these two measures as described by **(Eq: 2-5)** and **(Eq: 2-6)**.

The utility of the Fourier transform allows for an expedient manner to process stress relaxation and creep compliance test data that are pseudo-static. In turn, it can then be implemented to infer the dynamic behavior of the material. If the material is truly linear, then this should yield identical results to data obtained from the harmonic mode tests of section **4.3**.

The harmonic mode tests described in section **4.3** are configured such that the stimulus is an oscillating torque. This is somewhat of an artifact of the servomotor amplifier wiring configurations as described in section **3.2.1**. In this case **(Eq: 2-10)** is more relevant in correlating the pseudo-static results with those of the harmonic mode tests. If the stimulus is a displacement then **(Eq: 2-9)** is the function of choice. Stated earlier in this section, it is common practice to generate the impulse response function indirectly by taking the derivative of the step response. There is a well known theorem stating the time domain derivative is equivalent to multiplying by $i\omega$ in the frequency domain.[7] The derivatives of **(Eq: 2-9)** and

(Eq: 2-10) yield **(Eq: 2-11)** and **(Eq: 2-12)**. **(Eq: 2-11)** and **(Eq: 2-12)** now represent the impulse response in the frequency domain. Applying the fundamental definitions of complex variables in **(Eq: 2-13)** and **(Eq: 2-14)**, **(Eq: 2-11)** and **(Eq: 2-12)** are broken into real and imaginary constituents juat as for **(Eq: 2-3)** and **(Eq: 2-4)**. Those real and imaginary constituents correlate directly to the real and imaginary constituents of **(Eq: 2-3)** and **(Eq: 2-4)**. These constituents are given by **(Eq: 2-15)** through **(Eq: 2-18)**.

$$G_{relax}(i\omega) = E_\infty + \sum_{k=1}^{j} \frac{E_k \eta_k i\omega}{(i\eta_k\omega + E_k)} = E_\infty + \sum_{k=1}^{j} \frac{E_k \eta_k i\omega(-i\eta_k\omega + E_k)}{(i\eta_k\omega + E_k)(-i\eta_k\omega + E_k)} \quad \textbf{(Eq: 2-11)}$$

$$G_{creep}(i\omega) = D_0 + \frac{1}{\eta_\infty i\omega} + \sum_{k=1}^{j} D_k\left(1 + \frac{i\omega}{(i\omega + D_k\eta_k)}\right) = D_0 + \frac{1}{\eta_\infty i\omega} + \sum_{k=1}^{j} D_k\left(1 + \frac{i\omega(-i\omega + D_k\eta_k)}{(i\omega + D_k\eta_k)(-i\omega + D_k\eta_k)}\right) \quad \textbf{(Eq: 2-12)}$$

$$i^2 = -1 \quad \textbf{(Eq: 2-13)}$$

$$\frac{1}{i} = \frac{i}{i^2} = -i \quad \textbf{(Eq: 2-14)}$$

$$E'(i\omega) = \Re e\left[G_{relax}(i\omega)\right] = E_\infty + \sum_{k=1}^{j} \frac{E_k(\eta_k\omega)^2}{E_k^2 + (\eta_k\omega)^2} \quad \textbf{(Eq: 2-15)}$$

$$E''(i\omega) = \Im m\left[G_{relax}(i\omega)\right] = \sum_{k=1}^{j} \frac{E_k\eta_k\omega}{E_k^2 + (\eta_k\omega)^2} \quad \textbf{(Eq: 2-16)}$$

$$D'(i\omega) = \Re e\left[G_{creep}(i\omega)\right] = D_0 + \sum_{k=1}^{j} \frac{D_k}{(D_k\eta_k)^2 + \omega^2} \quad \textbf{(Eq: 2-17)}$$

$$D''(i\omega) = \Im m\left[G_{creep}(i\omega)\right] = \frac{1}{\eta_\infty\omega} + \sum_{k=1}^{j} \frac{D_k\eta_k\omega}{(D_k\eta_k)^2 + \omega^2} \quad \textbf{(Eq: 2-18)}$$

$$E_k = \frac{1}{D_k} \quad \textbf{(Eq: 2-19)}$$

$$(A + iB) = \sqrt{A^2 + B^2}\, e^{i\phi} \quad \textbf{(Eq: 2-20)}$$

$$\phi = \tan^{-1}\left(\frac{B}{A}\right) \quad \textbf{(Eq: 2-21)}$$

Ignoring the offset values for both relaxation and creep, E_∞ and D_0 respectively, as well as the linear term with respect to time for creep, the frequency behavior is enveloped within the series summation terms of **(Eq: 2-15)** through **(Eq: 2-18)**. Intuitive insight of the frequency response can be developed by examination of the spectra generated under the assumptions stipulated by **(Eq: 2-19)**. **(Eq: 2-19)** is simply stating that individual modulus and

compliance values of the individual segments of both the Weichert and Kelvin models, **Figure 2-1** and **Figure 2-2** respectively, are algebraic inverses of each other. In reality this is not necessarily the case but for the sake of insight it is convenient. Another convenient assumption is that the viscous damping elements of the individual segments are equivalent as well. These simplifying assumptions yield identical decay rates of the exponentials contained within the series terms of both **(Eq: 2-8)** and **(Eq: 2-9)**.

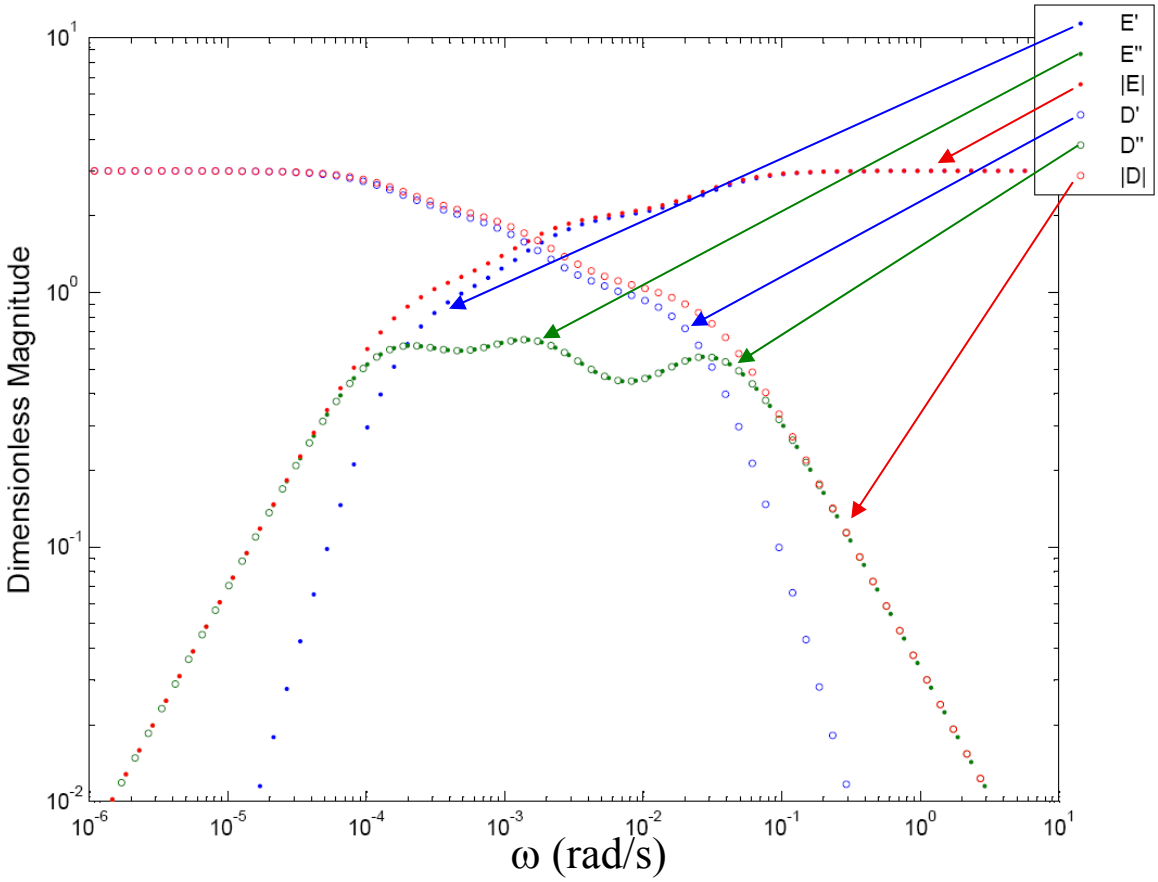

Figure 2-8: Relaxation & creep parameters magnitude spectra.

Applying these assumptions to the series summation terms of **(Eq: 2-15)** through **(Eq: 2-18)**, along with another special condition that all $E_k = 1.0$, results in the magnitude spectra depicted in **Figure 2-8**. The "loss" constituents for relaxation and creep, **(Eq: 2-16)** and **(Eq: 2-18)**, exhibit identical behavior. At low frequencies both E" and D" increase by ω. At a particular frequency both parameters level out and maintain a relatively constant value over a finite frequency band. The location of the initial rollover is an indication of the location of

slowest decay rate value, also referred to as the slowest pole. As the frequency becomes sufficiently large both E" and D" diminish by ω^{-1}. The location of the final rollover is an indication of the location of fastest decay rate value, also referred to as the fastest pole. The number of peaks and valleys within the frequency band where the magnitude remains relatively constant is a clue as to the order of the system. In other words, how many terms exist within the series summation of **(Eq: 2-15)** through **(Eq: 2-18)**. Moreover, the location of the peaks and valleys serves as clues to the values of the intermediate decay rates.

Unlike the "loss" constituents the "storage" constituents for both relaxation and creep do not exhibit identical behavior. However, they do appear to mirror each other in the sense that a symmetric axis can be defined about their intersection points. **Figure 2-8** indicates that E' increases by ω^2 for sufficiently low frequencies. At higher frequencies E' approaches an asymptotic value that is equivalent to the summation of all the elastic elements in each of the Maxwell segments of the Weichert model of **Figure 2-1**. This behavior is consistent with the series terms of **(Eq: 2-15)**. Conversely, **Figure 2-8** indicates that D' is asymptotic at low frequencies and diminishes by ω^2 for sufficiently high frequencies. This behavior is consistent with the series terms of **(Eq: 2-17)**.

The total magnitude is the combination of both the "loss" and "storage" constituents as indicated by **(Eq: 2-20)**. The total magnitude is indicated in **Figure 2-8** by solid circles for the relaxation modulus and open circles for the creep compliance. The phase relation for **(Eq: 2-20)** is given by **(Eq: 2-21)**. Applying the same assumptions as for **Figure 2-8** the phase spectra is depicted in **Figure 2-9**. A mirror-like relation is shown as well. This is due to the fact that the numerator of **(Eq: 2-21)** is identical between creep and relaxation but the denominator has the inverted or reciprocal behavior of the "storage" constituents with frequency as depicted in **Figure 2-8**.

Despite the assumptions and special conditions applied to construct both **Figure 2-8** and **Figure 2-9**, the frequency behavior or spectra structure of the series summation terms of either the creep or relaxation does not deviate even when the special conditions and

assumptions are not valid. In other words, the viscous dampers play no significant role in both the Weichert and Kelvin models of **Figure 2-1** and **Figure 2-2** respectively when the stimulus frequencies are sufficiently low. In this frequency regime the modulus of the Weichert model is E_∞. In the case for the Kelvin model, its compliance goes to infinity due to η_∞ If η_∞ is not present, and a solid connection is made to D_0, the resulting compliance would be due to series arrangement of the compliance elements of each Voigt segment as shown by **(Eq: 2-22)**.

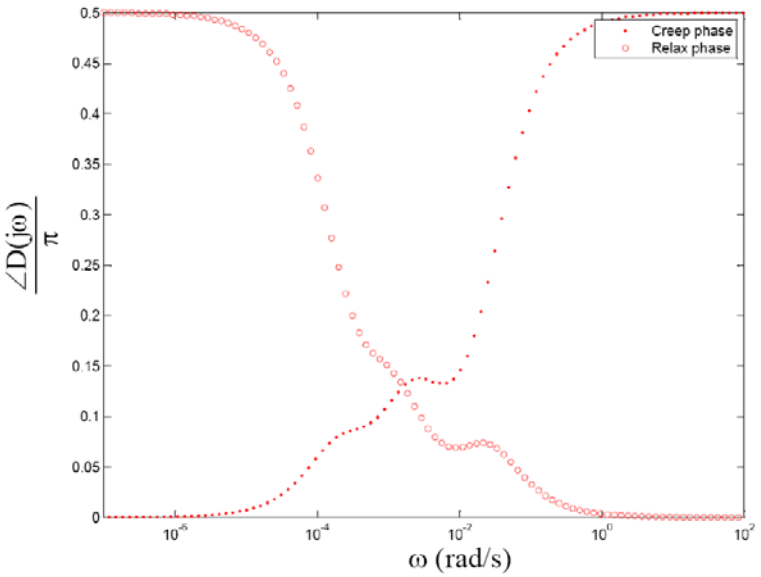

Figure 2-9: Relaxation & creep parameters phase spectra.

As the stimulus frequency increases to a sufficient level, the viscous elements begin to dissipate energy. That energy dissipation increases both models' resistance to motion, hence the magnitude of the relaxation modulus increases with frequency and reaches an asymptotic value. Conversely, the compliance diminishes from an asymptotic value with frequency.

As discussed earlier, there are two constituents for both creep compliance and relaxation modulus. The "storage" constituent is associated with the elastic elements E_k and D_k, whereas the "loss" constituent is associated with the viscous dampers. As the viscous dampers dissipate energy with increasing frequency, the magnitudes of both "loss" constituents increase by ω^2. However, in both cases the energy dissipation is finite; therefore the magnitude does not sustain the ω^2 dependence. The source of this finite dissipation can

come from a variety of mechanisms, but the underlying principle is that as the stimulus frequency increases more power is attempting to be deposited into the material. Depending on the material that power may be converted to heat or mass flow and the material has finite capability of transporting that energy. The consequence is that the impedance of the material increases and in turn the ability to transmit more energy or power into the material becomes exceedingly more difficult. The result is that the damper becomes more rigid.[9, 10]

One other matter to consider as the frequency transitions into the high frequency regime is that eventually inertial effects will begin to affect the response. If this were to occur a much different frequency spectrum would result, but that is a contribution that viscoelasticity does not account for as described earlier in this section regarding the paradox in assumptions for the step response.

The "loss" constituents' magnitude remains relatively constant over a finite frequency band before it eventually dissipates by ω^{-2}. This is now the high frequency regime where the viscous dampers essentially seize up. In this regime the Voigt segments of the Kelvin model also seize and the only element capable of supporting motion is the elastic element D_0. In the case of the Weichert model, the modulus is due to the parallel arrangement of the elastic elements of each Maxwell segment as shown by **(Eq: 2-23)**.

The fact that this consistency exists in frequency behavior makes it plausible to infer pole locations as described earlier for the creation of **Figure 2-4**. Moreover, through the utility of the Fourier transform, a figure such as **Figure 2-8** can be constructed from empirical data which can serve to locate the system poles as well. However, this is all predicated on the condition that the material does respond linearly with the stimulus. The linearity condition is a pervasive theme throughout this thesis. Nonlinearity renders the principle of superposition invalid upon which the Fourier transform relies.

$$D\left(\omega \to 0\right) = D_0 + \sum_{k=1}^{j} D_k \qquad \textbf{(Eq: 2-22)}$$

$$E\left(\omega \to \infty\right) = E_\infty + \sum_{k=1}^{j} E_k \qquad \textbf{(Eq: 2-23)}$$

2.3. Non-Linear Contingencies

In linear theory, the individual elements in both the Weichert and Kelvin models described in section **2.1** remain constant over the entire range of displacement or load as well as over any rate of change in the displacement or load. This is not the case in nonlinear materials, and one expects to observe nonlinearity in many biologic tissues. Fortunately, the scope of this research confined the load and displacement levels to be commensurate with physiologic conditions. Under physiologic conditions the material response is generally considered to be linear. Nonetheless, this device is capable of quantifying any nonlinear behavior since displacement and load rates and magnitudes can be controlled. Modifications to each of the four test modes covered in Chapter **4** can be adopted to quantify any nonlinear behavior.

3. Design

The test device is a digitally controlled drivetrain that converts rotational motion of two servomotors into linear displacements. **Figure 1-1** gives a contextual perspective as to the size of the device. The entire device without the servomotors fits within an open-palmed hand. The specimens that it tests are no larger than a 25 mm square.

Aside from longitudinal extension of the specimens, this device is capable of inducing shear. This is achieved via pivoting about the four specimen mounting points such that the load frame becomes a parallelogram, **Figure 3-1**. The acute angles of the parallelogram are designed to be 60° at their minimum. Much of this will be dictated by the modular design of the specimen brackets which is discussed in section **3.1.1**.

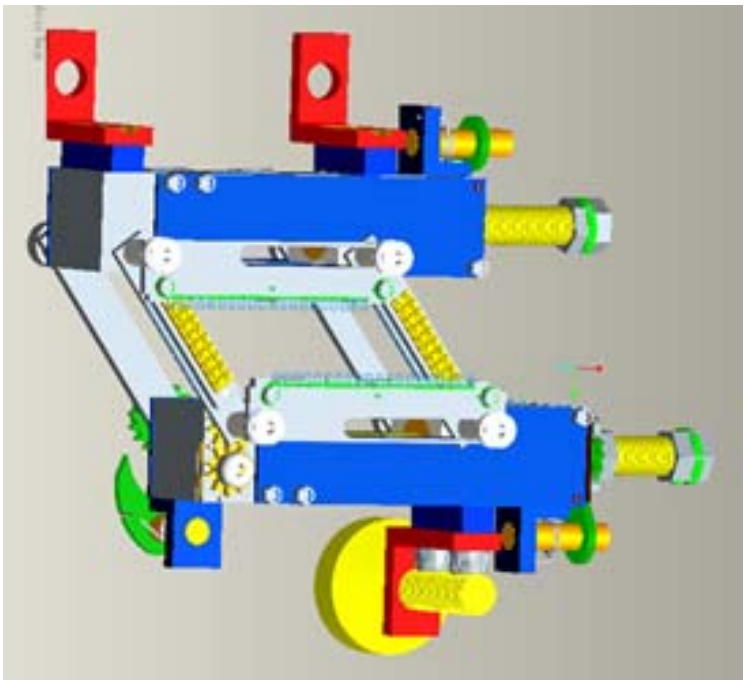

Figure 3-1: Shear test mode.

3.1. Device Load Frame

The load frame converts rotational motion of two servomotors into linear displacements via two 6-mm ball screws. Ball screw technology was selected over lead screws because of friction. Since many of the biologic tissues of interest are soft with respect to engineering materials it was deemed the additional cost of ball screws is well justified in order to keep the

relative magnitude of the friction low compared to the load seen as stress in the specimens. **Figure 3-3** indicates that the frictional coefficient of ball screws is an order of magnitude lower than that of lead screws.

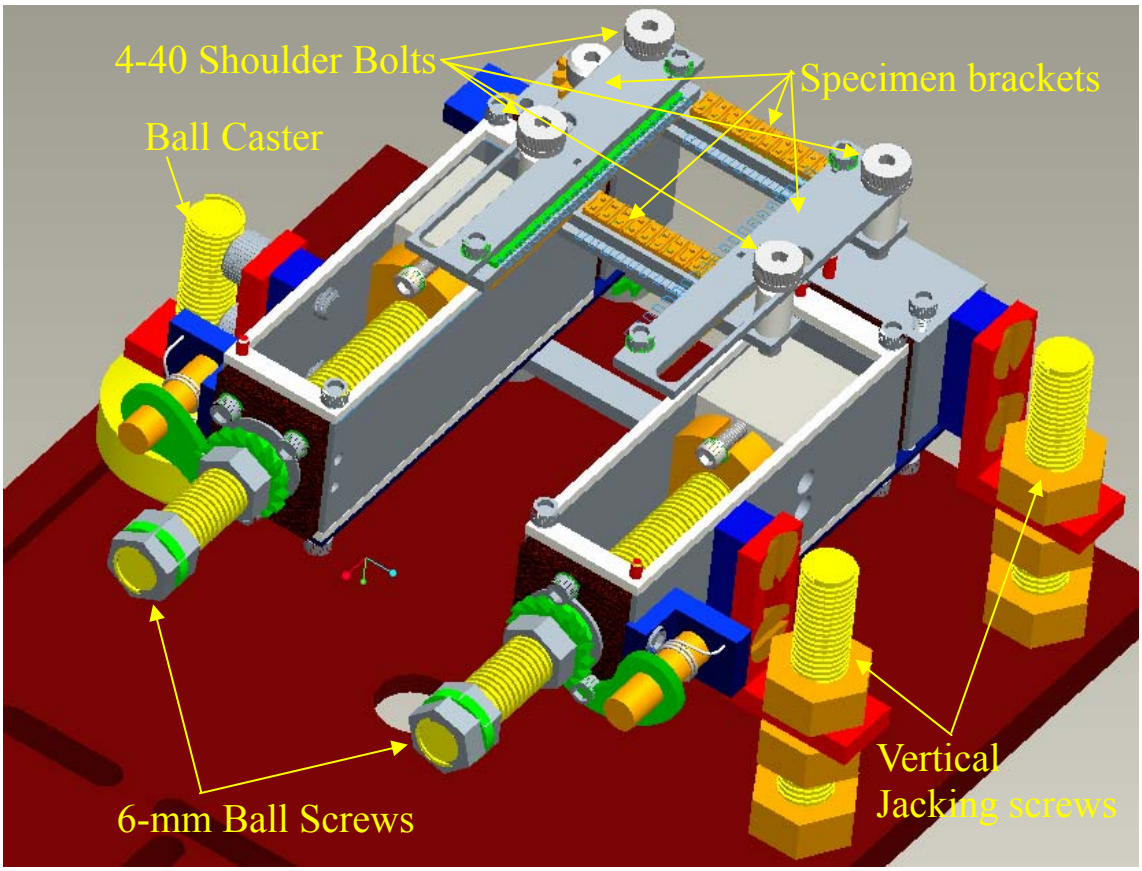

Figure 3-2: Load frame.

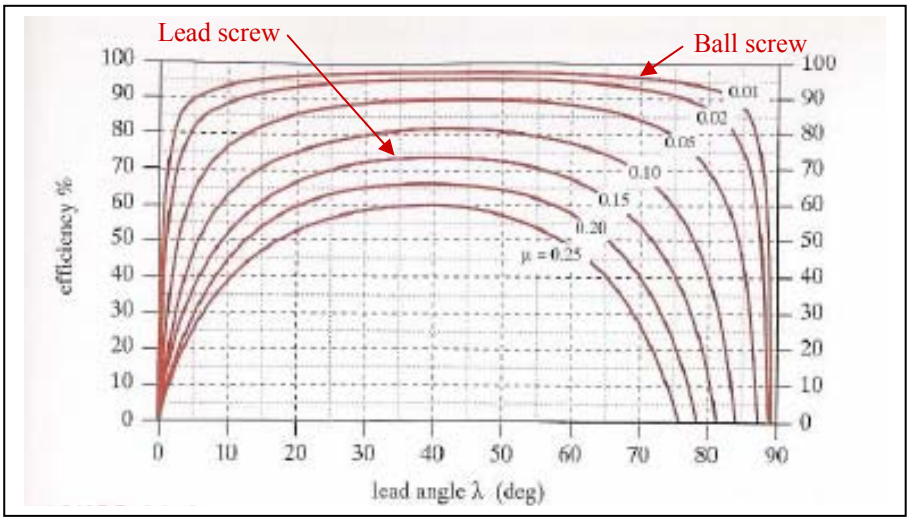

Figure 3-3: Benefit of ball screw.[11]

The ball screws are anchored within the two drive frames of **Figure 3-2** and held concentric via four precision 6-mm ball bearings. Those four ball bearings are seated via countersunk holes within the drive frames. The holes are concentric with the longitudinal axis of each drive frame within 0.001". The ball bearings are press-fit into the countersunk holes with the manufacturer's prescribed tolerances specified in **Appendix B.2**.

Figure 3-4 illustrates how the ball screws are longitudinally fixed. The original concept was to employ 6-mm spherical washers which are depicted in **Figure 3-4**. Unfortunately the spherical curvature of these washers is too generous such that the spherical surface contacts both the inner and outer racings of the ball bearings. So four nuts with shoulders were custom fabricated. These brass nuts had special threads machined such that they conform to the ball screw threads. The shoulder of the brass nuts butts against the inner racing of the ball bearings. Extreme caution had to be exercised on assembly because over-torque of these nuts tended to extrude the inner racing from the outer racing. These 6-mm ball bearings cannot bear much thrust load. So if a redesign is in order this is an area that could be examined in a future redesign.

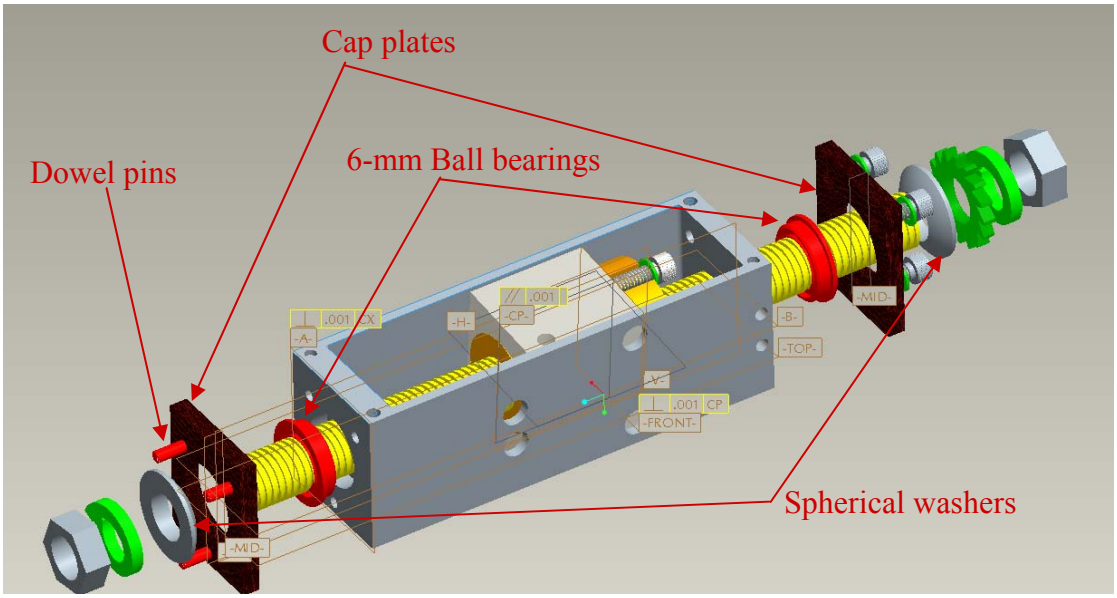

Figure 3-4: Anchoring of the ball screws.

Due to the thrust limitation of the ball bearings two cap plates with a recessed area pin the integral flange of the ball bearing outer racing. Some redundancy to keep the ball screw fixed longitudinally exists. **Figure 3-4** illustrates that the posterior cap plate is located via dowel pins, whereas the anterior cap plate is located by cap screws.

The ball screw frame mates with the anchor blocks via the three dowel pins in the posterior of the ball screw frame. The dowel pin locations are defined such that the orientation of the ball screw frame is unambiguous. Moreover, one sees in **Figure 3-5** that the location of the dowel pins has some tight tolerances so that the central axis of the ball screw is collinear with the threaded holes for the shoulder bolts that serve as the mounting column of the specimen and stabilizer brackets on the top and bottom planes of the load frame.

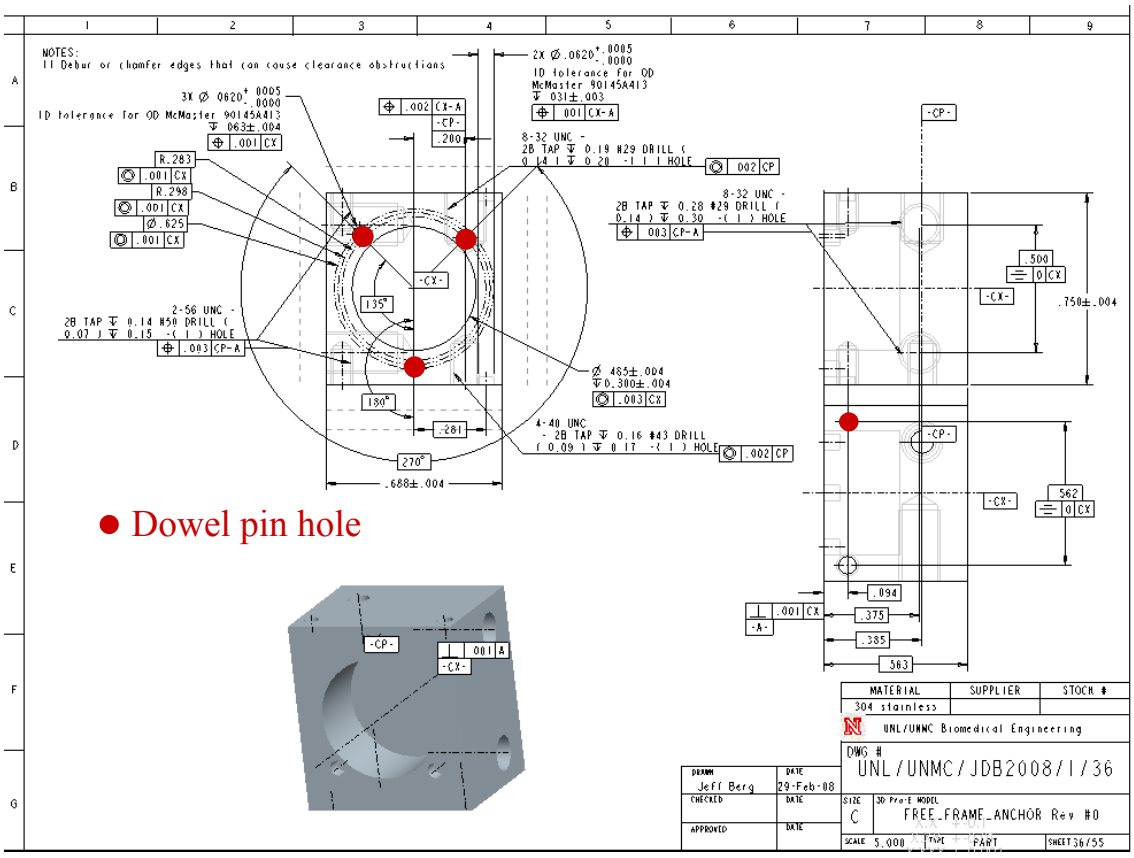

Figure 3-5: Dowel pin locations.

The anchor block and the ball screw frame are not secured by the dowel pins alone. They become fully coupled via a top and bottom guide plate. The subassembly drawings **Appendix**

Fig A-5 and **Appendix Fig A-6** show that the guide plates are precision located via dowel pins as well. This ensures that the oblong tracking through-hole for the shoulder bolts attached to the ball screw nut is aligned with the ball screw central axis.

The ball screw frames coupled to the anchor blocks via the guide plates constitute the two drive frames of **Figure 3-2**. The two drive frames become the load frame once they are coupled via the specimen brackets and the stabilizer brackets on the bottom plane of the load frame. The stabilizer brackets are more visible in **Figure 3-1**. The details of this coupling follow in section **3.1.2** since it factors into the kinematics of the load frame.

3.1.1. Modular Specimen Fixturing

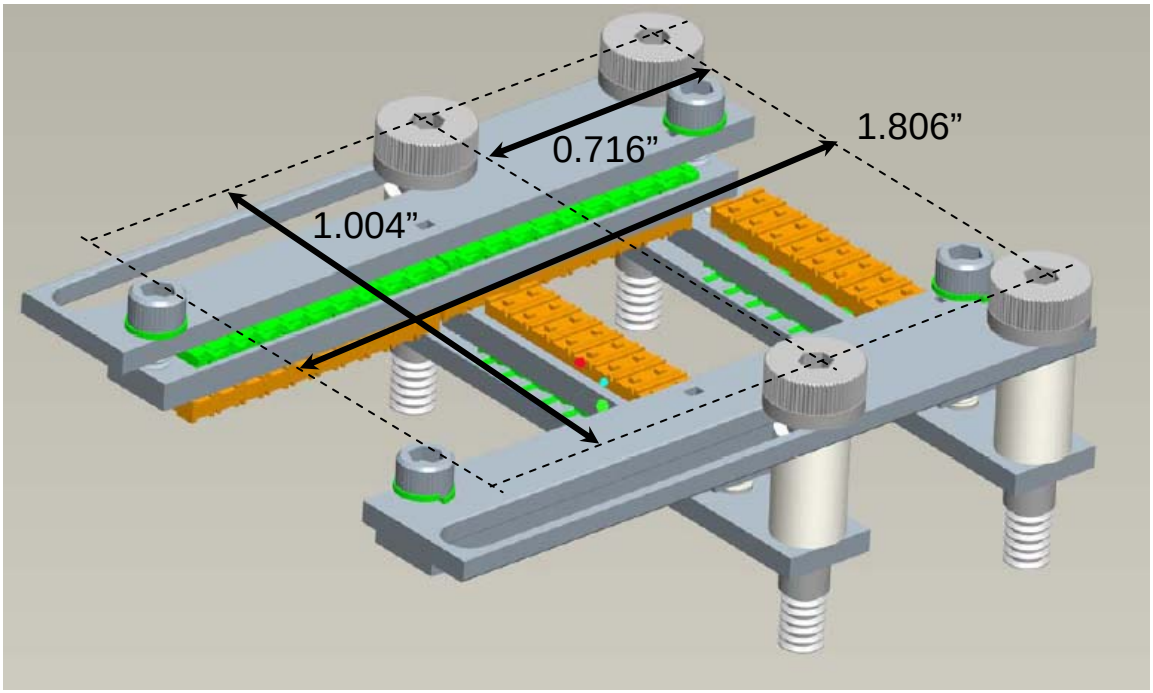

Figure 3-6: Specimen brackets.

As previously mentioned in Chapter **1**, boundary conditions can factor into the viscoelastic response of the specimen. So the design of the drivetrain and the specimen fixturing were segregated so that the drivetrain interface has a universal threaded connection. This allows the possibility that for any specific application the specimen brackets can be customized, and the drivetrain simply provides the basis to apply appropriate stimulus to evaluate the

specimen response. The two threaded holes in the anchor block of the load frame are 8-32 UNC and the two holes in the pivot/slide block attached to the ball screw are 4-40 UNC.

Figure 3-6 is the rendering of the specimen brackets specific to the research sponsored by Dr. James Hammel of UNMC. As previously mentioned the materials being evaluated are various implant materials for a cardiac septal defect in infants. The implants are sutured into place when deployed and the design of these brackets is to emulate the boundary conditions of those sutures. Likewise, for other materials the bracket design can be customized to emulate whatever physiologic conditions the material may experience.

In this particular case the brackets are configured to mimic the suture interval necessary for the implant application. The suture pattern has puncture holes of 0.5 mm spaced 2 mm apart. The first brackets fabricated allowed the physician to suture the specimen directly to the bracket with Vicryl thread. This proved to be labor intensive. To expedite specimen mounting, another bracket assembly incorporates MOLEX IDT connectors which have the precise pattern of the suture interval needed. These connectors are utilized in the electronics industry for connections of ribbon cables to PC boards (**Figure 3-7**). Their utility, aside from the speed with which they can be fastened, is in the ability to pierce the specimen and their interlocking mechanism that ensures the specimen is secure.

To validate the use of these connectors, tests were conducted on an INSTRON uniaxial mechanical test machine. There were concerns that the piercing of the material by the pins of these connectors could cause premature failure of the specimen. Both homograft and umbilical cord tissue were tested to failure. In conjunction with these tests, comparisons were drawn from this study between these materials from a conventional elastic response and failure strength perspective. A synopsis of those results is included in section **5.7**. It was concluded that these connectors are viable fixation devices for these materials.

The specimen brackets are secured to the load frame via four shoulder bolts. **Figure 3-6** illustrates the longitudinal extension degree of freedom the shoulder bolts allow. An additional design criterion was imposed on the specimen bracket assembly in that it has the

capability to subject the specimen to a shear mode test. **Figure 3-8** depicts the specimen bracket assembly pivoting into a shear test mode configuration. Two motives inspired this capability: one is that there are concerns if tissue implants for vascular applications incur out of plane deflections, and the other is that viscoelastic materials will often exhibit greater viscous or damping behavior when subjected to shear forces.

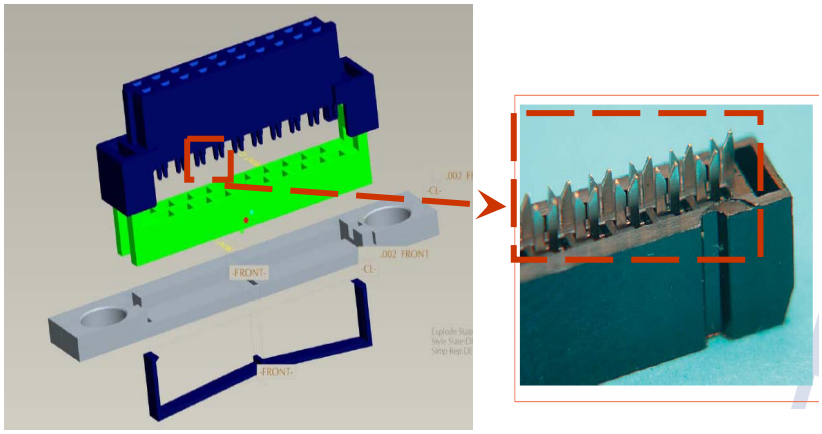

Figure 3-7: MOLEX IDT connector used for specimen mounting.

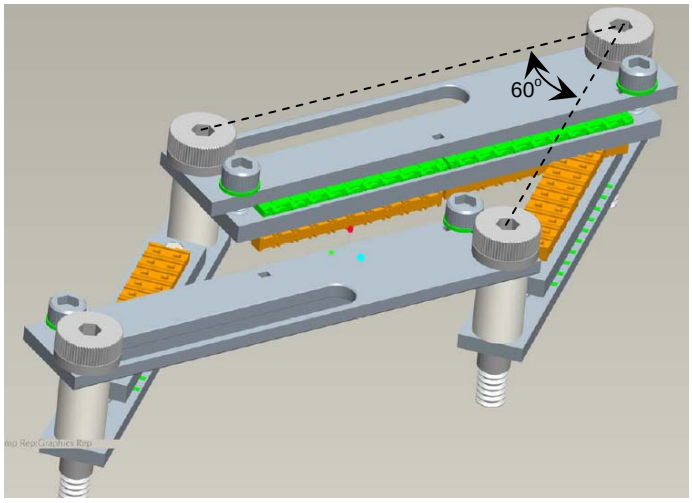

Figure 3-8: Shear test mode.

Three matters had to be addressed in the bracket assembly design to accommodate the design criteria. The foremost is that to accomplish shearing motion all four boundaries of the specimen must be fixated. The second is that to accomplish adequate shearing motion the brackets need to pivot a minimum of 45°. These two matters are in conflict with each other. To fixate the specimen, anchoring mechanisms are required. Attempting to fixate the specimen at or near pivot axes interferes with the shearing angle capability of the assembly.

So compromises have to be incorporated in the design. **Figure 3-8** depicts the interference potential at the pivot corners. The design of the MOLEX IDT connectors allow for the discretionary clipping of the gold-colored headers. This can be done on a case by case basis. Illustration of this clipping potential is in **Figure 3-9**.

The third matter is that the fixation of the specimen needs to be on the same vertical plane to not artificially induce out of plane distortions beyond what is induced by the shearing motion. This necessitates the Teflon standoff tubes that envelope the shoulder bolts colored in white.

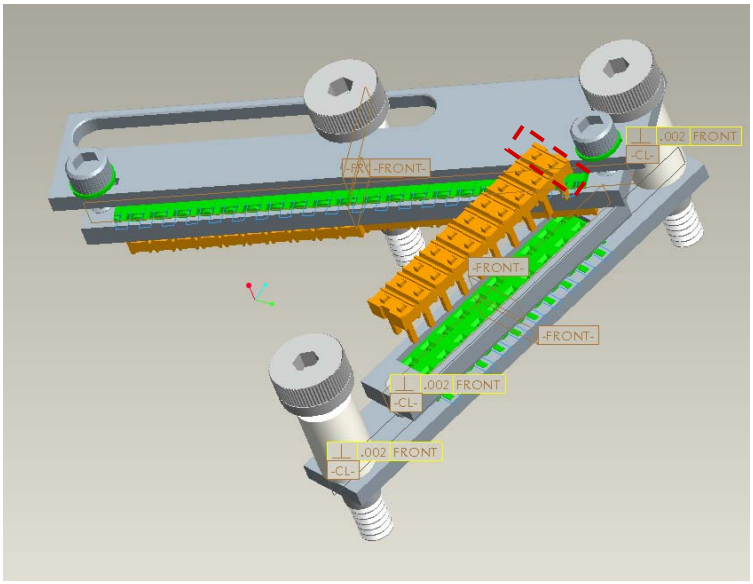

Figure 3-9: Clipping of MOLEX connectors.

The complications the shearing requirements impose on the device are accounted for in the design but the primary objective and capability focuses on the longitudinal test capacity of the servomotors to perform the four test modes outlined in Chapter **4**.

3.1.2. Load Frame Kinematics

As demonstrated in the previous section, the specimen brackets have the capability to extend and rotate. Longitudinal extension is achieved via conversion of rotational motion of the servomotors to linear translation through the ball screw. **Figure 3-10** demonstrates rotation actuation. There are two shoulder bolts in the same plane with spur gears concentric to the bolts. The shoulder bolt indicated by the red arrow can be rotated by an Allen wrench

or a servomotor with the appropriate coupling. The spur gear concentric to this bolt is brazed to the bolt and will be referred to as the pivot gear. The adjacent spur gear is fixed to the anchor block via dowel pins.

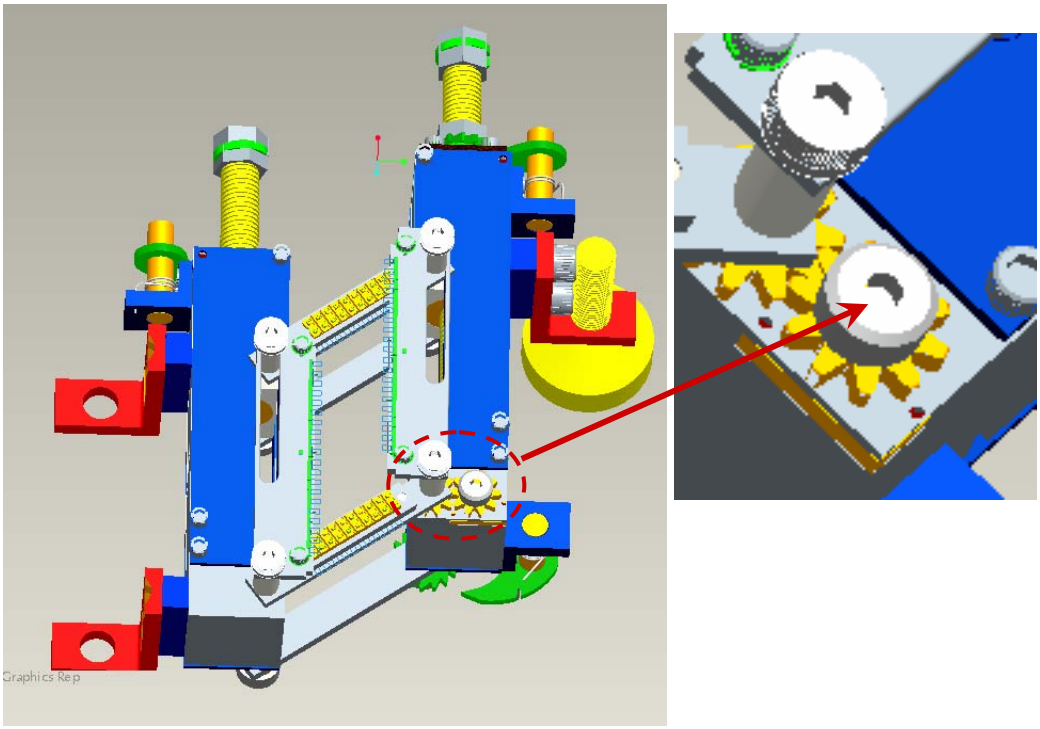

Figure 3-10: Rotation actuation.

The load frame is kinematically mounted to the base plate via two vertical jacking screws and a ball caster. This is illustrated in **Figure 3-2**. The four pivot points of the specimen brackets in conjunction with the ball caster allow for independent motion of the free-side axis of the load frame to which the ball caster is coupled. This mounting scheme minimizes binding between the two drive frames axes as the specimen is extended longitudinally. Moreover, this scheme promotes rotation actuation when torque is applied to the pivot gear. Note that it is necessary to disengage the servomotors from the ball screws to allow for this rotation.

One detrimental consequence of this scheme is that during longitudinal extension the servomotors must rotate in conjunction. If this does not occur the rotational degree of

freedom of the specimen and stabilizer brackets will result in a lateral binding of the free-side drive axis. More on this matter is discussed in the alignment issues of the next section **3.1.3**.

3.1.3. Drivetrain Alignment

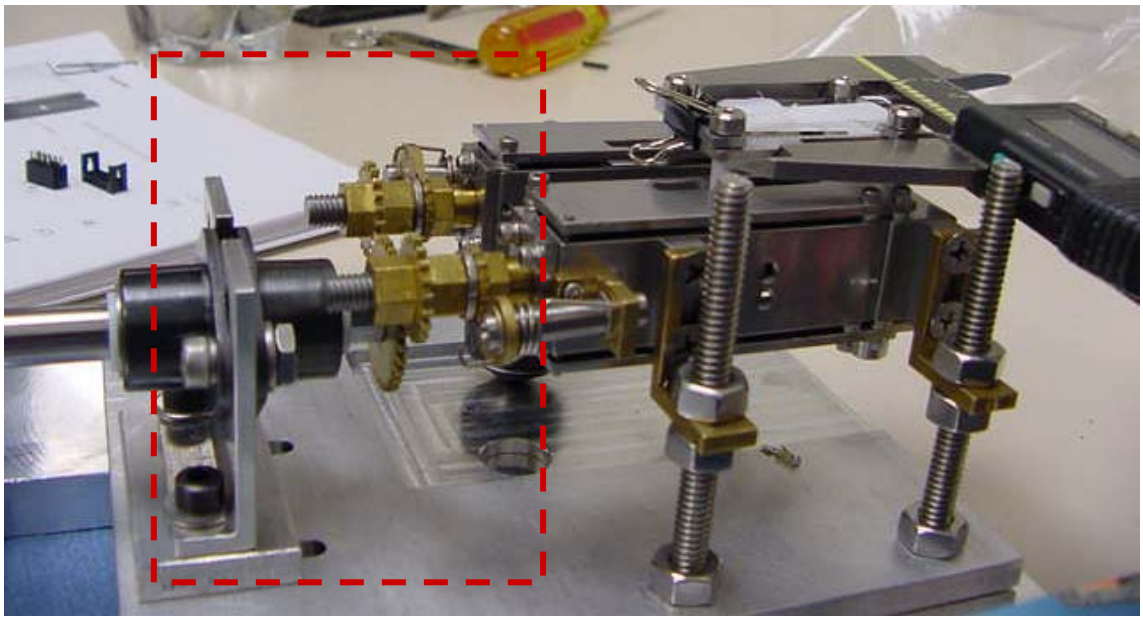

Figure 3-11: Manual actuation of one central gear.

The kinematic mounting scheme of the load frame as described in the previous section minimizes binding between the two axes of the load frame as the specimen is extended longitudinally. This benefit exists in the original design of the actuator mechanism which is manual rotation of a central spur gear via a calibrated torque wrench. The central gear meshes with two spur gears attached to the ball screws as depicted in **Figure 3-11**. This central gear assures that the rotation rate of both drive axes is identical. If the specimen tension varied spatially the free axis can compensate to counter the variation.

For example, if a tension gradient occurrs such that it is greater on the fixed axis a counter torque occurs over the span of transverse specimen brackets. This counter torque then translates forward the free axis via the degree of freedom the ball caster allows. There was a concern the manual suturing of the specimen to the brackets, if not standardized, would be sufficient to cause a translation that would unseat the meshing of the central gear with the two spur gears. Our experience was that this never happened. Unfortunately, what

did occur is that the specimens relaxed so quickly that the specimen tension could not be maintained through manual actuation.

The addition of the servomotors and their need to be directly coupled to the mounting plate and ball screws has diminished the benefit of the ball caster if not entirely negated it. Hence, the addition of the servomotors mandates meticulous alignment of the drivetrain. The entire assembly is aligned on an optical flat prior to specimen mounting. The alignment is done by a combination of mechanical techniques and manual feel. More precise techniques and instrumentation could be employed but the cost would increase substantially. Based on the designed load capacity of 40N as stipulated in section **5.1**, the friction in the drivetrain should remain below 5mJ given the friction load relation described in **Figure 5-1**.

As stated the alignment procedure is manually performed on an optical flat. The procedure is tedious and requires some standardization to yield suitable and repeatable results. The procedure details are contained in **Appendix C**.

In summary, the planarity between the two load frame axes is less than 0.13 mm in the vertical direction, which equates to 1.67 mrad. The parallelism between the central axes of the two ball screws is dictated by the alignment of the two servomotors and the tolerances in the specimen brackets. Precision gauge blocks which have parallel surfaces well under 1 mrad are used to square the specimen brackets, and this in turn squares the two axes of the drivetrain through the pivot axes. While the gauge blocks are in place, the servomotors are engaged to the nuts at the end of the ball screws. The mounts to the servomotors allow for translation in the three orthogonal directions and two rotations: pitch and yaw; to facilitate in alignment with the load frame axes. The mounts are then incrementally tightened to avoid disturbing the axial alignment. Parallelism precision achieved is under 1 mrad.

3.1.4. Drivetrain Servomotors

Specifying the servomotors requires knowledge of the limits of the torque required for the task. At the time of motor specification, the only knowledge of the material being investigated came from the INSTRON tests discussed in section **5.7**, and the experiments

conducted via manual actuation mention in section **1.1**. While that is useful there was absolutely no knowledge of the viscoelastic parameters within an order of magnitude whatsoever. There are two tasks that present the most demand on the servomotors and the load frame: 1) stress relaxation, 2) harmonic mode. The creep tests are the least taxing on the servomotors and load frame. The specifics on executing these tests are discussed in Chapter **4**. Nonetheless, the nature of the relaxation and harmonic tests need to be considered here to specify the requirements for the servomotors.

The relaxation test is to impose an instantaneous displacement while the decrease in load is monitored over time. The question is what constitutes an instantaneous displacement? If the displacement is 1 mm and it has to be executed in 1 msec that is equivalent to 1 m/s. That velocity seems benign but if the stiffness of the specimen is 100N/mm, the stiffness of the PTFE specimens tested in sections **5.3** and **5.4**, then the drivetrain must be capable of exerting 10^5 Nm/s, or 0.1 megawatt.[12] That is unrealistic for a handheld device.

Defining the timeframe is crucial in specifying the capability of the servomotors. The fluorocarbon PTFE has mechanical properties commensurate with vascular tissue. In fact, it has been used for vascular grafts in patients who have been victims of various traumas.[13, 14] DuPont data shows that relaxation time for this material is on the order of minutes.[12] So if the displacement occurs within one second then the relaxation time is at least two orders of magnitude larger. That is considered acceptable.[15, 16]

Typically most stress relaxation tests for polymers are executed such that the total specimen elongation is no greater than 20% so that the total strain is considered to be in the linear regime.[17] The specimen brackets can extend the specimen to a maximum length of 26mm. For 20% elongation the original length is 20.8mm for this scenario. So the total displacement is 5.2mm. The pitch of the 6-mm ball screws is 1 mm per revolution and the servomotors are coupled to the ball screws with a transmission ratio of 1:1. For the sake of conservatism specifying the extension time to be ½ second yields a rotational rate of 624 rpm. That is trivial for most servomotors.

The other parameter of concern is the torque level needed to conduct the relaxation test. Since the material is deformed plastically at the inception of the test the stress level within the specimen is approximately the yield strength of the material. The INSTRON data of section **5.7** indicate that the failure stress of these tissues is approximately 1 MPa. Applying conservatism and using that stress level over the yield strength for a specimen 2mm thick and 18mm wide the uniaxial load on the frame is 36N.

$$\theta = \tan^{-1}\frac{h}{\pi D_{screw}} \approx \frac{h}{\pi D_{screw}} = \frac{1}{\pi 6} radians \approx 3^0 \qquad \textbf{(Eq: 3-1)}$$

$$\rho_{leverage} = \mu \cos\theta \frac{D_{screw}}{2} \approx \mu \frac{D_{screw}}{2} \qquad \textbf{(Eq: 3-2)}$$

$$RPM = \frac{L_{specimen}\dot{\varepsilon}}{\phi_{pitch}} \times 60\frac{\sec}{\min} = \frac{25.4mm\left(2s^{-1}\right)}{1mm} \times 60\frac{\sec}{\min} = 3048RPM \qquad \textbf{(Eq: 3-3)}$$

$$P_{rating} = 2\omega T_{orq} = (2.0)2\pi f T_{orq} \qquad \textbf{(Eq: 3-4)}$$

$$= (2.0)2\pi \frac{3048RPM}{60\sec/\min}\left(\frac{25in\cdot oz}{16oz/lb}\right)(4.45N/lb)(.0254m/in) \approx 56.37\frac{J}{s} = 56.37watts$$

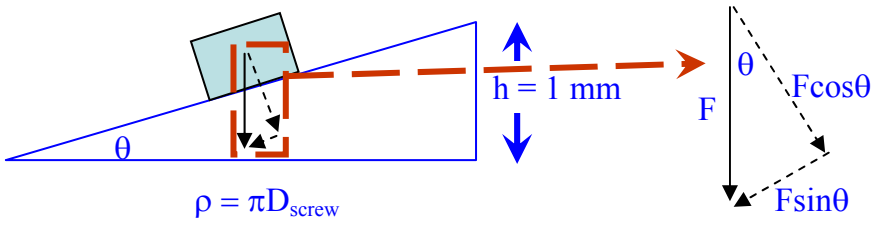

Figure 3-12: Friction on an inclined plane.

Converting the uniaxial load to a torque the "leverage coefficient" of the ball screw needs to be defined. It is common to model threaded rods or screws as an inclined plane. **Figure 3-12** is a free body diagram of a friction force acting on an inclined plane. **(Eq: 3-1)** indicates that for the 6mm ball screw with a 1mm pitch, θ = 3°. For this inclination angle and assuming the friction coefficient, $\mu \approx 0.1$, the "leverage coefficient" becomes $\rho_{leverage} \approx 0.0003$, as prescribed via **(Eq: 3-2)**. The product of the "leverage coefficient" and the axial load of 36N yields approximately 11 mJ. The product of this torque and the angular frequency, ω, yields a power requirement of 353mW.

The requirements defined above pertain to the relaxation test mode. The harmonic mode needs to be accounted for. Fung suggests that harmonic tests should be conducted at

frequencies that represent physiologic conditions. So the peak frequency should not exceed 10Hz.[18] Experiments conducted on anaesthetized sheep in vivo indicate that common physiologic strains under this condition ranged from 4% to 20%.[19] The low value probably pertains to venous tissue and the high value for arteries. The strain rates at 10Hz correspond to 40 to 200 percent per second respectively. This strain rate and a specimen 25.4 mm in length (1") **(Eq: 3-3)** requires a 3048 RPM capacity of the servomotors.

The torque level of 25 in-oz in **(Eq: 3-4)** is based on the experiments conducted by manual actuation of the assembly in **Figure 3-11**. Those experiments can be considered static due to the rate at which manual actuation is applied. The torque levels exerted by the specimens in those experiments were approximately 2½ in-oz per axis. Published literature on the complex modulus of vascular tissue suggests that the magnitude increases by a factor of 10 from a 1 Hz to 10 Hz stimulus hence, 25 in-oz.[18, 19, 20] The factor of 10 is a conservative in the context of torque specifications. There has been research suggesting substantially smaller increases.[21]

Appendix B.1 has the specifications boxed in red for the FAULHABER 2657WO24CR servomotors selected for this application. These servomotors are rated at 48 watts each so the parallel combination is more than sufficient for the harmonic test mode. Moreover, there is a margin factor of 2.0 applied in defining that requirement by **(Eq: 3-4)**.

3.2. Control System

Each test mode of Chapter **4** has a separate control scheme due to the requirements of the test mode. Nonetheless, there is commonality among all the modes in how the system communicates, signal conditions, and controls the servomotors. The cost of the system less the computer and the load frame described in section **3.1** is on the order of $2k - $3k. This cost is for the hardware alone and not the development time for the software.

3.2.1. System Components

Figure 3-13 shows all of the components to the control system along with the load frame and servomotors. Wiring connections are not included to avoid clutter. The WINDOWS XP computer communicates to the DAQ board via USB connection. This is convenient and

inexpensive to implement but there is a fundamental limitation to this technology. The computer cannot transmit and receive signals simultaneously.[22] That is acceptable if the computer simply acts as a data collection system or for an interface for the user to program any motion controller for the servomotors. However, in this case the computer is responsible for everything: user interface, motion control, and data collection. The DELL Lattitude D810 being used has only one CPU. In the case of the relaxation mode testing there have been times of loss of control. Nonetheless, the system does work. There are several factors that contribute to the occasional loss of control. The primary is the load on the CPU. The next contributing factor is the serial bus communication of the USB. Another significant point, the WINDOWS XP operating system can waver at times in performance because the sllocation of system resources cannot be prioritized. National Instruments can allocate operating system resources through LabVIEW on other operating system platforms. Having this capability would enhance control.

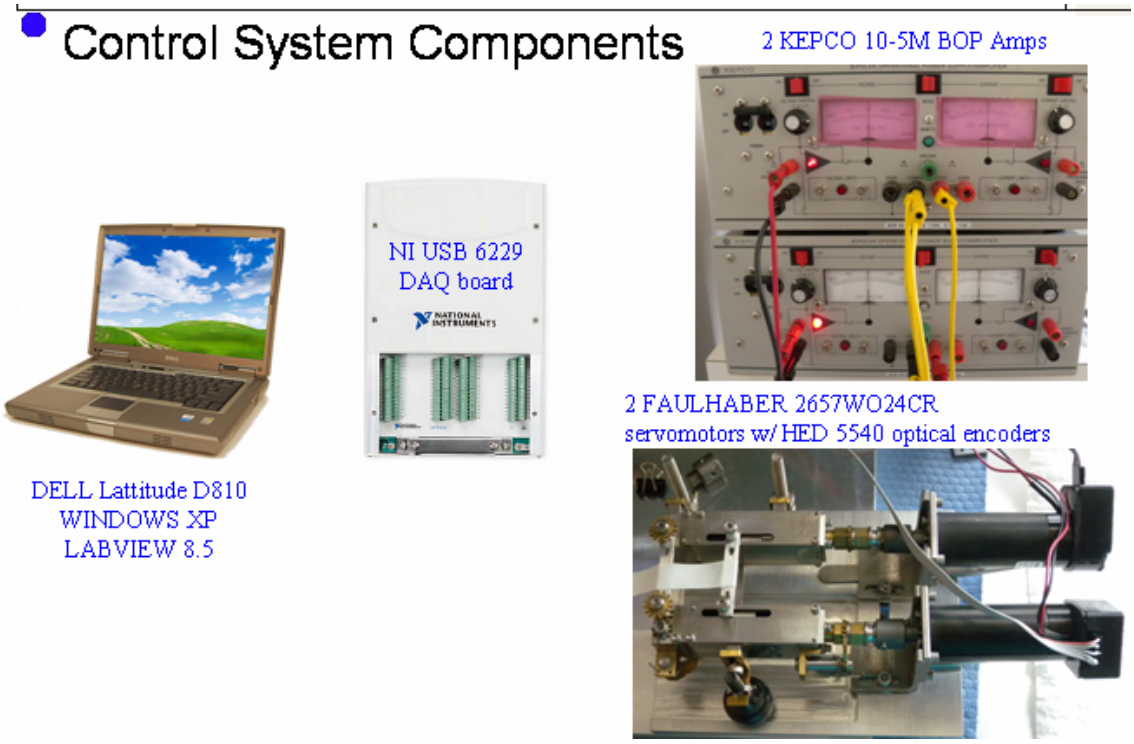

Figure 3-13: Control system components.

Detailed wiring schematics and DAQ board pin-outs for both the servomotors and the encoders are in **Figure 3-14** and **Figure 3-15**. The connections to the DAQ board do not

change regardless of control mode. However, the connections to the KEPCO amplifiers do differ when either attempting to control position or torque. In the case of position control the amplifier voltage needs to be controlled and the wiring schematic is in **Appendix Fig D-1**. Torque control requires current control of the amplifiers and the schematic is in appendices **Appendix Fig D-2**.

CAUTION NOTE: Proper switching must be toggled accordingly when switching from one mode to the other as specified in both **Appendix Fig D-1** and **Appendix Fig D-2**. It should be noted that any of the test modes within LabVIEW can operate regardless of the amplifier configuration. So **CAUTION** must be exercised to be sure the LabVIEW test mode is consistent with the amplifier wiring and switch configuration or the system can be severely damaged.

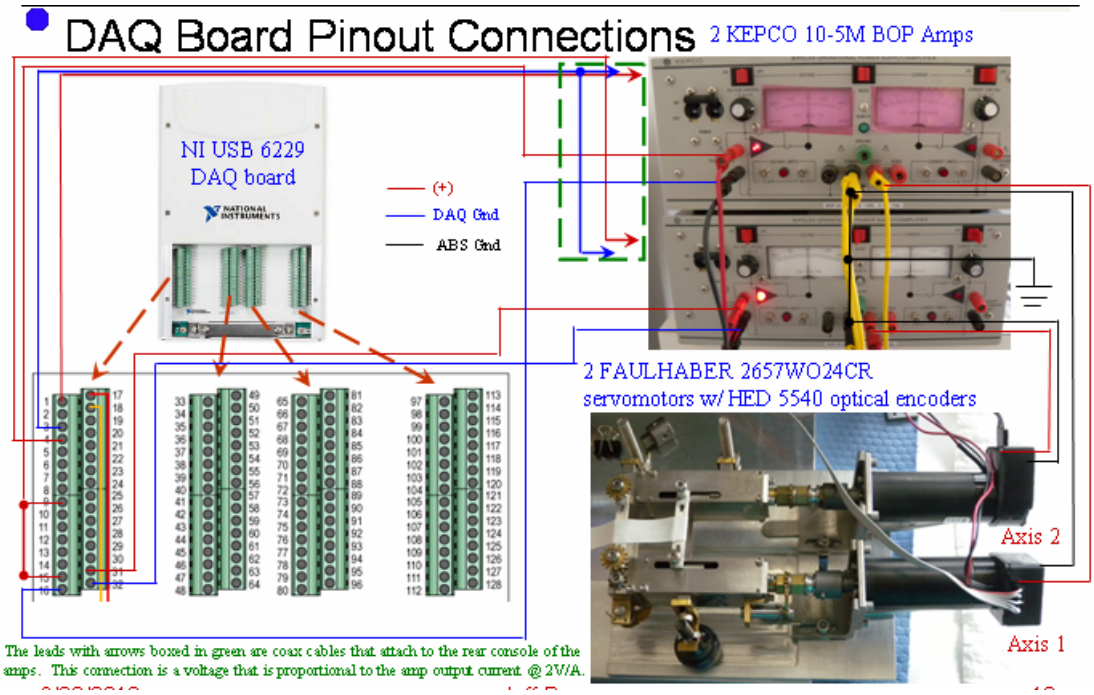

Figure 3-14: DAQ pin-out connections & wiring schematic of servomotors.

The analog inputs, pin-outs 1, 4, and 3 as shown in **Figure 3-14**, remain the same. They are connected via a coaxial connection to the rear console of the amplifiers. This rear console has a 50-pin edge connector with the pin-outs specified by the manufacturer in **Appendix Fig D-3**. The coaxial cable is jumped to pin 10 which is a voltage output that is proportional to the amplifier output current at 2V/A. This is an additional feature that allows monitoring of the current without having to add a load in series with the motors.

A PID controller is implemented within LabVIEW software. The details of PID control theory are outside the scope of this research but something can be said to give a conceptual perspective as to what a PID controller does. Understanding the concept requires little knowledge beyond ordinary differential equations.

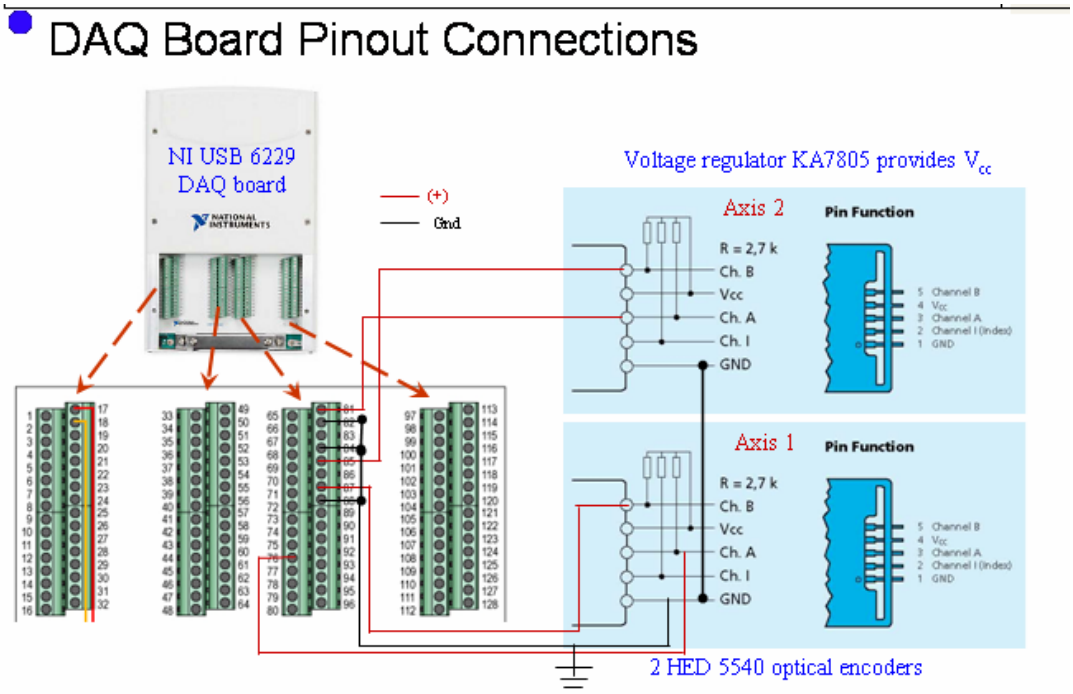

Figure 3-15: DAQ pin-out connections & wiring schematic of encoders.

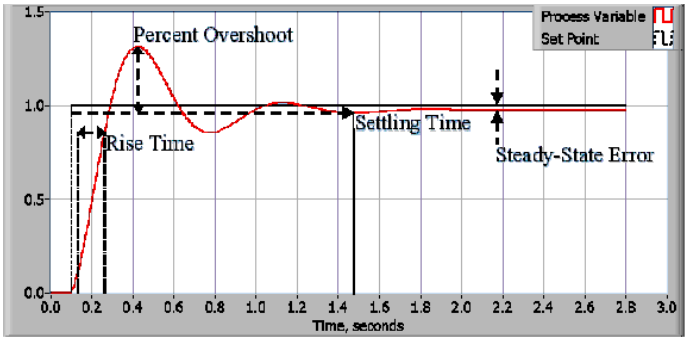

Figure 3-16: Step response of linear 2nd order system.[23]

Consider a generic linear second order system and its response to a step input depicted in **Figure 3-16**. The steady-state response is the same as the step input less some error. The transient response can either be over-, under-, or critically damped; if underdamped, the response is a damped sinusoid. If the PID controller is tuned correctly, the sinusoid will be

nearly critically damped. If this is accomplished the rise and settling time will be minimized as well as the percent overshoot. It is possible to get a zero overshoot but that requires overdamping which in turn increases rise and settling times. So critical damping can be thought of as the "sweet spot" of the PID control. Obtaining the "sweet spot" of the PID controller requires tuning which is not always trivial.

PID is actually an acronym for Proportional-Integral-Derivative (PID) control. The P term is associated with the proportional gain in the system. The greater it is, the quicker the system is to responding to any input stimuli (or instantaneous measured system error). Hence, the system is thought of as being stiff similar to a spring, k. If k is high then it is more difficult to displace it from the equilibrium position.

The D term is associated with the damping in the system. This identifier stems from the fact that linear viscous damping is proportional to velocity which is the "derivative" of position. Tuning a PID controller, one wants a high P which reduces rise time, but increases overshoot. Then one increases D to reduce overshoot and settling time. But caution has to be exerted in this process. The wrong combination of P and D can make the system dynamics unstable. So tuning is generally done by varying one parameter at a time.

The I term can be thought of as a DC gain of the system dynamics. This is not the traditional explanation of the "integral" gain. It is an alternative perspective from the frequency domain.[24] Ideally the DC gain would be unity so that there would be no reduction or amplification of the input stimulus which yields a steady-state error of zero. This can never be the case especially for a quick stimulus such as an impulse. A true impulse has frequency content through the entire range of the frequency spectrum. All dynamic systems act as some type of filter whether low- or high-pass or otherwise. So the I gain is increased to reduce the steady-state error. This parameter is generally the last to be tuned after the PD gains have been set. Again, the system dynamics can be coerced into an unstable condition if this gain is set too high. So this gain is generally set to zero until after the other two have been set.

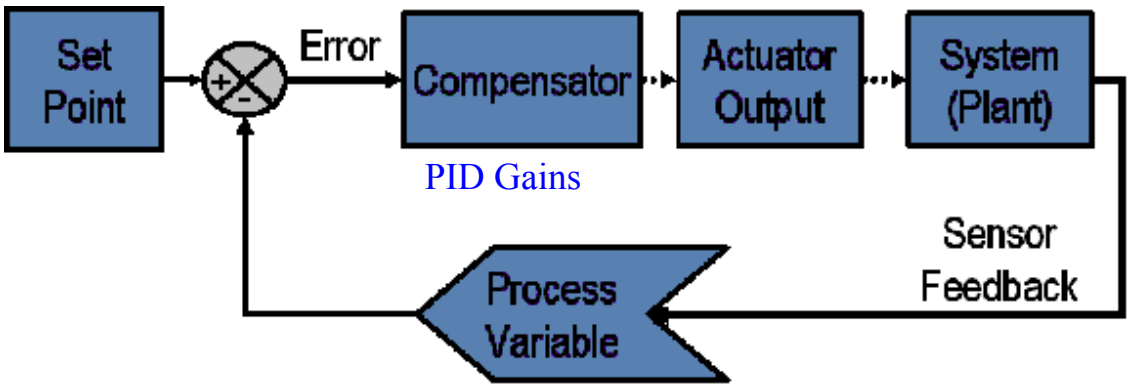

Figure 3-17: PID controller position in feedback loop.[23]

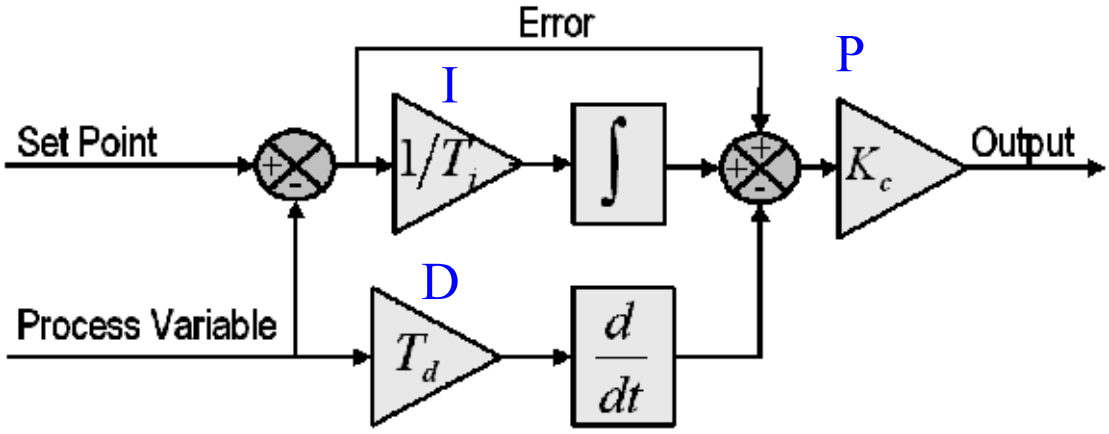

Figure 3-18: Relation of PID gains within the controller itself.[23]

Figure 3-17 and **Figure 3-18** relate how the PID controller factors into the control scheme and what signal each of the individual gains act upon to yield an output control signal for the servomotors. In short, LabVIEW defines the "Set Point." The "Process Variable" is read from the DAQ board and in all of the test modes of Chapter **4** this is the incoming signal from the optical encoders. The difference in these signals is the error signal. The error signal is weighted by the factor defined by the "I" gain and integrated over time and passed on to a summation terminal. The process variable is weighted by the "D" gain and differentiated with time and passed to the summation terminal. The summation of the error with the weighted integral error less the weighted differential process variable is the multiplied by the "P" gain. This now results in the output control signal that is passed from LabVIEW out the DAQ board to the servomotor amplifiers. It should be noted that there are two independent

control signals for each of the two servomotors despite only a single PID controller in the LabVIEW code. The PID controller is capable of handling multiple channels.

3.2.2. Signal Synchronization

There are four distinct needs listed in **Table 3-1** that mandate signal synchronization between the encoder signals and the servomotor control and torque signals. These needs seem obvious even to casual observers. Nonetheless, synchronizing signals within LabVIEW is not trivial and there are few effective example VIs available through the National Instruments website. National Instruments does sell separate hardware modules such as motion controllers, signal generators, oscilloscopes, spectrum analyzers, etc. that require a higher level of programming sophistication. Despite this National Instruments still markets LabVIEW as a tool that can be programmed to function as a replacement for all these types of devices. Synchronization can be difficult to achieve within the standard LabVIEW software unless one uses such specialized hardware, and in that sense LabVIEW can be considered more effective for pure data collection, as post-processing approaches are more easily implemented.

1	Correlate signals.
2	Measure phase change.
3	Control.
4	DAQ timing.

Table 3-1: Synchronizing signals, why?

Each of the viscoelastic test modes has all four needs indicated in **Table 3-1**, but their control scheme imposes different constraints on how synchronization can be addressed. The relaxation, creep, and strain rate modes have PID controllers whereas the harmonic mode does not. The presence of a PID controller mandates that parallel read and write DAQ tasks exist within the same loop. Despite the tasks being configured in parallel their execution has to occur serially since the PID controller needs to act upon the incoming data from the read task before sending command signals to the write task. This presents obstacles to the DAQ timing. Conversely, the harmonic mode test separates the read and write DAQ tasks into

parallel loops. This reduces obstacles on the DAQ timing, but the loops may not iterate at the same rate. This presents obstacles correlating output signals with stimulus signals.

3.2.2.1. Synchronization for the PID Controllers

Starting with the case for the test modes with PID controllers, **Figure 3-19** is the LabVIEW block diagram of initiating the DAQ tasks for those tests. The first thing to note is that there are two parallel COUNTER tasks boxed by the blue dashed lines in the center, whereas there appears to be a single READ (bottom) and WRITE (top) in parallel with the counters. The READ and WRITE tasks can handle multiple channels. There are two, one for each servomotor. The COUNTER can only accommodate a single channel. There are technical aspects about this fact. The READ and WRITE tasks are analog while the COUNTER is digital. Furthermore, the encoders themselves are three-channel output devices, see **Appendix B.1**. The analog tasks are only sending or receiving an individual signal on each channel.

To facilitate synchronization, all of the tasks are clocked at the same rate and the yellow shaded boxes are the DAQ timing VI's which are clocked by the internal clock governing the analog output signal of the DAQ board. The clock rate is user defined within the "PID Utility" sub-VI which is discussed more in detail in Chapter **4**. For the degree of gain required for the relaxation and strain rate tests the recommended setting is 125 kHz. It can be less, but all DAQ tasks in **Figure 3-19** will be clocked at the same rate. Furthermore, note that all of the tasks clocking occurs on the rising edge of the clock pulse. It can be the falling edge as well but all of the tasks must have the identical trigger to be synchronized.

The green shaded box in **Figure 3-19** initiates a 0V output signal to the servomotors prior to execution of the control loop of **Figure 3-22**. The WRITE task within the control loop will not initiate any signal transmission until the command signal from the PID controller becomes available. If the DAQ is not sending any signal to the servomotors while waiting for the command signal, a DAQ timing error will occur, hence the need to transmit an initial 0V signal. It should be noted that it would be more appropriate to send a voltage level

commensurate with the pretension level defined within the "Pretension" sub-VI discussed in detail in Chapter **4**. It is possible to pass that value out of the "Pretension" sub-VI for this purpose. The 0V signal allows for the specimen to recoil from the pretension to the extent of the time span that signal is transmitted.

The blue shaded box in **Figure 3-19** highlights the error wiring from the COUNTER tasks to the WRITE task. LabVIEW has a dataflow protocol mandating that no VI can initiate execution until all data or signals on incoming wiring terminals are available. The sequential path of the error wiring in the blue shaded box ensures that the COUNTER tasks have armed or energized the encoders prior to execution of the control loop of **Figure 3-22**. If this is not done prior to the control loop then any delay in arming the encoders will result in a delay between the encoder and the command signals which will destabilize the system.

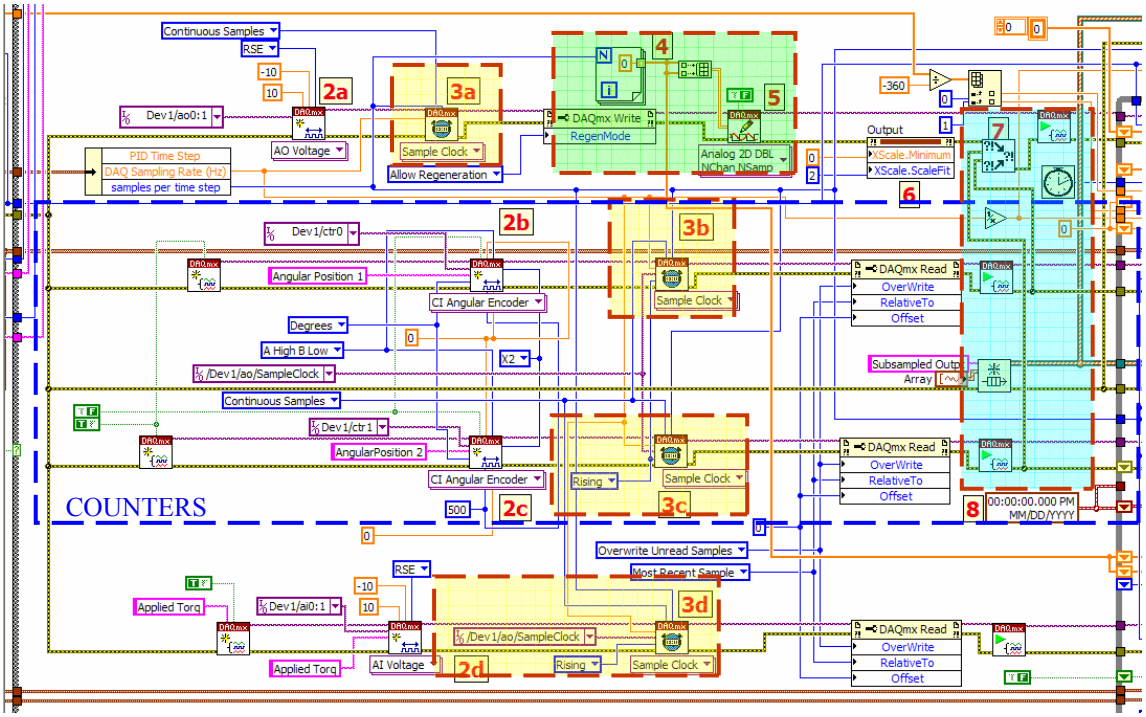

Figure 3-19: Synchronizing the timing of parallel DAQ tasks WRITE, COUNTERS, and READ.

Once all of the signals of setting up the DAQ tasks within **Figure 3-19** are available for the control loop of **Figure 3-22** execution of the control loop is initiated. The green shaded box within the control loop envelopes the processes that occur between the counters obtaining the encoder signals and the DAQ transmitting commands from the PID controller. The

control loop reads in 50 samples at 125 kHz, processes it and determines an appropriate output signal via the PID controller, and writes out the 50 samples of the control output at the 125 kHz rate. The read and write DAQ tasks of the signals takes a total of 0.8 msec. The loop iteration rate achieved is approximately 200 Hz. So the processes within the green shaded box span no less than 4.2 msec. This delay does not present complications for DAQ timing. It does present challenges in control stability, which is discussed in section **3.2.3**.

3.2.2.2. Synchronization for the Harmonic Mode Tests

Since no PID controllers are needed for the harmonic mode tests the different types of DAQ tasks can operate in independent parallel loops which help DAQ timing issues. However, each of the loops can operate at different rates. This presents different challenges in synchronization.

For simplicity of presentation, the three types of DAQ tasks in **Figure 3-19** without the need for the PID controllers can now be split into three parallel loops. There is also a fourth which collects the information from the first three and processes, displays, and archives the data. This VI architecture allows the DAQ loops to iterate at a rate strictly dependent on the ratio of the DAQ sampling rate and buffer size. The fourth loop, the processing loop, proceeds at whatever rate is dictated by the processing, displaying, and storing of the data. However, there is one underlying obstacle within LabVIEW that does interfere with the independent iteration of all four loops. The nature of how LabVIEW communicates data between parallel loops requires DRAM from the computer. In general, if the loops generate and process data at equivalent rates, then the demands of the DRAM are managed well and program execution is not impeded. Unfortunately, the DAQ can generate data faster than a lot of the processing, which imposes a backup of data accumulating in the DRAM, which can bring program execution to a crawl. So if information needs to be shared, then independent iteration is not feasible. So many checks and balances are implemented to be sure these tests can execute correctly.

The interactive GUI for the harmonic mode tests compound the synchronization issues described above. The user is allowed to change test parameters during test execution. While the user is entering these changes the specimen stimulus is not interrupted. This is a significant programming achievement to not allow the activity on the interactive GUI to interfere with specimen testing. Once the test parameters are redefined, the DAQ timing will be redefined, which then means all of the loops will need to be resynchronized. So triggers are implemented within the program as well.

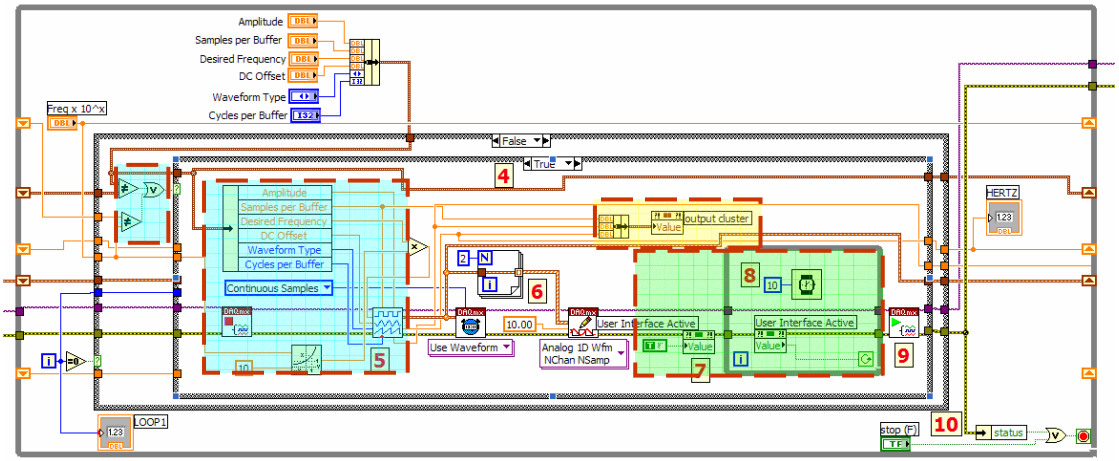

Figure 3-20: Synchronizing the timing of independent parallel loops.

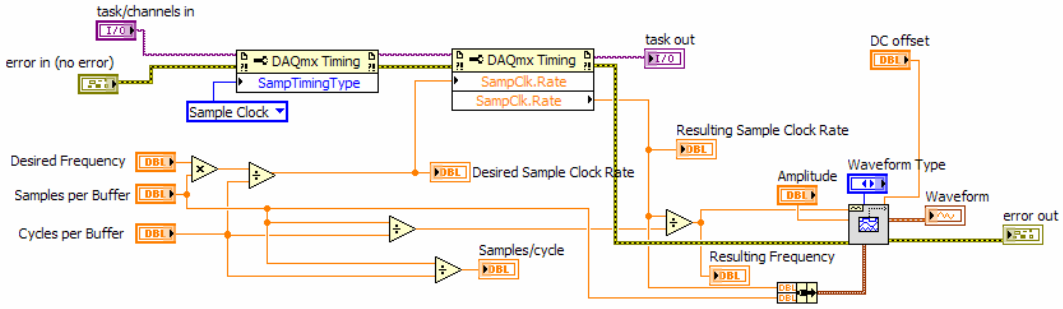

Figure 3-21: Computing waveform timing parameters.

Figure 3-20 is the loop that controls the interactive GUI and defines the timing parameters that will synchronize all of the loops for this test mode. The blue shaded boxes establish if the interactive GUI is active and if so acquires the pertinent information for the signal waveform from the GUI and then computes the required timing parameters. The first blue box envelopes the logic VIs that continuously monitor the input waveform parameters

which are input from the GUI. The GUI is activated if the user changes just one of those parameters. The logic VIs compare the current parameter values to those of the previous loop iteration which are passed in via a shift register. If indeed they have changed then a nested inner case structure is activated to accept the current values.

In the meantime the servomotors are still actuating the load frame with the previous waveform. So specimen stimulus continues without interruption. This is possible because the waveform is buffered into the DAQ memory. In other words, since the waveform for this test mode is periodic it is not necessary for this loop to continuously transmit magnitude and time information onto the DAQ. One period of the waveform is computed and stored in the memory of the DAQ so the DAQ can continuously transmit to the servomotor amplifiers while the user interacts with the GUI.

As the user changes the input parameters, they are accepted into the nested inner case structure and passed into a custom VI which is enveloped by the second blue shaded box and is identified by the ID numeral 5. **Figure 3-21** is the block diagram of that VI. The sample clock rate for this loop and the other two parallel loops that receive the servomotor torque and encoder signals is determined by this VI. The sample clock rate is the ratio of the product between waveform frequency and buffer size to the number of waveform periods the user defines to be stored in the buffer. The number of cycles is usually one, but many times the user will define more because the GUI displays in the time domain the waveform over the time period dictated by the number of cycles. Most users like multiple cycles.

Once the timing parameters and waveform computations are complete, the timing parameters are passed to what is known as a “Property Node” which is enveloped by the yellow shaded box in **Figure 3-20**. This makes this information available to the entire program globally. So now the other two parallel loops with DAQ tasks have access to this timing information and can use it to set the clock rates in those tasks.

The green shaded box of **Figure 3-20** also employs a “Property Node” to notify the other loops that the GUI has been activated and new timing parameters are now available to

receive. The property node identified as "User Interface Active" is set to the Boolean value of true. There is a "WAIT" loop downstream of this property node in the green shaded box. This loop suspends or interrupts progression of this loop until "User Interactive Active" is toggled to false by the loop that receives servomotor torque signals, which is the bottom loop depicted in **Figure 3-22**. That loop has to rearm the timing trigger in the blue shaded box. Note that the trigger VI identified by the ID numeral 25 is set to look for the trigger coming from the analog signal from the loop of **Figure 3-20**. Once the trigger is armed, the "User Interface Active" is toggled to false which then suspends the "WAIT" loop in **Figure 3-20**. The WRITE task is executed in **Figure 3-20**, which sends out a μsec pulse which is the trigger that synchronizes the loops in both **Figure 3-20** and **Figure 3-22**, and all 3 DAQ loops proceed at the same clock rate.

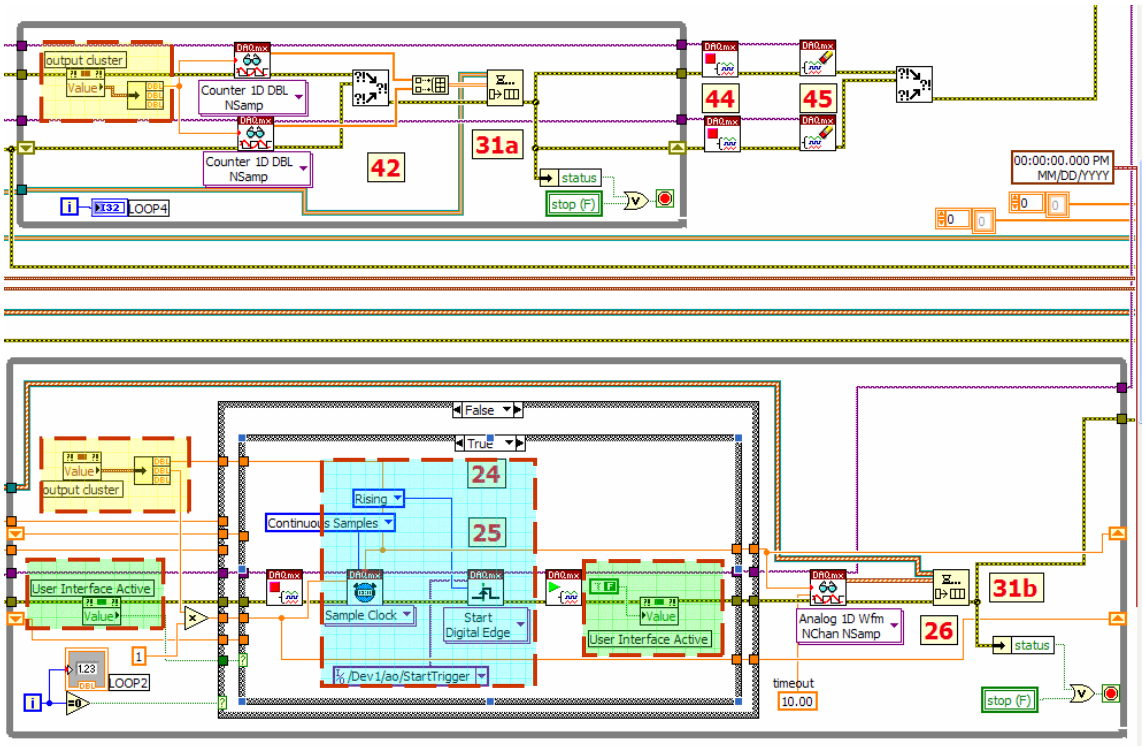

Figure 3-22: Handshaking and triggering role in synchronizing independent parallel loops.

The 3 DAQ loops of both **Figure 3-20** and **Figure 3-22** proceed at the clock rates defined by the VI of **Figure 3-21,** but if the processing loop does not keep pace the DRAM demands will impede the program progression. There is no coordinated handshaking and triggering as

for the 3 DAQ loops. The sophistication of the VI in **Figure 3-21** that defines the timing parameters does so based on the waveform defined by the user. Since the harmonic mode tests discussed in section **4.2.3** don't exceed 10 Hz the DAQ sampling rate should not ever exceed 10 kHz unless the user defines a buffer size to be excessive, greater than 1000 samples. There are no caps defined in that VI, but that would be straightforward to implement. As long as the DAQ sampling rate remains reasonable, less than 10 kHz, the processing loop should keep pace with the loops designated for the DAQ tasks.

3.2.3. Stress Relaxation Mode

P	40
I	0
D	3×10^{-7}

Table 3-2: PID settings for relaxation test mode.

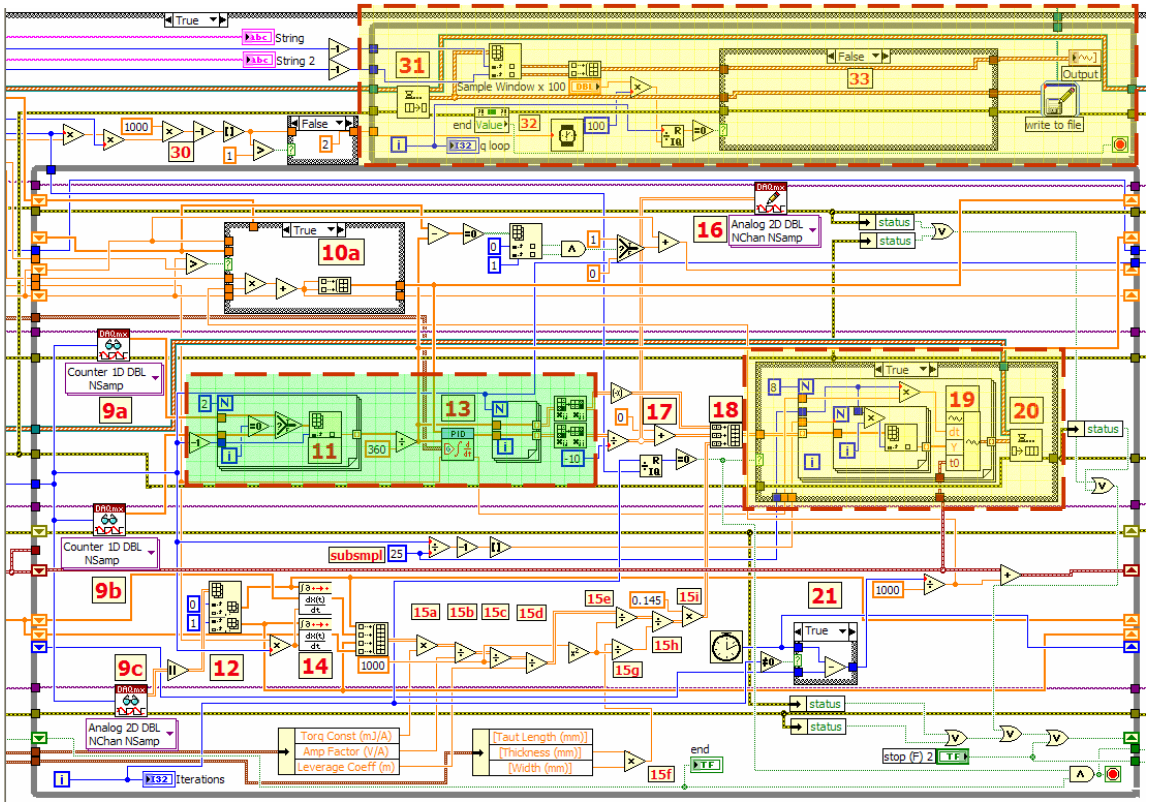

Figure 3-23: Parallel loop structure for data collection and GUI display along with sub-sampling logic structure to enhance iteration rate of the control loop. These structures are highlighted by yellow shaded boxes outlined by red dashed lines.

Without redundant discussion on the methodology covered in detail by section **4.1**, this test mode requires position control of the two servomotors. So the wiring configuration must comply with **Appendix Fig D-1**.

The servomotors are equipped with optical encoders with 500 lines per revolution. Their signals are passed into the PID controller that has the gains set according to **Table 3-2**. The P parameter is quite high due to the stiffness requirements of this test mode. This high gain specification requires the iteration rate of the control loop in the LabVIEW code to be as short as possible to reduce delays on acting upon the incoming encoder signals. The maximum rate capability in the WINDOWS OS is approximately 1 kHz for a loop that is executing some very simple tasks. In general, aside from any operating system delays, the loop iteration rate is dictated by the DAQ board sampling rate and sample size as long as the loop has no processing or logic contained within the same loop. If data collection is the priority, then processing can be passed off to a parallel loop to preserve loop iteration speed. Since control is needed, and the PID controller acts on encoder signals obtained by the DAQ READ tasks, the processing associated with the PID controller cannot be delegated to a parallel loop.

As presented in section **3.2.2.1**, the time span for receiving encoder signals and transmitting command signals for 50 samples at 125 kHz is 0.8 msec. The actual loop rate achieved is approximately 200 Hz. So the processing is dominating the loop burden. Since the PID controller is only operating on a single sample point from the sample set of 50, an attempt to reduce the processing burden by reducing the number of samples divulged some limitations of the hardware. The reason the sample size is not simply one is that the USB 6229 DAQ board does not support “single-point” READ and WRITE tasks. Hence, the data arrays must have a finite length. The sample size was reduced to 40, 30, and next to 20. As the data rates increased, the burden on the CPU, monitored via the WINDOWS Task Manager, eventually saturated at 100%. Once this occurs the computer is not keeping up with the task even if the DAQ board is. So the bottleneck appears to be the PID controller demand on the CPU. The system seems well behaved if the sample size does not go below 40.

For the sample size of 50, the burden on the CPU time varies from 70-90%; sometimes there are intermittent 100% peaks but the burden does not dwell at that level. The consequence of this is that all other applications have to be shut down when executing these tests. It is prudent practice to freshly boot the computer prior to conducting these tests to clear any residual memory demands from earlier applications. The control system is capable of performing the tasks as prescribed by section **4.1.** However, the system is very much at the limit given the hardware limitations. The PID settings in **Table 3-2** below yield stable behavior only for the conditions described in section **4.1**. If the test conditions change, specifically the ramp rate of the specimen offset, then it is necessary to check the stability of the system and retune the gains as needed.

The processing associated with data collection and the GUI display is delegated to a parallel loop as shown in **Figure 3-23**. In addition to the parallel loop a logic structure defines sub-sampling since collection and display of every single data point is unnecessary. Sub-sampling reduces burden on memory and the CPU.

3.2.4. Creep Compliance Mode

P	1
I	0
D	0

Table 3-3: PID settings for creep test mode.

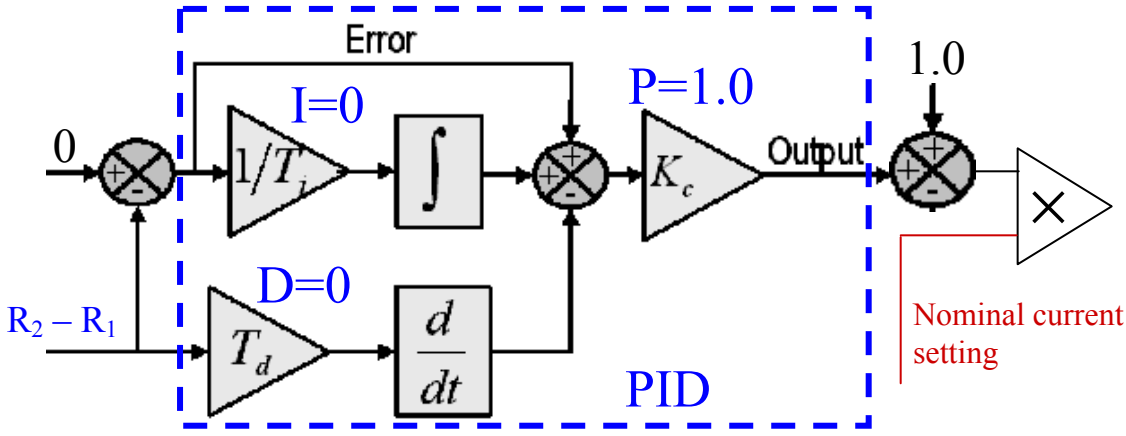

Figure 3-24: Torque correction between the two axes based on rotation difference.

Without redundant discussion on the methodology covered in detail by section **4.2** this test mode requires torque control of the two servomotors. So the wiring configuration must comply with **Appendix Fig D-2**. Heed should be given to the cautionary note of section **3.2.1**.

The PID controller has the gains set according to **Table 3-3**. These settings do not threaten the stability of the system for this test mode. The P gain at 1.0 and the others at 0 results in the error signal becoming the output command as indicated by **Figure 3-24**. For this test mode the "set point" is 0.0 and the "process variable" is the difference between the rotations between the two axes. Due to specimen variations or even stiction between the two drive frames, applying identical torque commands to the two servomotors results in one axis proceeding at a different rate than the other.

As discussed in section **3.1.2**, the kinematics of the load frame with the addition of the servomotors mandates the servomotors to rotate in conjunction during longitudinal extension of the specimen. If this does not occur, the rotational degree of freedom of the specimen and stabilizer brackets will result in a lateral binding of the free-side drive frame. So the PID controller monitors the difference and compensates by varying the torque applied to each axis. **Figure 3-24** indicates that if $R_2 - R_1 = 1$, this corresponds to 2π radians and 1mm linear extension, the output of (-1) will emerge from the PID controller and be summed with (+1) yielding (0 × nominal current setting for the torque level desired). Since the PID handles both channels, the other axis will see a command signal of (2.0 × nominal current setting for the torque level desired). The control scheme for this test mode is based on this logic; however, a cap in the difference in the command signal is defined not to exceed the envelope of 1.2:0.8 between the two axes. So the torque level between the two axes can never differ more than 20% from the nominal value and 50% relative to one another.

This correction scheme seems to be effective. Depending on load magnitudes and the specimen characteristics the correction ratio can be adjusted. **Figure 3-25** shows how the torque correction factor can be adjusted within the LabVIEW code. There are two parameters to be adjusted. One is the difference in rotation between the two axes so that the logic

recognizes a discrepancy that is becoming excessive, and the other is the cap value. Note that the cap value is half of the discrepancy in the rotation parameter.

The LabVIEW code for the creep mode applies an identical parallel loop and sub-sampling logic structure as the relaxation mode depicted by **Figure 3-23**.

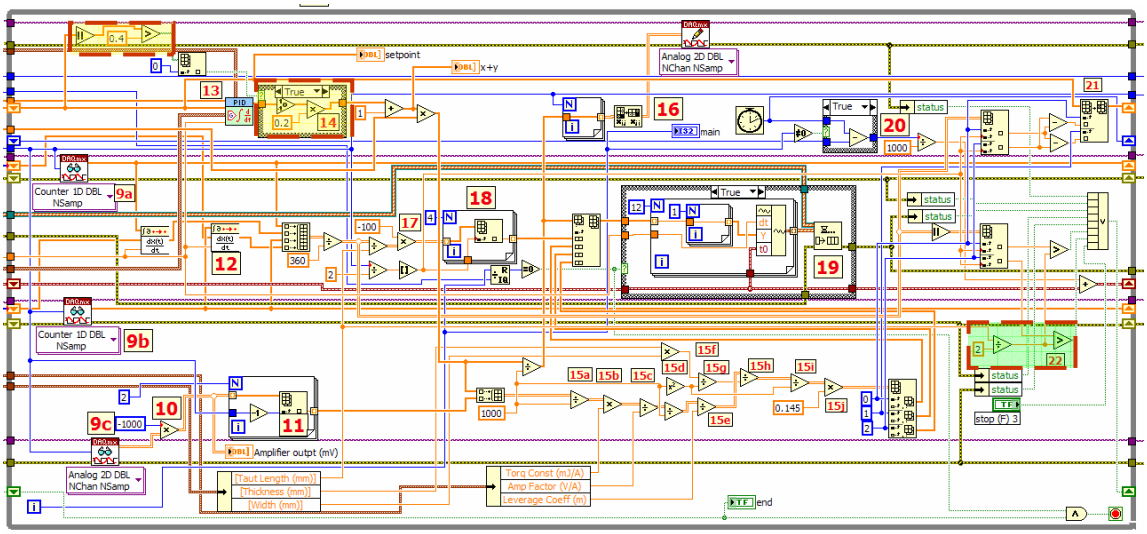

Figure 3-25: Where to redefine the torque correction ratio in yellow shaded boxes.

3.2.5. Harmonic Mode

Without redundant discussion on the methodology covered in detail by section **4.2.3** this test mode requires torque control of the two servomotors. So the wiring configuration must comply with **Appendix Fig D-2**. Heed should be given to the cautionary note of section **3.2.1**

The control scheme for this test mode is open loop so a PID controller is not necessary. This scheme does not have stability issues barring user induced excessive displacements. The challenge this mode presents is the signal synchronization issue as discussed in **3.2.2.2**. In addition to the synchronization challenge the interactive GUI compounds the challenge.

3.2.6. Strain Rate Mode

The control scheme for this test mode is identical to the relaxation mode. In fact, this test is the relaxation mode test but it is executed at a much lower ramp displacement rate as discussed in section **4.1.2**. The user terminates the experiment immediately upon cessation of extension of the specimen.

4. Methods

There are numerous techniques to assess viscoelastic behavior in materials. The two most common and the first two brought to practice, starting in the 1800s, are the creep and stress relaxation tests.[25] At that time, these tests were conducted on glass, metals, and rubbers. From these experiments, Woldemar Voigt and James Clerk Maxwell developed their models which were later incorporated by Dieter Weichert and Lord Kelvin (William Thomson) to model the "standard linear solid." Note that the above names were giants in the field of electromagnetism, and in fact, these models they proposed had already been used to model the behavior of electrical circuits.

These two techniques are considered to be static tests. However, as discussed in section **2.2**, the Fourier transform is a method to correlate the results to infer dynamic behavior. These techniques are usually experiments that require very long time spans. They are simple to conduct but costly in terms of time and data storage. Another technique is to conduct conventional tensile tests at different strain rates in a mechanical testing machine. The duration of these tests is much shorter, but multiple tests are needed in order to get an accurate response dependency on the strain rates. Moreover, careful specimen preparation needs to be exercised in order to avoid stress concentrations which can skew the results.

Another technique which yields results in a much shorter time and also yields strain rate dependency is commonly referred to as "DMA," dynamic mechanical analysis. These tests monitor the material's steady-state response to a forced oscillation stimulus which could be either a displacement or force. The frequency of the oscillation can be varied to yield the strain rate dependence. These tests can be conducted at stresses or strains that are sufficiently low such that stress concentration issues can be reduced as compared to the tests already mentioned. Moreover, if the material tested is truly linear with strain rate, then these results can be used to predict the material response to any arbitrary load profile, including static loading.

The only concern is that the load frequency must remain below a certain threshold such that the inertial density of the material does not contribute to the response. This stipulation, also discussed in section **2.2**, is primarily an artifact of the assumptions applied in the construction of the models posed in **Figure 2-1** and **Figure 2-2**. Neither of those models account for mass. The consequence of this is that the system response behaves as if the differential equation of motion is 1st-order. If the strain rates (frequencies) are sufficiently high, then the inertial mass contributes to the response and the equation of motion becomes higher order.

The device posed in this thesis is capable of testing specimens in any of the four testing modes previously described. There are other test methods that do operate at higher frequencies such as modal vibration of a membrane, atomic force microscopy in dynamic mode, pressure wave attenuation, and others. However, there are concerns regarding biologic tissues in attempting to extrapolate viscoelastic behavior from high frequency tests to predict behavior at physiologic conditions.[26] For example, there is debate on the use of ultrasound data to infer viscoelastic behavior of vascular tissue at 3 Hz, which would be the peak heart rate under the most extreme circumstances. So the device is designed to have stimulus frequencies commensurate with physiologic conditions.

4.1. Stress Relaxation

As stated in section **2.1**, both the Weichert and Kelvin general models can represent relaxation and creep behavior of a linear viscoelastic solid. Without belaboring the details of solving the governing differential equations of each model, the solutions under step input are presented in **(Eq: 2-7)** and **(Eq: 2-8)**. The behavior of the individual elements of each model reveals the logic behind the preference of the Weichert model for stress relaxation.

In the case of stress relaxation, the input is a step function in strain. The instantaneous application of strain in time results in the viscous damper element in both models exerting an infinite stress to counter that discontinuous displacement. The Voigt element seizes in position at the time of application due to this infinite counter-stress. Conversely, the series

configuration of the Maxwell element results in a finite instantaneous stress proportional to the elasticity value, E_i.

As time increases from the time of application, the viscous damper reduces the counter-stress since the time derivative of the step input becomes identically zero. For the parallel configuration of the Voigt element, the counter-stress decays to a non-zero value of $(D_i)^{-1}$. For the series configuration of the Maxwell element, the counter-stress does decay to zero. So this instantaneous and steady-state behavior of the constituent elements of the two models explains the preference of the Weichert model for stress relaxation.

4.1.1. Stress Relaxation Specimen Preparation

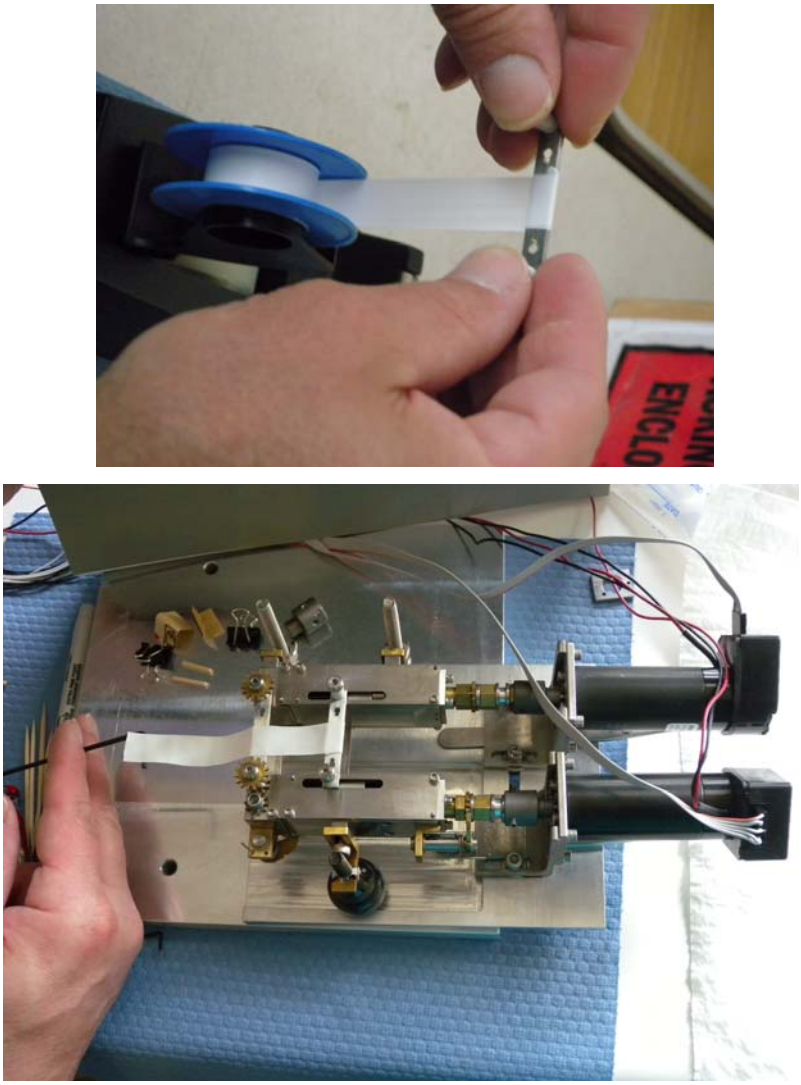

Figure 4-1: Mounting of PTFE specimens to specimen bracket assembly.

As stated in section **3.1.1**, the specimen brackets are modular and anchored to the load frame via four shoulder bolts. For the inaugural testing of the drivetrain, the fluoropolymer material polytetrafluoroethylene (PTFE) was chosen to validate the test procedures. As stated in section **3.1.4**, PTFE has mechanical properties that are similar to vascular tissue. The mounting scheme of the PTFE specimens is simply to wrap the 0.0025" thick film about the specimen brackets as depicted in **Figure 4-1**. This mounting scheme was favored over the use of the MOLEX IDT connectors described in section **3.1.1** due to simplicity and to minimize boundary effects on the response of the material.

The specimen brackets are set at a prescribed distance apart that is measured via calipers. Both sides near each frame axis are measured to be sure the brackets are square. The specimen is then wrapped a number of times about the brackets and tension is maintained during that process using an Allen wrench as depicted in **Figure 4-2**. The most optimal number of wraps seems to be five. Due to static friction in the load frame it is desirable to have more specimen wraps so that the torque provided by the motors to displace the specimen far exceeds the frictional torque. However, with greater specimen load, the static friction also increases by 1.1mJ per every 9.81N of additional axial load as described in section **5.1**.

Once the specimen is wrapped and prior to clamping, the servomotors are rotated by hand to remove slack in the specimen. Once the specimen is taut, the onset of tension is very discernible by tactile sensation. The distance between the specimen brackets is again measured. If the brackets are square, the specimen is then clamped via binder clips as shown in **Figure 4-4**. LabVIEW is now activated and a "Pretension" sub-VI is invoked. LabVIEW instructs the user to pretension the specimen to a prescribed level that is pre-programmed into the VI. The pretension value needs to exceed the threshold of the static friction in the load frame. The static friction, as discussed in section **5.1**, is dependent on the axial load imposed by the specimen. Consequently, the specimen material does affect the friction. So it may be necessary to reprogram the torque value in the "Pretension" sub-VI. The sub-VI could

allow the user to input the pretension torque value, but currently it is not allowed due to the probability that the user could input an incorrect value and damage the drivetrain. The location where this value is preprogrammed is the yellow shaded box within **Figure 4-3**.

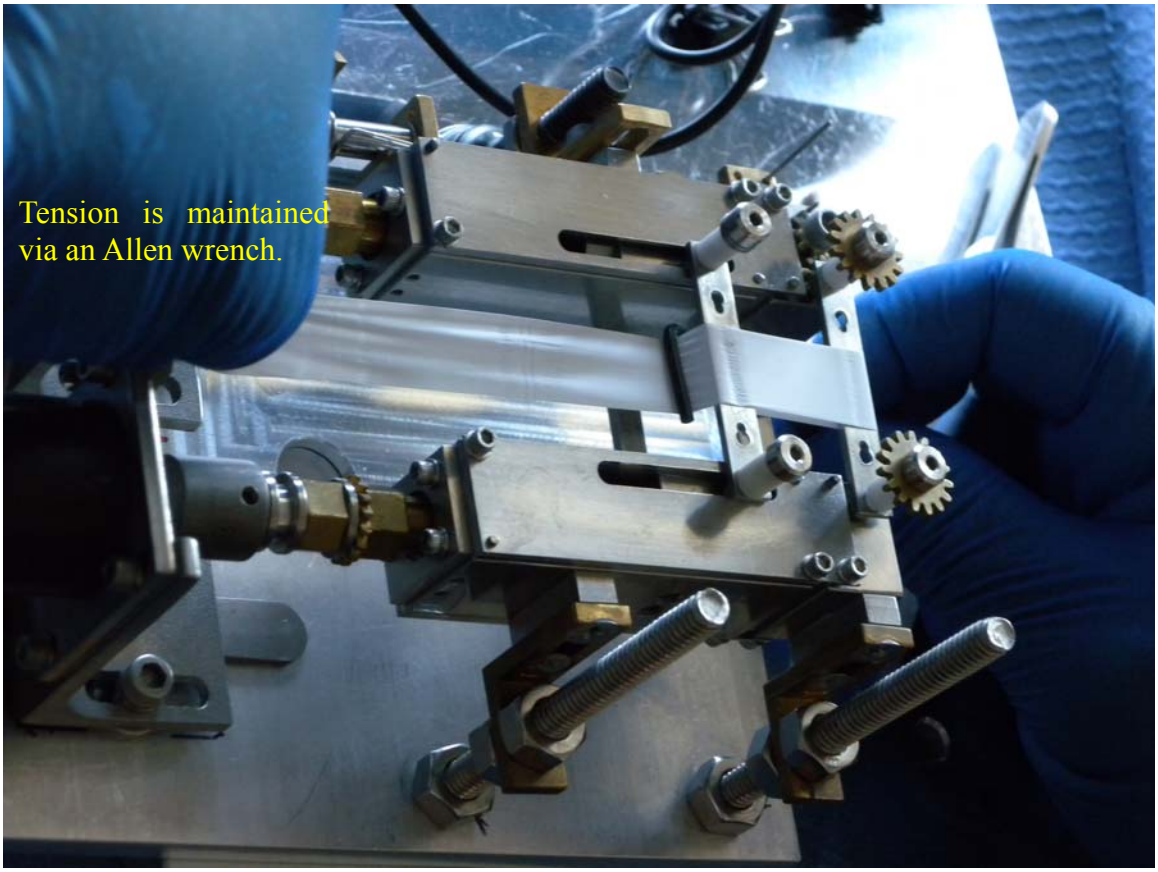

Figure 4-2: Mounting of PTFE specimens to specimen bracket assembly**.**

In the case of 5 layers of PTFE, with a width of 12 mm, that torque level is approximately 1 mJ or ½ mJ per axis. This torque value is based on the stiction level and the conversion factor of 1.1mJ per 9.81N axial load as stipulated in section **5.1**. For a pretension level of 50psi the corresponding axial load is slightly above 1N. Given the torque-current conversion factor for the servomotors specified in **Appendix B.1** of 34.8 mJ/A the corresponding current amplitude is approximately 0.03A. As mentioned in section **3.2.1** the KEPCO servomotor amplifiers have a voltage channel output that is proportional to the current output to the servomotors at 2V/A. So 60mV is the value that is preprogrammed into the "Pretension" sub-VI.

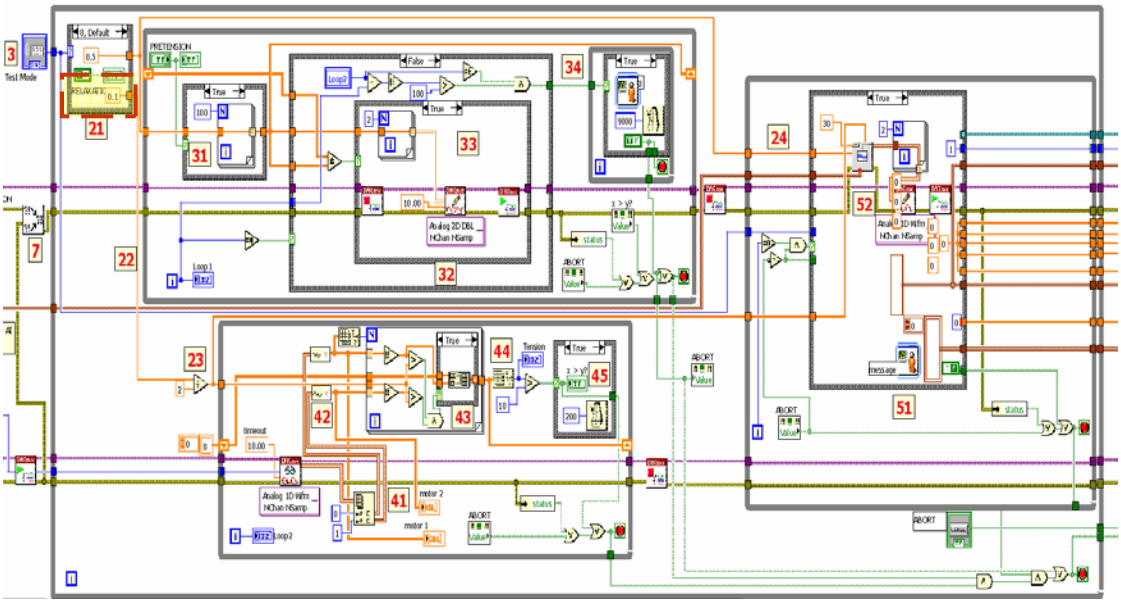

Figure 4-3: Preprogrammed torque value within the "Pretension" sub-VI**.**

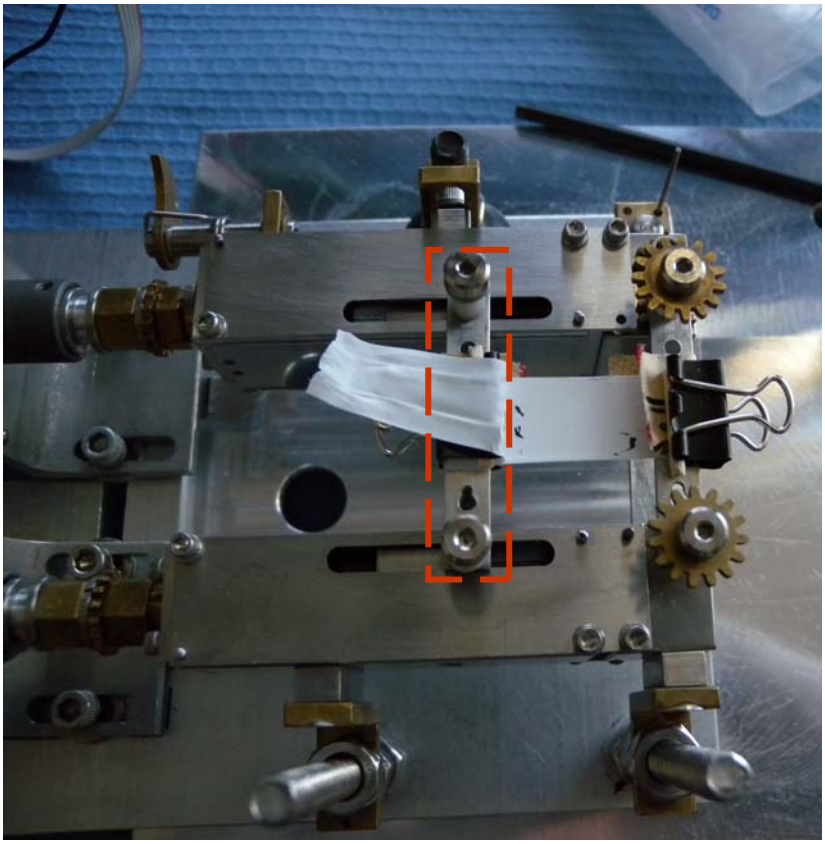

Figure 4-4: Specimen clamping and fiducial marks**.**

Once the specimen is pre-tensioned, another sub-VI is invoked for the user to input specimen parameters and PID controller gains. At this time, the distance between the

brackets is again measured. If there is a discrepancy between the two axes, it is easy to adjust the distance by manual rotation of the servomotors. This is a very fine adjustment to be sure the frame is square. Once the final length is measured, fiducial marks are placed on the specimen as in **Figure 4-4**. These marks serve as indicators showing if the specimen slips during the experiment. If the specimen does not slip or tear during the initial displacement of the relaxation test, the marks will remain in the same position but distort due to strain elongation.

The clamping mechanism for the PTFE specimens is implemented using binder clips. It should be noted that due to the low friction of PTFE, the specimens are capable of slipping through the clips without the use of an abrasive material between the specimen and the clips. 50 grit Al_2O_3 sandpaper is used to counter this effect. Extra margin on clamping power is also provided by incorporating a toothpick, which is visible in **Figure 4-4**.

4.1.2. Stress Relaxation Procedure

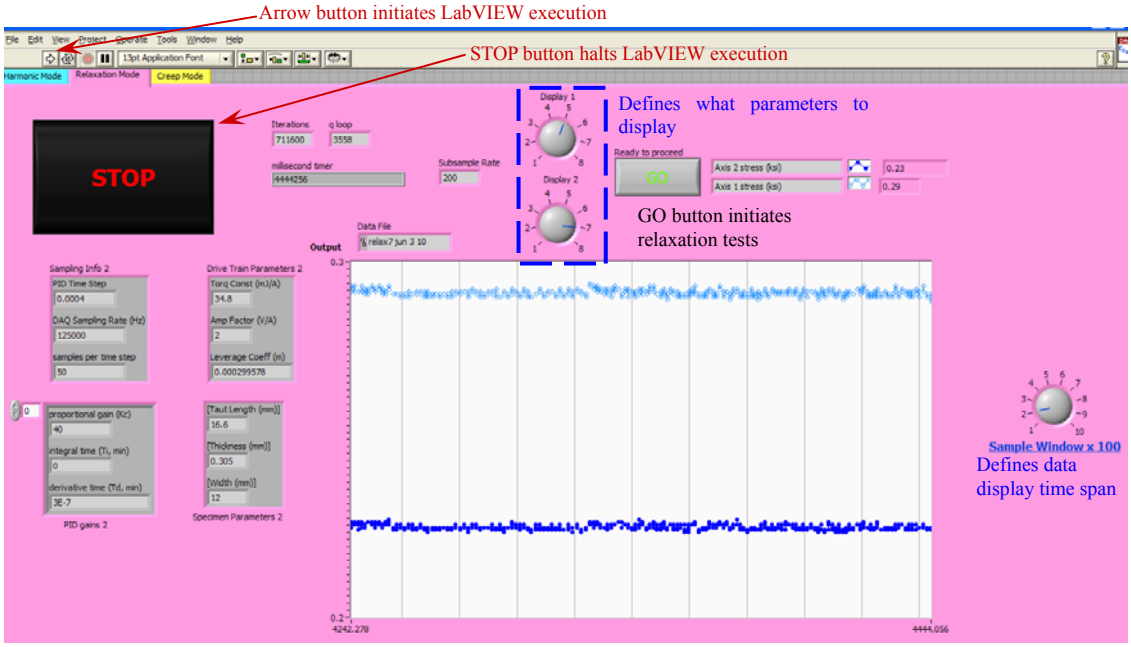

Figure 4-5: GUI display of the stress relaxation test mode.

As described in the previous section, the specimen preparation and mounting includes pretension of the specimen to remove any slack in the system. But to initiate LabVIEW execution, the user must depress the RUN arrow that is indicated in **Figure 4-5**. Once

execution initiates, the span of the data display needs to be set by the knob to the far right of the GUI display. **Figure 4-5** indicates that the setting for that particular run is 200 data points, so the time span is 200/(sub-sampling frequency). The two knobs at the top of the data display allow the user to select what parameters are to be displayed. A pop-up dialog window, not shown, instructs the user on the data options. **Figure 4-5** is displaying the specimen stress level. Once the user defines the settings, then to initiate the relaxation mode, the GO button is depressed. Once executed, LabVIEW steps the user through the process. **Figure 4-6** is the GUI display for the "Pretension" sub-VI. The user pretensions the specimen through the PRETENSION switch boxed in red. The blue vertical fill bar is grey if there is no tension in the specimen. As the tension increases, the fill bar rises in blue just as a conventional thermometer does with temperature. Once the tension reaches the prescribed level as defined in the previous section, the fill bar is all blue and the green indicator light is activated. Immediately after activation of the green indicator light, a user dialog box appears with instructions to the user that the next step is to measure the specimen, and the specimen parameters along with PID control settings of **Table 3-2** need to be entered. The user is prompted to hit the OK button; in doing so the "PID Utility" sub-VI is activated, and **Figure 4-7** is the GUI display that pops up for the user.

All of the user inputs are within the yellow shaded console panel. The values displayed in **Figure 4-7** are the settings specific to the relaxation tests on the PTFE specimens, for which the results are presented in section **5.3**. It is important to note that the DAQ timing is determined by the parameters that are boxed in red. The gain requirements for this test mode do not allow for much margin on adjusting the settings displayed in **Figure 4-7**. Different settings are likely to drive the system into instability.

Within the blue shaded console are control parameters that are passed from this sub-VI to the main control loop of the top level VI to control the servomotors. It should be noted that the DAQ sampling frequency for these tests is 125 kHz. That is the maximum sampling rate for the USB 6229 DAQ board to drive two output channels. As discussed in section **3.2.2.1**, at

this sampling rate the iteration rate of the main control loop does not exceed 200 Hz. The sub-sampling rate defined within the user inputs of the yellow console is set at 200 which means that every 200th sample point is being recorded to the data file. So the time resolution of the experiments is no less than 1 second. Since the time resolution cannot be shorter due to the demands on memory and CPU, it is necessary to define a ramp rate for the initial specimen displacement. Since the P-gain of 40 is so high, there is a possibility of overshoot. Overshoot implies that the specimen is overstretched, which results in very little residual stress in the specimen when the servomotors reach equilibrium position. To be able to resolve any overshoot, the time resolution of the experiment has to be shorter than the rise time of the displacement. Hence, the target strain is defined as 10% elongation and is to occur at a rate of 5%/sec. The ramp time for these experiments is 2 sec.

In principle, the initial specimen displacement should be instantaneous, but given the limitations of the control system, this is not possible. Furthermore, as noted in section **3.1.4**, an instantaneous displacement mandates an infinitely rigid load frame, and the servomotors need to have infinite power capacity. So reality dictates a ramp. The more gradual the ramp, the less likely overshoot will occur. Moreover, the more gradual the ramp, the less likely inertial accelerations within the material will contribute to the response, as discussed early in Chapter **4**. In essence, having to define a ramped displacement pigeonholes the relaxation test mode response to be 1st-order as described by **(Eq: 2-7)**. This is why these experiments are considered to be static.

After the required parameters have been input, the user depresses the OK button and the "PID Utility" sub-VI relinquishes to the top-level VI with the control loop, and the GUI display of **Figure 4-5** returns. The drivetrain induces the initial specimen displacement, but the servomotors are not capable of obtaining the targeted position. Inspection of **Figure 3-17** indicates that as the servomotors approach the set point the error signal approaches zero. The consequence of this is that the command output of the PID controller tends to zero. Therefore, arrest of the servomotors occurs prematurely. The arrested position is the result of

equilibrium between the servomotor, specimen stiffness, and static frictional torque. As the specimen relaxes, the residual torque in the servomotors induces an intermittent displacement as they strive to meet the targeted position. This movement compromises the essence of a relaxation test. To minimize this intermittent motion, the PID set point is reset once the servomotors are arrested immediately after that initial displacement in the 2-second timeframe. It is deemed that this is beneficial but not absolutely necessary. More on this is presented in the results of section **5.3**.

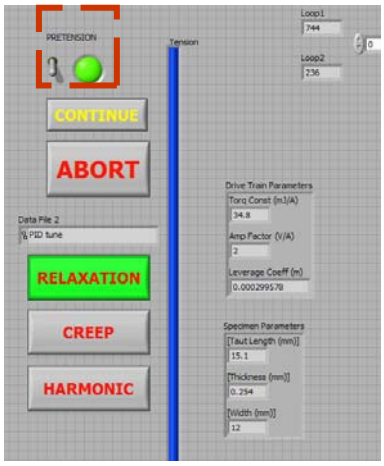

Figure 4-6: GUI display of the "Pretension" sub-VI**.**

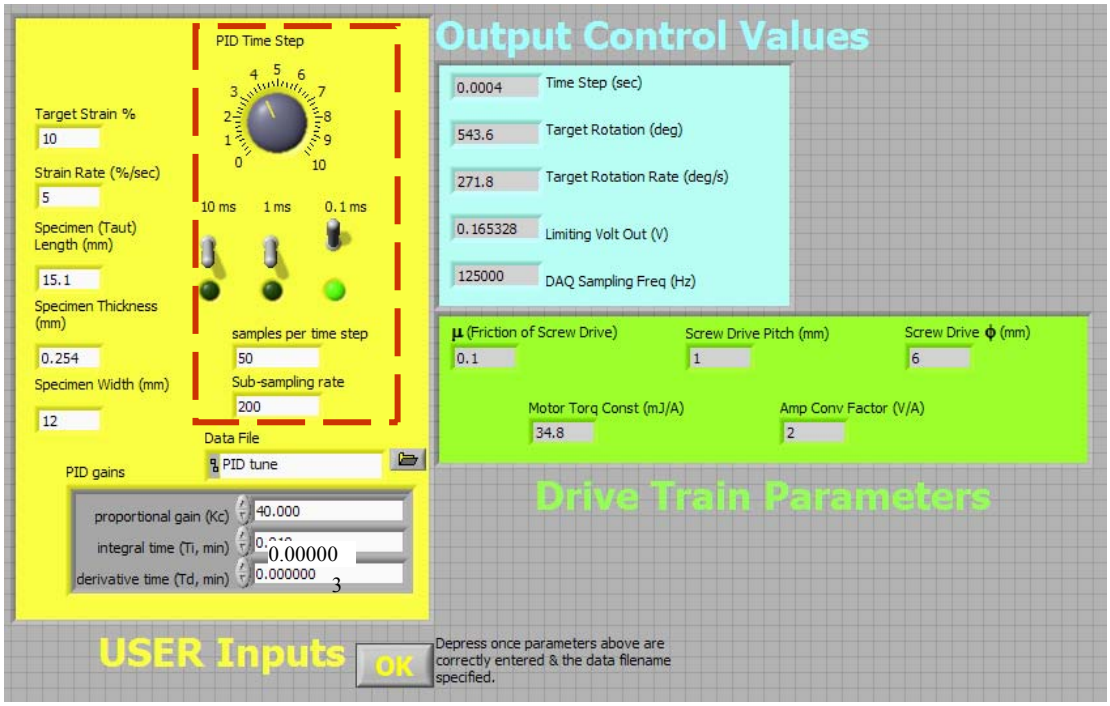

Figure 4-7: GUI display of the "PID Utility" sub-VI**.**

A further note on this aspect of PID control is that it is not used in the "Pretension" sub-VI. The rotations in specimen pretension are sufficiently small that the PID controller would not prevent specimen recoil. In fact, the current open-loop servomotor actuation scheme of the "Pretension" sub-VI does not prevent specimen recoil either. This is an artifact of wiring configuration of the amplifiers as described for the relaxation test mode in **Appendix Fig D-1**. Fortunately, the recoil is sufficiently small that the results presented in section **5.3** are not compromised.

As the drivetrain remains stationary, the residual torque in the servomotors is monitored over a time span of one hour or greater. The user terminates the experiment per his/her discretion dependent on the specimen behavior. The results for PTFE in section **5.3** suggest that 1 hour is sufficient and 2 hours provides an additional margin.

4.1.3. Procedural Modification for Non-Linear Contingency

Previously stated in section **2.3** in linear theory, the individual elements in both the Weichert and Kelvin models remain constant over the entire range of displacement or load as well as over any rate of change in the displacement or load. The Weichert model as discussed in section **4.1** is the preferred model to represent relaxation behavior. Examination of **(Eq: 2-7)** indicates that the relaxation time constants of the individual Maxwell elements are proportional to the ratio $\frac{\eta_i}{E_i}$. If the individual springs and viscous dampers possess non-linear characteristics, then the decay rates will be affected. Given the control scheme as described in section **3.2.3** the logical manner to probe non-linear response is to alter the amount of prescribed displacement as well as the ramp rate for this displacement.

Noting the constitutive relations of **(Eq: 2-1)** and **(Eq: 2-2)**, the spring elements would be affected by the displacement amplitude, whereas the viscous damper would be affected by the ramp rate.

Assessing non-linear responses is outside the scope of this thesis, but the proposed modification of the test procedure gives this device the capacity to execute such an endeavor.

4.2. Creep Compliance

In the case of creep compliance, the input is a step function in stress. The instantaneous application of stress results in the viscous damper element in both the Weichert and Kelvin general models of section **2.1**, exerting an equivalent counter-stress. This yields an instantaneous strain rate that is proportional to that stress and a zero strain at the time of application. The configuration of the viscous damper in parallel with the spring of the Voigt element yields a zero displacement at the time of load application. Conversely, the series configuration of the Maxwell element results in a finite instantaneous strain that is inversely proportional to the elasticity value, E_i.

As time increases from the time of application, the strain rate will reach a steady-state value that may or may not be zero. The parallel configuration of the spring, E_∞, in the Weichert model forces the steady-state strain rate to be zero and the final strain to be finite. The generalized Kelvin model of **Figure 2-2** allows the steady-state strain rate to be either zero or non-zero. Hence, the Kelvin model is preferred for creep compliance.

4.2.1. Creep Compliance Specimen Preparation

As described in section **4.1.1**, the specimen is wrapped about the specimen brackets. The clamping mechanism of the specimen is identical to that described in section **4.1.1**, but the pretension is modified to exploit the feature of controlling torque. Note that the wiring configuration of the amplifiers must comply with configuration specified by **Appendix Fig D-2**. Heed should be given to the cautionary note of section **3.2.1**.

Prior to activating LabVIEW, the clamp mechanism on the specimen extension bracket boxed in red in **Figure 4-4** is not in place, whereas it is on the fixed specimen bracket. After slack in the specimen is removed manually and the brackets are squared, LabVIEW is activated and the "Pretension" sub-VI is invoked. As in the relaxation mode, LabVIEW instructs the user to pretension the specimen to a prescribed level that is pre-programmed into the VI.

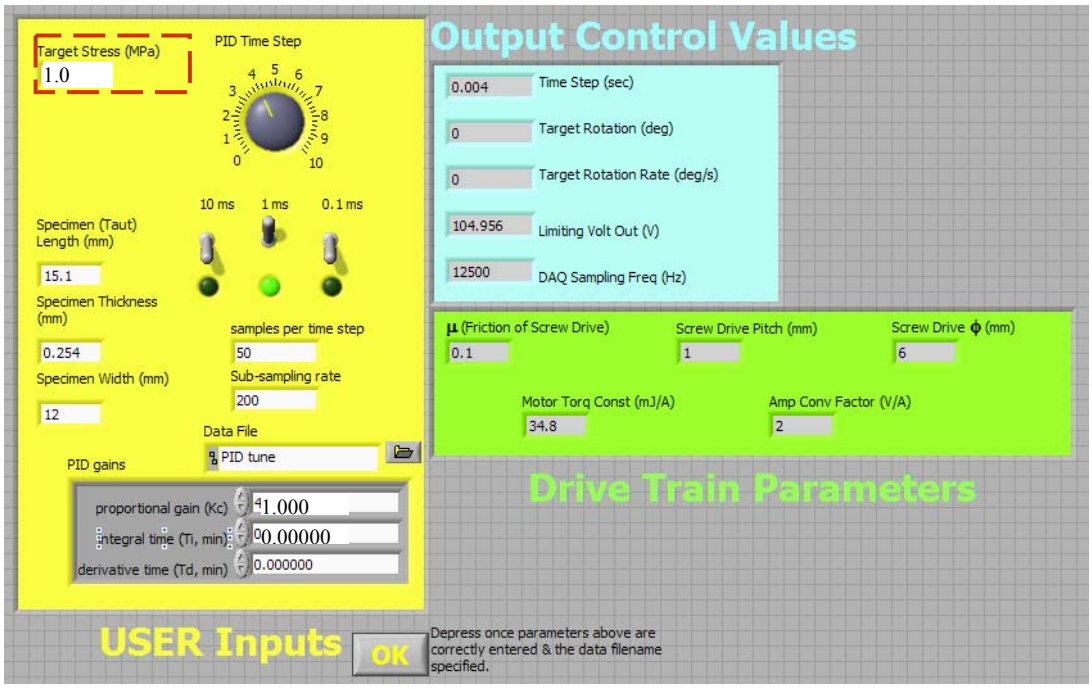

Figure 4-8: GUI display of the "PID Utility" sub-VI to pretension in the creep compliance mode**.**

Once the specimen is taut, with only one clamp in place, another sub-VI is invoked for the user to input specimen parameters and PID controller gains. The user is prompted to hit the OK button, and in doing so the "PID Utility" sub-VI is activated; **Figure 4-8** is the GUI display that pops up for the user. All of the user inputs are within the yellow shaded console panel. The values displayed in **Figure 4-8** are the settings for the creep compliance mode, and boxed in red is the target specimen stress. Since the current output of the amplifiers is being controlled, the pretension stress can be sustained after the user depresses the OK button. In doing so the "PID Utility" sub-VI relinquishes to the top-level VI with the control loop. The drivetrain applies a torque that is commensurate with the target stress level specified by the user. The stress level specified in **Figure 4-8** is well below the stress level to induce creep but high enough to overcome static friction in the system.

Once the pretest stress level has been imposed, the distance between the brackets is again measured. If there is a discrepancy between the two axes, it is easy to adjust the distance by manual rotation of the servomotors even while the servomotors are attempting to maintain a constant torque load. This is a very fine adjustment to be sure the frame is square. Once the

brackets are square, the second clamp mechanism is placed, and the brackets are rechecked to verify if they are square and adjusted if necessary. The top-level VI is terminated by depressing the STOP button on the GUI display. The specimen will recoil, but when LabVIEW is reactivated the specimen extension bracket will return to position. The user goes through the same process to pretension the specimen, now with both clamps in place. All the user inputs in **Figure 4-8** will be identical except the final length and the target stress. The final length is measured, and fiducial marks are placed on the specimen as in Figure 4-4. These marks serve as indicators of whether the specimen slips during the experiment. If the specimen does not slip or tear during the test, the marks will remain in the same position but distort due to strain elongation. The target stress is what is deemed capable of inducing creep. The threshold for PTFE is considered to be 3 – 4 MPa.

There is one flaw in the "Pretension" sub-VI that should be corrected over the long term but has not adversely affected any of the results presented in section **5.4**. Once the pretension stress obtains its prescribed level, a signal is transmitted to the servomotors to have them oscillate about this pretension value as the user inputs the required parameters as prescribed in **Figure 4-8**. Currently, as the sub-VI is programmed, the signal oscillates about a zero torque instead of the pretension value. This is straightforward to rectify by defining a DC offset value into the signal generator, but it has not yet been corrected.

4.2.2. Creep Compliance Procedure

As described in the previous section, the specimen preparation and mounting includes pretension of the specimen to remove any slack in the system. LabVIEW steps the user through the process as it does for the relaxation mode discussed in section **4.1.2**, but the procedure is modified as specified in section **4.2.1**. The GUI display for the creep mode is depicted in **Figure 4-9**. The only setting the user needs to define is the span of the data display. The data display only monitors the specimen strain, so there are no options to have to select from as there was in the case of the relaxation mode testing.

The values displayed in **Figure 4-8** are the settings specific to the creep tests on the PTFE specimens for which the results are presented in section **5.4**. However, a number of tests were conducted at various target stress levels. Given the PID gain settings in **Figure 4-8**, the system is not likely to become unstable even if the timing parameters are changed.

Unlike the relaxation mode, there is no ramp rate associated with the load application on the specimen. This is confirmed by altering the sub-sampling rate specified in **Figure 4-8**. The rate specified in **Figure 4-8** is to keep the size of the data file to a reasonable level. It is confirmed given the DAQ sampling rate of 12.5 kHz that the torque level reaches the specified level within the 80 μsec commensurate with 12.5 kHz as long as the servomotor axes are rigidly constrained.

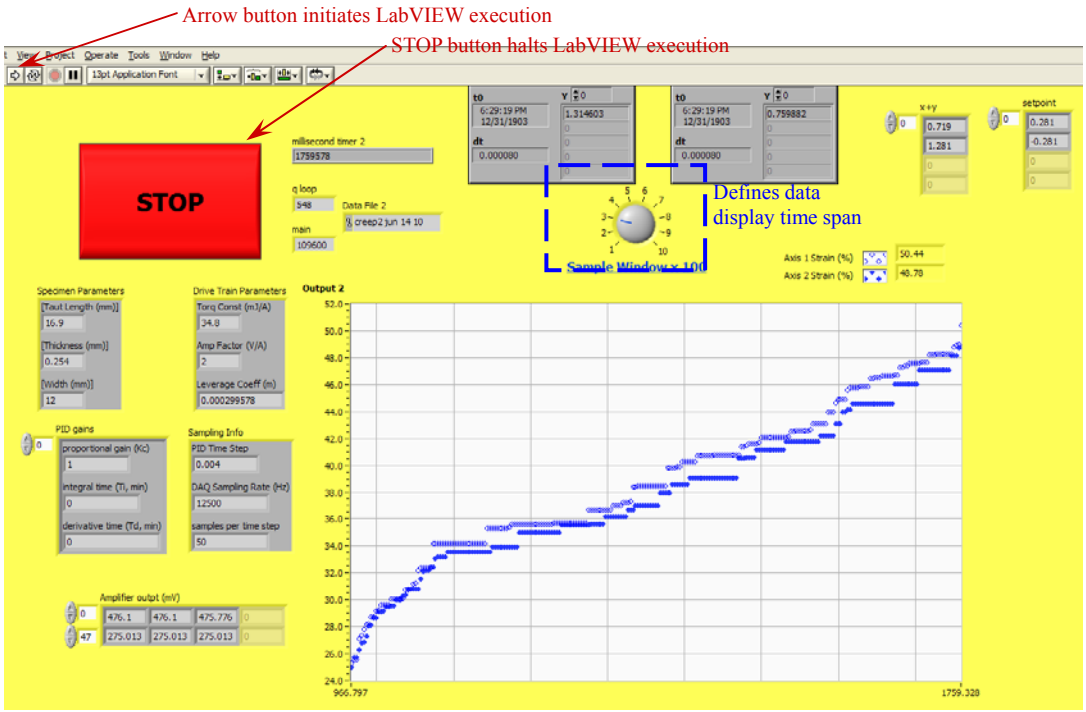

Figure 4-9: GUI display of the creep compliance mode.

After the required parameters have been input, the user depresses the OK button and the "PID Utility" sub-VI relinquishes to the top-level VI with the control loop. The drivetrain applies the prescribed stress instantaneously and the specimen displaces accordingly. However, due to specimen spatial variations and frictional differences between the two load frame axes, the initial displacement may differ between the two axes. Due to the kinematics

described in section **3.1.2** a difference in rotation between the 2 axes induces lateral binding of the free-side axis. This binding can lead to a cascading event that compounds frictional discrepancy between the axes such that the entire drivetrain will either lockup, or the free-side axis could disengage itself from the servomotor, causing the fixed axis to spin without constraint. The control scheme described in section **3.2.3** does not eliminate this possibility but does minimize it. Moreover, an additional precaution is implemented in the control loop to prevent damage to the drivetrain if this cascade event occurs. The green shaded box of **Figure 3-25** is a logic structure that shuts down output control signals to the servomotors if the extension of either axis exceeds 50% of the specimen length. This can be adjusted if the specimen length is sufficient such that 50% elongation can exceed the travel limits of the drivetrain.

As the drivetrain extends the specimen, the encoder signals are monitored in time. The experiment ceases autonomously once either axis extension exceeds 50% of the specimen length.

4.2.3. Procedural Modification for Non-Linear Contingency

Previously stated in section **2.3** in linear theory, the individual elements in both the Weichert and Kelvin models remain constant over the entire range of displacement or load as well as over any rate of change in the displacement or load. The Kelvin model, as discussed in section **4.2** is the preferred model to represent creep behavior. Examination of **(Eq: 2-8)** indicates that the relaxation time constants of the individual Voigt elements are proportional to $D_i\eta_i$. As in the case for the relaxation mode, non-linear behavior will affect the exponential function time constant. The consequence is that the rise time of the creep curves will be affected. Given the control scheme as described in section **3.2.4** the only manner to probe non-linear response is to alter the stress magnitude.

Applying a ramp rate to the torque of the servomotors is plausible, but the current LabVIEW VI would need to be modified. Assessing non-linear responses is outside the scope

of this thesis, but the creep tests on the PTFE specimens were conducted at different stress magnitudes; the results are presented in section **5.4**.

4.3. Harmonic Forced Oscillations

The most common and accurate method to assess both the real and imaginary components of **(Eq: 2-9)** and **(Eq: 2-10)** is by applying forced oscillations to the material and monitoring the forces and deflections along with the phase difference between the two. The frequency of the oscillations is varied so that the complex behavior is known over a frequency band. As mentioned in section **2.2** if the material is truly linear, then the same results can be generated from the static relaxation and creep tests. Conversely, the static behavior of the linear viscoelastic material can be inferred from the DMA tests by presuming the frequency is zero. So if this is indeed the case, then it is likely more cost effective to perform the DMA tests and forego the time and expense of the static tests.

If the material is nonlinear with strain rate, then the results will not concur, and that nonlinearity can be quantified via the DMA results moreso than by the static results.

4.3.1. Harmonic Mode Specimen Preparation

As described in section **3.2.5**, the harmonic mode has an identical wiring configuration of the servomotor amplifiers as the creep mode specified by **Appendix Fig D-2**. Hence, specimen preparation and pretension are identical to those described in section **4.2.1**. Heed should be given to the cautionary note of section **3.2.1**.

Note that as mentioned in section **3.2.5** there is no need for the PID controller. The "PID Utility" sub-VI still pops up but only requests inputs for the specimen parameters.

4.3.2. Harmonic Mode Procedure

As described in the previous section, the specimen preparation and mounting includes pretension of the specimen to remove any slack in the system. LabVIEW steps the user through the process as it does for the relaxation mode discussed in section **4.1.2** but the procedure is modified as specified in section **4.2.1**. The GUI display for the harmonic mode is depicted in **Figure 4-10**. The user interface for this test mode is more interactive than the

other three test modes. The consequence is that the GUI display has more complexity. Nonetheless, the theme of the user interface follows the architecture of a typical oscilloscope. So if the user is familiar with oscilloscope operation, then this user interface will seem intuitive.

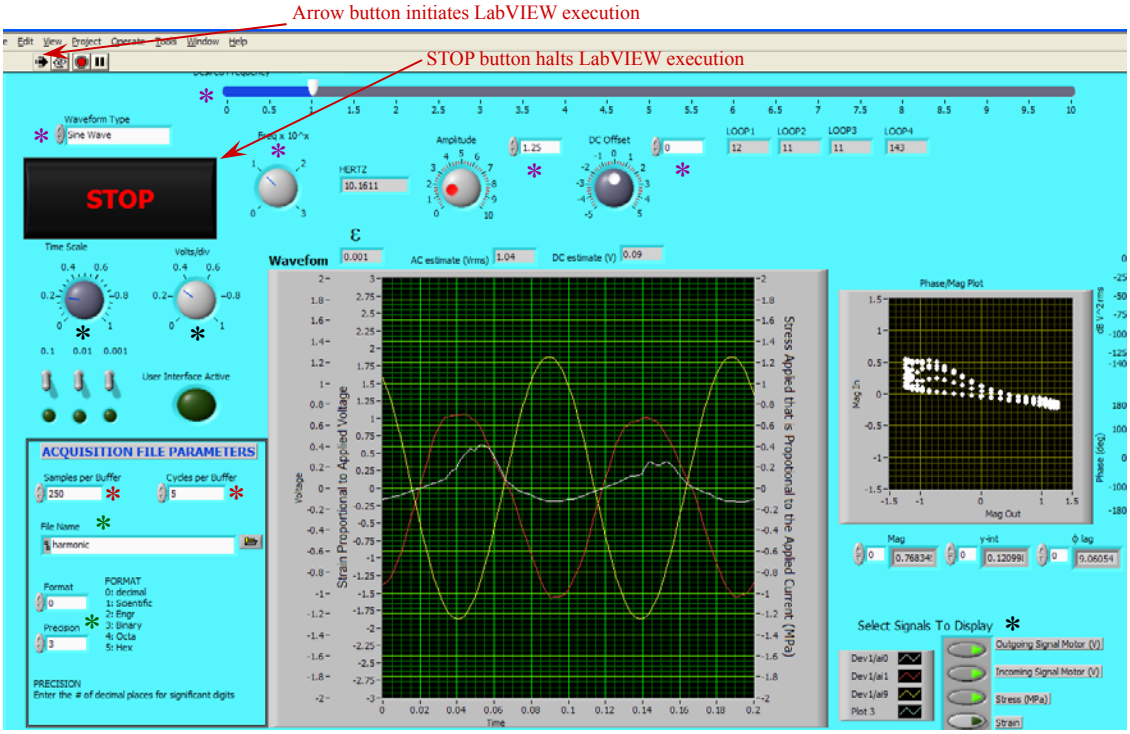

Figure 4-10: GUI display of the harmonic mode**.**

The GUI controls fall into five categories: 1) Execution control (Start and Stop);
2) * Data format and storage;
3) * DAQ parameters;
4) * Signal characteristics;
5) * Display control.

The GUI controls are highlighted by category in **Figure 4-10** with colored asterisks as denoted above except for the execution control which is denoted by arrows. Items on the GUI that are not denoted are simply displays for the user to monitor. Before discussing test procedures, operation of the GUI controls will be covered by each category aside from execution control which is the same as in the other three modes.

Data format and storage denoted by the green asterisks requires input as to the filename for archiving the digital data. There are 6 options as to what form the data is saved which is

labeled in the lower left corner of the GUI display. The most common selection is decimal form. Moreover, the precision or the number of significant digits is requested by the "Precision" control box. The number can be typed in directly or the increment button can be utilized.

DAQ parameters, denoted by the red asterisks, require input as to buffer size and the number of periodic cycles of the waveform signal to store. As dictated by **Figure 3-21**, the DAQ sampling rate is the ratio of the product between waveform frequency and buffer size to the number of waveform periods the user defines to be stored in the buffer. This customization of the DAQ timing as discussed in section **3.2.2.2** minimizes the demand on the computer DRAM. Nonetheless, the user should attempt to keep the DAQ sampling rate below 10kHz.

Signal characteristic controls denoted by the purple asterisks require input as to waveform type, amplitude, frequency, and DC offset. LabVIEW is capable of forming custom waveform types, but for this application the options are confined to sinusoid, square, triangle, and sawtooth. This control is located at the top left corner of the GUI display.

At the top middle of the display are two knobs: one for the amplitude and the other for the DC offset. The unit associated with those knobs is voltage. However, as specified in **Appendix Fig D-3**, the voltage to current conversion factor is 2V/A, and the torque to current conversion factor is 34.8 mJ/A as specified in **Appendix B.1**. This correlates to 17.4 mJ/V. Note that the voltage scale depicted in **Figure 4-10** is to 10V. The servomotors are rated at 44 mJ so the amplifiers will not drive the motors any harder past 2.5V. The scale peak has been set to 2.5V in LabVIEW despite what is shown in **Figure 4-10**. However, the user must exercise caution if applying a DC offset. Currently the LabVIEW code does not correct the peak voltage due to an applied offset. The consequence is that the amplifiers can overheat the motors. To avoid this, the oscillation amplitude can be reduced exactly by the amount of the DC offset.

The signal frequency has two control inputs. At the top of the display is a sliding scale knob with a scale of 0 to 10. Just below the slide scale and on the left side is a round knob with a scale of 0 to 3. The round knob controls the frequency by powers of 10. The slide scale controls the scale factor. For the setting of 3 on the round knob that corresponds to 10^3, or 1000, and the slide scale set on 3 yields 3×1000, or 3000Hz.

The display controls are denoted by the black asterisks. The time scale for the display is controlled by a round knob on the far left of the display along with three toggle switches immediately below this knob. In **Figure 4-10** the settings of the time scale is 0.2 seconds. Note that all three of the toggle switches are in the down position and the three LEDs below are OFF. If the middle toggle switch was in the up position then the LED below it would be illuminated and the corresponding time scale for the display would be 0.2×0.01 which is 2 msec. So the timescale for the display can range from 100μsec to 1 sec depending on the user selections. The LabVIEW code will not allow the user to have multiple toggle switches in the ON position. If the user attempts this, an alert message pops up with appropriate instructions to correct the situation.

The magnitude scale is controlled by the round knob immediately to the right of the timescale knob. Note that the units are in terms of V/div, but on the waveform display there are three vertical scales. There is also strain on the left along with volts, and on the right is stress. This one knob controls them all. The LabVIEW code has the conversion factors relative to voltage and automatically adjusts all three scales simultaneously.

To the far right lower corner of the display is the selection control for which signals to display. There are four: 1) outgoing voltage from the DAQ board to the servomotor amplifiers;
2) incoming voltage from amplifiers that is proportional to the current;
3) specimen stress based on the specimen parameters set by the user;
4) strain in percent.

The harmonic mode tests apply a torque to the servomotors, and via the load frame this is translated into an extensional load on the specimen. The load is harmonic in nature, and as the frequency changes so does the load rate. The specimens are tested to near static

conditions, 0.1 Hz up to 10Hz. The magnitude of the stress applied is targeted to be 4MPa with an oscillating stress of ±½ MPa. This stress level is around the lowest stress values that are applied in the creep mode tests. The GUI settings appropriate for these tests are specified in **Table 4-1**. The frequency is simply changed by the user via the slide bar.

The relationship between the voltage levels and the specimen stress levels is provided in **Appendix E**. The voltage levels listed in **Table 4-1** are pertinent to the PTFE specimens configured in the manner prescribed earlier in sections **4.3.1** and **4.2.1**.

The harmonic mode tests provide an order of magnitude more data than the static test modes and accomplish it in minutes instead of hours. Moreover, if the material is truly linear then the static behavior can be inferred from these tests. If non-linear characteristics exist the test procedure for the harmonic mode remains the same, unlike the static tests. The frequency change affects the strain rate, and the magnitude of the stimulus is simply altered by the amplitude knob of **Figure 4-10**. This test mode leaves little ambiguity in material behavior, whereas the static tests do.

Waveform type	Sine
DC Offset (mV)	210
Amplitude (mV)	26
frequency scale knob	0
Buffer Size	$100 \leq n \leq 1000$
# cycles per buffer	$1 \leq n \leq 10$
Time scale toggle switches	OFF
Time scale knob	Adjust according with freq
Filename	User preference
Data format	User preference
Precision	User preference
Signals Displayed	User preference

Table 4-1: Control settings for harmonic test mode.

4.4. Strain Rate Mode

As mentioned in section **3.2.6**, the strain rate mode is identical to the relaxation mode tests other than the strain rate is reduced. Hence, the specimen preparation will be identical to section **4.1.1** and the procedure will be a modification of the relaxation procedure of section **4.1.2**. Heed should be given to the cautionary note of section **3.2.1**.

As stated in section **3.1.4** regarding the servomotor specifications, the maximum rotational rate for the relaxation mode tests is 624 RPM. This rotational rate is on the low end of the spectrum for the servomotors for such low torque loads. Moreover, the control scheme of this mode coincides with the relaxation mode which is position control. The manner in which speed can be limited is to define a ramp of position with time. The gains defined for the PID controller in **Table 3-2** for the relaxation mode maximizes the stiffness of the servomotors. These gains are not ideal for speed control because the servomotors will exhibit a jittery response. So tests have been deferred until optimal PID tuning parameters can be defined.

A brief effort was exerted to attempt to control servomotor speed via pulse width modulation, but the hardware designated within this thesis is not sufficient for this capability.

5. Results

As mentioned in Chapter **1** the initial impetus for the development of this device was to evaluate the potential for human umbilical tissue to serve as a vascular graft material. Since the fluorocarbon polytetrafluoroethylene (PTFE) has been used for vascular grafts this material is a logical choice to validate the effectiveness of the device before attempting to work with actual biologic specimens.[13, 14]

Furthermore, the practice of applying the Fourier transform to analyze transient data while not unique, it is not common in viscoelasticity. What can be found in the literature is that the material parameters evaluated from these pseudo-static tests in the time domain have been used to infer the dynamic response of the material via the Fourier transform of the time series equation model of these materials expressed by **(Eq: 2-9)** and **(Eq: 2-10)**. Transient data on two other polymers are analyzed as well via the Fourier transform to investigate the feasibility of the technique. These materials were not tested in the device; instead the data were obtained from published literature.[27, 28] This effort resolved the issues associated with the application of the "discrete" Fourier transform on data that is considered non-periodic and has virtually no frequency component contained within the poles of the material response. These issues are discussed in detail within section **2.2**.

Also presented are results from conventional "INSTRON" tests that validated the effectiveness of the MOLEX IDT connectors in anchoring vascular specimens as an alternative to suturing the specimens. These tests also provided insight on expectations of material strength and stiffness that assisted in establishing the device specifications. These specifications include requirements on the frictional torque within the device. Results of friction tests are included to show the limitations of the device.

Also presented with less emphasis is a discussion on results of the PTFE specimens as to whether the material responds linearly or not. Much of the discussion hinges on obtaining sufficient data from harmonic mode tests.

5.1. Friction Characterization

It was recognized early in the design process of the load frame that the compliance of biologic specimens is quite large; this raises concern that friction in any mechanical load frame could overshadow the mechanical resistance of the specimen to strain in a measurement. This motivated the use of ball screws as described in section **3.1**. The friction contribution can also be countered by increasing specimen thickness, hence the wrapping of the PTFE specimens about the specimen brackets as described in section **4.1.1**. Moreover, as the specimen is extended, the tension compounds the friction in the system. If the load frame is sufficiently rigid, this tension will not compromise alignment, and the increase in friction should be linear with tension. If misalignment occurs, then binding is encountered and the relationship will be nonlinear.

The load frame friction was tested using a low friction pulley system with weights suspended in the vertical orientation by a nylon filament attached to the specimen bracket assembly. No sophisticated alignment tools were utilized, but manual distance measurements via calipers assessed that the force vector through the filament acted relatively perpendicular to the bracket assembly and on the same horizontal plane. Electrical current to the servomotors was incrementally increased until the onset of motion was detected. This is considered the threshold of static friction.

The maximum load capacity required for the device is considered to be 40N, which corresponds to a suspended mass slightly over 4kg. The tests were only conducted to 1kg because misalignment of the pulley system with the load frame became significant for higher loads. This was not due to the load frame, but the fixation of the pulley system. The static friction results are depicted in **Figure 5-1** and the linear behavior is shown. The linear slope indicates that for every 1kg or 9.81N axial load, a corresponding frictional torque of 1.1 mJ is required to overcome static friction. This work exerted to move the suspended mass of 1kg is actually less than the 1.6 mJ theoretically expected by **(Eq: 5-1)**. This surprising result might be an artifact of the measurement technique or possibly the applied load to the ball

screw relieves some of the preload that is designed within the ball screw itself. Regardless of the cause of the result it is reasonable to suggest that tension in the specimen will not compound the friction in the load frame beyond the expected linear relation of 1.6 mJ per 9.81N in axial load.

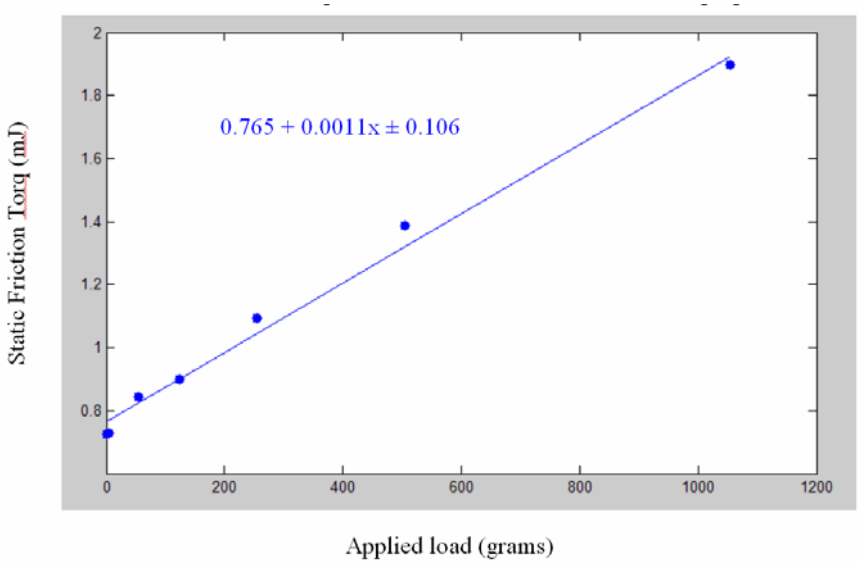

Figure 5-1: Static frictional torque of the load frame.

$$\frac{mg\cos\theta\phi_{pitch}}{2\pi} = \frac{1kg\left(9.81ms^{-2}\right)\cos\left(3^{0}\right)\left(0.001m\right)}{2\pi} \approx 1.6mJ \qquad \textbf{(Eq: 5-1)}$$

In regards to the rolling friction it was evaluated by tests conducted in similar fashion to the static friction tests but with the torque increased beyond the static friction threshold. The drive frame axes are held stationary as the current level is set and then the axes are allowed to spin freely. The torque values are recorded once the rotation acceleration transients have dissipated and the rotation rate has reached steady-state.

The results of these tests are considered inconsequential for both the relaxation and creep mode tests since motion in these tests is primarily stationary. The harmonic mode tests are affected by rolling friction. Nonetheless, absolute quantification is unnecessary since the contribution is easily subtracted from the results. The rolling friction manifests itself in the phase shift. Each time a harmonic mode test is conducted the phase contribution from friction can be assessed by conducting a test without the specimen mounted to the specimen

brackets. This is also a good diagnostic tool as to the wear condition of the load frame and if any parts may need replacement.

5.2. Viscoelastic Response of Polyamide/Graphite Composite and Superpave

As mentioned earlier in this chapter creep and relaxation data on two other polymers were obtained and analyzed to validate the analysis technique as described in section **2.2** to assess the real poles of the material. The two data sets chosen are deemed to represent opposing ends of the spectrum in terms of both relaxation and creep responses. The two limiting cases are if the material is highly viscous or nearly elastic. Therefore, it is expected that the response of biologic specimens will likely reside within this spectral range. Provided this basis then the analysis technique should be sufficient in establishing the material parameters of most biologic specimens of interest capable of sustaining tensile loads. It should be noted that not all biologic tissues can support tensile loads. The two materials chosen are polyamide/graphite composite and superpave. Superpave is an asphalt type polymer composite.

Figure 5-2 and **Figure 5-3** represent the relaxation and creep behavior of the two polymers respectively. These two figures are both normalized with respect to time and magnitude so that the data for both materials could be displayed on the same plot scaling. The timescale in both figures is normalized with respect to the duration time of the experiment. The magnitude in **Figure 5-2** is normalized with respect to E(t=0), whereas for **Figure 5-3** the magnitude is normalized by $D(t=t_{final})$. Other normalization strategies could be applied but this was deemed the most effective to display both data sets within the same plot scale and distinguish the difference between the behavior of the two materials.

In the case of superpave, note in **Figure 5-3** how the specimen continues to elongate even in steady state. Conversely, the polyamide/graphite composite not only reaches a definitive finite elongation but it happens rather quickly as compared to the asphalt. So this composite,

even though it is viscoelastic, is far more elastic in behavior than the asphalt. Another note is that the duration of the data set for the composite is ten times longer than that of the asphalt, and the magnitude of both the creep and relaxation of the asphalt is an order of magnitude greater. This is not apparent due to the normalization of these figures.

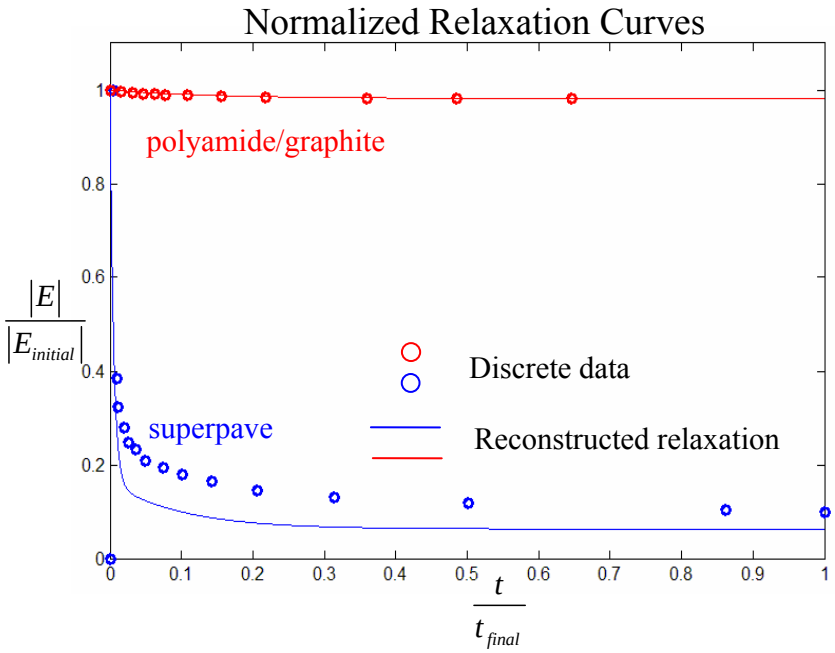

Figure 5-2: Relaxation empirical data versus computed relaxation (normalized).8,9[27, 28]

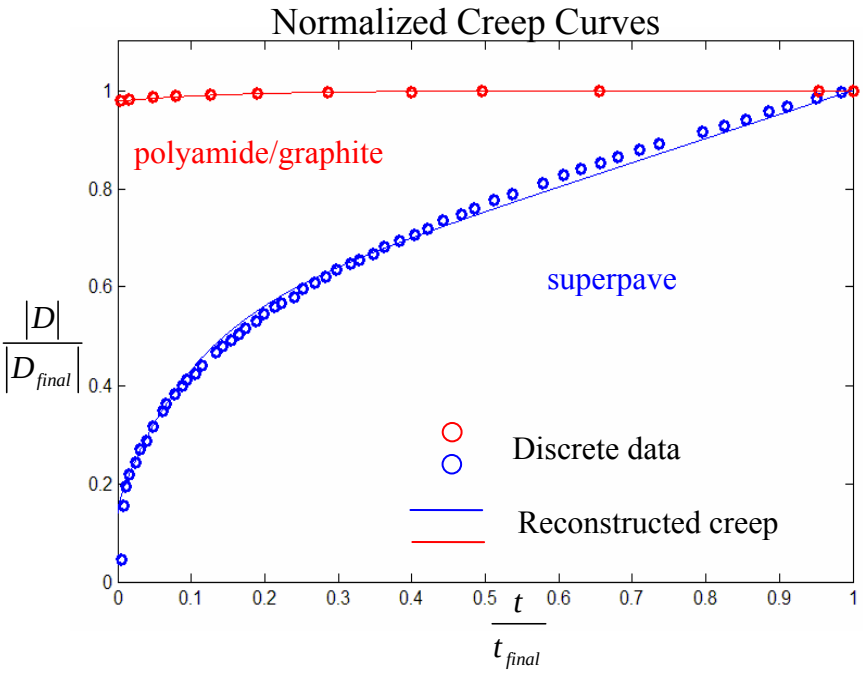

Figure 5-3: Creep empirical data versus computed creep (normalized).10[27, 28]

Other factors in choosing these materials for proof testing are the duration of the time scale of their data sets as well as the fact that their viscoelastic responses only possess real-valued poles. It is expected that the duration of these tests is much longer than what is expected for biologic specimens. These two aspects present the greatest demand on computational effort of the software to perform the discrete Fourier transform. Previously mentioned in section **2.2**, it is not a trivial task to generate the Fourier transform of a non-periodic signal via the discrete Fourier transform. It is presumed that if the correct behavior can be accurately computed for these extreme cases then the software is more than capable for data sets on biologic specimens.

Both **Figure 5-2** and **Figure 5-3** also depict the reconstructed signals from the Fourier transforms of the empirical data sets. Inspection shows that accurate reconstruction of the more elastic material, polyamide/graphite, was obtained for both creep and relaxation tests. For the more viscous asphalt the creep results were reconstructed very well, but some discrepancy in the empirical data with the reconstruction is evident in the relaxation tests. However, it should be noted that the number of samples for the creep data set for this material was a factor of 3 greater; therefore, the time resolution for the creep data set was much better and is the most probable contribution for the discrepancy. The explanation for this resides in the fact that an interpolation algorithm is applied to the discrete data set to enhance time resolution. Enhancing time resolution increases the bandwidth in the frequency domain. As described in section **2.2**, the real poles of the material are assessed from the frequency spectrum. So, poor time resolution propagates through the procedure of pole assessment.

Figure 5-4 is the normalized magnitude spectrum for both the creep and relaxation tests, note the deviation on the spectrum for the superpave. As discussed for both **Figure 2-3** and **Figure 2-4**, it is possible to exploit this deviation to locate the poles of the system; indeed, this was correctly computed for this material, which yielded two decay time constants of 5 and 100 seconds.

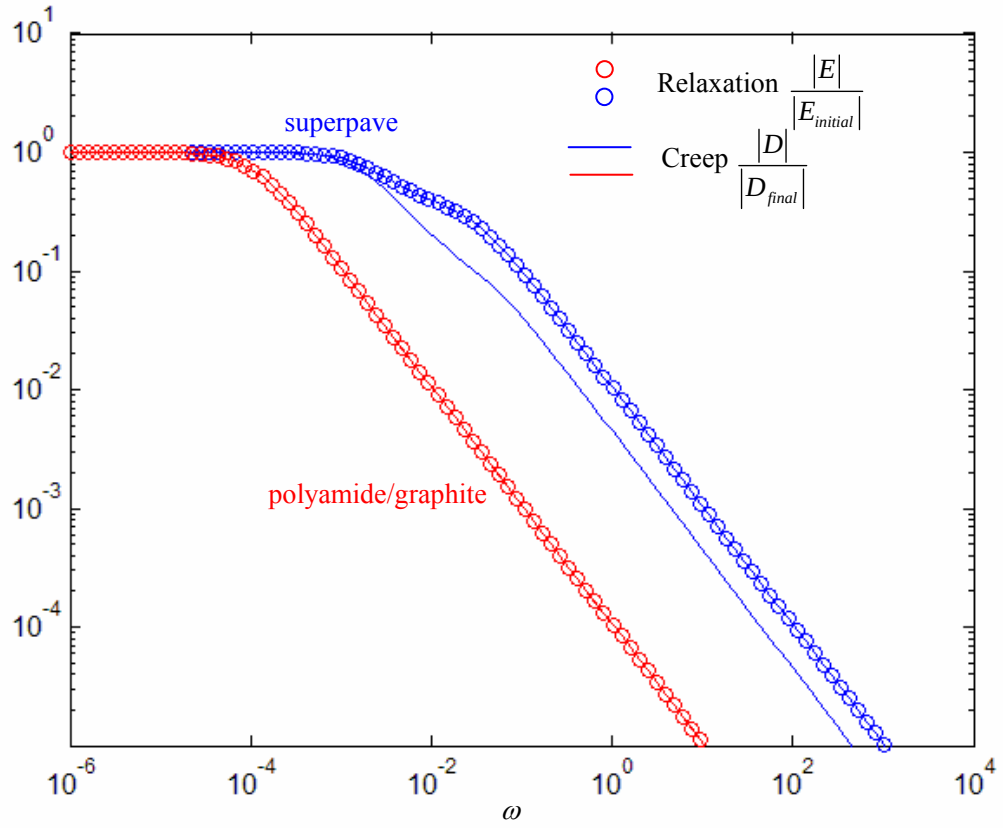

Figure 5-4: Normalized magnitude spectrum of both creep and relaxation tests.

5.3. Stress Relaxation of PTFE

Previously mentioned in this chapter the fluorocarbon polytetrafluoroethylene (PTFE) is a logical choice to validate the effectiveness of the device before attempting to work with actual biologic specimens. **Figure 5-5** depicts relaxation data sets for PTFE obtained from the device and data obtained from the manufacturer DuPont. A couple of observations of note are that the DuPont data is much less noisy than the data obtained from the device. Moreover, the magnitude of the stress for the DuPont data seems significantly higher.

A number of factors account for these observations. The foremost is that the DuPont data are obtained from bulk specimens of PTFE. The material tested in the device is 0.002 inch PTFE film. Since the stress is computed with assumed dimensions of the specimen then slight variation in the film thickness easily accounts for such a discrepancy in magnitude. Since evaluation of the relaxation parameters do not require an exact knowledge of the stress magnitude then the relative change in magnitude in the decay is more relevant. **Figure 5-6**

is a scaled version of **Figure 5-5** that has the vertical axis normalized with respect the final stress value at the termination of the experiment. Aside from the noise the data from DuPont and the device are commensurate.

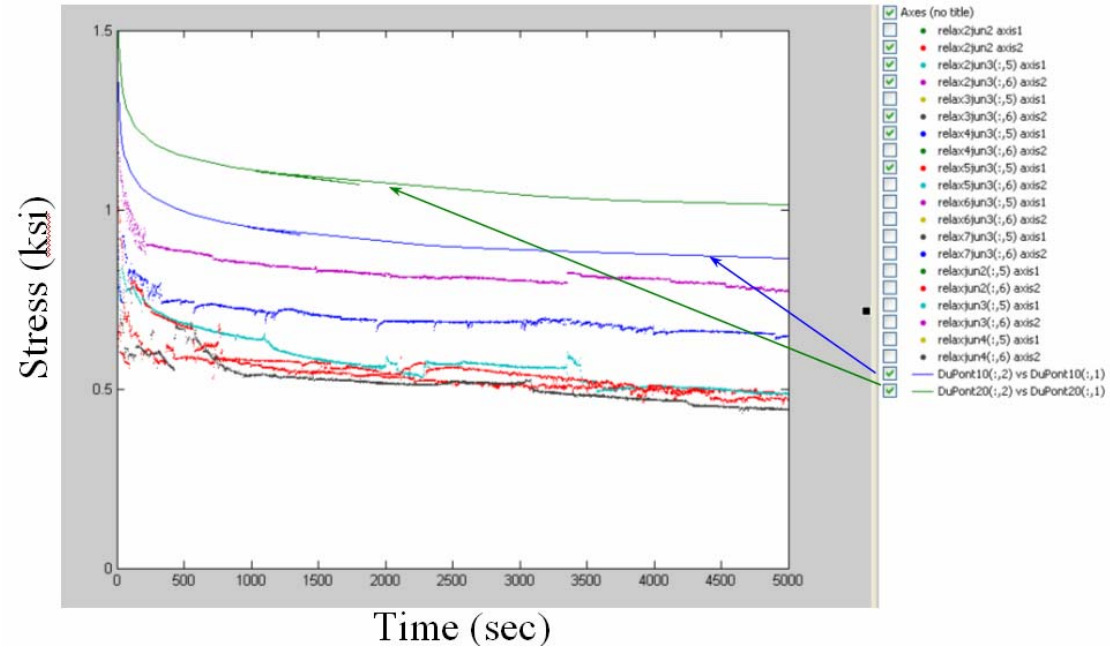

Figure 5-5: Stress relaxation data comparison with industry standard from DuPont. [15]

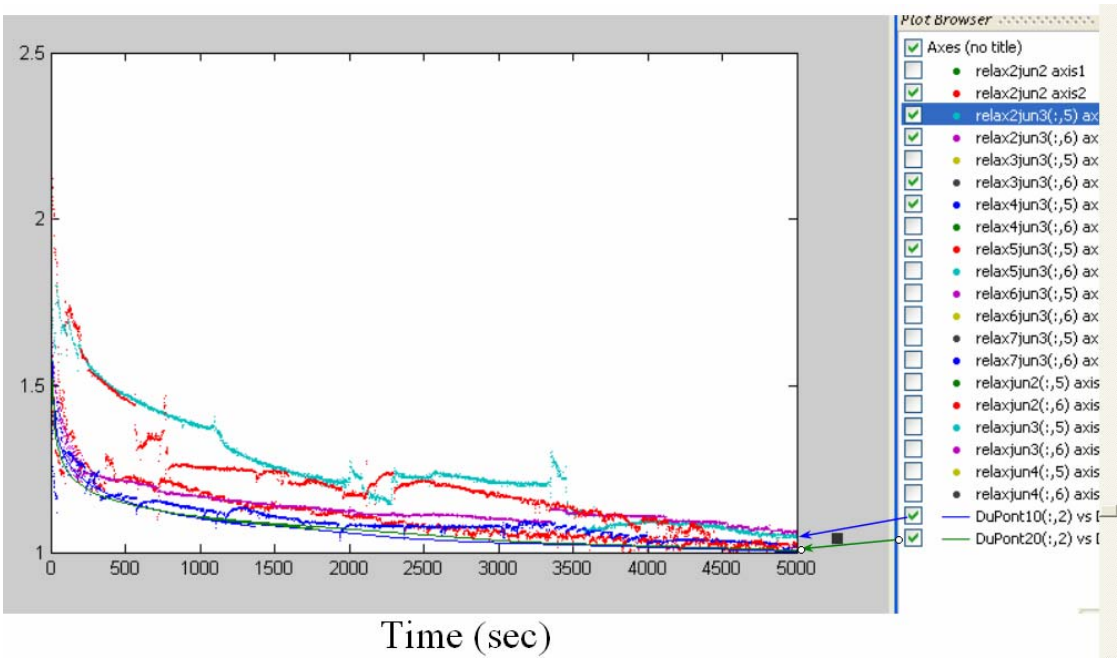

Figure 5-6: Stress relaxation magnitude normalized with respect to final stress.

With regards to the noise, the discussion in section **4.1.2** raised the issue that the PID controller signal diminishes in magnitude as the servomotors approach the specified rotation

set point. The consequence of this is that as the specimen relaxes the residual torque in the servomotors induces an intermittent displacement as they strive to meet the targeted rotation. This intermittent displacement is the primary source of the noise in the data sets generated by the device. Moreover, since DuPont was testing bulk material they had the luxury of employing well-tuned conventional test apparatus that meet industry standards.

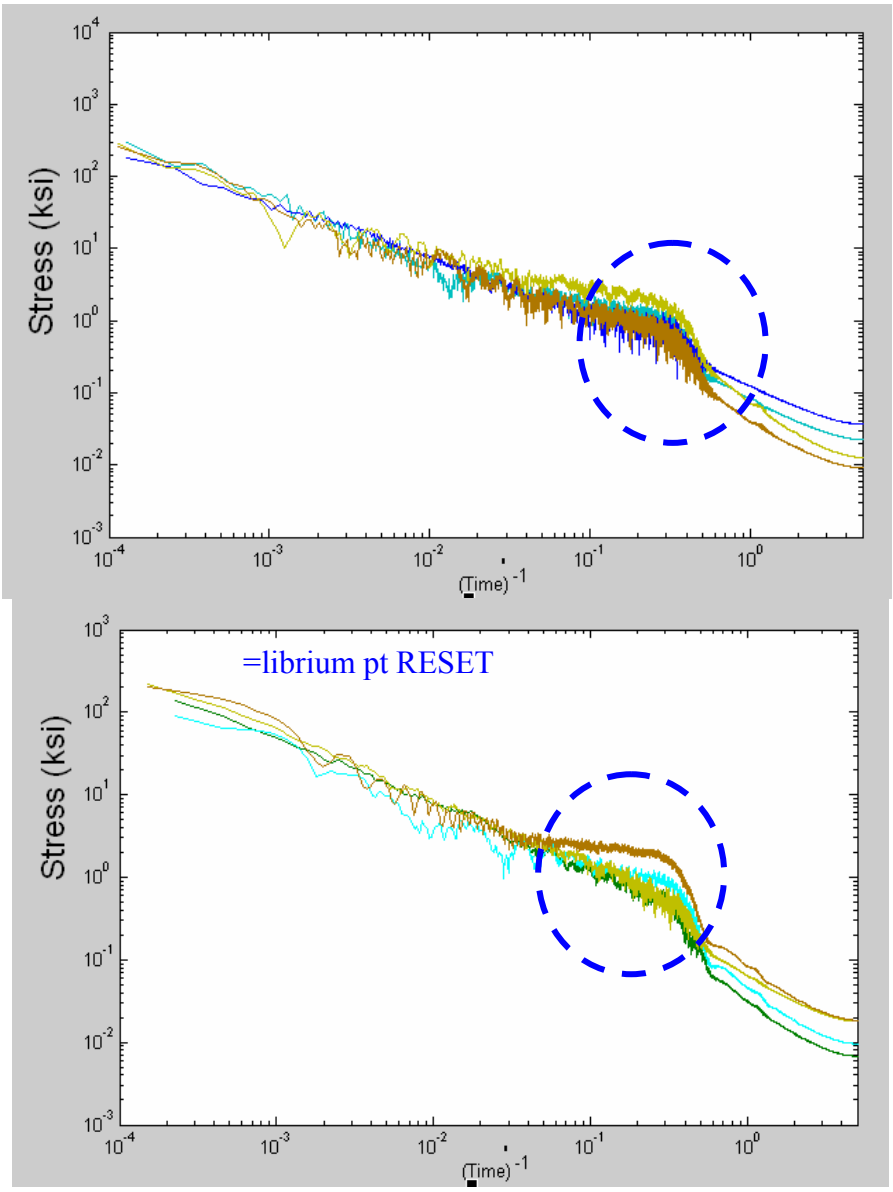

Figure 5-7: Noise suppression in relaxation data.

An effort to minimize this intermittent motion by resetting the PID equilibrium set point once the servomotors are arrested after the initial displacement proved to be of some benefit. Nonetheless, **Figure 5-7**, the transform of the data into the frequency domain shows a

reduction in the noise but the complex pole at 0.3Hz still exists. While this can also be deduced from the time domain data set this is another demonstration of the utility of the Fourier transform. It can identify potential issues with the test equipment.

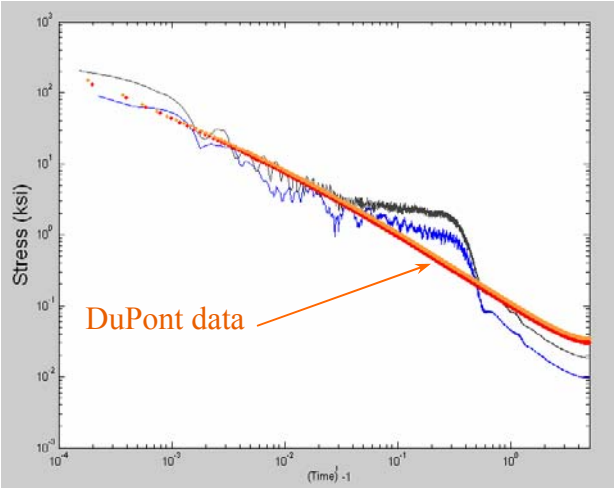

Figure 5-8: Fourier transform of relaxation data.

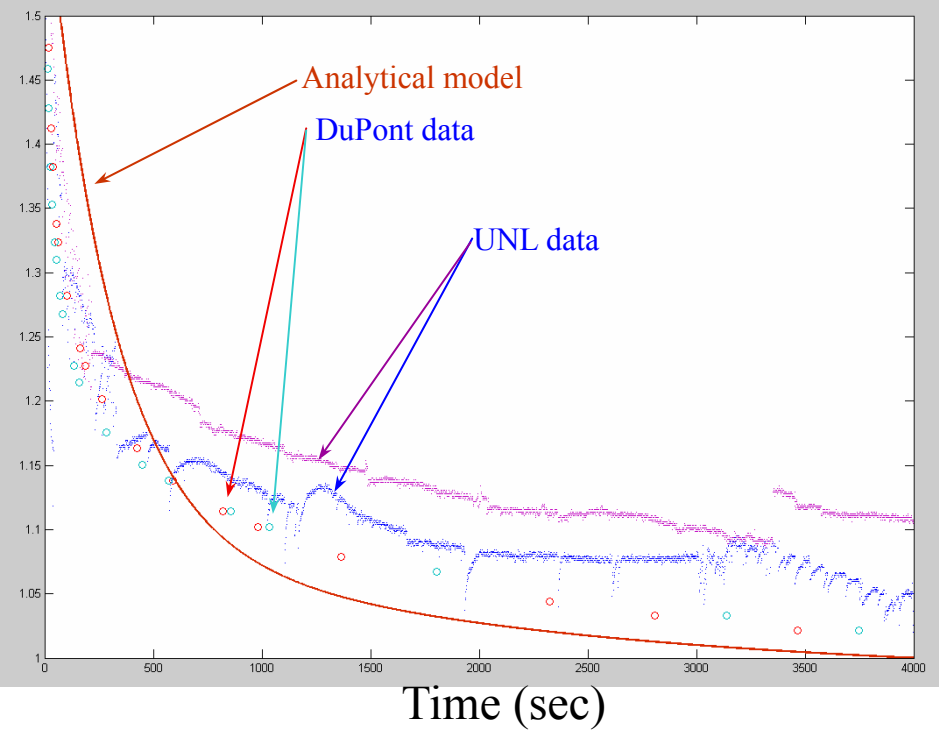

Figure 5-9: Analytical model correlation to empirical data sets.

Figure 5-8 overlays the transform of the DuPont data with data obtained from the device. Aside from the prominence of the complex pole at 0.3Hz in the device data the overall trend as in the time domain indicates the data sets are commensurate with one another. The

analysis technique as described in section **2.2** to assess the real poles of the material yielded three decay time constants of 0.01, 300 and 2000 seconds. A validity check of these poles is done by plotting the analytical model against the empirical data set in **Figure 5-9**. The vertical scale is normalized in an identical manner to that employed by **Figure 5-6**. What is interesting is that a better correlation can be attained by a higher-order model, but the 3rd-order system is an adequate approximation of the material response for data sets that were obtained independently from one another. Moreover, the noise associated with the device data did not hinder the modeling.

5.4. Creep Compliance of PTFE

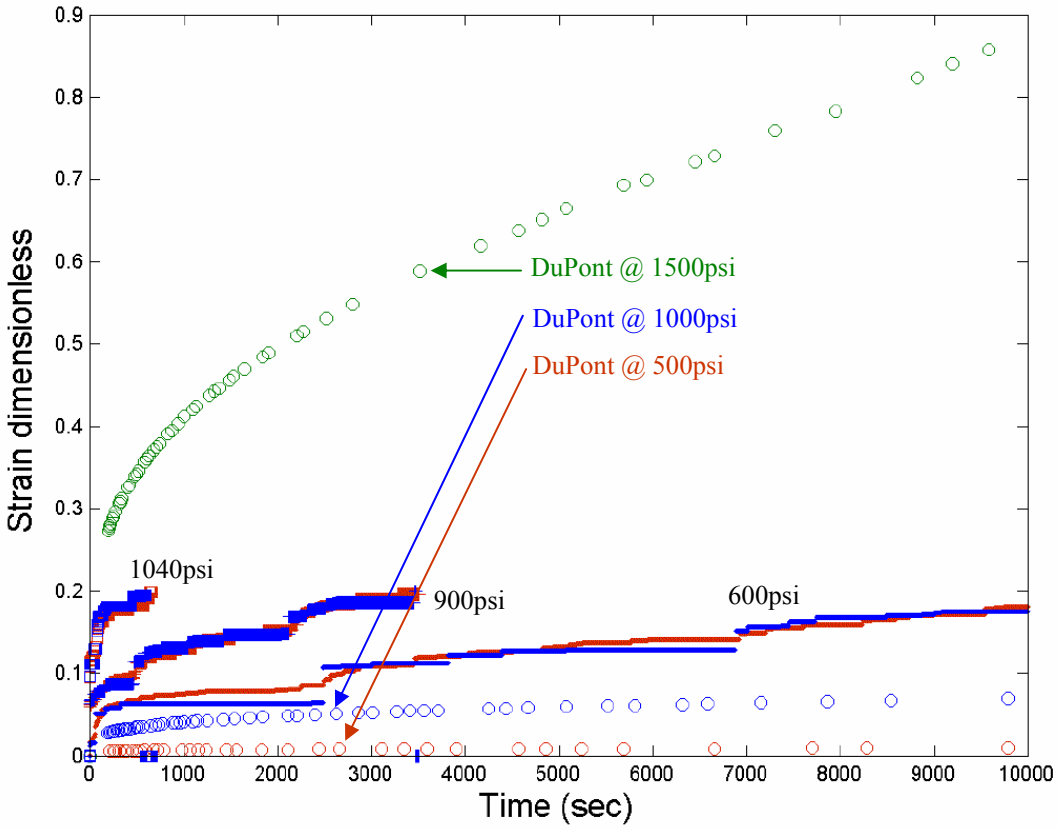

Figure 5-10: Creep response from manufacturer's published results versus UNL data on PTFE 0.002" film.[15]

It is well established that the creep response of a material is a function of the stress level within the specimen. **Figure 5-10** depicts creep data sets for PTFE obtained from the device as well as data published by the manufacturer at various stress magnitudes. Unlike the

relaxation data the creep data do not concur with DuPont's published curves. It was not known if this discrepancy is attributable to either uncertainty in the specimen stress level in the film specimens due to thickness variations or if the PTFE film is subjected to plane strain. Bulk specimens distribute strain energy along three orthogonal axes. The film specimens are not afforded this luxury and the potential consequence might be that the rate of strain increase might be greater. Due to the discrepancy in the data the PTFE film was also tested on a BOSE ElectroForce 3200 series mechanical test machine. Data from these tests are depicted in **Figure 5-11**.

Since the specimen tested in the BOSE device was allowed to deform well past the 20% extension ratio **Figure 5-11** presents three strain curves for this data set. The manner in which that strain is computed is contained in formulations depicted in the figure **Figure 5-11**.

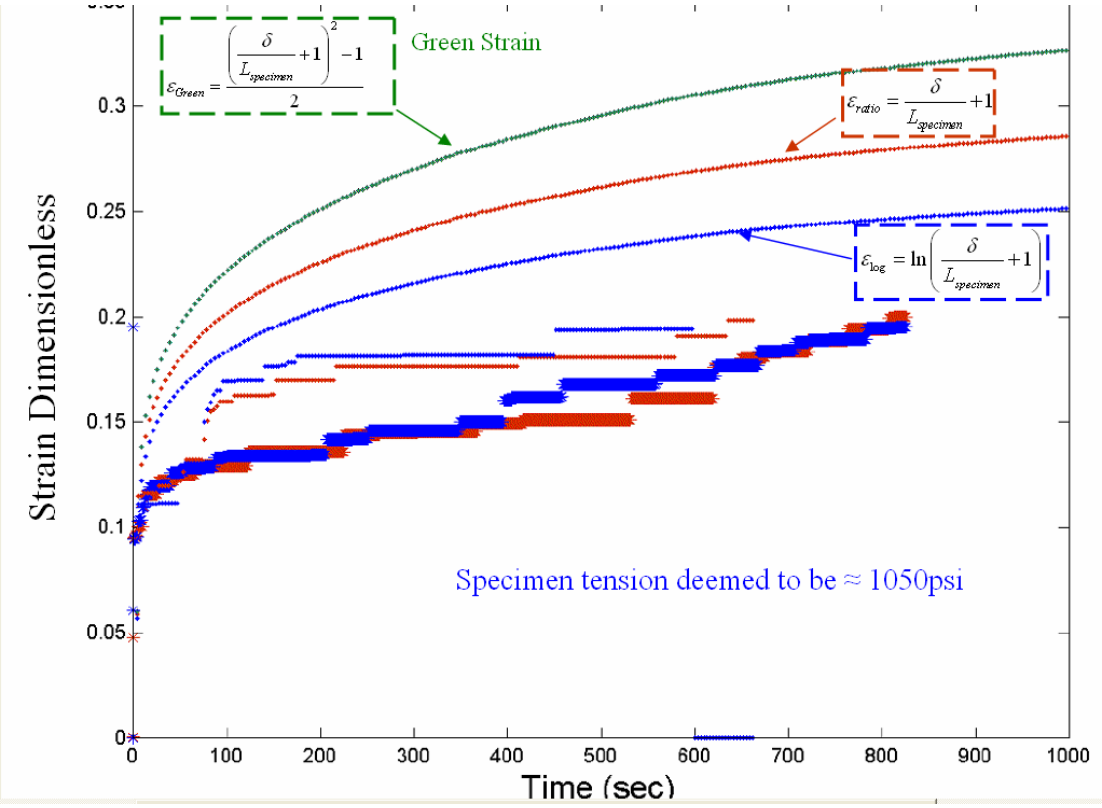

Figure 5-11: Creep response on PTFE 0.002" film obtained from the device versus data from the BOSE ElectroForce 3200 series mechanical test machine.[29]

The timescales between the data sets within **Figure 5-11** match better than those of **Figure 5-10**. It is fair to note that noise in the BOSE data is virtually nonexistent, whereas the data from the device being validated appears more erratic. The source of the noise as discussed previously in both sections **3.1.3** and **4.2.2** is that the rotations of the 2 axes of the drivetrain must maintain phase relative to each other to avoid excessive binding. To assure this the control scheme makes variable adjustments in torque level between the two axes. This variation is depicted in **Figure 5-12** The level of variation can be adjusted within the LabVIEW code as described by **Figure 3-24**. The variations in **Figure 5-12** may appear large but they are symmetric and are effective in avoiding binding. The drawback is the noise in the data and this is where the utility of the Fourier transform can be of assistance once again.

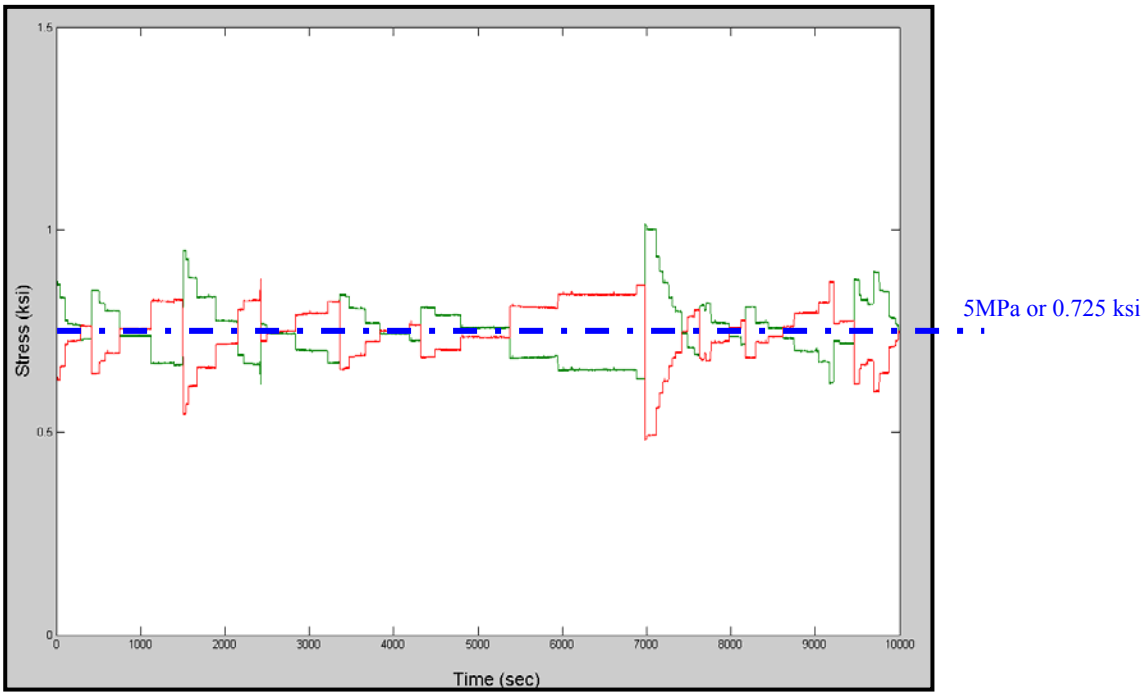

Figure 5-12: Torque variations between the 2 drivetrain axes.

$$\frac{d}{dt}\left[\sum_{i=1}^{j} D_i\left(1-e^{\frac{-1}{D_i\eta_i}t}\right)\right]=\sum_{i=1}^{j}\frac{D_i}{D_i\eta_i}e^{\frac{-1}{D_i\eta_i}t}=\sum_{i=1}^{j}\frac{1}{\eta_i}e^{\frac{-1}{D_i\eta_i}t} \qquad \textbf{(Eq: 5-2)}$$

Discussion of transforming the creep data must be predicated by the manner in which the creep signal is processed within LabVIEW. As prescribed by **(Eq: 2-8)** the creep response of

the Kelvin general model contains three terms. The first, D_0, is the initial offset of the specimen at the instant in time load application occurs. LabVIEW subtracts this value from the signal. The second term is linear with time. LabVIEW differentiates the signal and is left with a constant value of $1/\eta_\infty$. This is subtracted as well. What remains of the differentiated signal is **(Eq: 5-2)**. This is similar to the relaxation differentiated signal. It is a series of decaying exponentials and the Fourier transform of this allows for the evaluation of the poles as done for the relaxation signal in sections **5.2** and **5.3**.

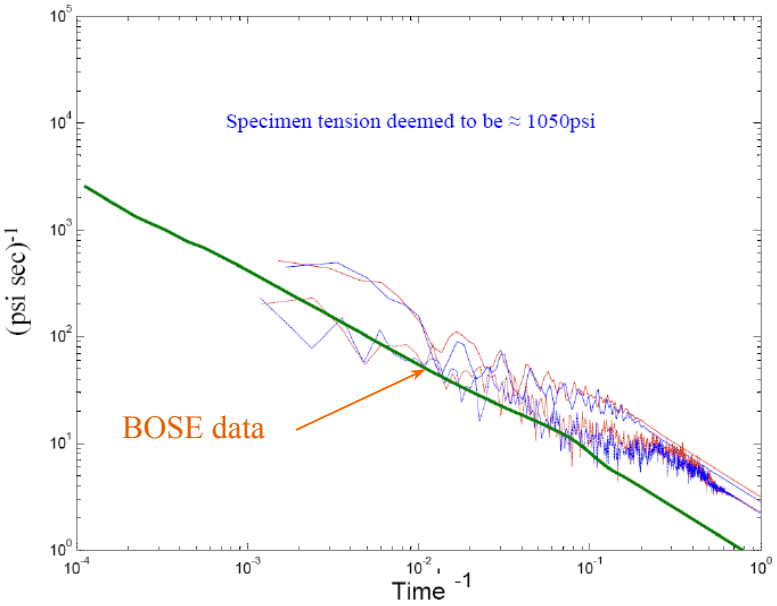

Figure 5-13: Fourier transform of creep data.

Figure 5-13 overlays the transform of the BOSE data with data obtained from the device. Aside from the prominence of the noise the overall trend as in the time domain indicates the data sets are commensurate with one another. The analysis technique as described in section **2.2** to assess the real poles of the material yielded three decay time constants of 50, 300 and 2000 seconds. A validity check of these poles is done by plotting the analytical creep model responses against the empirical data sets in **Figure 5-14**.

The two solid curves represent the model responses. Both curves have the same 3 decay or rise constants but are offset on the vertical scale by the constant representing D_0 of **(Eq: 2-8)**. One curve tracks the BOSE data and the other tracks the data obtained from the drivetrain. The offset infers a different D_0 evaluation between the two test devices. This

discrepancy can be attributed to a couple of factors which can only be resolved with further testing.

One factor which is the most likely culprit is the initial slack in the system or the specimen. Great effort to pretension the specimen in both test devices was applied but in the case of the BOSE system the specimen is oriented vertically. The consequence of this is that mounting of the specimen was hindered by gravity. There was no fine adjustment of the specimen clamp position to detect the onset of tension. Instead the vertical position of the lower clamp base is adjusted manually until the force display on the computer monitor is perturbed.

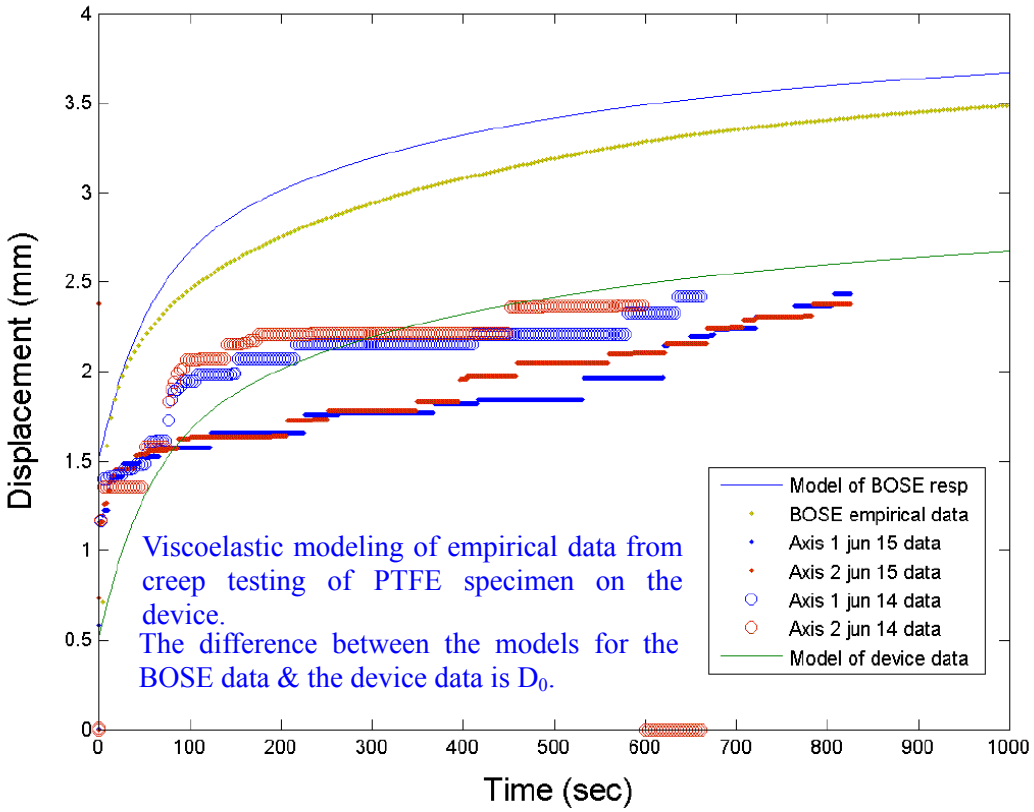

Figure 5-14: Analytical creep model correlation to empirical data sets.

The second factor which is an issue discussed in the relaxation test results of the previous section is that variations in specimen dimensions contribute to uncertainty in the stress level. Since D_0 can be dependent on the stress level this provides another source of error.

Aside from the uncertainty of D_0 and the noise inherent to the servomotor drivetrain the 3rd order system represents both data sets reasonably well. It is worth noting the cost of BOSE device was $66K at the university discount. So to obtain equivalent viscoelastic information but with less noise can cost a commercial company in excess $100K, whereas this device is no more than $5K without the computer.

5.5. Harmonic Forced Oscillations

As described in **3.2.5**, the harmonic mode has the identical wiring configuration of the servomotor amplifiers as the creep mode specified by **Appendix Fig D-2**. However, at this juncture the LabVIEW code has not been updated for this wiring configuration. The previous iteration of the LabVIEW code to validate the capability of synchronizing signals is configured for the wiring of the servomotor amplifiers as specified by **Appendix Fig D-1**. In order to accurately assess phase differences between the stimulus and response signals synchronization is absolutely required. The wiring configuration of **Appendix Fig D-1** was more conducive for this validation procedure.

Despite this need for software updates **Figure 5-15** depicts an anticipated response spectrum based on the creep data of the previous section. Since the input stimulus to the specimen is an oscillation in torque the response is a displacement. Due to this arrangement it is more appropriate to apply **(Eq: 2-10)** versus **(Eq: 2-9)** to generate a response spectrum. The spectrum of **Figure 5-15** will only be correct if PTFE is linear viscoelastic. It is documented that PTFE is not linear, but over certain stress and displacement levels it is. So the presumption is that the device can oscillate about a defined nominal stress level and the displacements reasonably small the spectrum of **Figure 5-15** will be reproduced by harmonic mode testing.

The magnitude spectrum of **Figure 5-15** is rather mundane but the phase spectrum of **Figure 5-16** reveals more on the validity of the viscoelastic model. At very low frequencies the stress and strain will be in phase relative to one another due to the fact that the viscous dampers of the Kelvin model in **Figure 2-2** have little impact if the strain rate is sufficiently

low. As the frequency increases the effect of the dampers eventually induce a phase lag approaching 90^0. Eventually the phase again approaches zero at high frequencies. Since the phase shift is directly attributable to the "loss" constituent of the complex creep compliance as discussed in section **2.2**, the behavior of the phase frequency response correlates exactly with that of **Figure 2-8**. The physics of this behavior is discussed in section **2.2** and is attributable to the rate of energy dissipation, but a simplistic analogy is useful to understand **Figure 5-16**.

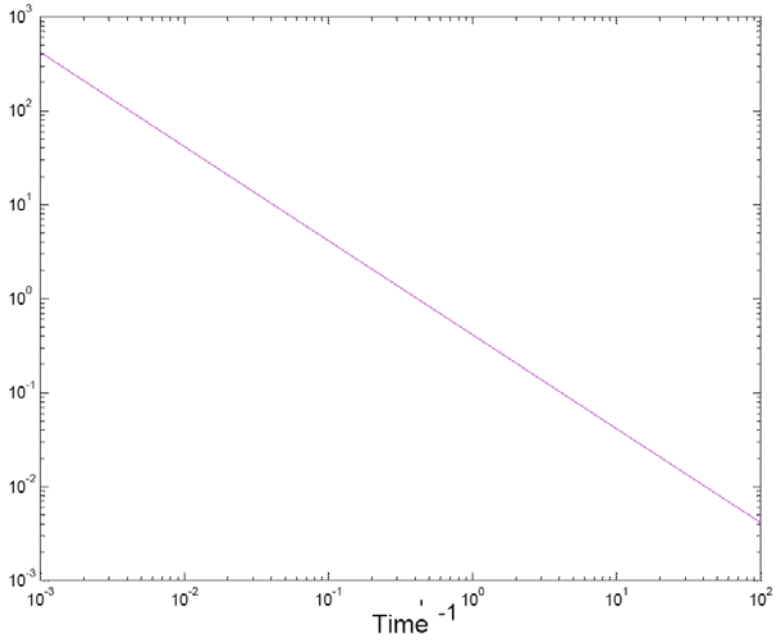

Figure 5-15: Anticipated magnitude spectrum generated from the creep response data of the previous section.

The Kelvin model possesses the viscous damper η_∞ in series with the spring element D_0 as shown in **Figure 2-2**. This viscous damper will become rigid at sufficiently high frequencies and so will all of the other dampers in the Voigt segments of the Kelvin model. The consequence is that the oscillating stress stimulus will directly couple into the displacement of the lone spring element D_0, hence the stress and displacement will again be in phase. So the phase spectrum yields more information on the material.

However, the test procedure only specifies that the test frequency to be carried out to 10Hz. Nonetheless, if the 3rd order system presented in section **5.4** is correct and linear

viscoelastic assumptions are correct then the phase change at 10 Hz will concur with the phase lag 87^0 as indicated in **Figure 5-16**.

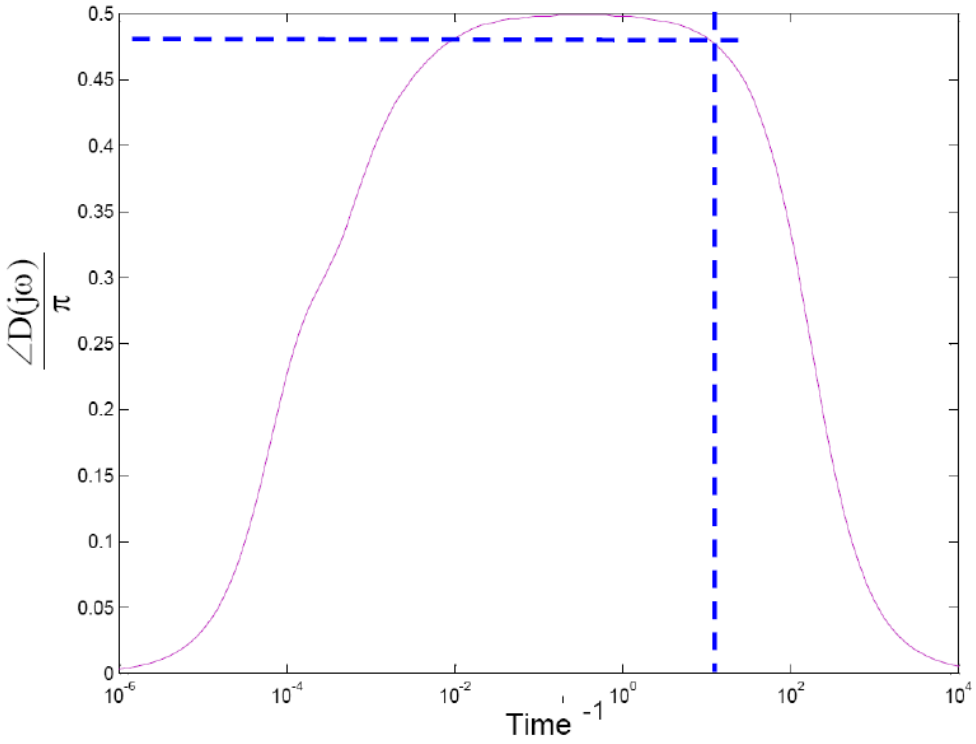

Figure 5-16: Anticipated phase spectrum generated from the creep response data of the previous section.

5.6. Strain Rate Mode

As mentioned in section **4.4**, the PID control parameters need to be retuned for the strain rates required for this test mode.

5.7. INSTRON Tests

As described in section **3.1.1**, the interface of the specimen brackets with the drivetrain is modular. Since boundary conditions can factor into the viscoelastic response of the specimen the design of the drivetrain and the specimen fixturing were segregated. **Figure 3-6** is the rendering of the specimen brackets specific to the research sponsored by Dr. James Hammel of UNMC. As previously mentioned the materials being evaluated are various implant materials for a cardiac septal defect in infants. The implants are sutured into place and the design of these brackets is to emulate the boundary conditions of those sutures. The bracket assembly incorporates the use of MOLEX IDT connectors which have the precise pattern of

the suture interval required. These connectors are utilized in the electronics industry for connections of ribbon cables to PC boards. Their utility, aside from the speed with which they can be fastened, is in the ability to pierce the specimen and their interlocking mechanism that ensures the specimen is secure.

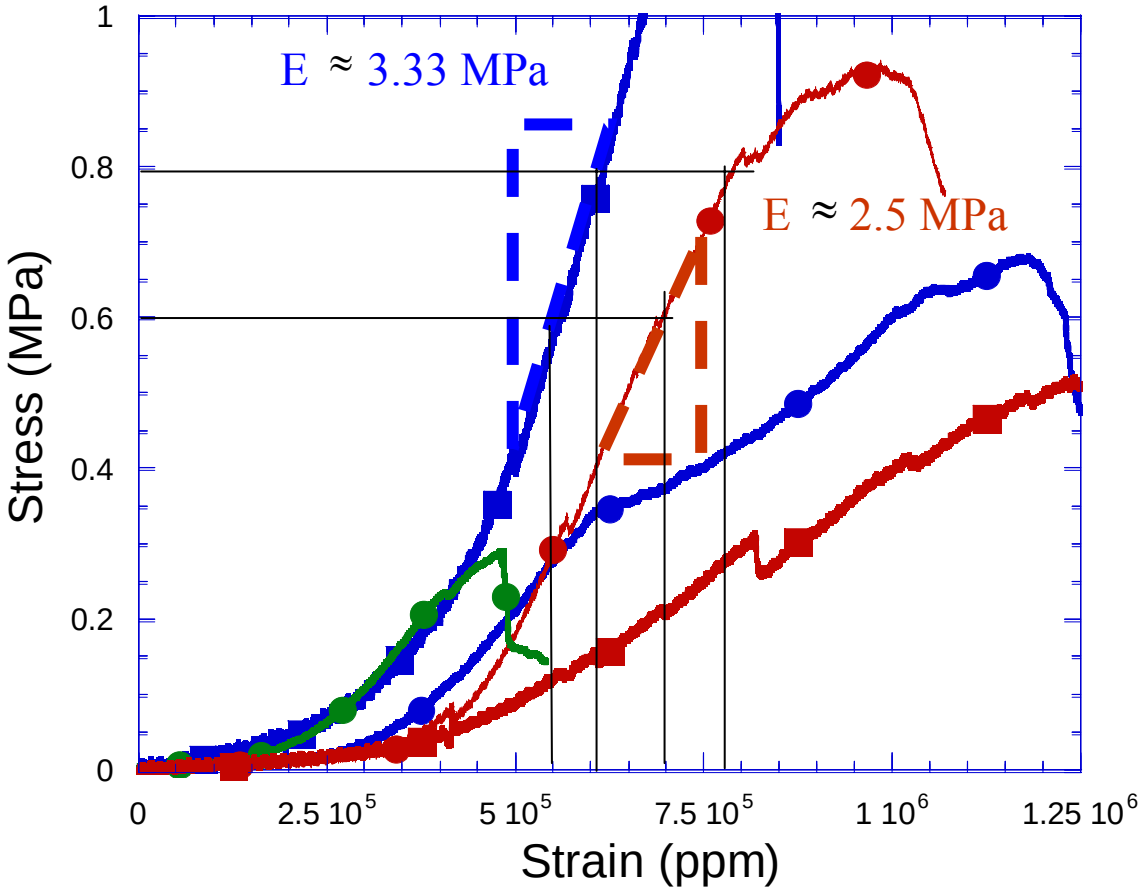

Figure 5-17: Stress/strain tests on homograft with the use of MOLEX IDT connectors as the fixturing mechanism.

To validate the use of these connectors, tests were conducted on an INSTRON uniaxial mechanical test machine. There were concerns that the piercing of the material by the pins of these connectors could cause premature failure of the specimen. Both homograft and umbilical cord tissue were tested to failure. **Figure 5-17** contains the results. The results were compared to literature to be sure premature failure was not induced via stress concentrations at the punctures. In fact, utilizing these connectors proved out statistically to outperform the grips supplied by the manufacturer for the INSTRON machine. The linear

modulus values and the failure stresses depicted in **Figure 5-17** are consistent with values listed in literature.

6. Summary & Conclusions

As previously discussed, all biologic tissues exhibit viscoelastic behavior. This behavior is characterized by hysteresis in the response of the material to load or strain. Well documented techniques exist for engineering materials such as the polymers PTFE, polyamide, polyethylene, etc. While procedures have been developed for evaluating the engineering polymers the techniques for biologic tissues are not as mature.

A digitally controlled drivetrain capable of conducting four different viscoelastic test modes has been developed. The four test modes are stress relaxation, creep, harmonic induced oscillations, and controlled strain rate tests. The initial impetus for the development of this device was to evaluate the potential for human umbilical tissue to serve as a vascular graft material. The consequence is that the load frame is configured for membrane type specimens with rectangular dimensions no more than 25mm per side. The design load capacity of the drivetrain is to impose an axial load of 40N on the specimen.

The stress level in the specimen is be dependent on the specimen width and thickness. The width of the specimen cannot exceed 25mm as indicated in **Figure 3-6**. The specimen thickness is primarily be dependent on the specimen bracket design which is modular. The end user specifications drive the design of the brackets and the bracket interface with the drivetrain is through the four shoulder bolts as discussed in section **3.1.1**. The brackets proposed for the vascular graft application in this thesis are capable of accommodating a specimen as thick as 5mm and the fixation technique via MOLEX IDT connectors was validated.

Since the fluorocarbon PTFE has mechanical properties commensurate with vascular tissue and the viscoelastic properties of this material have been published, hardware and software validation of the drivetrain was accomplished by testing PTFE. The creep and relaxation data generated are consistent with published literature. Moreover, to generate the same information can cost a commercial company in excess of $100K if they need to procure commercially available devices that generate similar information.

Augmentation of the device capabilities is realized via application of the Fourier transform on post-processing of the data. The LabVIEW program developed in conjunction with the device generated a relatively accurate viscoelastic model of PTFE and the reconstructed relaxation and creep response of the model compared well with the empirical data as shown in **Figure 5-9** and **Figure 5-14**.

It is outside the purview of this thesis, but the opinion of this author is that the industry practice of stress relaxation and creep tests to avoid inertial effects in the material response might be shortsighted. Without question an instantaneous displacement of a test specimen is not realistic due to the need for an infinitely rigid load structure and infinite power requirements on actuation, but if the ramp rate is sufficiently high and the data acquisition system quick enough inertial accelerations can be can be induced. Monitoring the oscillation which will be damped is an indicator of the viscoelastic behavior as well. Moreover, it might be possible able to infer all of the poles from that decaying oscillation by analysis of the phase. If this can be done then the need for these long pseudo-static tests might be eliminated. A fair amount of research and testing would have to be done to prove this out, but it might be plausible.

.

Appendix A. Assembly drawings

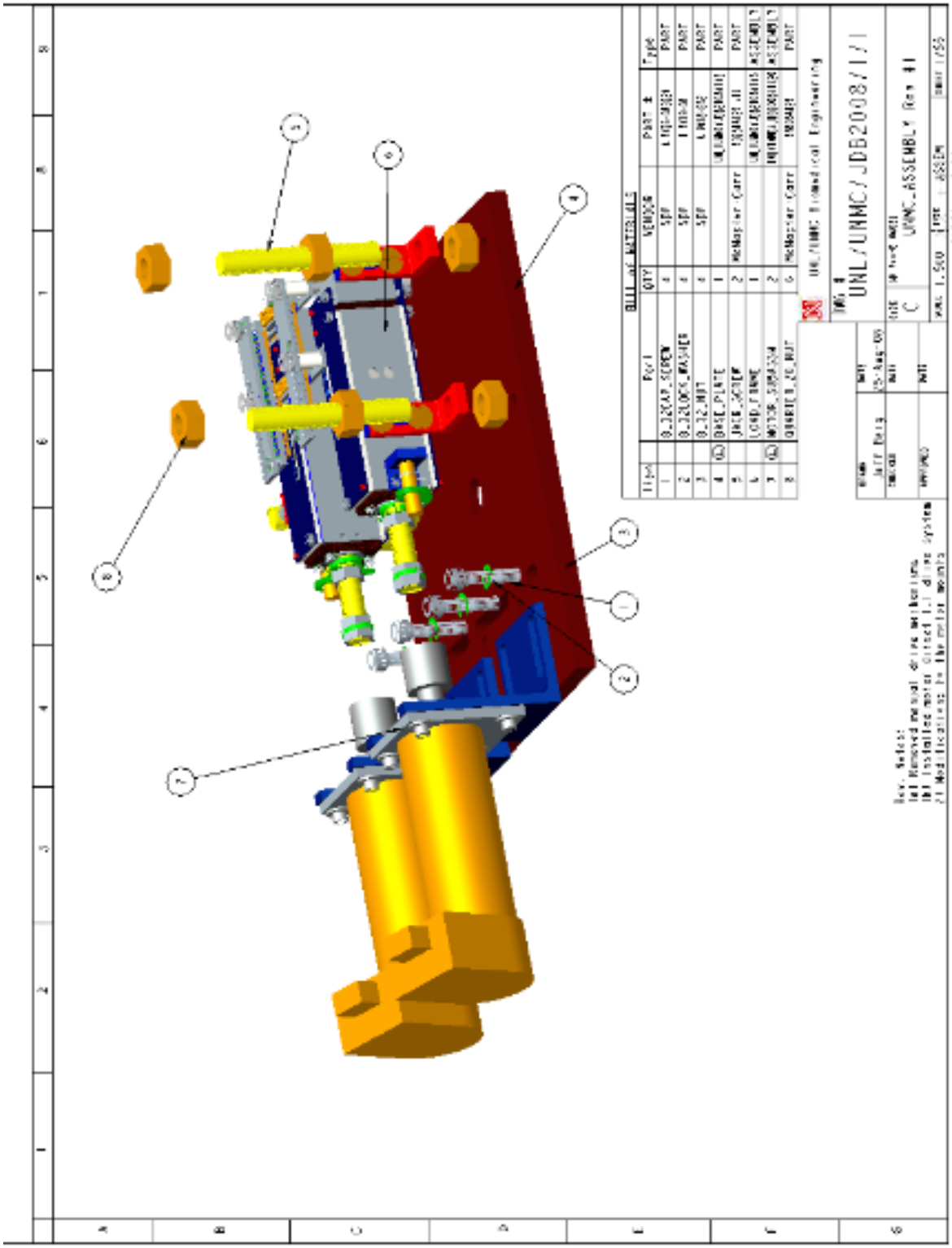

Appendix Fig A-1: Top level assembly drawing.

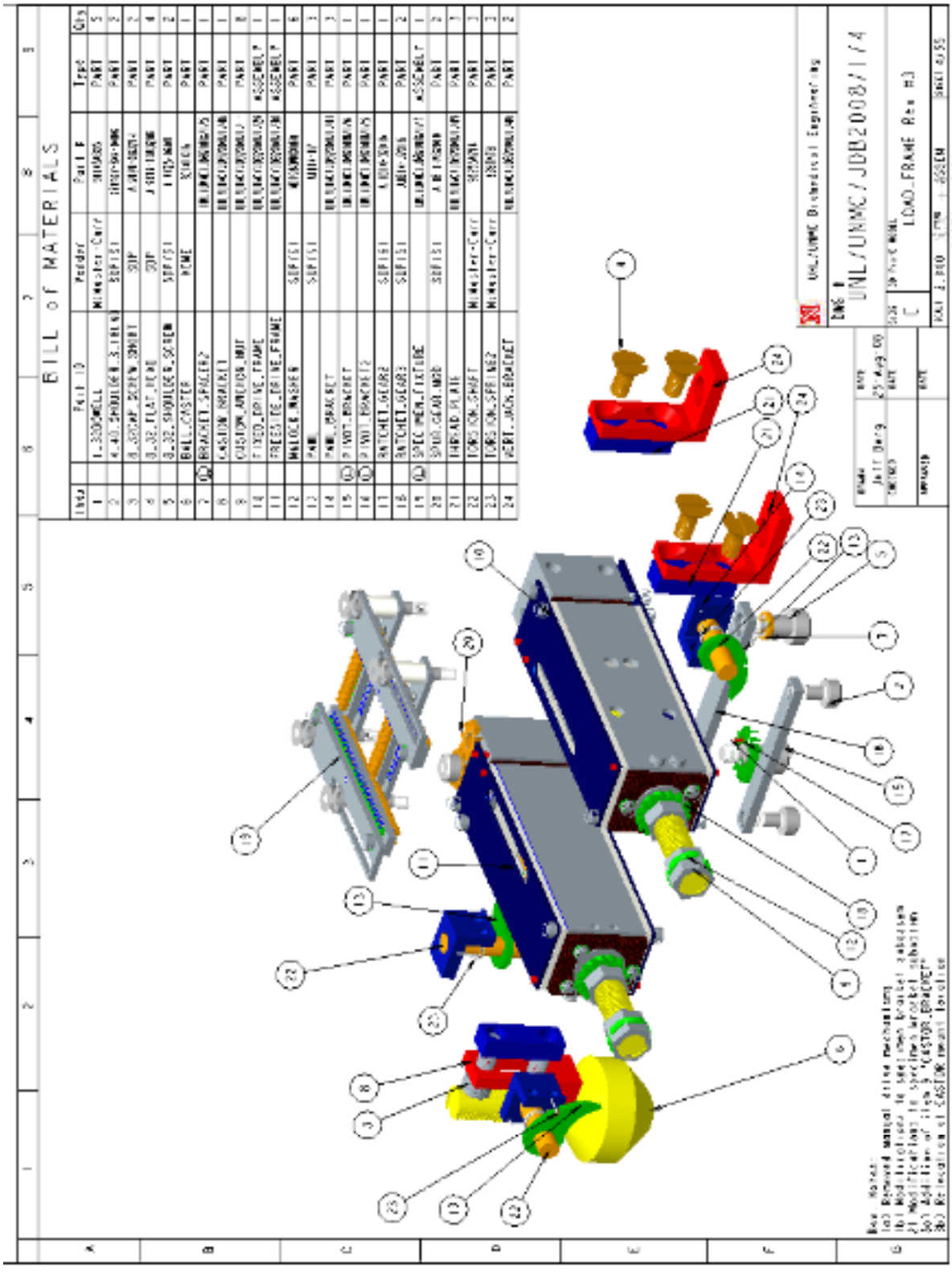

Appendix Fig A-2: Load frame subassembly drawing.

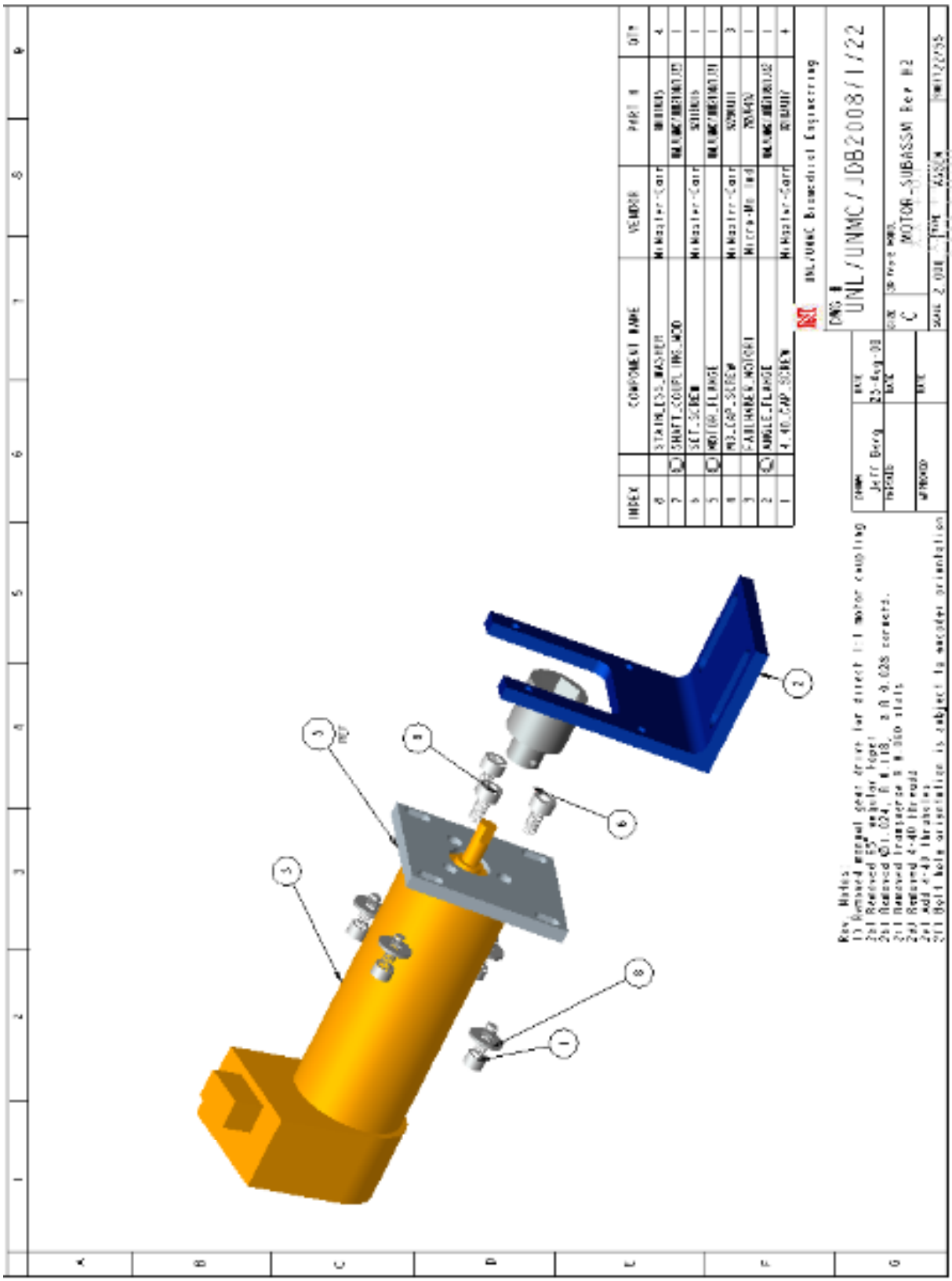

Appendix Fig A-3: Servomotor subassembly drawing.

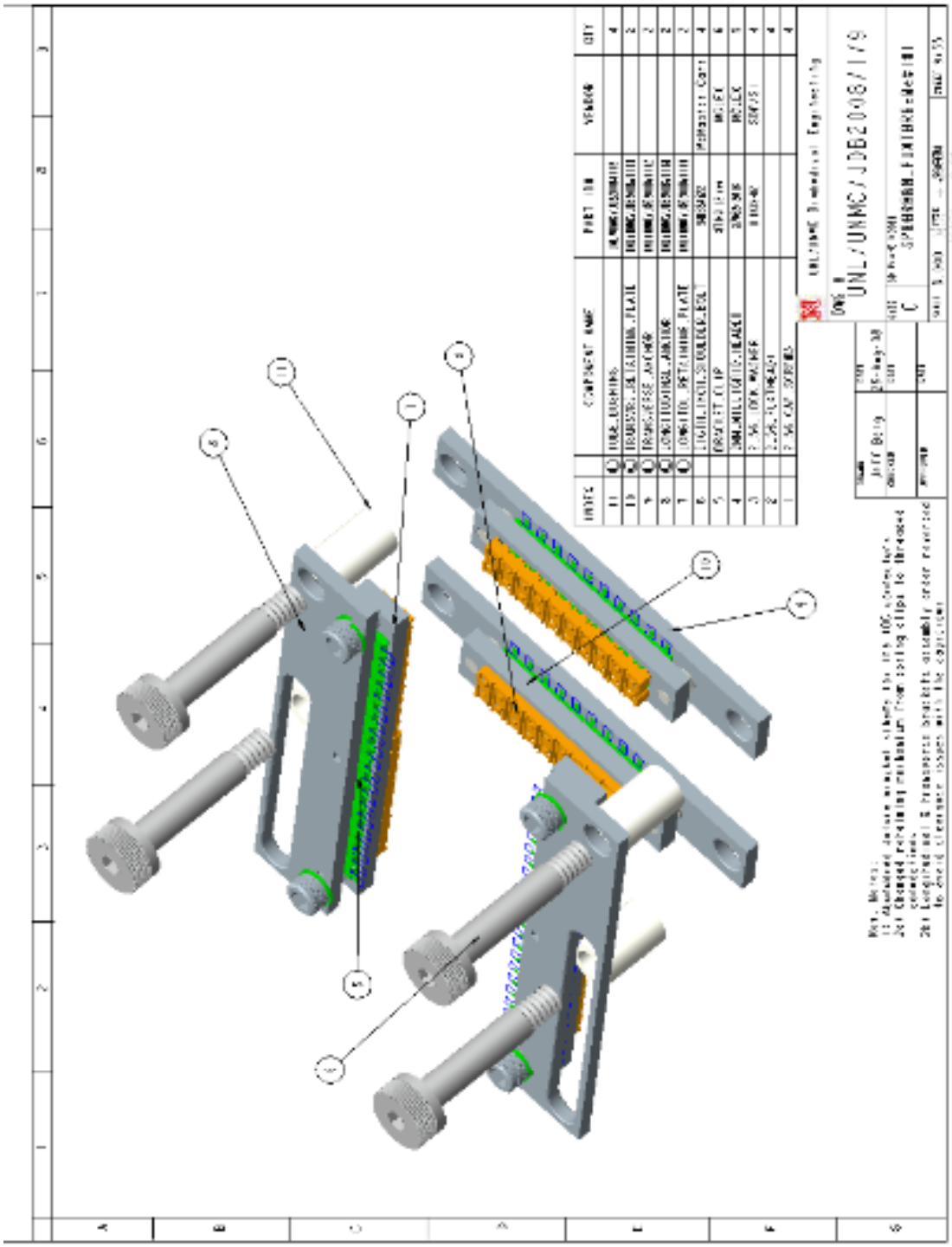

Appendix Fig A-4: Specimen bracket subassembly drawing.

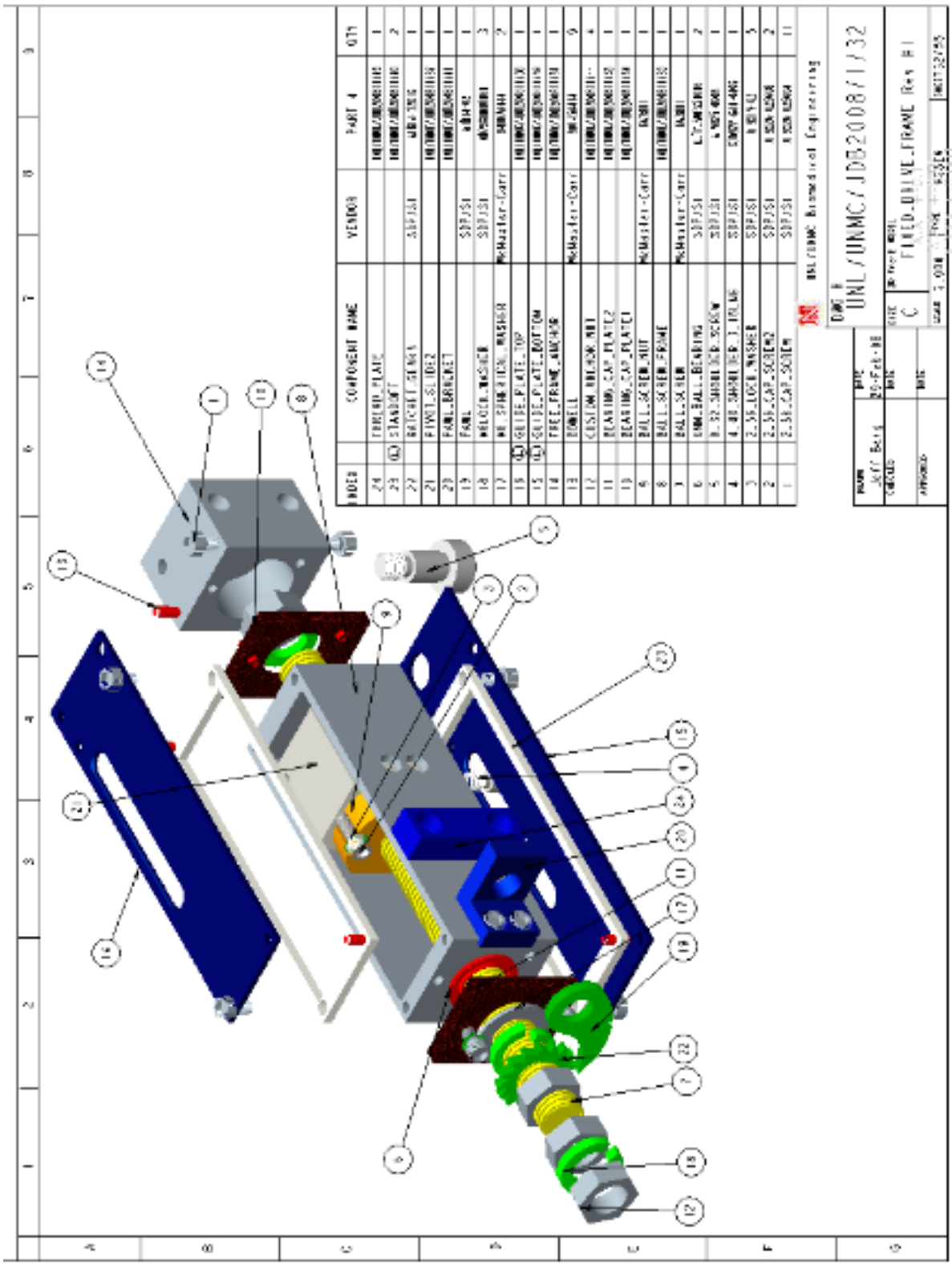

Appendix Fig A-5: Drive frame1 subassembly drawing

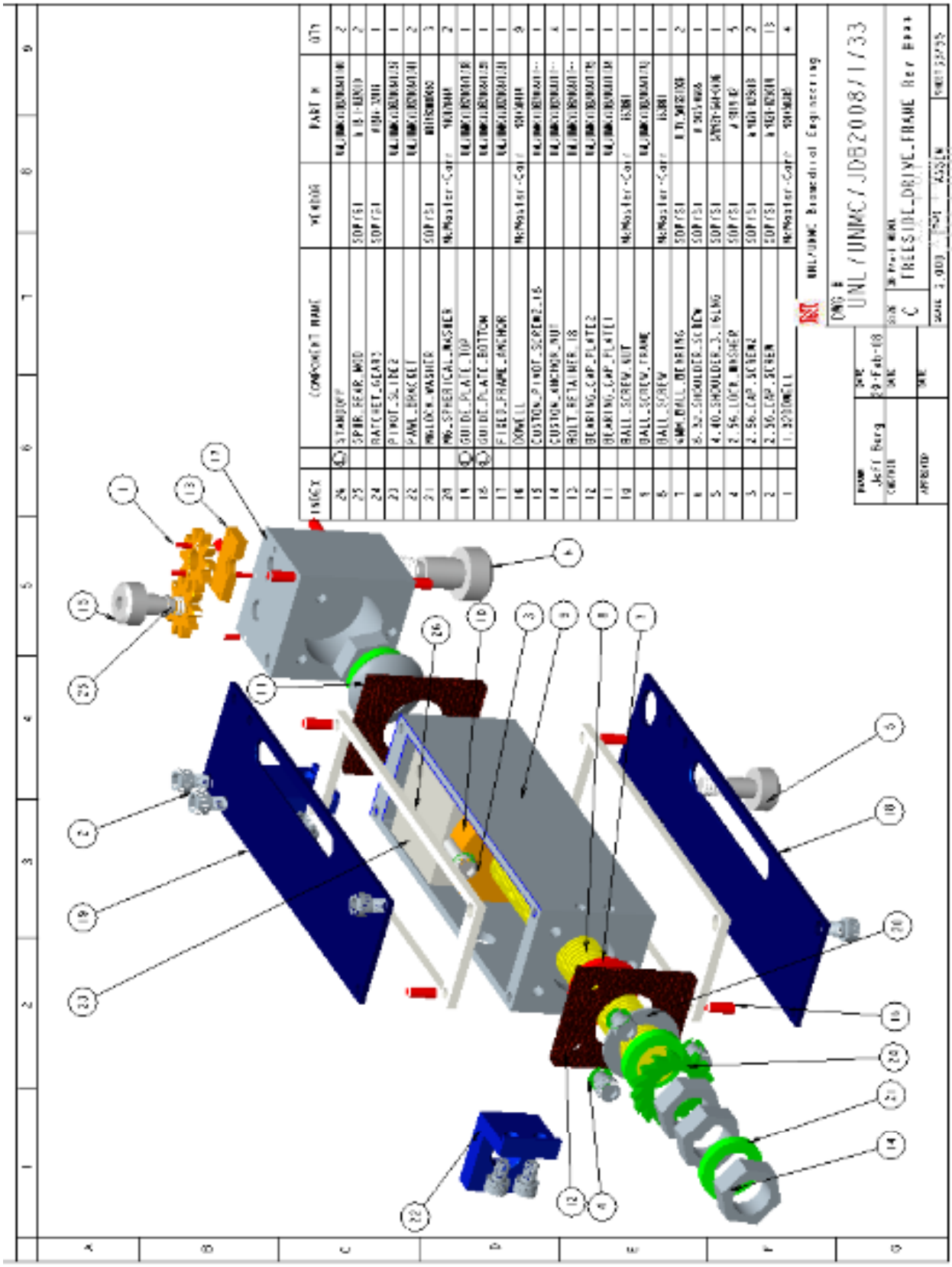

Appendix Fig A-6: Drive frame2 subassembly drawing.

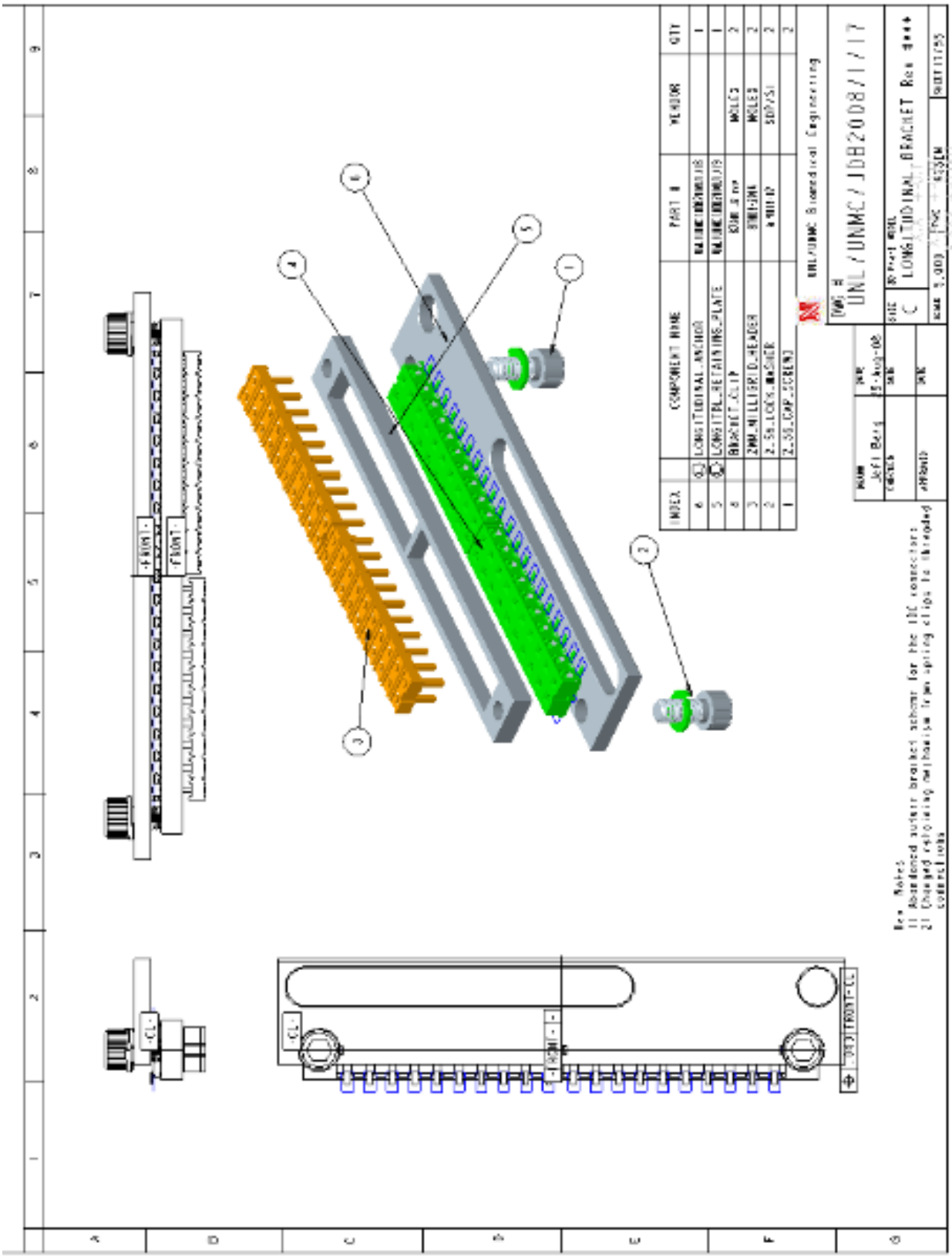

Appendix Fig A-7: Specimen longitudinal bracket subassembly drawing.

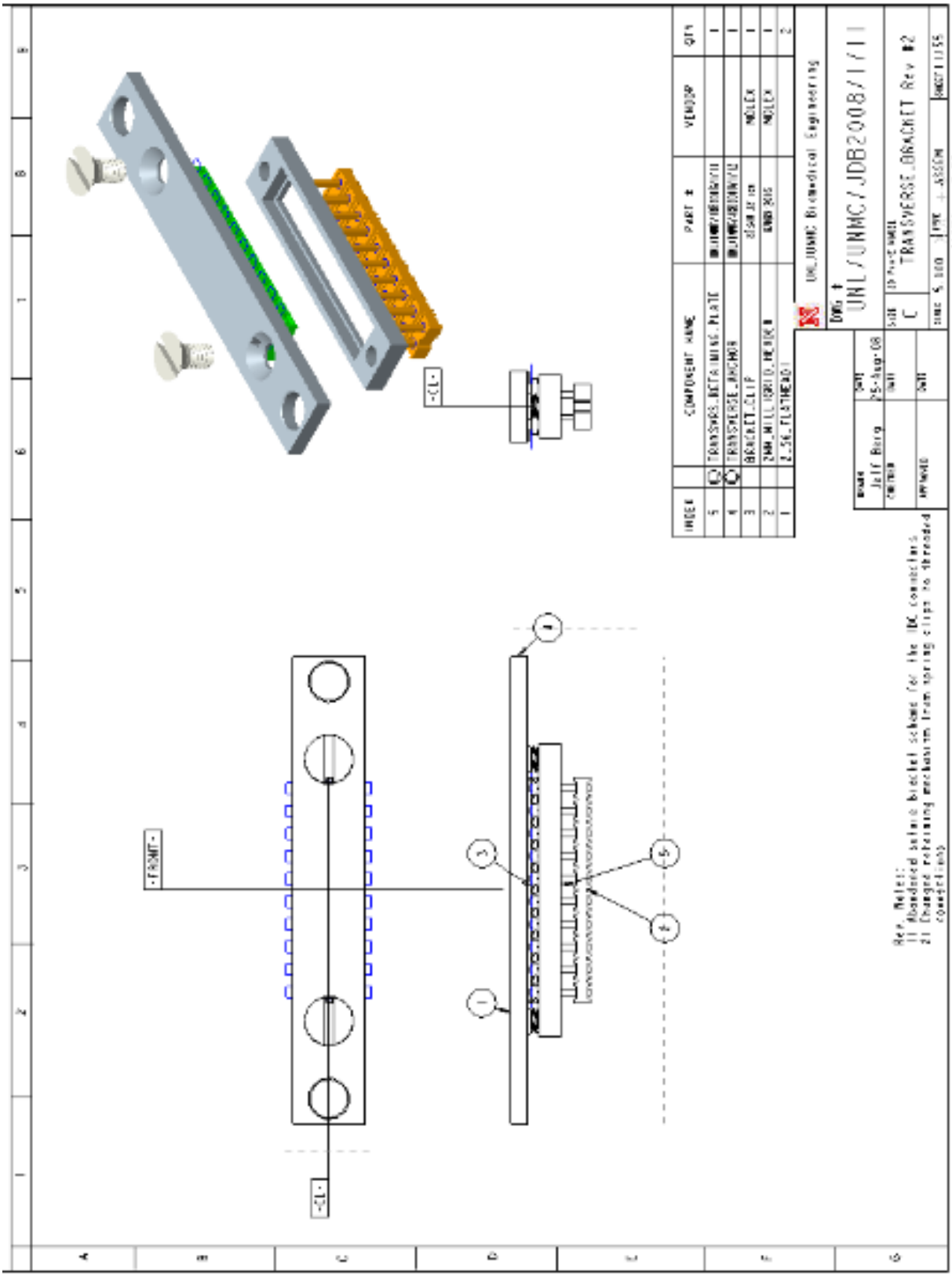

Appendix Fig A-8: Specimen transverse bracket subassembly drawing.

Appendix B. Individual Component Specs

Appendix B.1. Servomotors with Encoders

FAULHABER

DC-Micromotors

Graphite Commutation

44 mNm

For combination with (overview on page 14-15)
Gearheads:
26A, 26/1, 30/1
Encoders:
IE2 – 16 ... 512, 5500, 5540

Series 2657 ... CR

		2657 W		012 CR	024 CR	048 CR	
1	Nominal voltage	U_N		12	24	48	Volt
2	Terminal resistance	R		0,71	2,84	12,50	Ω
3	Output power	$P_{2\,max.}$		45,9	47,9	44,5	W
4	Efficiency	$\eta_{max.}$		84	85	84	%
5	No-load speed	n_0		6 300	6 400	6 400	rpm
6	No-load current (with shaft ø 4,0 mm)	I_0		0,115	0,058	0,028	A
7	Stall torque	M_H		278	286	265	mNm
8	Friction torque	M_R		2	2	2	mNm
9	Speed constant	k_n		552	274	136	rpm/V
10	Back-EMF constant	k_E		1,81	3,65	7,37	mV/rpm
11	Torque constant	k_M		17,3	34,8	70,4	mNm/A
12	Current constant	k_I		0,058	0,029	0,014	A/mNm
13	Slope of n-M curve	$\Delta n/\Delta M$		22,7	22,4	24,2	rpm/mNm
14	Rotor inductance	L		95	380	1 550	µH
15	Mechanical time constant	τ_m		3,9	3,9	3,9	ms
16	Rotor inertia	J		16	17	15	gcm²
17	Angular acceleration	$\alpha_{max.}$		170	170	170	10^3rad/s²
18	Thermal resistance	$R_{th\,1}$ / $R_{th\,2}$	1,9 / 9				K/W
19	Thermal time constant	τ_{w1} / τ_{w2}	10 / 580				s
20	Operating temperature range:						
	– motor		– 30 ... + 125				°C
	– rotor, max. permissible		+ 155				°C
21	Shaft bearings		ball bearings, preloaded				
22	Shaft load max.:						
	– with shaft diameter		4,0				mm
	– radial at 3 000 rpm (3 mm from bearing)		20				N
	– axial at 3 000 rpm		2				N
	– axial at standstill		20				N
23	Shaft play:						
	– radial	≤	0,015				mm
	– axial	=	0				mm
24	Housing material		steel, black coated				
25	Weight		156				g
26	Direction of rotation		clockwise, viewed from the front face				
Recommended values - mathematically independent of each other							
27	Speed up to	$n_{e\,max.}$		6 000	6 000	6 000	rpm
28	Torque up to	$M_{e\,max.}$		44	44	44	mNm
29	Current up to (thermal limits)	$I_{e\,max.}$		3,10	1,54	0,73	A

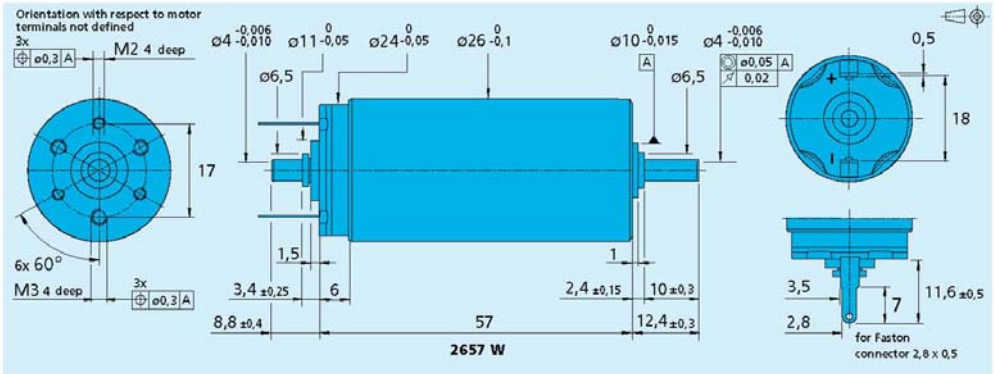

For details on technical information and lifetime performance refer to pages 28-34.

Edition 2006-2007

For options on DC-Micromotors refer to page 64.

www.faulhaber-group.com

FAULHABER

Encoders

Optical Encoders

Features:
100 to 1024 Lines per revolution
2 or 3 Channels
Digital output

Series 5500, 5540

		HEDS 5500	HEDS 5540	HEDM 5500	
Lines per revolution	N	100 - 500	100 - 500	1 000 -1 024	
Signal output, square wave		2	2+1 index	2	channels
Supply voltage	V_{CC}	4,5 ... 5,5			V DC
Current consumption, typical (V_{CC} = 5 V DC)	I_{CC}	17	57	57	mA
Pulse width	P	180 ± 45	180 ± 35	180 ± 45	°e
Phase shift, channel A to B	Φ	90 ± 20	90 ± 15	90 ± 15	°e
Logic state width	S	90 ± 45	90 ± 35	90 ± 45	°e
Cycle	C	360 ± 5,5	360 ± 5,5	360 ± 7,5	°e
Signal rise/fall time, typical	tr/tf	0,25 / 0,25			µs
Frequency range [1]	f	up to 100	up to 100 [2]	up to 100	kHz
Inertia of code disc	J	0,6			gcm²
Operating temperature range		– 40 ... + 100		– 40 ... + 70	°C

[1] Velocity (rpm) = f (Hz) x 60/N
[2] HEDS 5540 requires pull-up resistors of 2,7 kΩ between pins 2, 3, 5 and 4 (V_{CC})

Ordering information

Encoder type	number of channels	lines per revolution	For combination with:
HEDS 5500 C	2	100	**DC-Micromotors and DC-Motor-Tachos**
HEDS 5500 A	2	500	**Series**
HEDS 5540 C	2+1	100	**2230, 2233, 2251**
HEDS 5540 A	2+1	500	**2342**
HEDM 5500 B	2	1000	**2642, 2657**
HEDM 5500 J	2	1024	**3242, 3257, 3557, 3863**
			brushless DC-Servomotors
			Series
			2036, 2057, 2444, 3056, 3564

Interlocking connector options: extension cables 300 mm length, on request.

Features

These incremental shaft encoders in combination with the DC-Micromotors and brushless DC-Servomotors are designed for indication and control of both, shaft velocity and direction of rotation as well as for positioning.

A LED source and lens system transmits collimated light through a low inertia metal disc to give two channels with 90° phase shift.

The single 5 volt supply and the two or three channel digital output signals are interfaced with a 5-pin connector.

Motors with ball bearings are recommended for continuous operation at low and high speeds and for elevated radial shaft load.

Details for the Motors and suitable reduction gearheads are on separate catalogue pages.

Output signals / Circuit diagram / Connector information

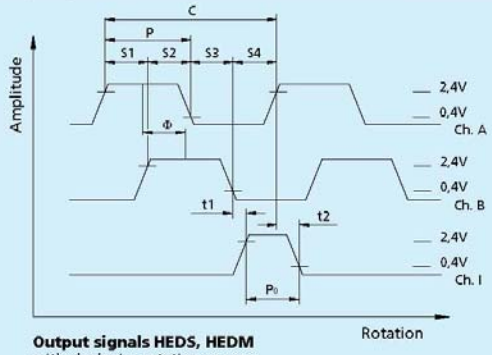

Output signals HEDS, HEDM
with clockwise rotation as seen from the shaft end

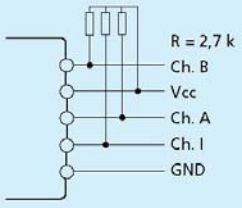

Connection diagram
HEDS 5540 requires pull-up resistors

Pin Function

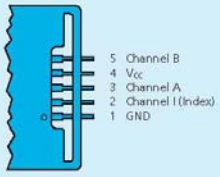

Connector
suggested connectors
AMP 103686-4/640442-5,
Molex 2695/2759
FCI 65039-032 / 4825x-000

For details on technical information and lifetime performance refer to pages 140-142.

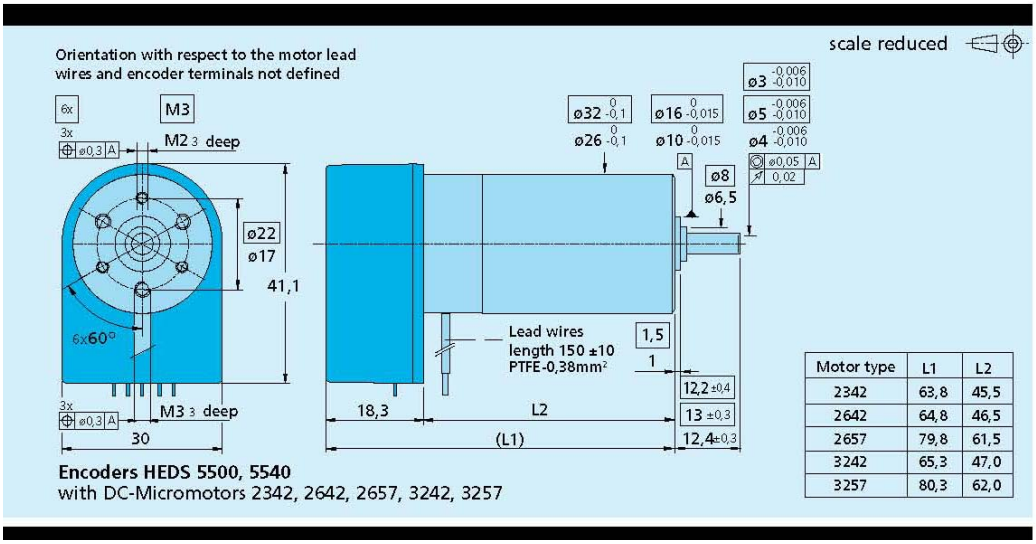

Motor type	L1	L2
2342	63,8	45,5
2642	64,8	46,5
2657	79,8	61,5
3242	65,3	47,0
3257	80,3	62,0

Appendix B.2. Ball Bearings

ABEC Ball Bearing Tolerances

Metric Sizes, mm

	ABEC-1		ABEC-3		ABEC-5		ABEC-7	
For Shaft Dia., mm	For Shaft Dia. Tolerances, mm	Width Tolerances, mm	For Shaft Dia. Tolerances, mm	Width Tolerances, mm	For Shaft Dia. Tolerances, mm	Width Tolerances, mm	For Shaft Dia. Tolerances, mm	Width Tolerances, mm
0.6 to 2	———	———	———	———	–0.005 to +0	–0.005 to +0.005	———	———
2.5 to 10	–0.008 to +0	–0.120 to +0	–0.007 to +0	–0.120 to +0	–0.005 to +0	–0.040 to +0	–0.004 to +0	–0.040 to +0
11 to 18	–0.008 to +0	–0.120 to +0	–0.007 to +0	–0.120 to +0	–0.005 to +0	–0.080 to +0	–0.004 to +0	–0.080 to +0
19 to 30	–0.010 to +0	–0.120 to +0	–0.008 to +0	–0.120 to +0	–0.006 to +0	–0.120 to +0	–0.005 to +0	–0.120 to +0
31 to 50	–0.012 to +0	–0.120 to +0	–0.010 to +0	–0.120 to +0	–0.008 to +0	–0.120 to +0	–0.006 to +0	–0.120 to +0
51 to 80	–0.015 to +0	–0.150 to +0	–0.012 to +0	–0.150 to +0	–0.009 to +0	–0.150 to +0	———	———

	ABEC-1	ABEC-3	ABEC-5	ABEC-7
OD, mm	OD Tolerances, mm			
2 to 5	———	———	–0.005 to +0	———
6 to 18	–0.008 to +0	–0.007 to +0	–0.005 to +0	———
19 to 30	–0.009 to +0	–0.008 to +0	–0.006 to +0	–0.005 to +0
31 to 50	–0.011 to +0	–0.009 to +0	–0.007 to +0	–0.006 to +0
51 to 80	–0.013 to +0	–0.011 to +0	–0.009 to +0	–0.007 to +0
81 to 120	–0.015 to +0	–0.013 to +0	–0.010 to +0	———
121 to 150	–0.018 to +0	–0.015 to +0	–0.011 to +0	———
151 to 180	–0.025 to +0	–0.018 to +0	–0.013 to +0	———

Ball and Roller Bearings

Part Number: **7804K141** $10.82 Each

Type	Ball Bearings
Ball Bearing Style	Flanged Double Shielded
Ball Bearing Type	General Purpose
System of Measurement	Metric
For Shaft Diameter	6 mm
Outside Diameter	10 mm
Width	3 mm
Flange Outside Diameter	11.2 mm
Flange Thickness	.6 mm
ABEC Precision Bearing Rating	ABEC-5
Dynamic Radial Load Capacity, lbs.	112
Maximum rpm	53,000
Temperature Range	-65° to +250° F
Bearing Material	Stainless Steel
Stainless Steel Material Type	Type 440C Stainless Steel
Shield Material	Type 300 Series Stainless Steel
Specifications Met	Not Rated

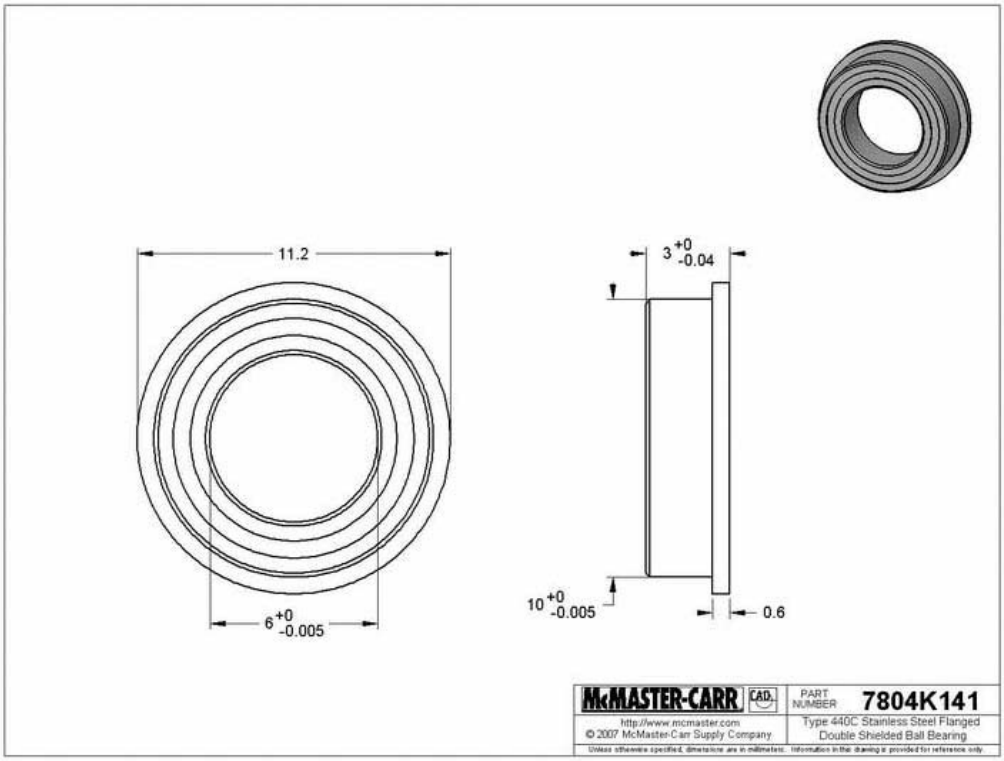

Appendix B.3. Ball Screws

Phone: 1-800-554-8466
Website: www.ballscrews.com

Precision Miniature
4mm to 14mm Diameter

Type A - End Cap Design

The end-cap type ball recirculation system allows the nut length to be reduced and minimizes the outer diameter. No return mechanism protrudes outside the nut body diameter. Double flats on the flange make the unit ideal for use in small spaces.

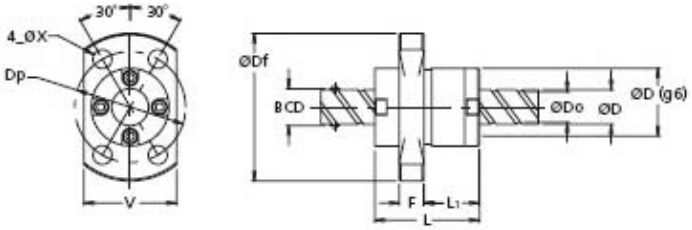

MODEL NUMBER	SCREW SHAFT OD	LEAD (mm)	BALL DIA. (mm)	MAX THREADED LENGTH (mm)	SUGGESTED BEARING SIZE (mm)	SCREW ROOT DIA. (mm)	LOAD RATING (N)	
							C_a (DYNAMIC)	C_{oa} (STATIC)
PRM0401	4	1	0.8	100	N/A	3.3	560	790
PRM0504	5	4	0.8	220	N/A	4.3	470	720
PRM0601	6	1	0.8	265	4	5.3	680	1200
PRM0606	6	6	1.0	265	4	5.2	870	1450
PRM0801	8	1	0.8	360	6	7.3	780	1650
PRM0802	8	2	1.59	360	6	6.6	2400	4100
PRM0805	8	5	1.59	360	6	6.6	1850	3000
PRM0808	8	8	1.59	360	6	6.7	2200	3800
PRM0812	8	12	1.59	360	6	6.7	2200	4000
PRM1002	10	2	1.59	355	6	8.6	2700	5300
PRM1010	10	10	2.0	405	6	8.4	3300	5900
PRM1015	10	15	2.0	405	6	8.4	3300	6400
PRM1020	10	20	1.59	405	6	8.7	2100	4000
PRM1202	12	2	1.59	395	8	10.6	3000	6400
PRM1312	13	12	2.38	700	8	11.0	5000	9900
PRM1320	13	20	2.38	700	8	11.0	5000	10700
PRM1402	14	2	1.59	445	8	12.6	3200	7500
PRM1404	14	4	2.38	445	8	11.8	5700	11600

Please contact the factory for sizes not listed.
Units in millimeters. Divide by 25.4 to get inches.
1N = 0.225 lbs.

Appendix C. Drivetrain Alignment Procedure

Appendix D. Wiring Schematics

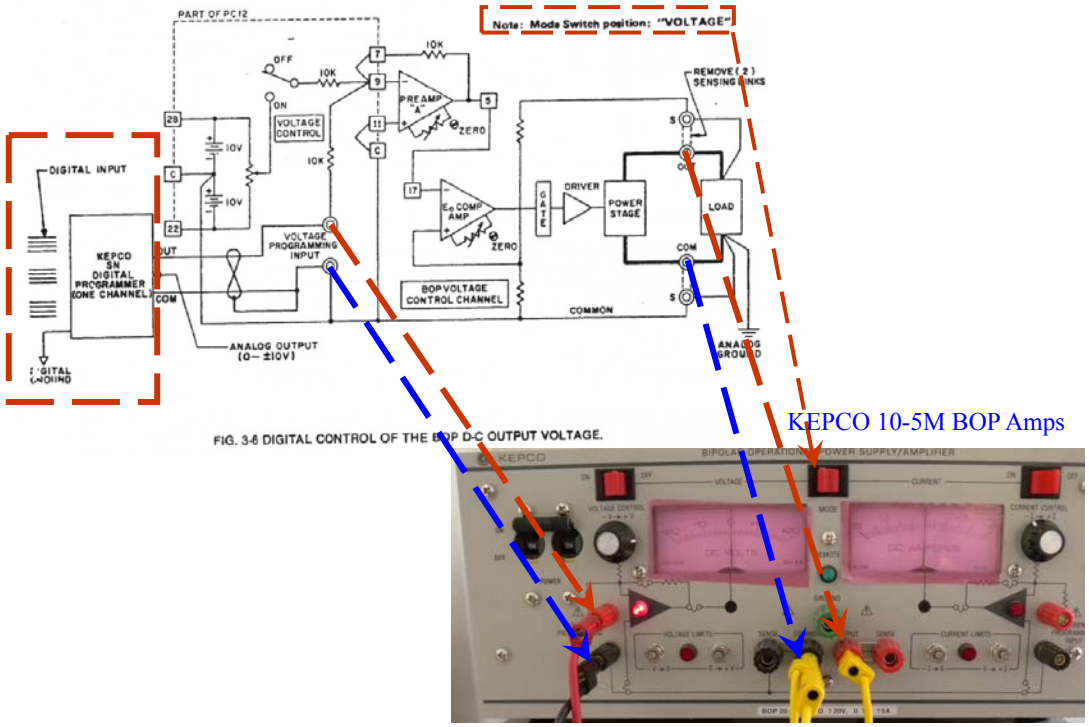

FIG. 3-6 DIGITAL CONTROL OF THE BOP D-C OUTPUT VOLTAGE.

Appendix Fig D-1: Manufacturer's wiring schematic for voltage control.

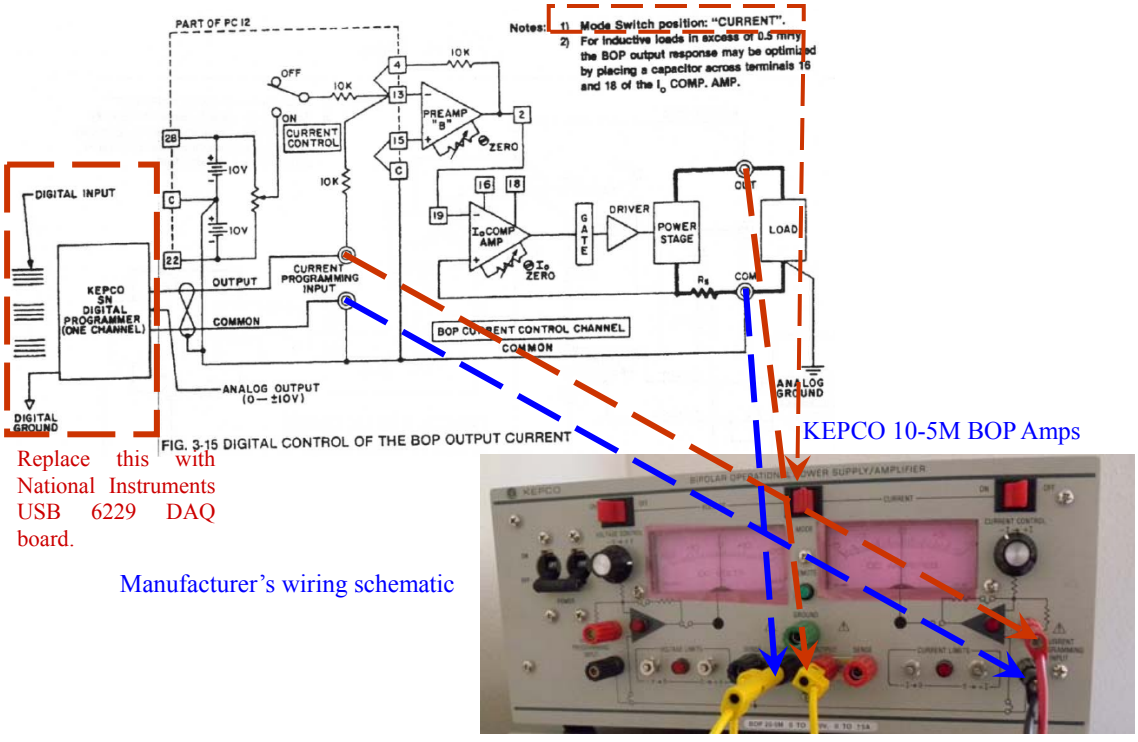

FIG. 3-15 DIGITAL CONTROL OF THE BOP OUTPUT CURRENT

Replace this with National Instruments USB 6229 DAQ board.

Manufacturer's wiring schematic

Appendix Fig D-2: Manufacturer's wiring schematic for current control

B) REAR PROGRAMMING CONNECTORS (See Table 2-2, items 22 and 23)

1) The external rear programming connector, called "PC-12" throughout this manual, is an unwired 50-pin edge connector, providing access to all circuit features. The BOP is delivered with one(1) PC-12 connector, with jumpers wired for local (front-panel) operation. Spare connectors may be purchased from Kepco under the model number "PC-12" for the unwired connector and "PC-15" for a connector wired for local operation. The pin-out for the rear programming connector or (PC-12) is shown below.

PIN	FUNCTION	DESCRIPTION
1	CURRENT LIMIT BIAS	Section III, paragraph 3-31
3	VOLTAGE LIMIT BIAS	Section III, paragraph 3-34
11, 9, 5, 7	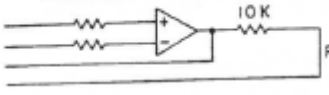	Section III, paragraph 3-11 for example
15, 13, 2, 4	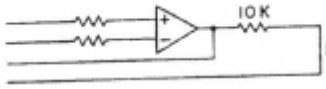	Section III, paragraph 3-28 for example
6	$+E_o$ LIMIT INPUT	Section III, paragraph 3-34
8	$+I_o$ LIMIT INPUT	Section III, paragraph 3-31
32	$-E_o$ LIMIT INPUT	Section III, paragraph 3-34
34	$-I_o$ LIMIT INPUT	Section III, paragraph 3-31
10	CURRENT SENSING AMP. OUTPUT	Analog output voltage (0 to ±10V, 1mA max.) proportional to the prevailing BOP output current for remote metering or monitoring.
20	VOLTAGE MONITOR AMP. OUTPUT	Analog output voltage (0 to ±10V, 1 mA max.) proportional to the prevailing BOP output voltage.
21,43, 44,45,46	NOT USED	
12,14	RESERVED (NOT TO BE USED)	
16,18	CURRENT MODE COMPENSATING TERMINALS	Section I, paragraph 1-10D
26,36	TURN-OFF SIGNAL OUTPUT	Section IV, paragraph 4-25
24	CKT BREAKER CONTROL	Section IV, paragraph 4-25
41	NON-ISOLATED TURN-OFF SIGNAL INPUT	Section IV, paragraph 4-25
47,49, 48,50	OPTICALLY ISOLATED TURN-OFF SIGNAL INPUT	Section IV, paragraph 4-25
17	VOLTAGE COMPARISON AMP. INPUT	An analog input voltage of 0 to ±10V will produce 0 to ± full output voltage or current.
19	CURRENT COMPARISON AMP. INPUT	
22	−10V REFERENCE VOLTAGE, 4mA MAX.	Section III, paragraph 3-11 for example
28	+10V REFERENCE VOLTAGE, 4mA, MAX.	
23, 25, 27, 29, 31, 33	SENSING COMMON	————
30	VOLTAGE MODE COMMAND	Section I, paragraph 1-10L
35	LOCAL/REMOTE OUTPUT FLAG	Section IV, paragraph 4-30
37	+5V	Built in TTL logic supply, 5V @ 40mA max.
38	I_o LIMIT FLAG	Section IV, paragraph 4-30
39	E_o LIMIT FLAG	Section IV, paragraph 4-30
40	E_o MODE FLAG	Section IV, paragraph 4-30
42	I_o MODE FLAG	Section IV, paragraph 4-30

connection is a voltage that is proportional to the amp output current @ 2V/A.

1-5

BOP—05-1186A

Appendix Fig D-3: Pin-out of 50-pin edge connector on the rear console of the KEPCO amplifiers.

Appendix E. Specimen Stress to Current & Voltage Conversions

w	0.012 (m)
t	50.8 (μm)
$\rho_{leverage}$	300 (μm)

$$\frac{T_{orq}}{n} = \sigma w t \rho_{leverage}$$

$$(0.012m)(50.8\times10^{-6}m)(300\times10^{-6}m)(1\times10^{6}Pa)$$

$$0.00018288Nm$$

$$183\frac{\mu J}{MPa}$$

$$\frac{V}{n} = \frac{n\sigma w t \rho_{leverage}}{k_M \rho_{amplifier}}$$

$$\frac{183\mu J/MPa}{(34800\mu J/Amp)(0.5Amp/V)}$$

$$0.01051\frac{V}{MPa}$$

$$10.51\frac{mV}{MPa}$$

Table Apx 1: Torque and voltage conversion factors based on specimen stress level and the number of wraps or layers.

Appendix F. Individual Component CAD Drawings

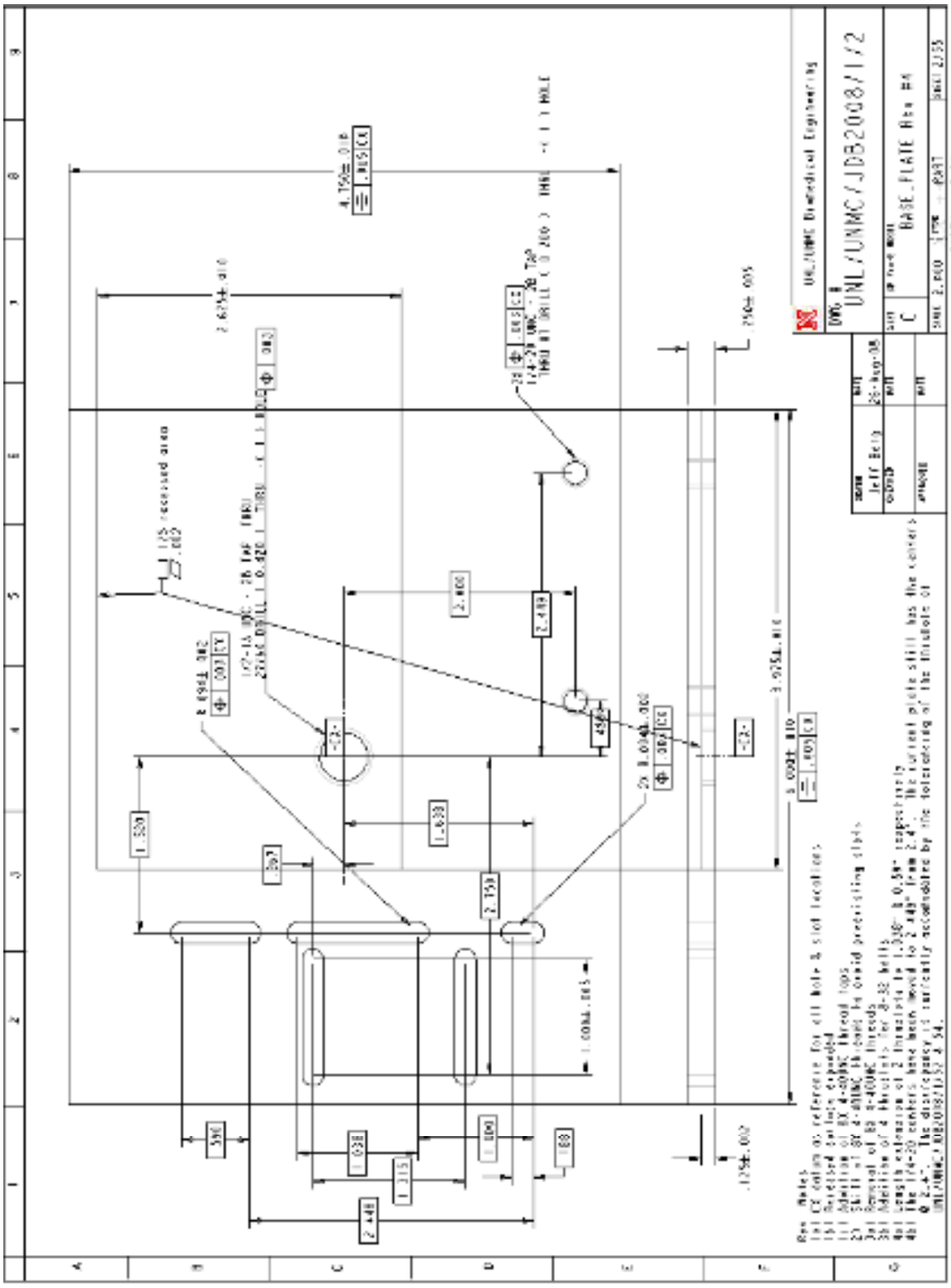

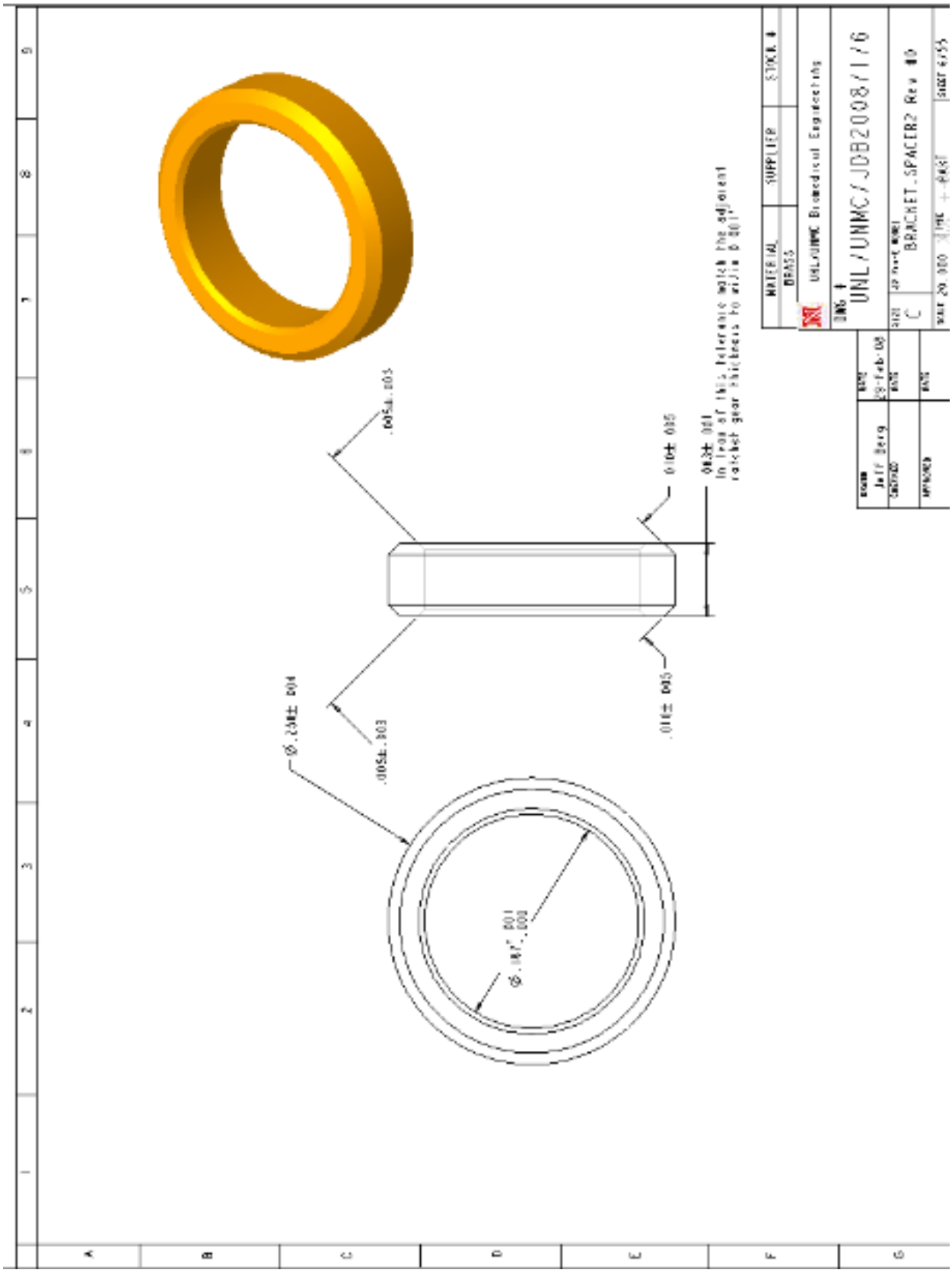
UNL/UNMC/JDB20081176
BRACKET_SPACER2 Rev #0
UNL/UNMC Biomedical Engineering
MATERIAL
BRASS
SUPPLIER
Jeff Berg
28-Feb-08
C
.005± .003
.010± .005
.010± .005
.005± .003

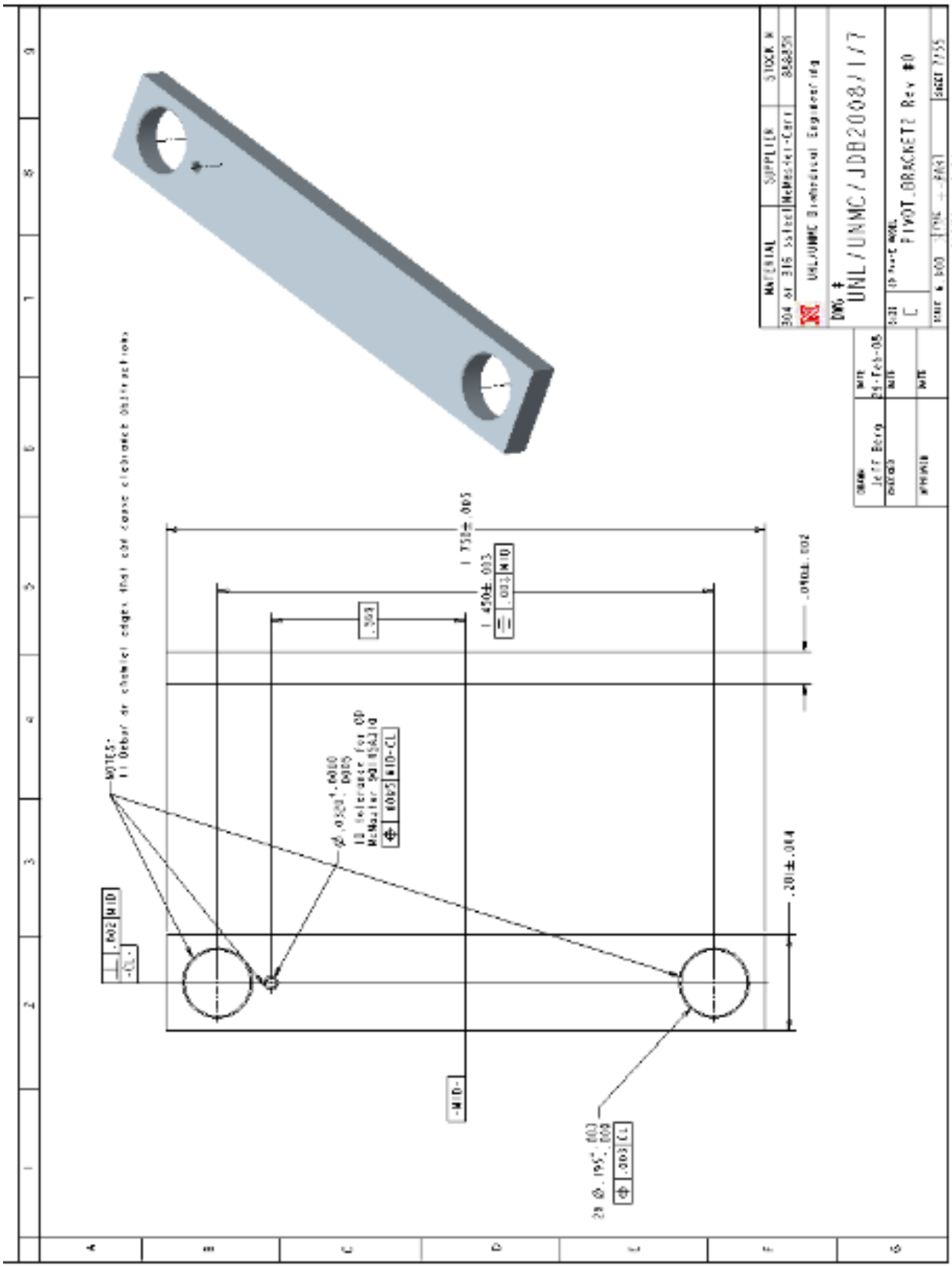
UNL/UNMC/JDB20081117
PIVOT_BRACKET2 Rev #0
304 or 316 Steel
McMaster-Carr
Jeff Berg
24-Feb-05
1.750±.005
1.450±.003
.393
.201±.004
.050±.002
.195"
.303 C1
-MID-
-C1-
NOTES:
1) Break or chamfer edges that can cause clearance interactions.

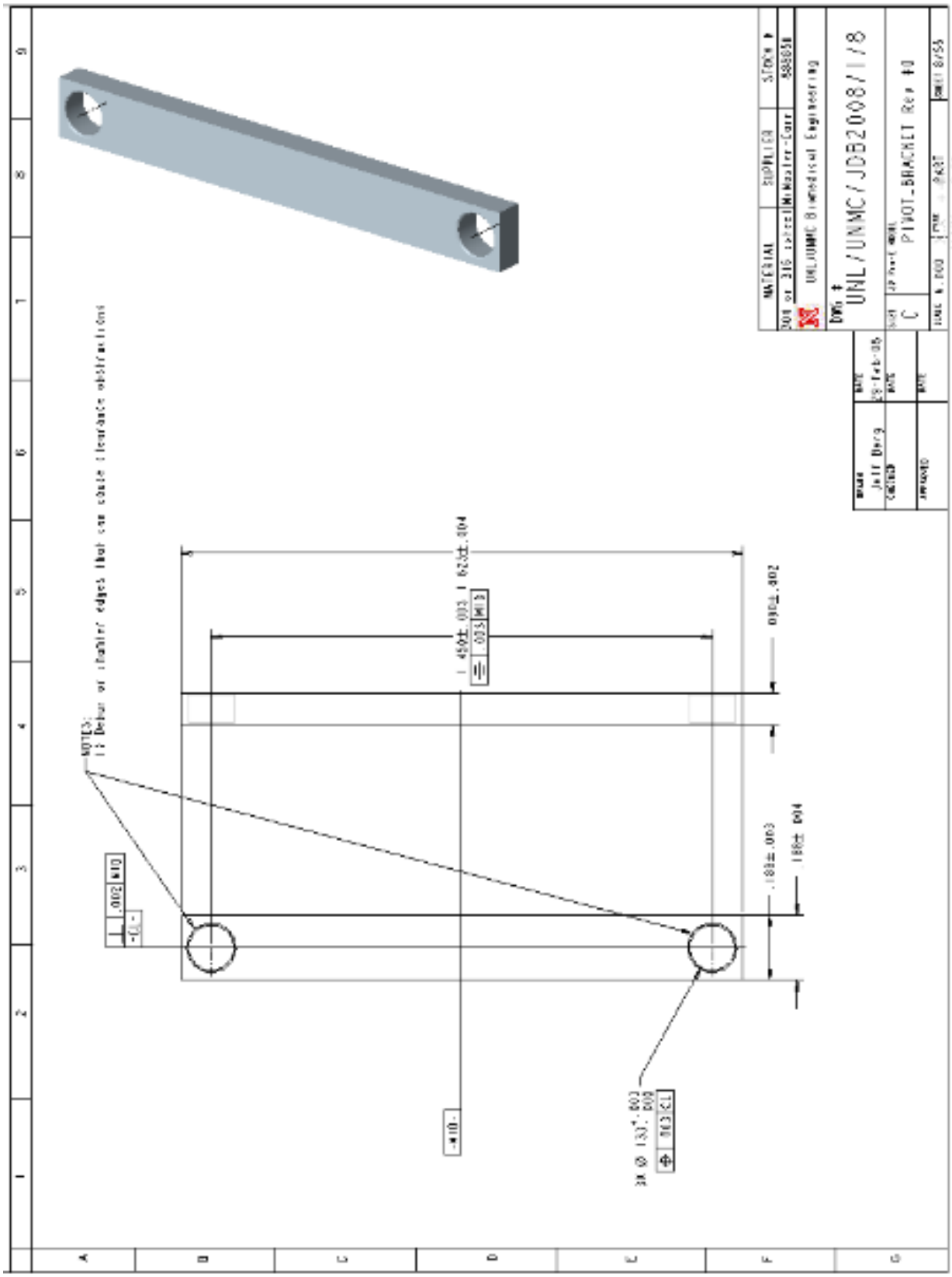
UNL/UNMC/JOB20080118
PIVOT_BRACKET Rev #0
UNL/UNMC Biomedical Engineering
Jeff Berg
29-Feb-08
C
SHEET 1 OF 1

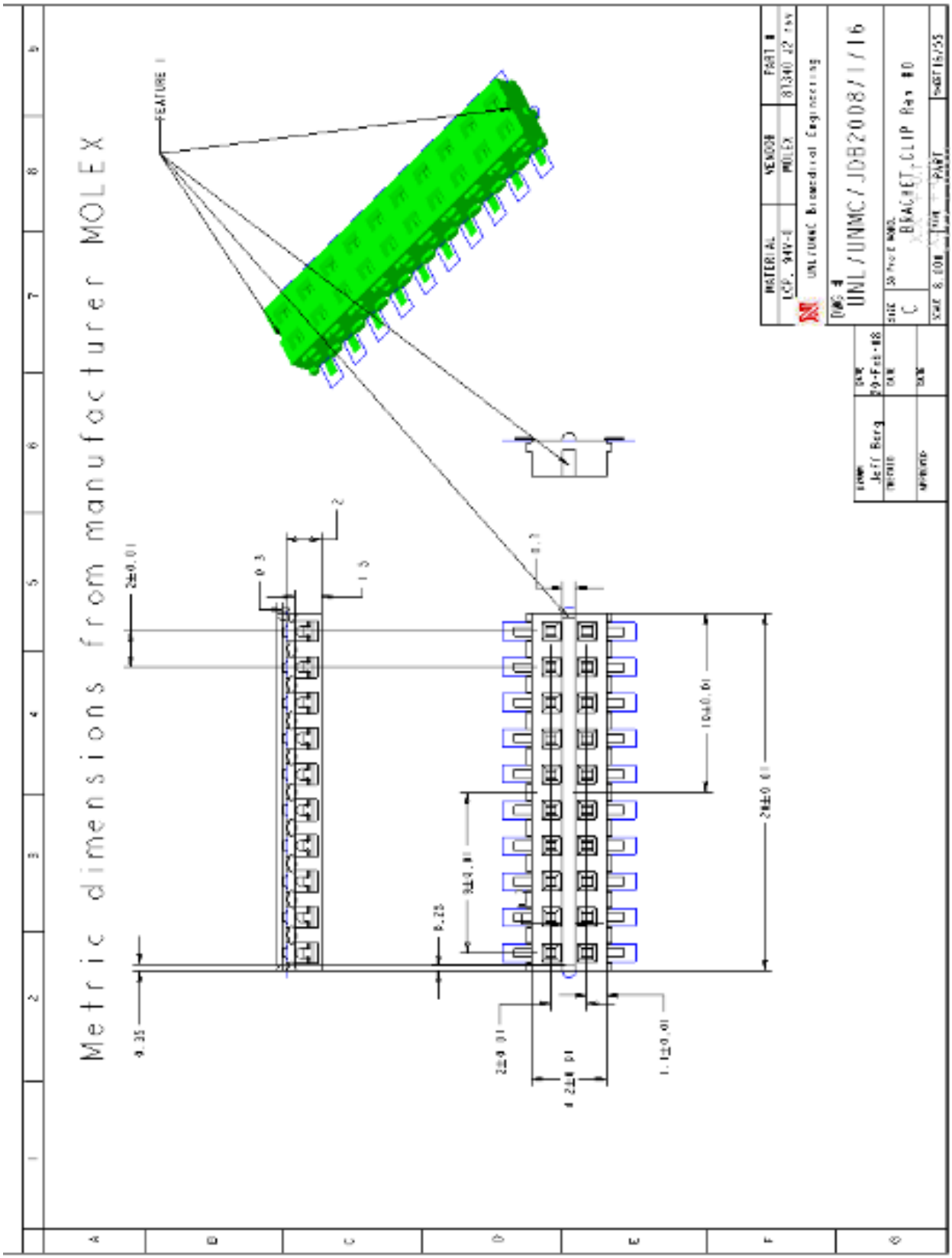
Metric dimensions from manufacturer MOLEX
FEATURE 1
UNL/UNMC/JDB20080116
BRACKET,CLIP Rev #0
Jeff Berg
29-Feb-08
MOLEX

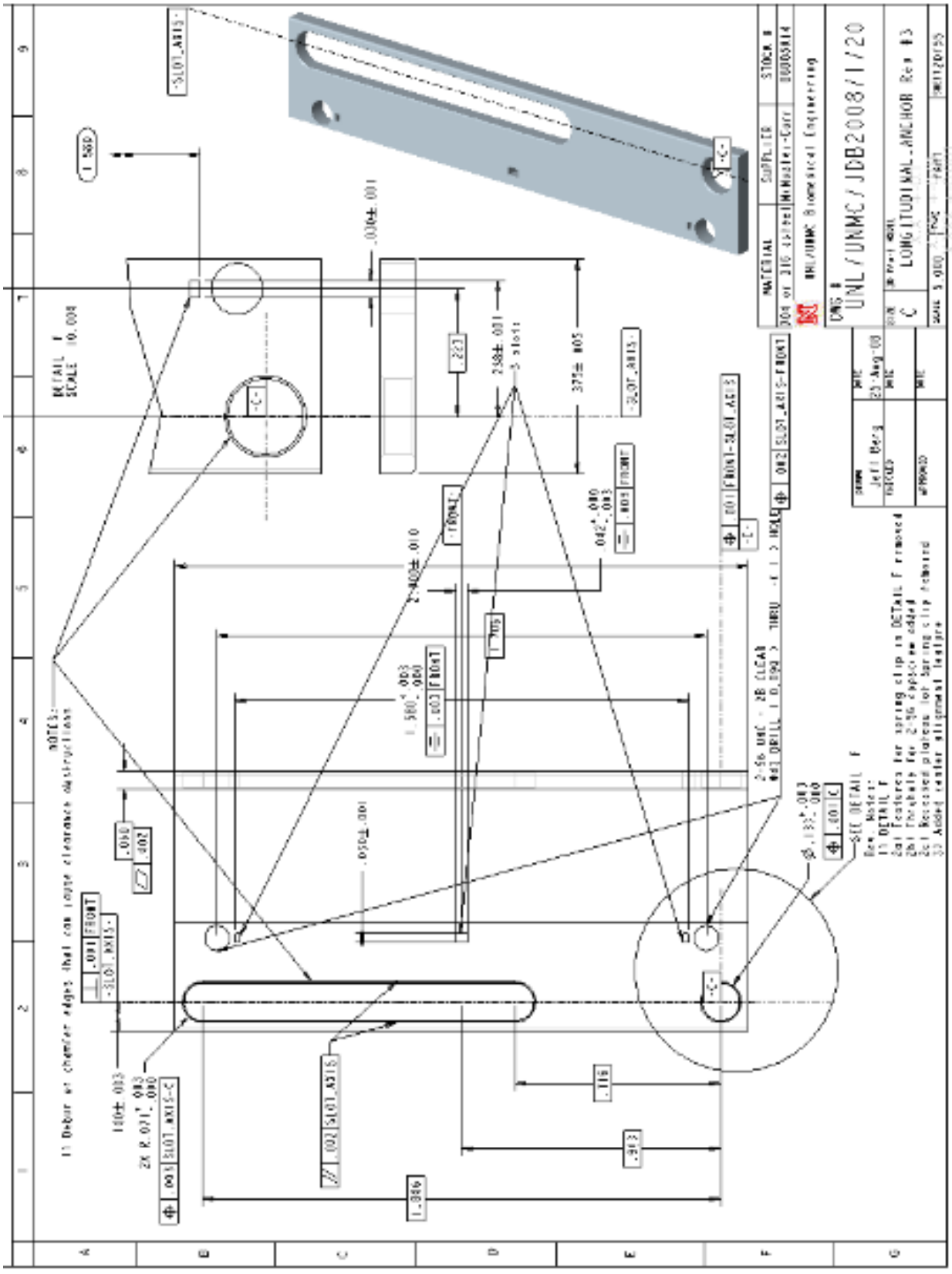
UNL/UNMC/JDB20081120
LONGITUDINAL_ANCHOR Rev #3
Jeff Berg
23-Aug-08
DETAIL F
SCALE 10.000
SEE DETAIL F
.375± .005
.238± .001
.004± .001
.116
.913
1.386

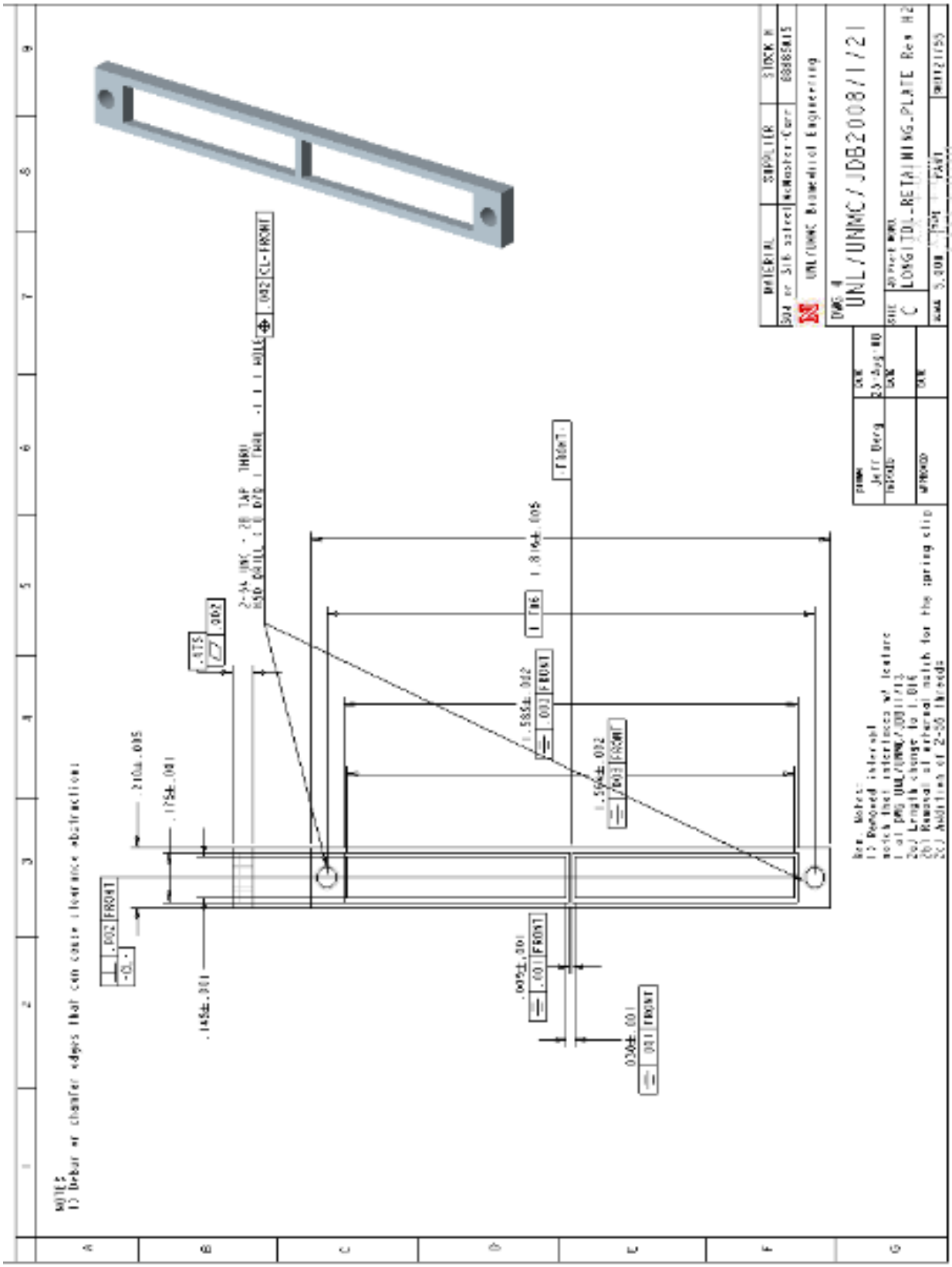
UNL/UNMC/JDB20080111/21
LONGITDL-RETAINING-PLATE Rev H2
UNL/UNMC Biomedical Engineering
Jeff Berg
23-Aug-08
Notes:
1) Deburr or chamfer edges that can cause tolerance obstruction
2) Removed interrupt
notch that interferes w/ feature
3) Length change to 1.016
4) Removed all tapered math for the spring clip
5) Added thru cl 2-56 threads

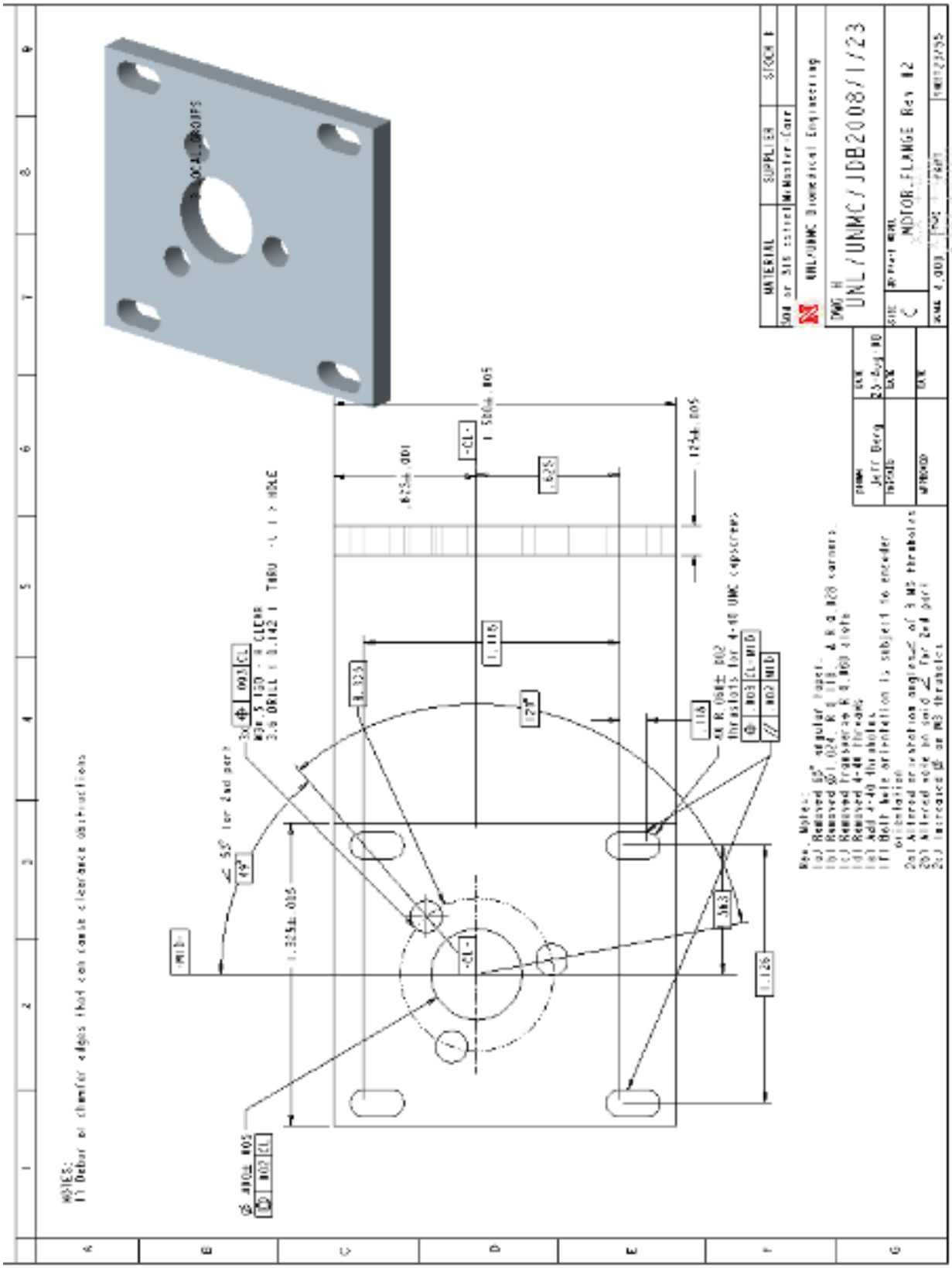
UNL/UNMC/JDB20081123
NDFOR_FLANGE Rev B2
Jerr Berg
UNMC Biomedical Engineering

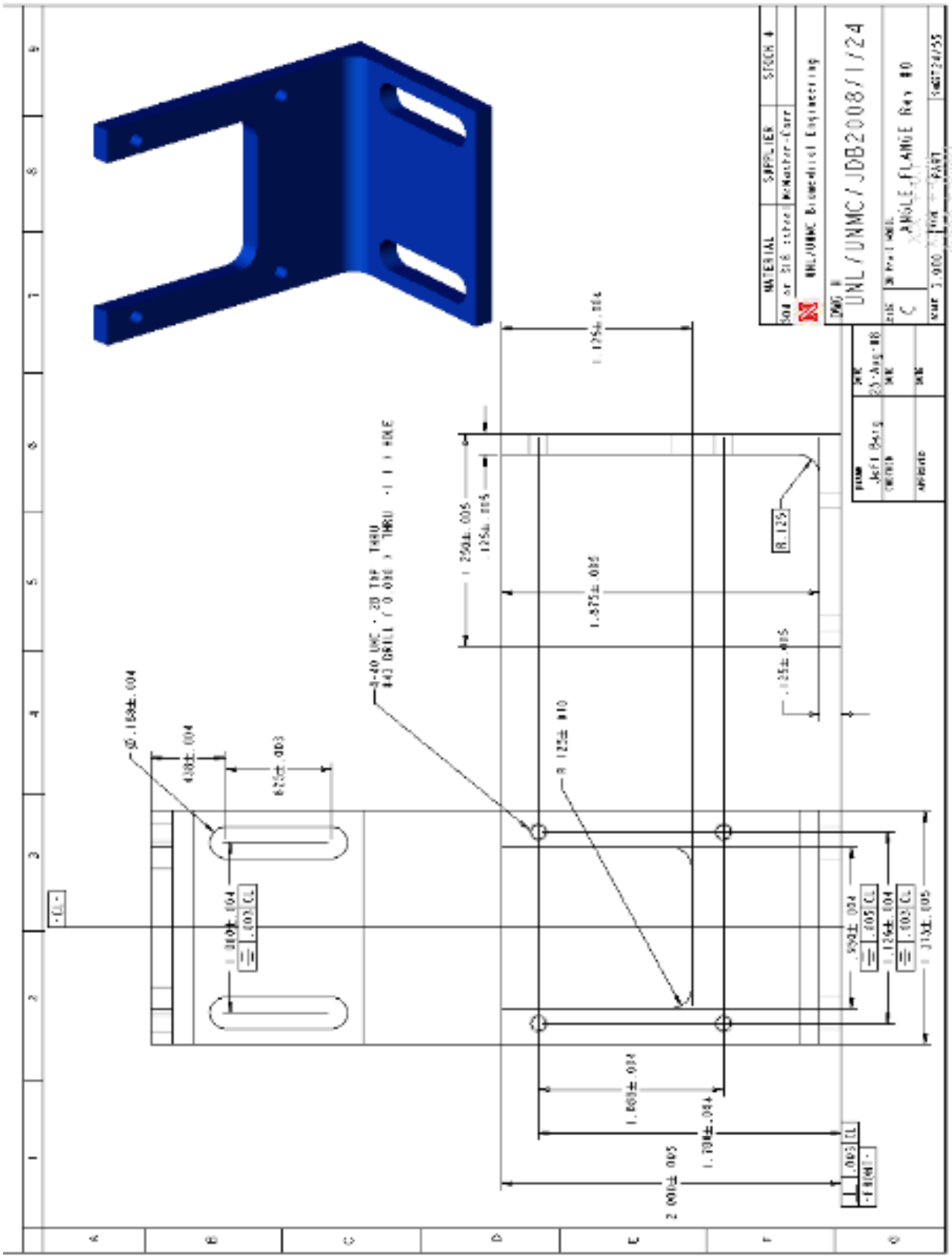
UNL/UNMC/JDB2008/1/24
ANGLE,FLANGE Rev 00
UNL/UNMC Biomedical Engineering
MATERIAL
SUPPLIER
STOCK #
Jeff Berg
25-Aug-08
SCALE: 1.000
WEIGHT:
SHEET 1 OF 1

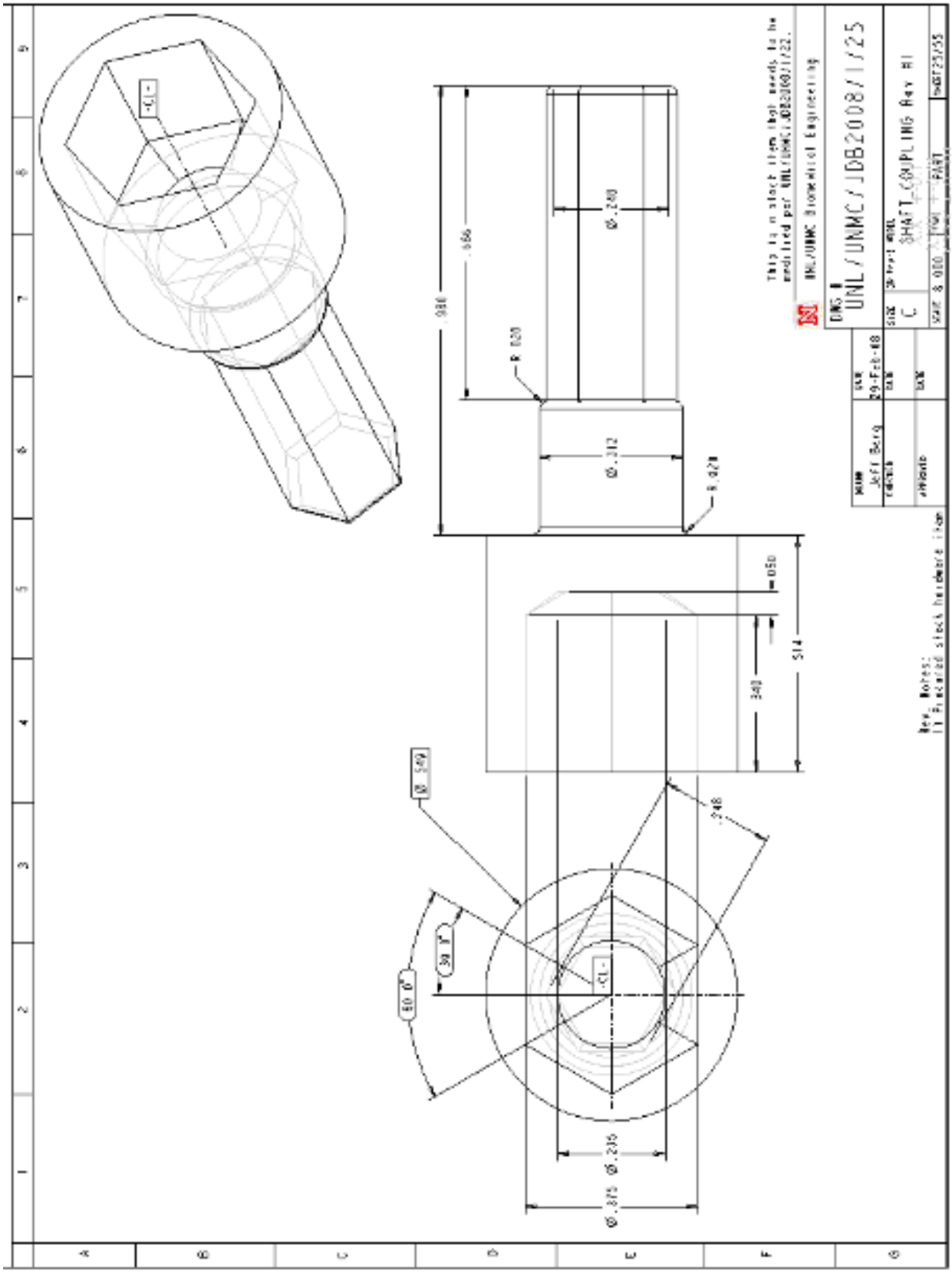
UNL/UNMC/JDB20081125
SHAFT_COUPLING Rev B1
Jeff Berg
29-Feb-08
Ø.240
Ø.312
Ø.875
Ø.235
.248
.514
.340
.050
.986
.856
R .020
60.0°
30.0°

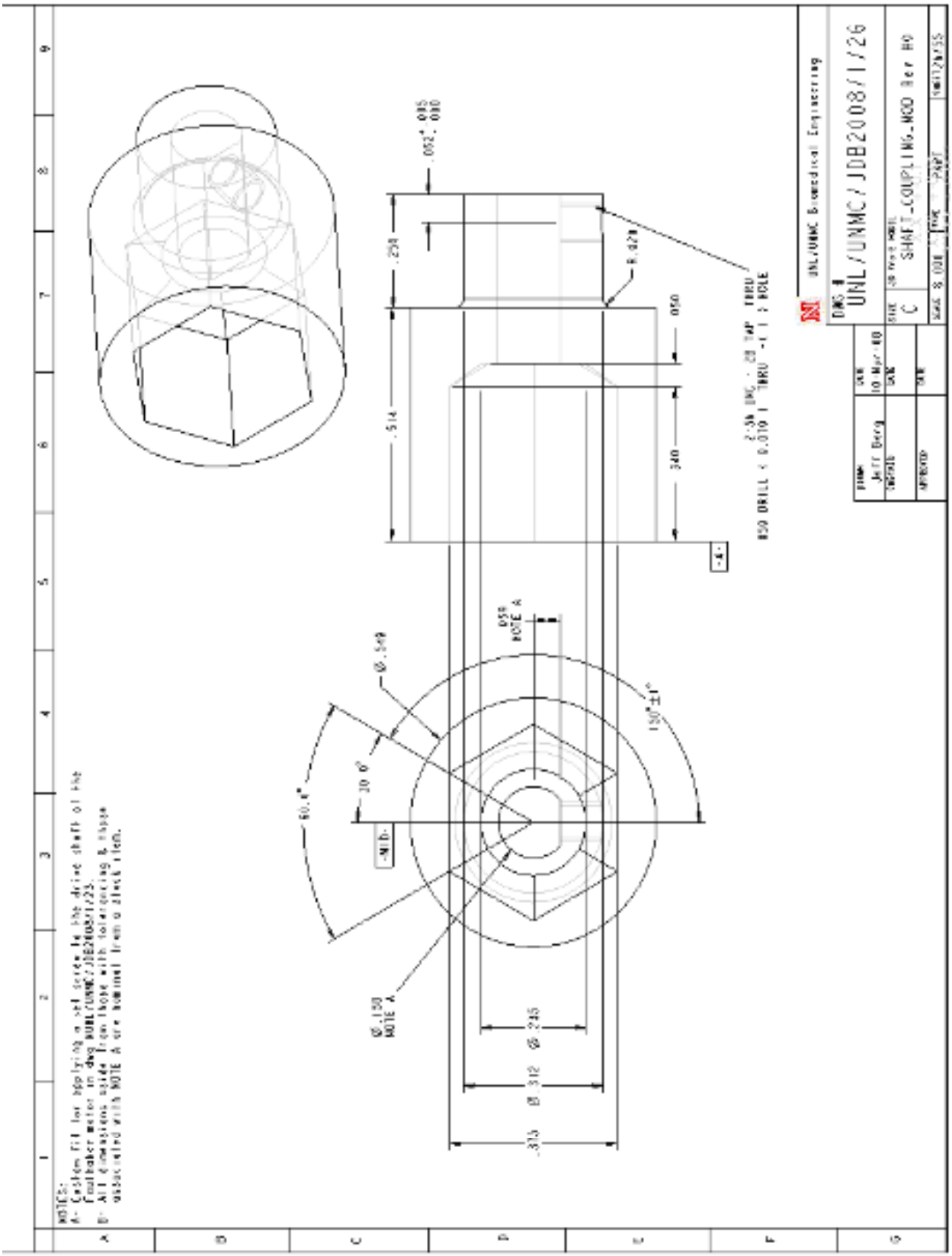
NOTES:
A- Custom fit for applying a set screw to the drive shaft of the
Faulhaber motor in dwg UNL/UNMC/JDB20080111/23.
B- All dimensions apply from shop with tolerancing & shape
calculated with NOTE A are nominal from a check item.
UNL/UNMC Biomedical Engineering
DWG #
UNL/UNMC/JDB20080111/26
Jeff Berg
10-Mar-08
SIZE
C
SHAFT-COUPLING-MOD Rev B0
SCALE: 8/1
SHEET 1 OF 1
.052" .035
.259
.514
.050
.340
.313
Ø.312
Ø.245
Ø.150
NOTE A
Ø.349
.059
NOTE A
60.4°
30.0°
150°±1°
-A-
-B-
-C-

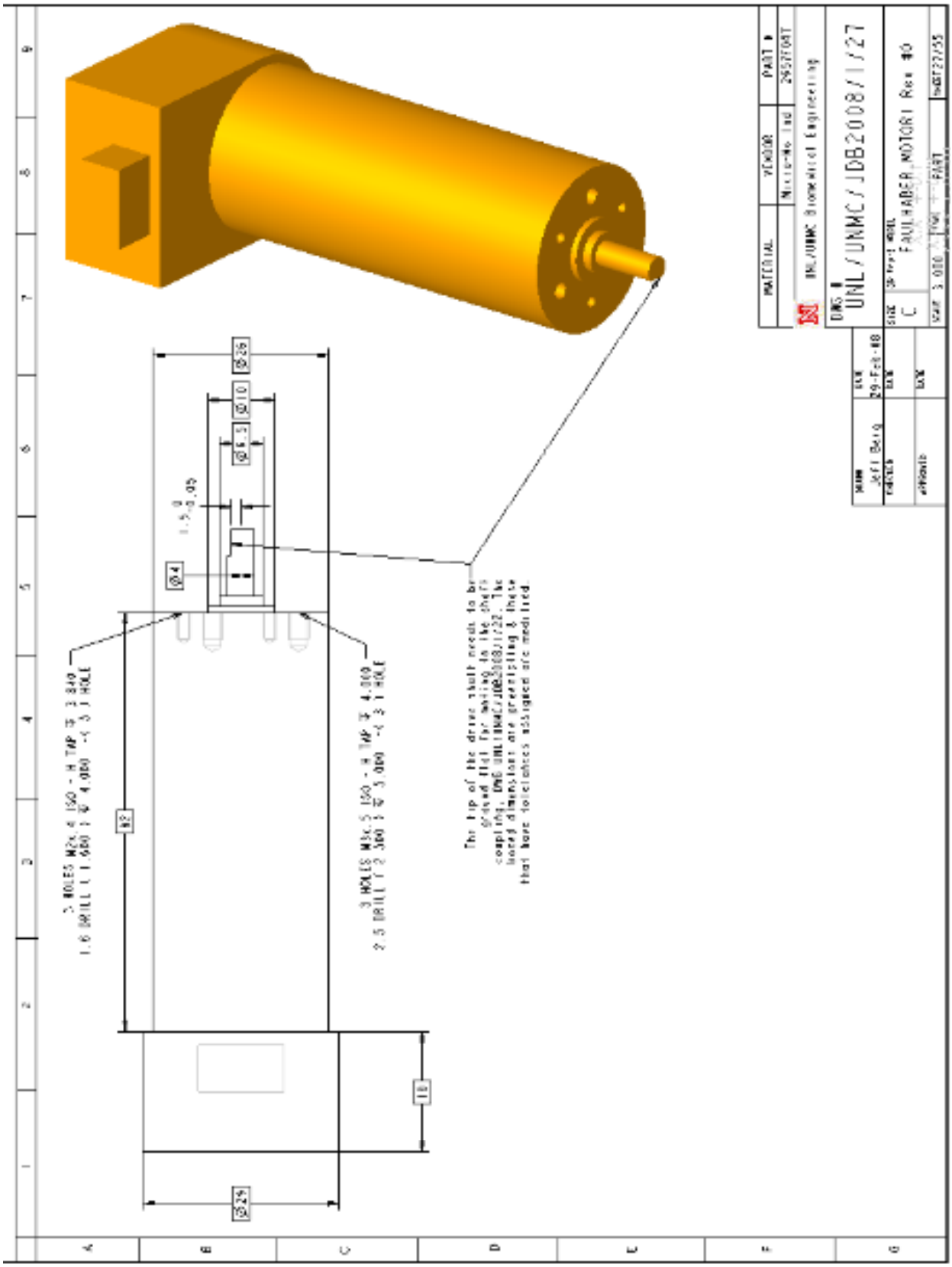
UNL/UNMC/JOB20081/127
FAULHABER MOTOR1 Rev #0
UNL/UNMC Biomedical Engineering
MATERIAL
PART #
2657T06T
Jeff Berg
29-Feb-08
SIZE
C
SCALE: 3.000
WEIGHT:
SHEET 1 OF 1
3 HOLES M2x.4 ISO - H THP ↧ 3.849
1.6 DRILL ↧ 4.000 ⌖ Ø 4.000 <4 3 1 HOLE
3 HOLES M3x.5 ISO - H THP ↧ 4.000
2.5 DRILL ↧ 3.000 ⌖ Ø 3.000 <4 3 1 HOLE
Ø26
Ø10
Ø6.5
Ø4
Ø24
B2
18

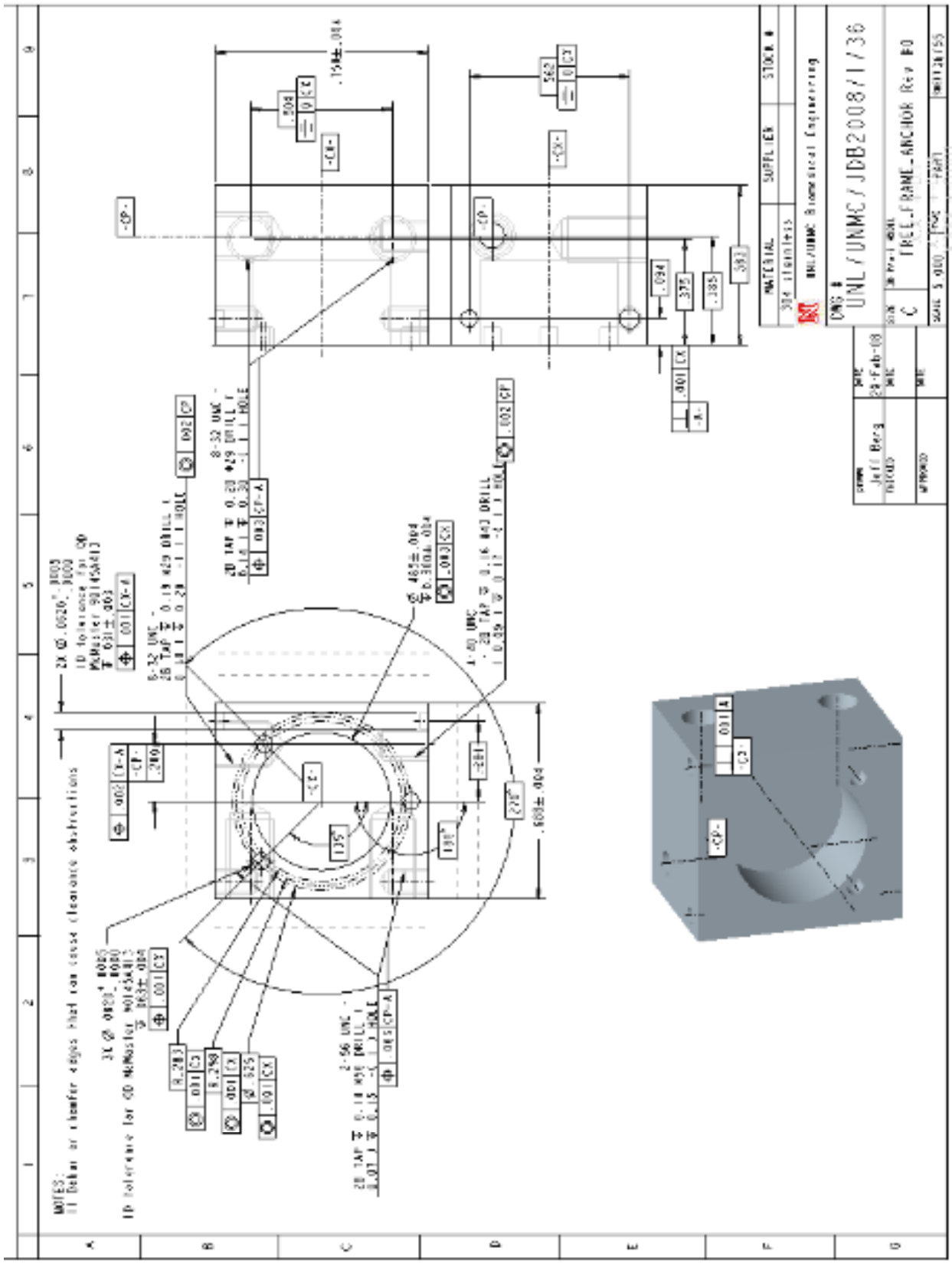
UNL/UNMC/JCB20080111/36
TREE_FRAME_ANCHOR Rev #0
Jeff Berg
28-Feb-08
316 stainless
UNL/UNMC Biomedical Engineering

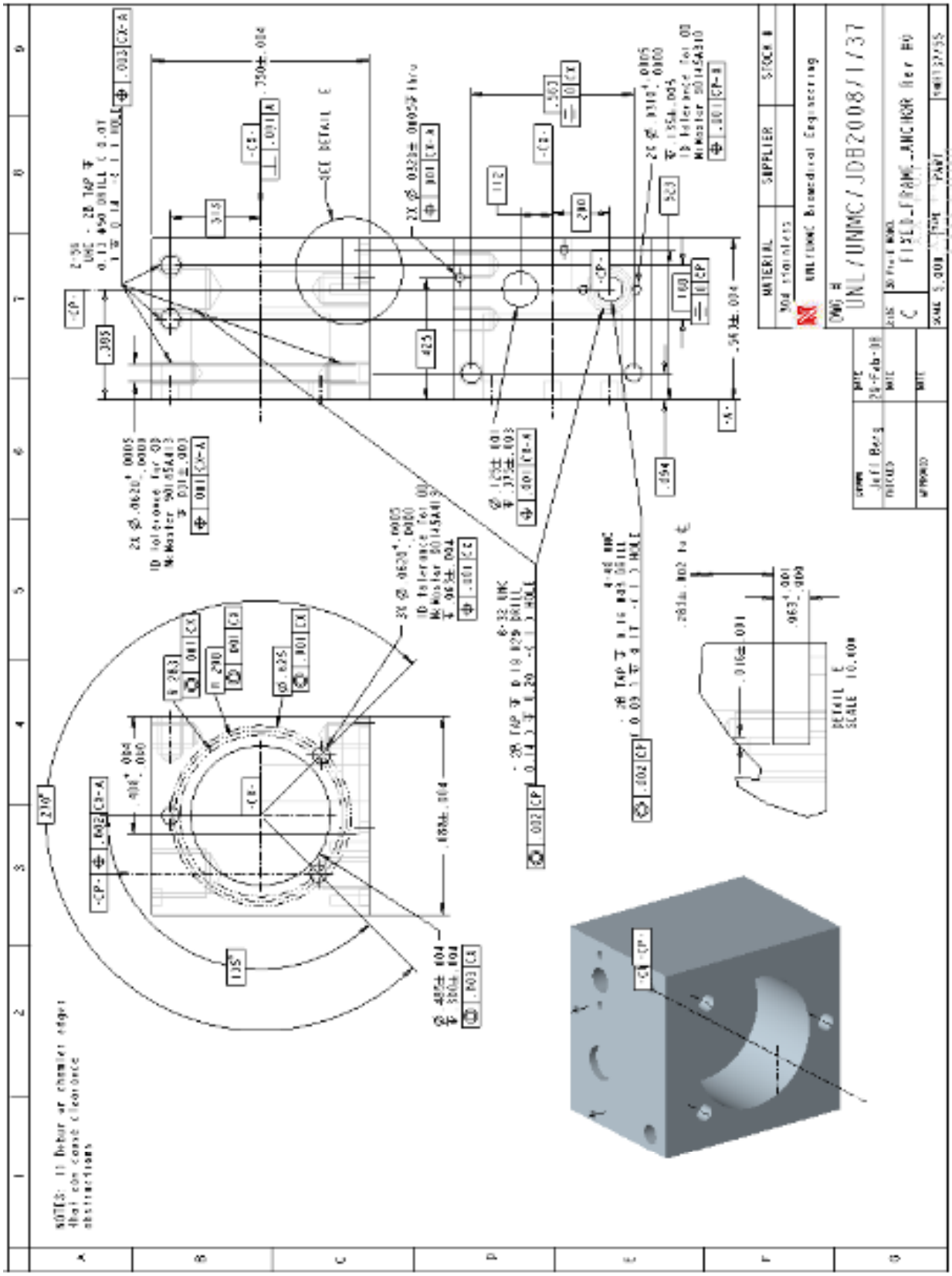
NOTES: 1) Deburr all chamfer edges
that can cause clearance
obstructions
UNL / UNMC / JOB2008 / 137
FIELD_FRAME_ANCHOR Rev B
Jeff Berg
29-Feb-08
SCALE 0.500
SHEET 1 OF 1
MATERIAL
SUPPLIER
STOCK #
304 stainless
UNL/UNMC Biomedical Engineering
DETAIL E
SCALE 10.000
SEE DETAIL E

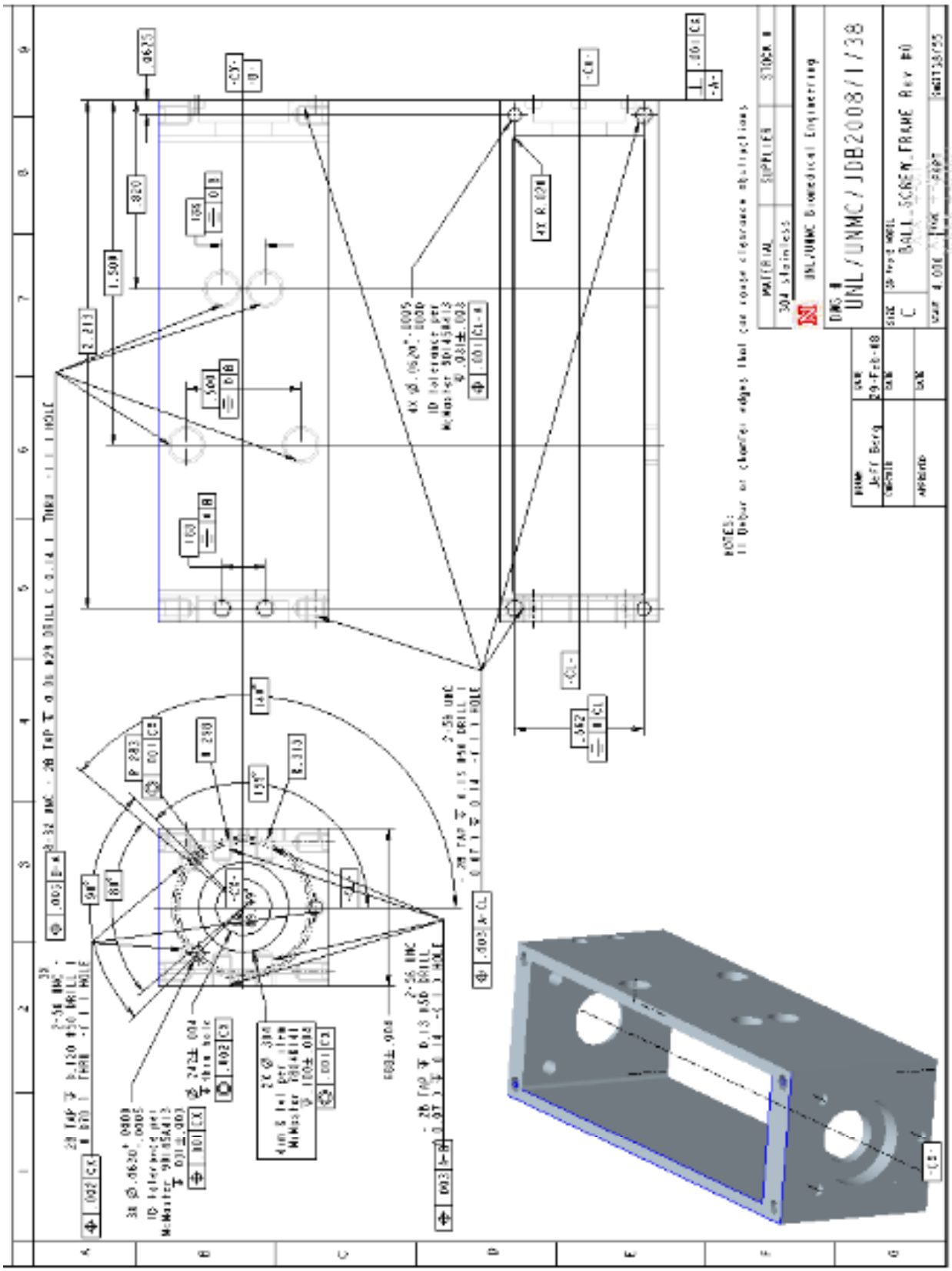
UNL/UNMC/JDB20081138
UNL/UNMC Biomedical Engineering
BALL_SCREW_FRAME Rev B0
304 Stainless
Jeff Berg
29-Feb-08
NOTES:
1) Deburr all chamfer edges that can cause clearance obstructions

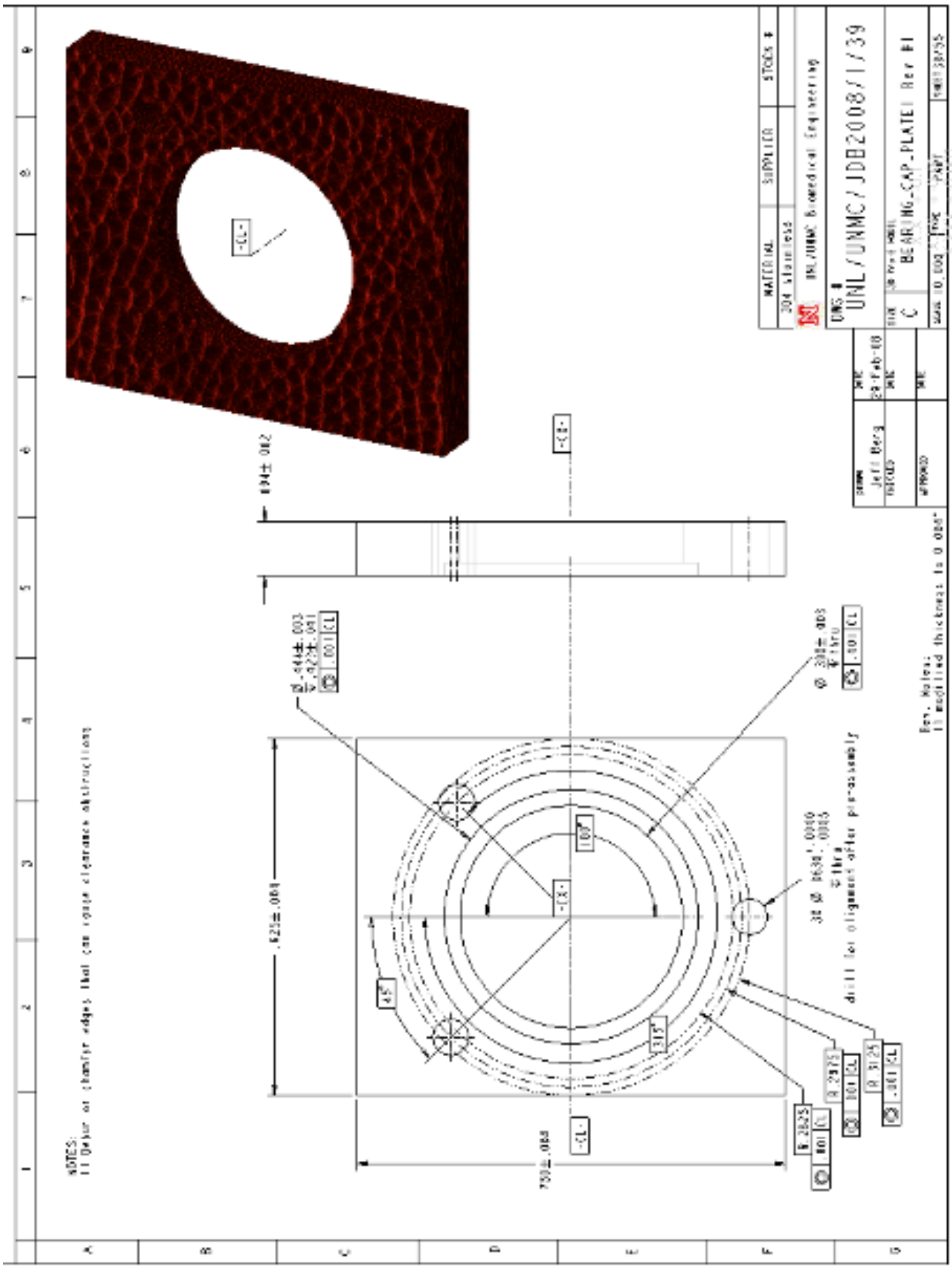
UNL/UNMC/JDB20081139
BEARING-CAP-PLATE1
304 stainless
Jeff Berg
29-Feb-08
NOTES:
1) Deburr or chamfer edges that can cause clearance obstructions
drill for alignment after preassembly

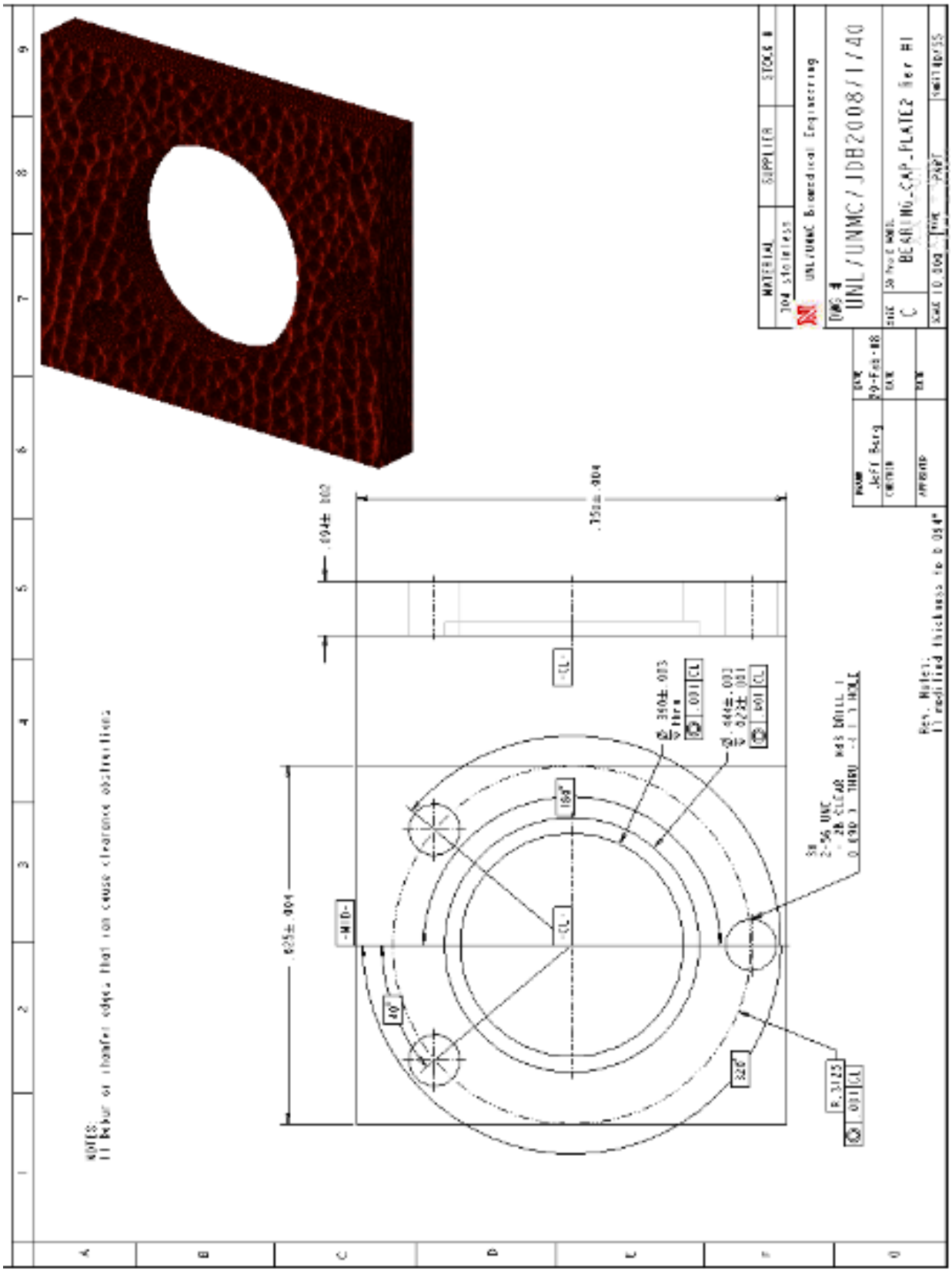
UNL/UNMC/JDB20081140
UNL/UNMC Biomedical Engineering
BEARING_CAP_PLATE2 Rev #1
304 stainless
Jeff Berg
C
SCALE 1.000
SHEET 1 OF 1
NOTES:
1) Deburr all chamfer edges that can cause clearance obstructions
Rev. Note:
1) modified thickness to 0.054"

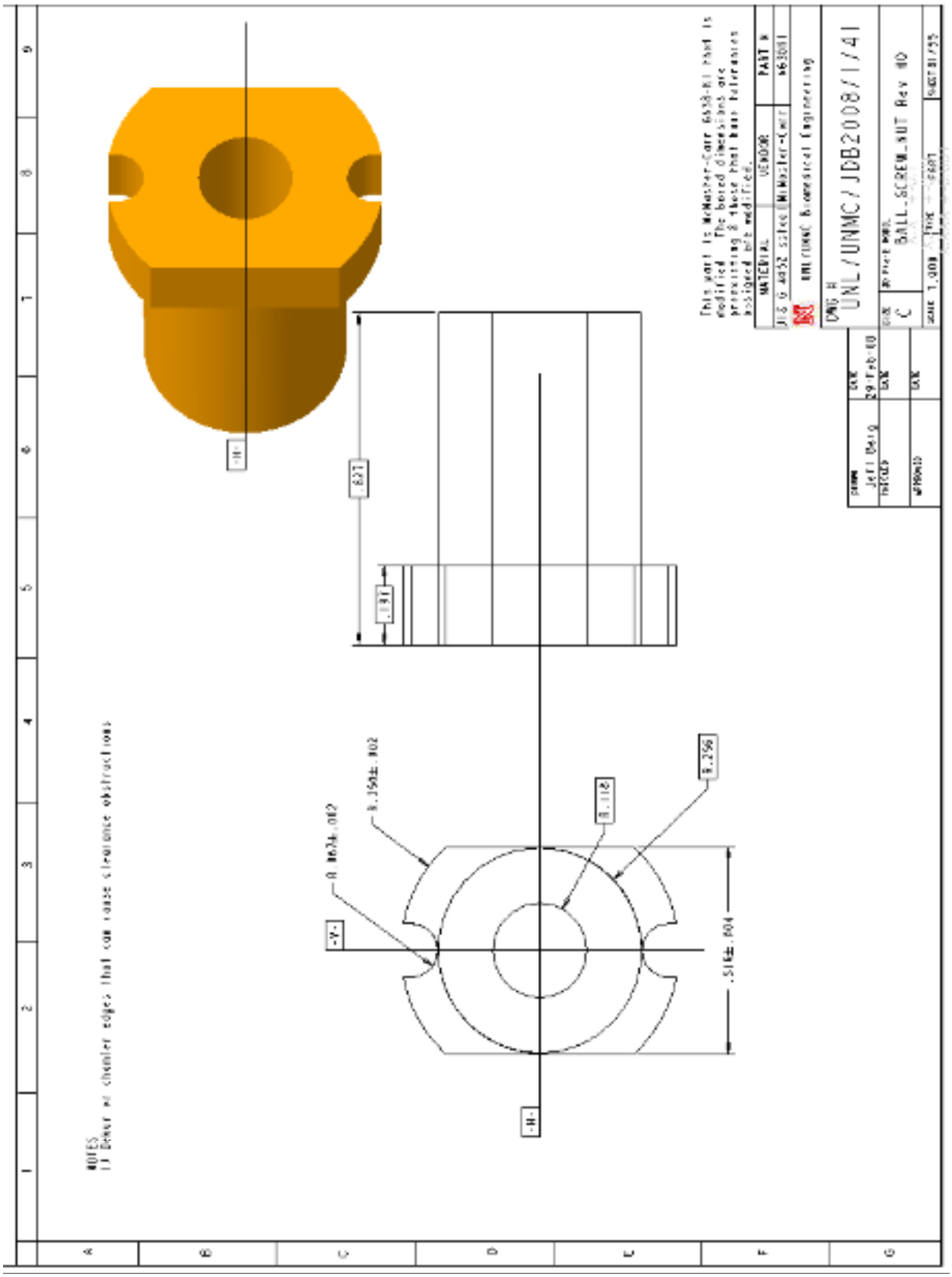
NOTES
UNL/UNMC/JDB20080114
BALL_SCREW_NUT Rev 00
Jeff Daily
29-Feb-08
C
SIZE
DWG #
MATERIAL
VENDOR
PART #
UNL Mechanical Engineering
-H-
-Y-
.827
.181
.118
.256
.1562 .804

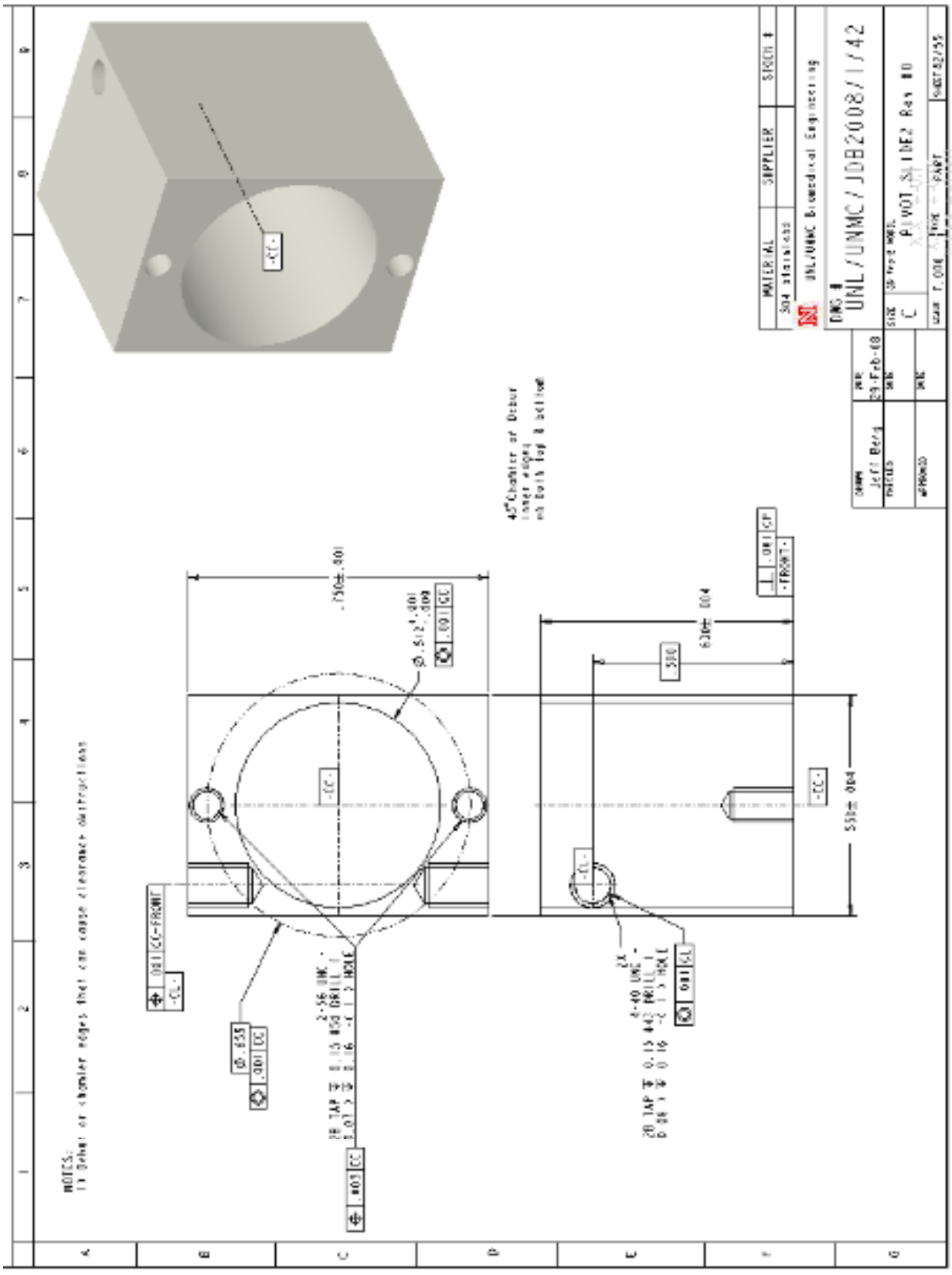
UNL/UNMC/JDB20080112
PIVOT SLIDE2 Rev B0
MATERIAL
SUPPLIER
SIZE
SCALE
DATE
23-Feb-08
UNL/UNMC Biomedical Engineering
NOTES:
45°Chamfer or Orbor
inner edges
on both top & bottom
-CC-
-CL-
-FRONT-
.500
.750±.001
Ø.512 +.001 -.000
Ø.655
.001 CC-FRONT
.001 CC
.003 CC
.001 CL
.001 CF
2X
4-40 UNC -
2B TAP THRU
2-56 UNC -
2B TAP THRU

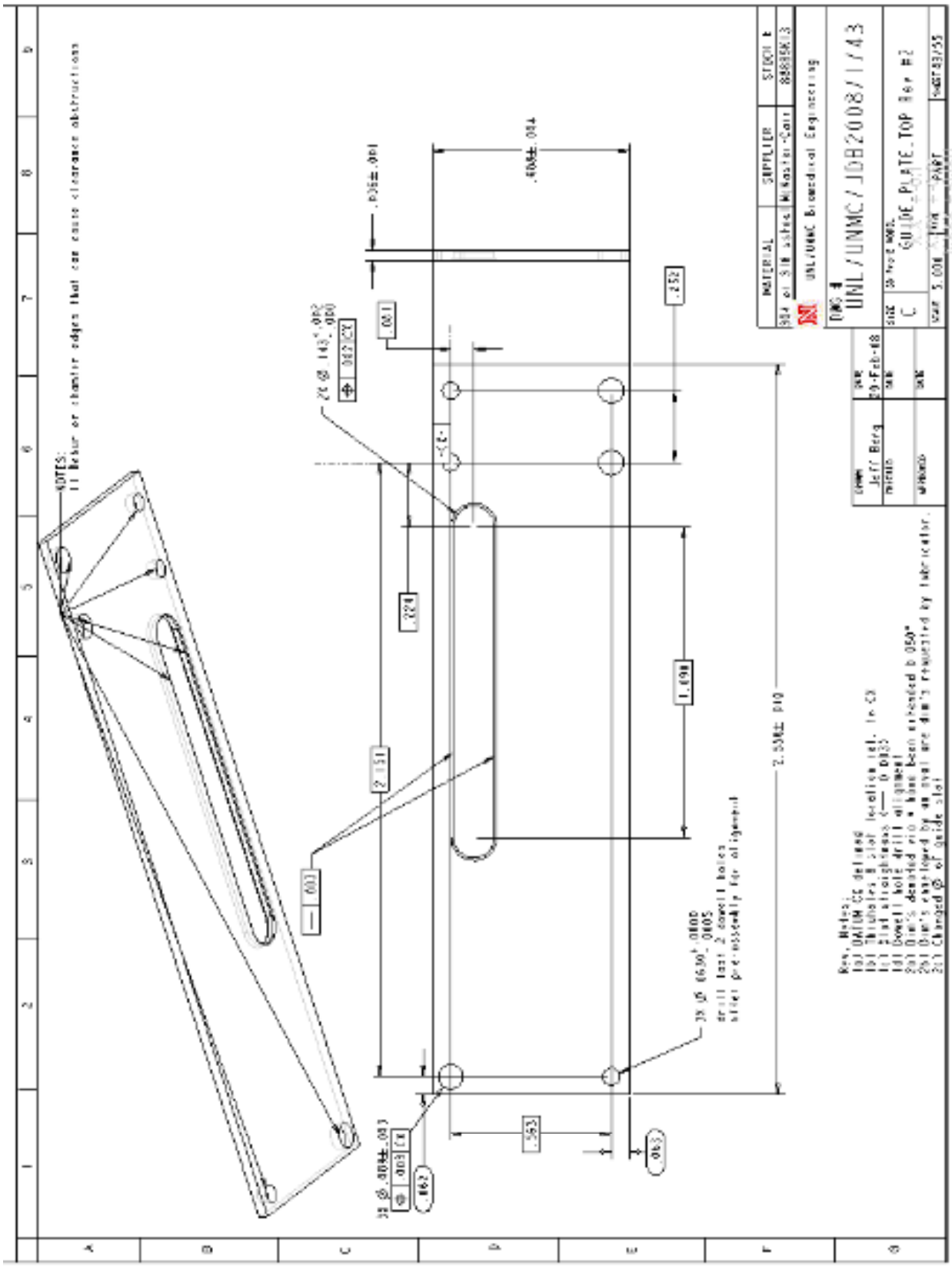
NOTES:
1) Deburr or chamfer edges that can cause clearance obstructions
UNL/UNMC/J0820081/143
GUIDE_PLATE_TOP Rev #2
UNL/UNMC Biomedical Engineering
Jeff Berg
09-Feb-08
MATERIAL
SUPPLIER
STOCK #
Rev. Notes:
1) DWGM CC delete
2) Thickness & slot location tol. to CO
3) Flat straightness C — 0.005
4) Dowell hole drill alignment
5) Dim's denoted rio a bone bean extended 0.050"
6) Dim's employed by AB that are don't requested by fabricator.
7) Changed Ø of guide slot

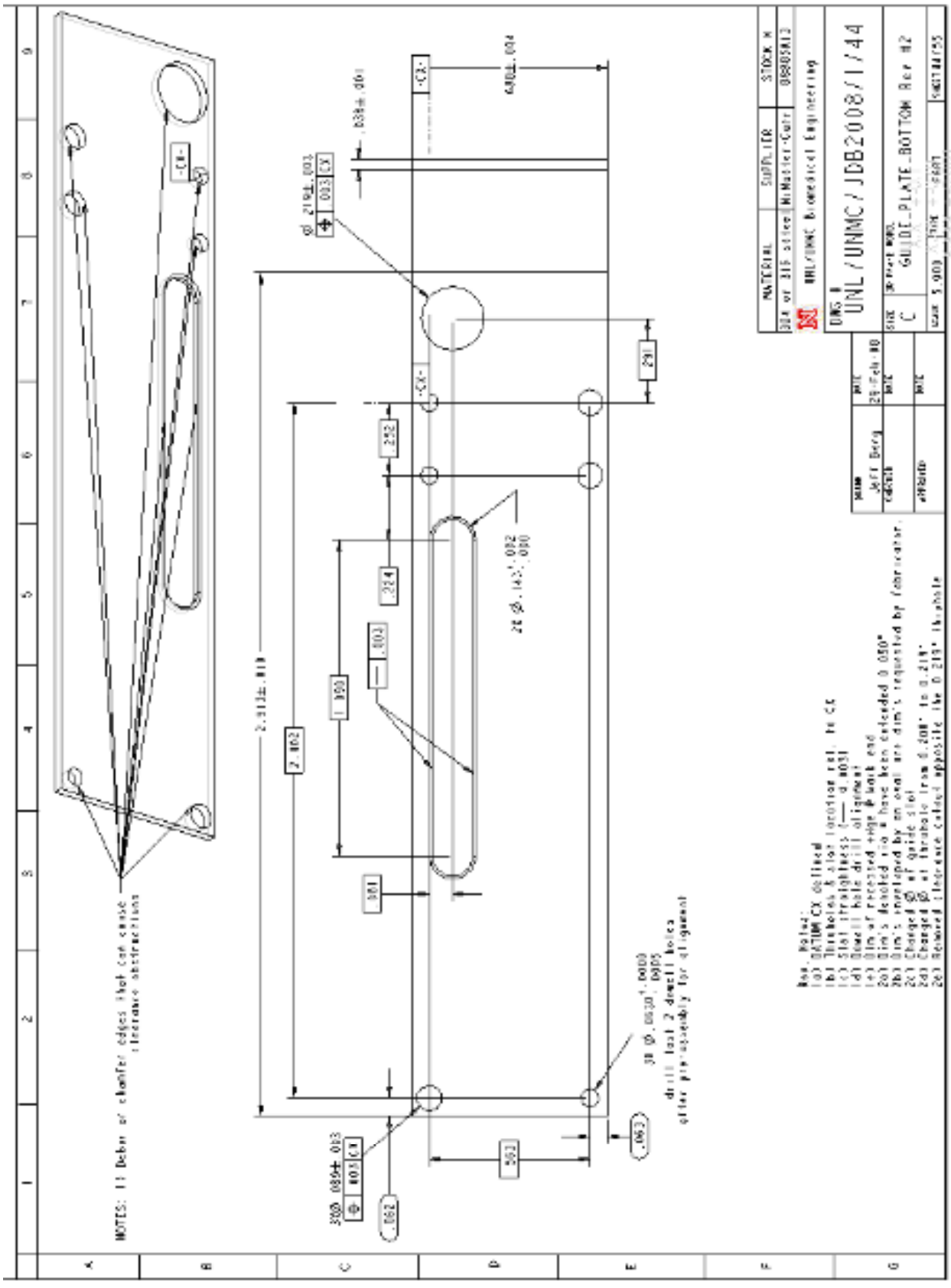
UNL/UNMC/JCB20080111/44
GUIDE_PLATE_BOTTOM Rev #2
UNL/UNMC Biomedical Engineering
MATERIAL
SUPPLIER
STOCK #
SIZE
C
SCALE 5.000
WEIGHT
DRAWN
Jeff Berg
25-Feb-08
CHECKED
APPROVED
DATE
NOTES: 1) Debur or chamfer edges that can cause
interface obstructions
Rev. Notes:
1a) DATUM CX defined
1b) Thickness & slot location rel. to CC
1c) Slot straightness (—) 0.003
1d) Dowell hole drill alignment
1e) Dim's denoted +Hgh & Lwk end
2a) Dim's denoted +Hgh & Lwk have been extended 0.050"
2b) Dim's unaffected by an addl src dim's requested by fabricator.
2c) Changed Ø of guide slot
2d) Changed Ø of threhole from 0.208" to 0.219"
2e) Removed clearance called opposite the 0.219" threhole
drill last 2 dowell holes
after pre-assembly for alignment

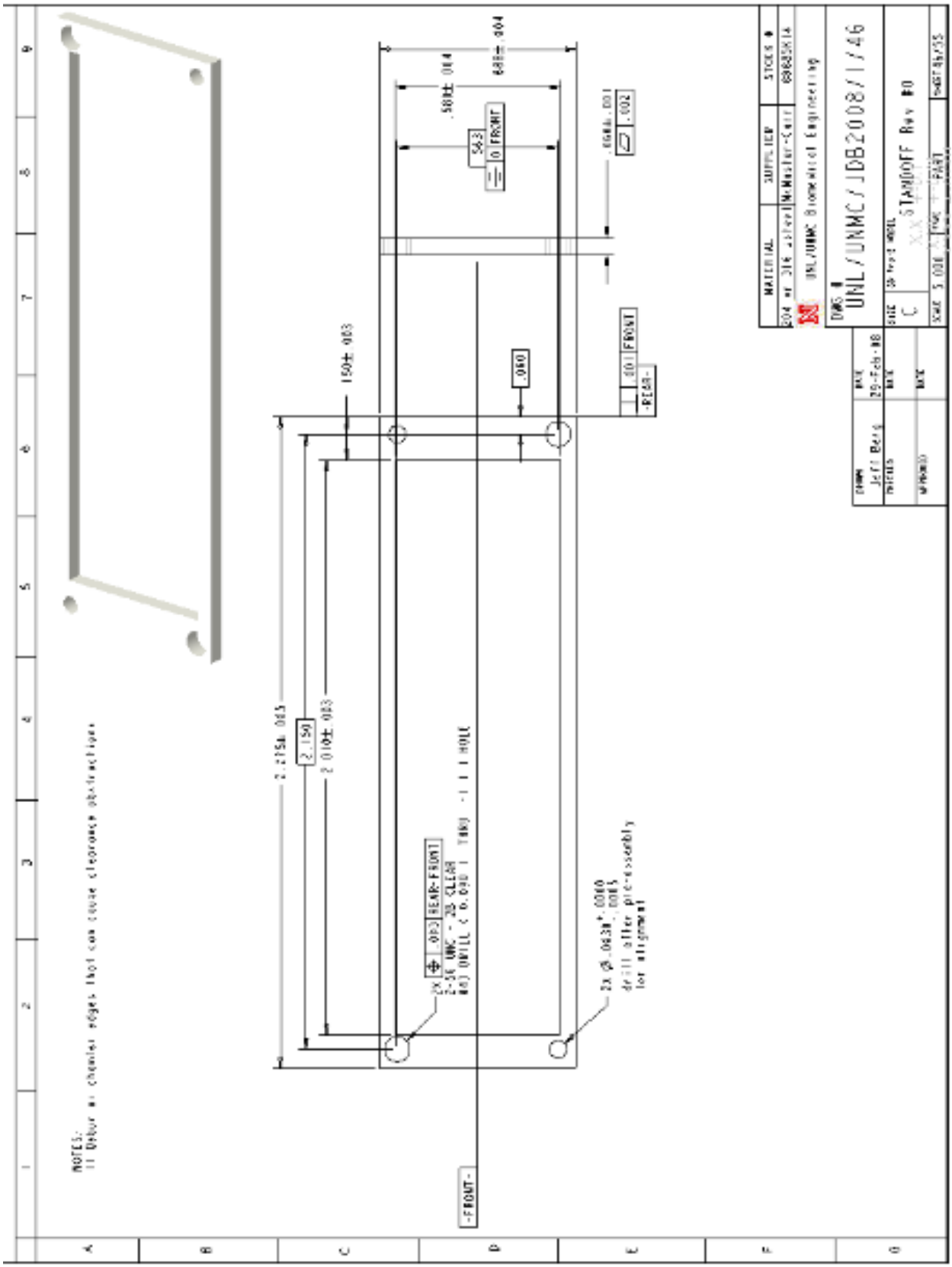
NOTES:
1) Deburr all chamfer edges that can cause clearance obstructions
2.215± .005
2.150
2.010± .003
150± .003
.060
.001 FRONT
-REAR-
.002
.500± .004
.688± .004
.543
0 FRONT
.688± .001
2X #10-32 UNF - 2B CLEAR
.060 DRILL x 0.040 [1.00] -I- I I HOLE
2x Ø.0638" +.0060 -.0065
drill after pre-assembly
for alignment
-FRONT-
MATERIAL
SUPPLIER
STOCK #
6063-T6 Aluminum
McMaster-Carr
6983K514
UNL/UNMC Biomedical Engineering
DWG #
UNL/UNMC/J0820008/1/46
Jeff Berg
29-Feb-08
C
STANDOFF Rev #0
SCALE: 5.000
WEIGHT:
SHEET 1 OF 1

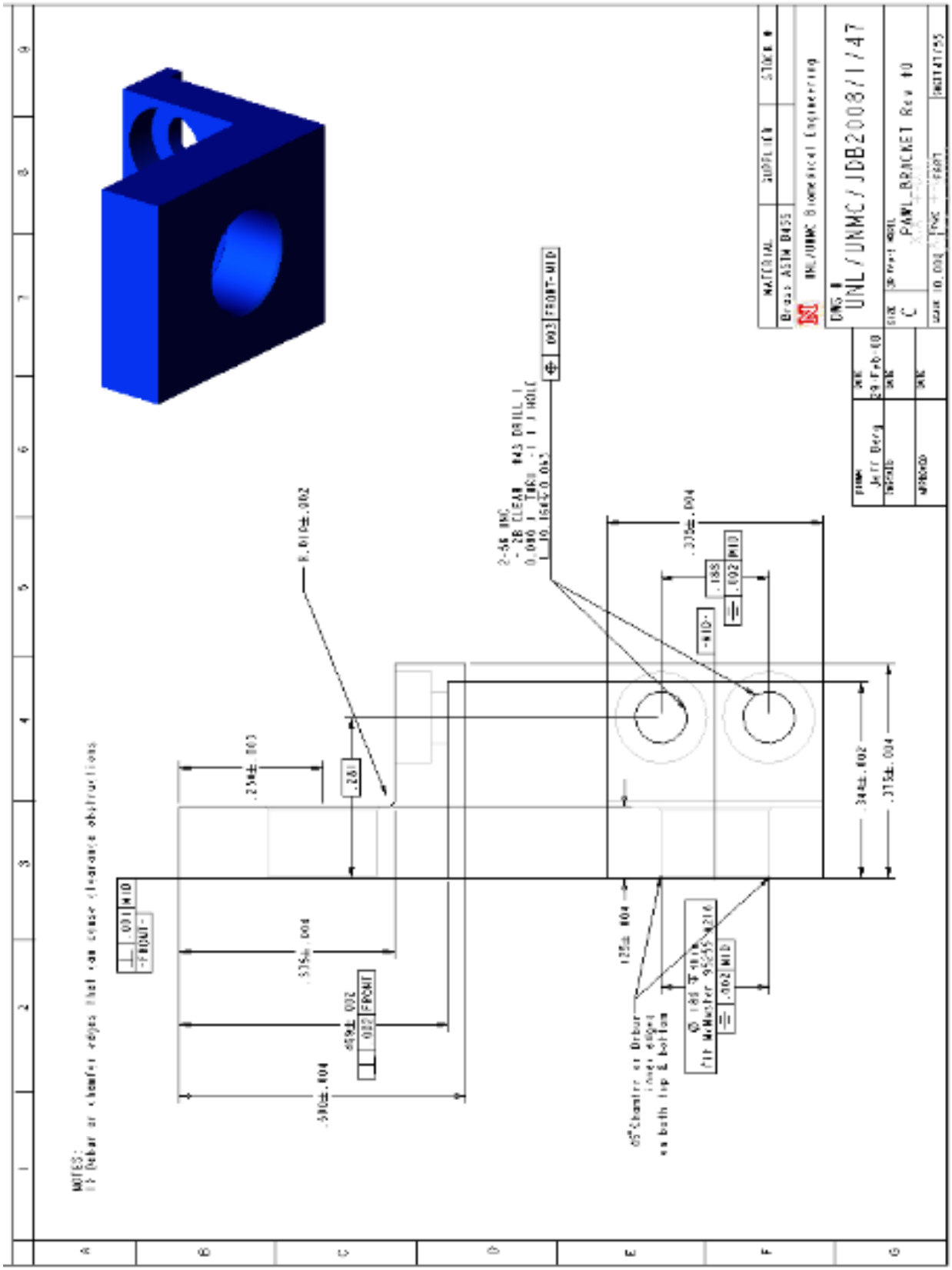
UNL/UNMC/JDB2008/1/47
PANEL_BRACKET Rev 10
Brass ASTM B455
UNL/UNMC Biomedical Engineering
Jerr Berg
.380±.004
.315±.004
.344±.002
.250±.003
.335±.004
R.810±.002
.281
.188
.002 MID
.001 MID
.002 FRONT
.003 FRONT-MID
.125±.004

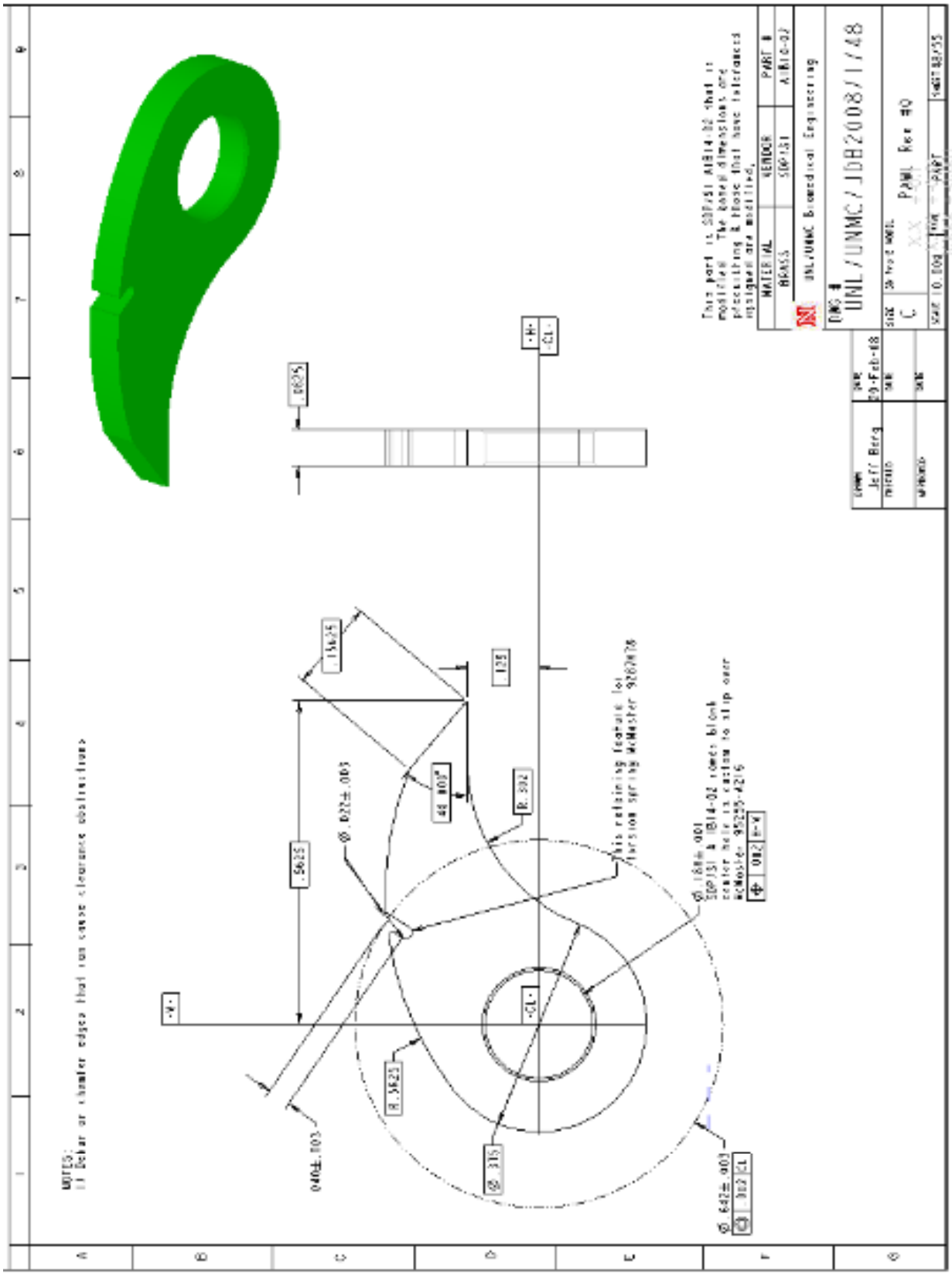
UNL / UNMC / JDB20080111/48
PANL Rev #0
UNL/UNMC Biomedical Engineering
Jeff Berg
29-Feb-08
MATERIAL
BRASS
VENDOR
SOPISI
PART #
AIB14-02
NOTES:
1) Deburr or chamfer edges that can cause clearance obstructions
This retaining feature is for Torsion spring McMaster 9260K78
Ø.642± .003
.5625
.0404± .003
.15625
.125
R.392
R.3623
Ø.315
Ø.022± .003
45° ±0°

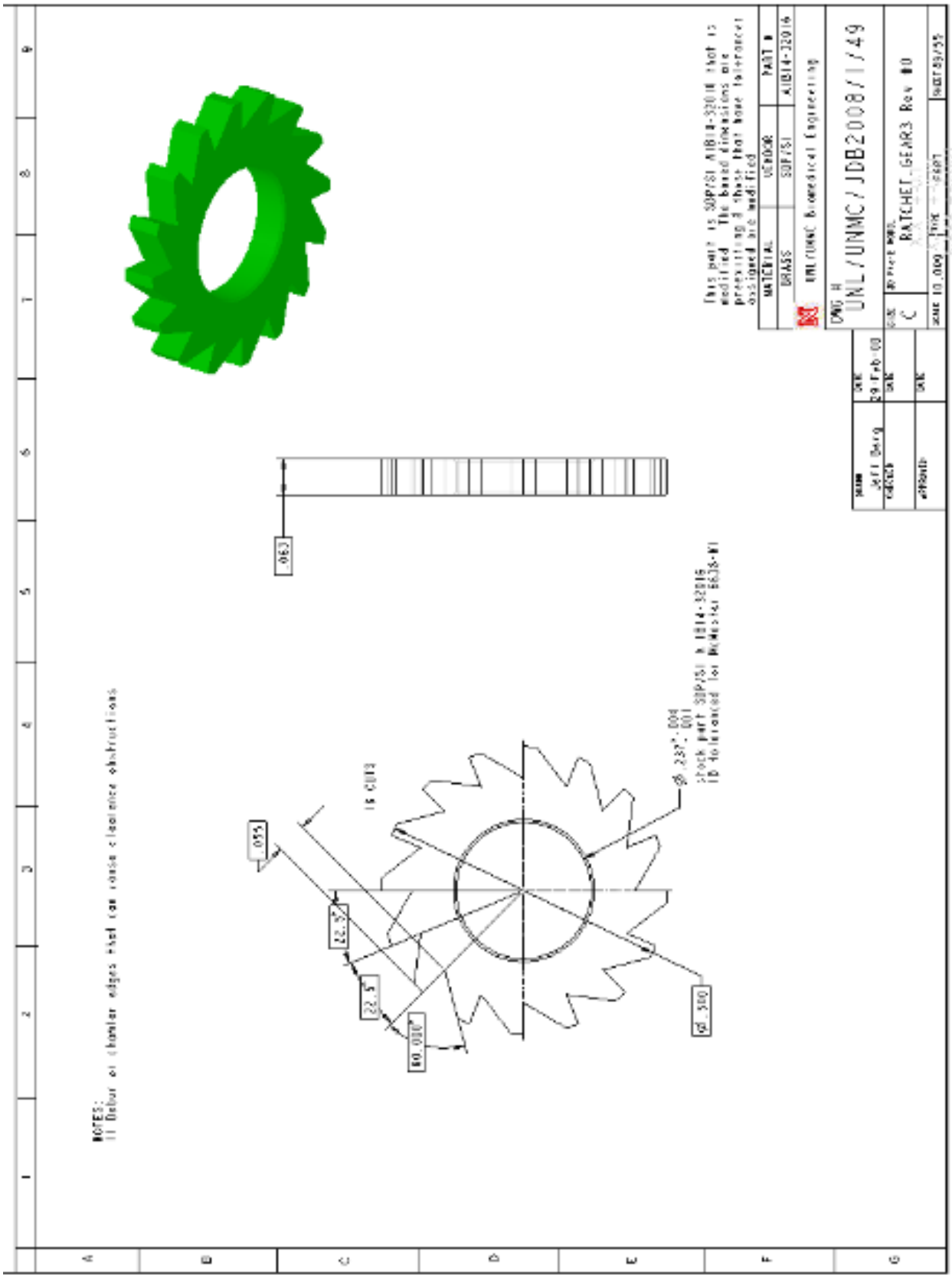
NOTES:
UNL/UNMC/JDB20080711/49
RATCHET_GEAR3 Rev B0
MATERIAL
VENDOR
PART #
BRASS
SOFTSI
AIB14-32016
Jeff Berg
29 Feb 08
SCALE: 10.000
WEIGHT: 0.00 lbs
SHEET 1 OF 1

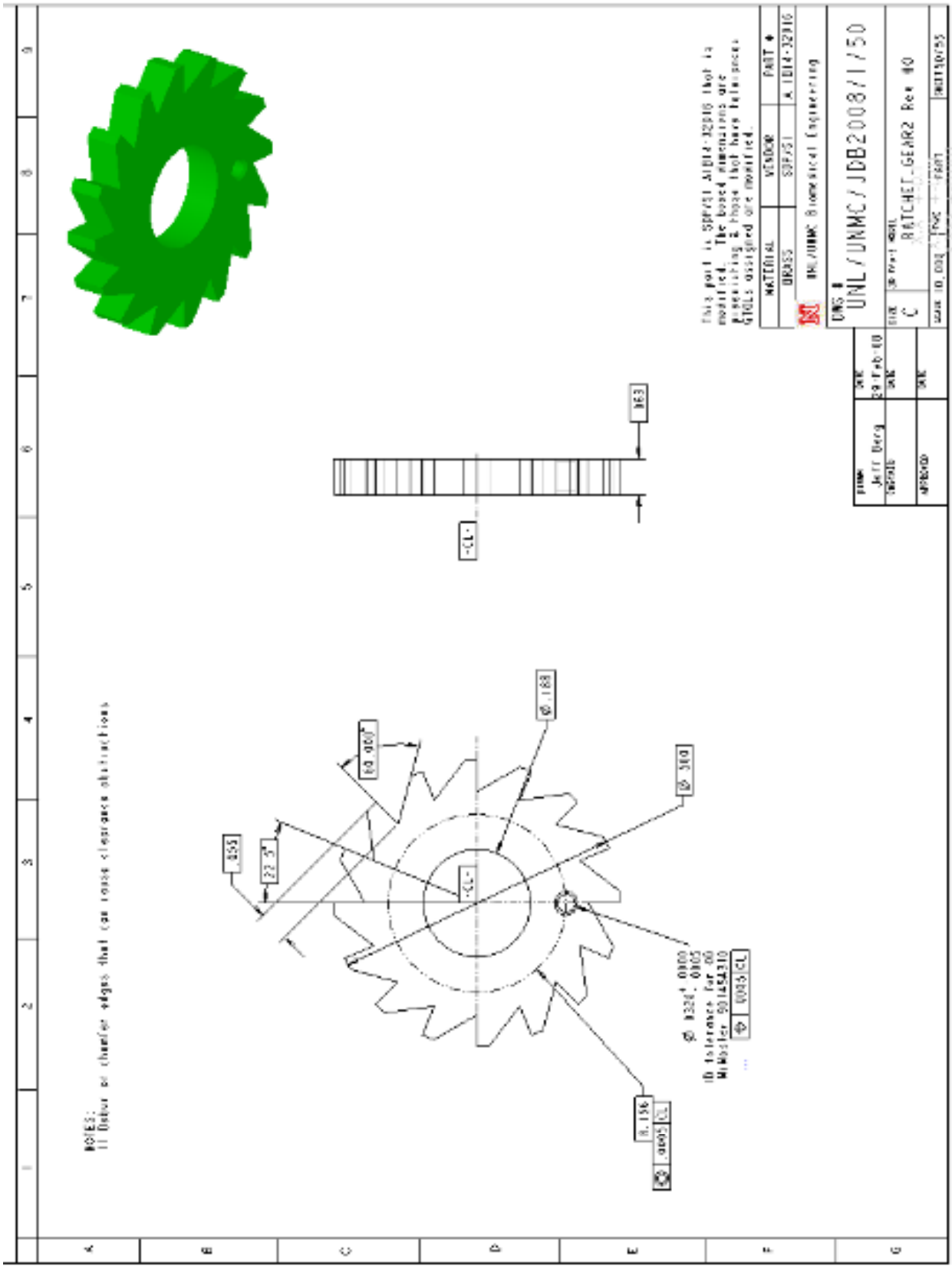
UNL / UNMC / JGB20081150
RATCHET_GEAR2 Rev 00
UNL/UNMC Biomedical Engineering
MATERIAL
BRASS
WISDOM
SRP451
PART #
A-1014-32016
NOTES:
11 Deburr all chamfer edges that can cause clearance obstructions
Ø.188
Ø.380
.855
22.5°
60.000°
.163
.156
.0005 CL
Ø.3281 .000 .005
.0005 CL

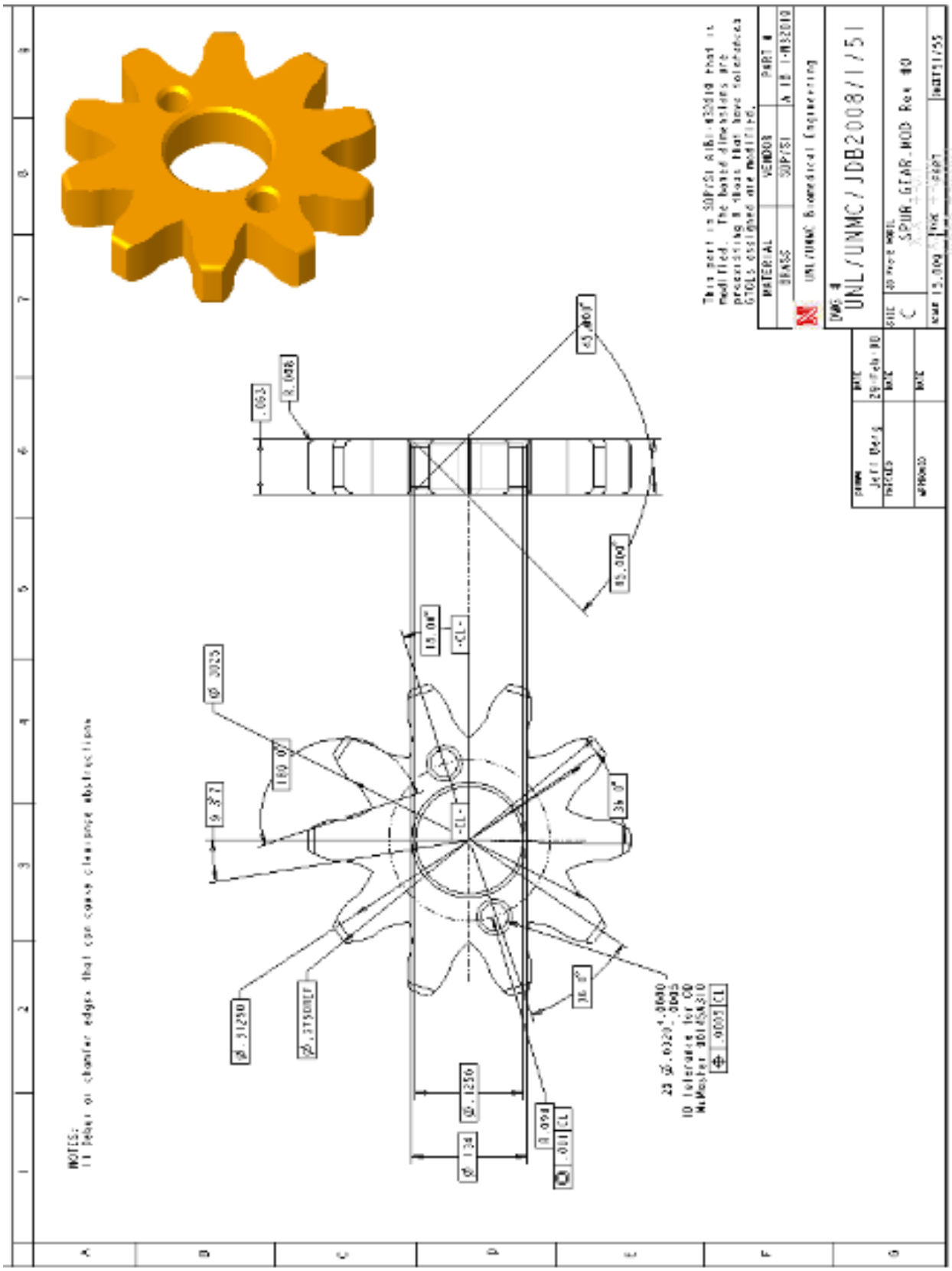
UNL/UNMC/JDB20080711/51
SPUR_GEAR_MOD Rev 00
MATERIAL
BRASS
VENDOR
SOPTSI
PART #
A 10 1-MS2010
UNL/UNMC Biomedical Engineering
NOTES:
11 Debur or chamfer edges that can cause clearance obstructions
Ø.3125
Ø.375DRILL
Ø.1250
Ø.134
.094
.011 CL
.0005 CL
.063
.036
45.00°
15.00°
-CL-
Ø.3025
180.0°
9.357
36.0°
36.0°
15.00°

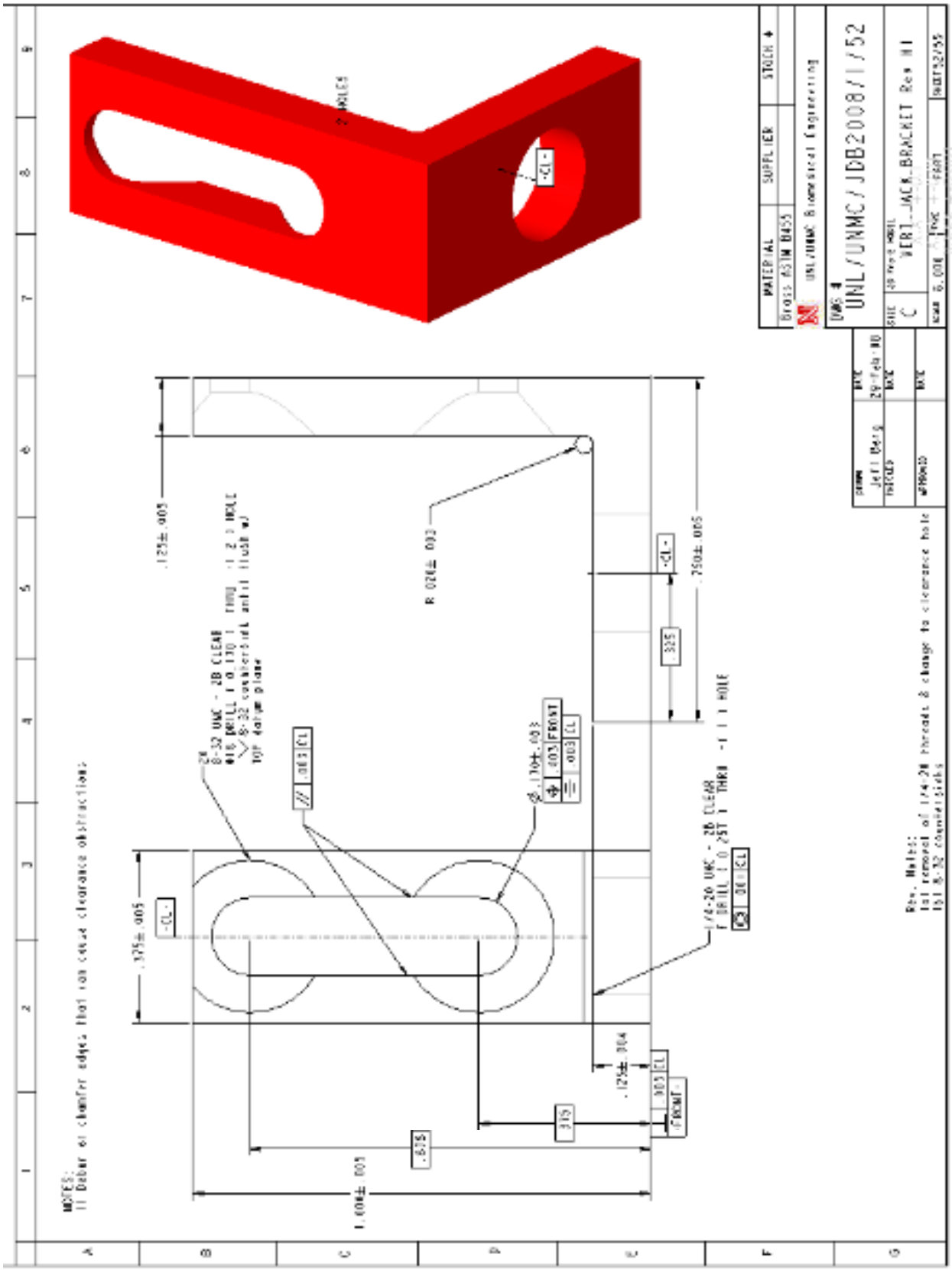
UNL/UNMC/JDB20081152
VERT_JACK_BRACKET Rev 01
MATERIAL
SUPPLIER
STOCK #
Gross ASTM B455
SIZE
C
SCALE 0.008
SHEET 2/35
NOTES:
1) Deburr all chamfer edges that can cause clearance obstructions
Rev. Notes:
1a) removed all 1/4-20 threads & change to clearance hole
1b) 8-32 countersinks

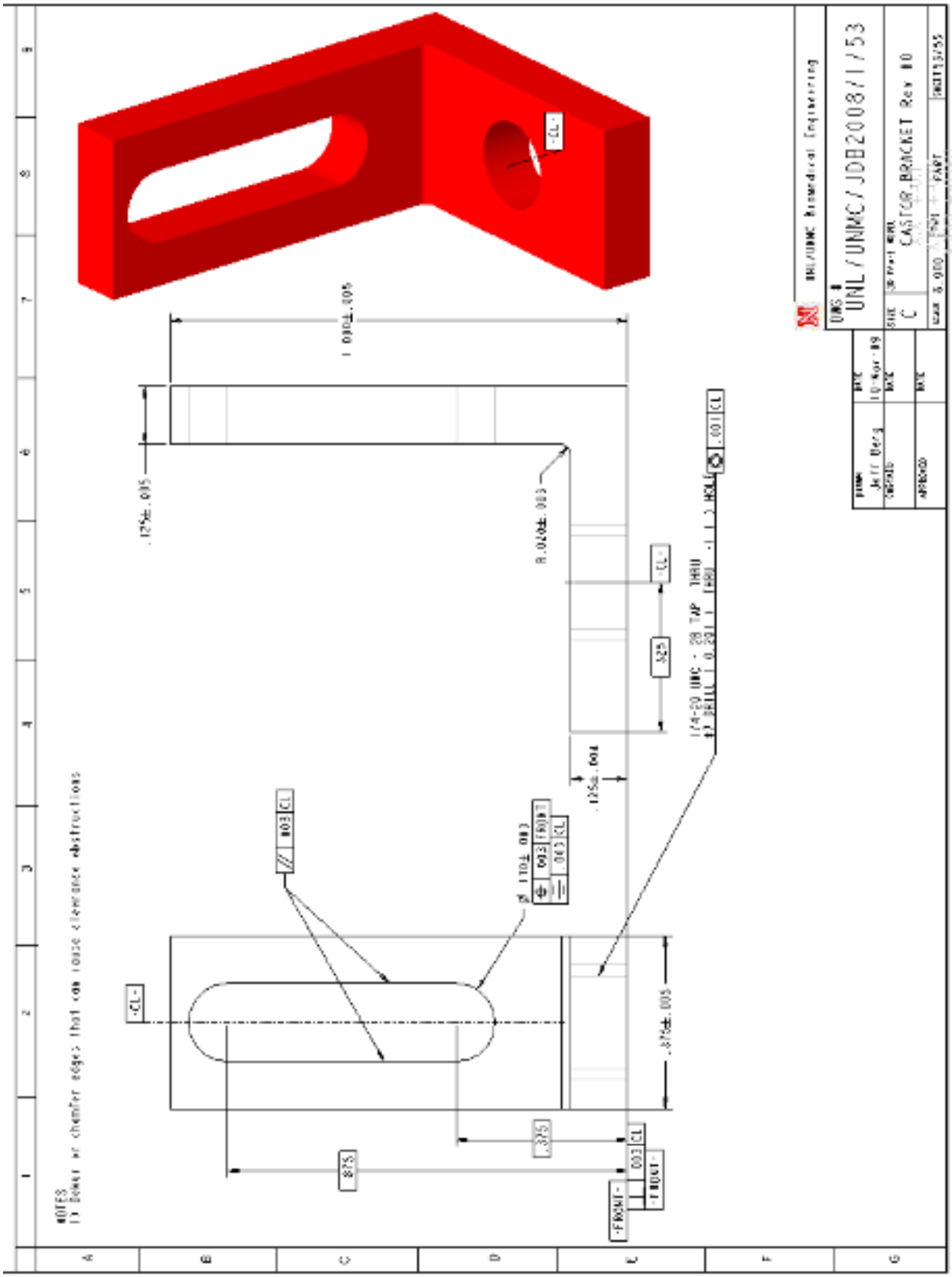
UNL/UNMC/JOB20087/153
CASTOR BRACKET Rev #0
UNL/UNMC Biomedical Engineering
Jeff Berg
10-Nov-09
SIZE
C
SCALE: 6.000
SHEET 1 OF 1
1.000±.005
.125±.005
8.020±.003
.125±.004
.875±.005
.375
.875
.325
1/4-20 UNC - 2B TAP THRU
NOTES
1) Break or chamfer edges that can cause clearance obstructions

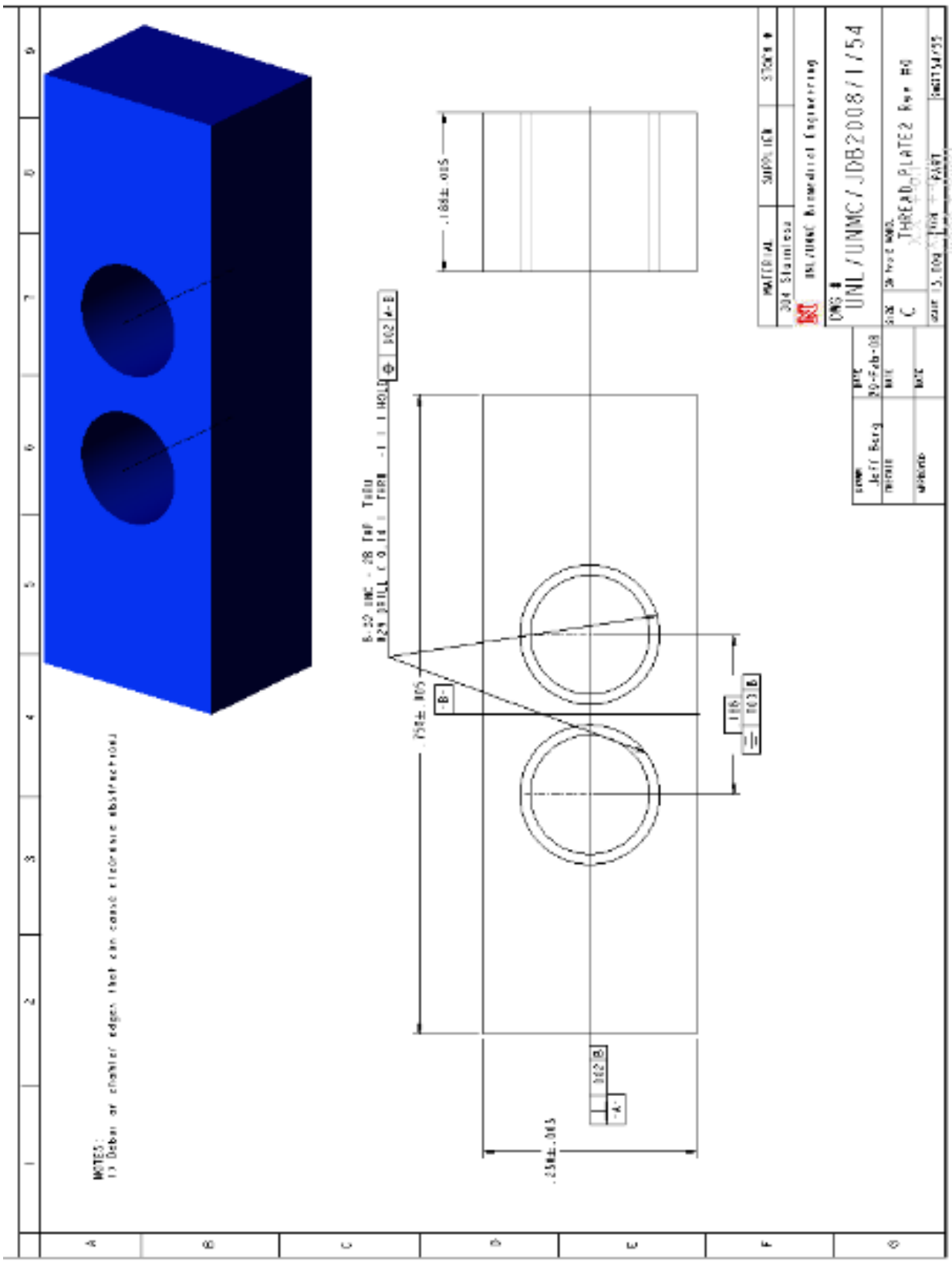
UNL/UNMC/JDB20081754
THREAD_PLATE2 Rev B0
304 Stainless
Jeff Berg
30-Feb-08
.188± .015
.750± .005
.250±.005

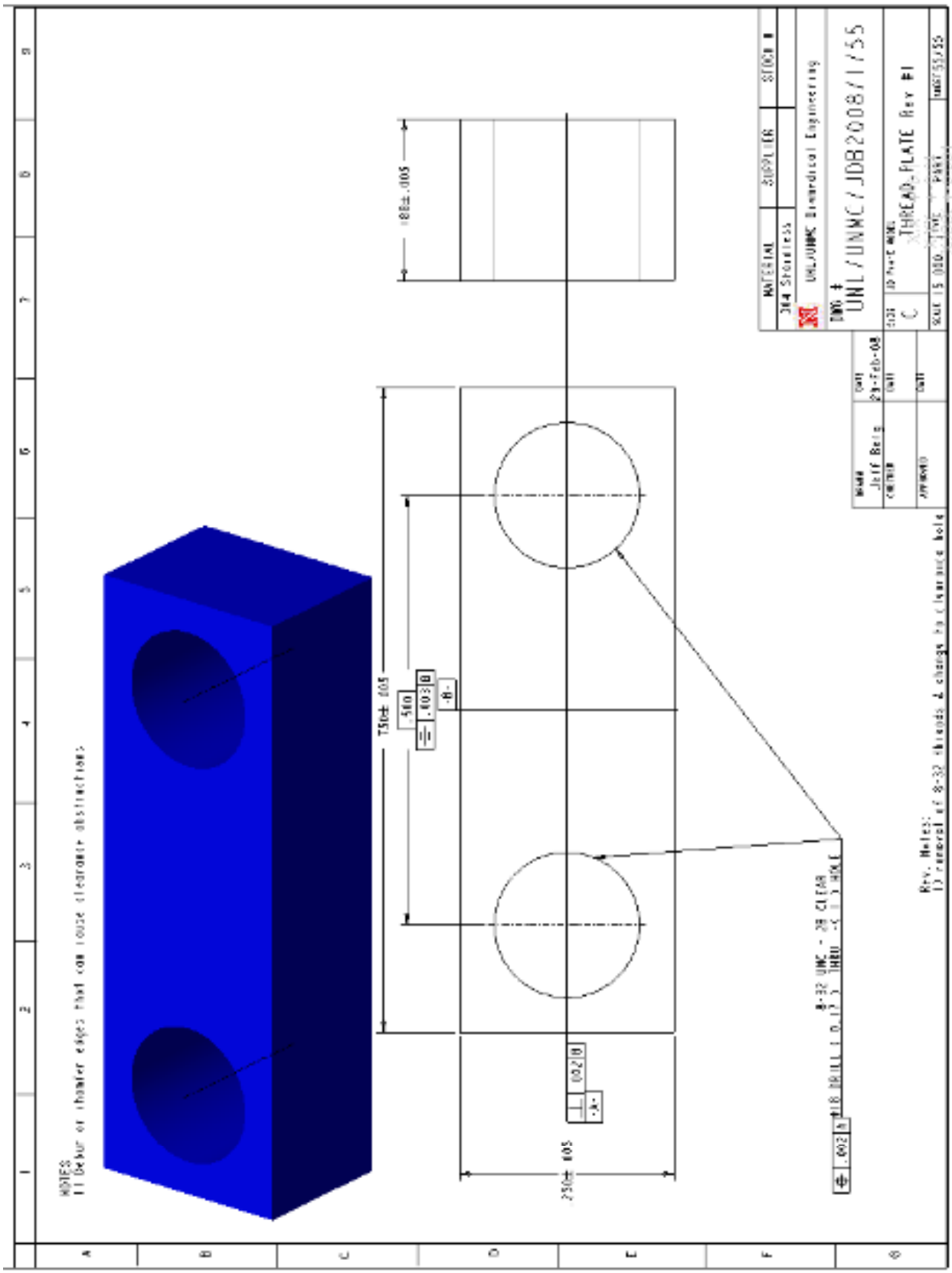
UNL/UNWC/JDB20081755
THREAD_PLATE Rev B1
UNL/UNWC Biomedical Engineering
Jeff Berg
29-Feb-08
188±.005
750±.005
250±.005
.560
.003 B
-B-
.002 B
-A-
8-32 UNC - 2B CLEAR
Rev. Notes:
1) removal of 8-32 threads & change to clearance hole

[1] ASTM D4065 - 06 "Standard Practice for Plastics: Dynamic Mechanical Properties: Determination and Report of Procedures", Vol. 8.02, **ASTM International**, Dec. 2006.
[2] ASTM D5992 - 96(2006)e1 "Standard Guide for Dynamic Testing of Vulcanized Rubber and Rubber-Like Materials Using Vibratory Methods", Vol. 9.01, **ASTM International**, Dec. 2006.
[3] R. M. Christensen, Theory of Viscoelasticity, 2nd ed., Academic Press, NY, 1982.
[4] Schapery, R.A., MEMA Course 651 notes, unpublished.
[5] Brinson, Catherine & Brinson, Hal, Polymer Engineering & Viscoelasticity: An Intro., Springer Science, 2008.
[6] Edwards, C., and D. Penney. Elementary Differential Equations with Boundary Value Problems. 5th ed. Upper Saddle River, NJ: Prentice Hall, 2003. ISBN: 013145773X.
[7] Harris, F.J., 1978. "On the Use of Windows for Harmonic Analysis with the Discrete Fourier Transform," Proceedings of the IEEE, **68**(1): 51-83.
[8] Erwin Kreyszig, Advanced Engineering Mathematics., 8th ed., John Wiley & Sons, 1999.
[9] Lawrence E. Kinsler, Austin R. Frey, Alan B. Coppens, James V. Sanders, Fundamentals of Acoustic, 4th ed., John Wiley & Sons, NY, 2000.
[10] Frank M. White, Viscous Fluid Flow, McGraw Hill Science, 3rd ed., NY ,2006.
[11] Norton, Robert L.,Machine Design An Integrated Approach, Prentice Hall, 1998.
[12] DuPont "Fluoroproducts Properties Handbook", H-37051-4, E. I. du Pont de Nemours & Co., Wilmington, DE.
[13] Philip B. Dobrin, Raul Mirande, Steven Kang, Quan Sheng Dong, and Robert Mrkvicka, "Mechanics of End-to-End Artery-to-PTFE Graft Anastomoses", *Annals of Vascular Surgery*, Volume 12, Number 4 / July, 1998, Springer, New York, 1998.
[14] Robert M. Blumenberg, James M. Anderson, Michael L. Gelfand, Paul S. Skudder, Carol A. Bowers, "Histologic Evaluation of Dacron® and PTFE Graft Material Explanted From Humans After 4 to 20 Years In Vivo", *Vascular and Endovascular Surgery*, Vol. 34, No. 6, 505-512 (2000).
[15] J.M Crissmana and L.J Zapas, "Approximate relations for the analysis of single-step stress-relaxation data in uniaxial extension from experiments involving a finite step time", *Polymer*, Volume 30, Issue 3, March 1989, pp 447-452.
[16] A. Flory and G.B. McKenna, "Finite Step Rate Corrections in Stress Relaxation Experiments: A Comparison of Two Methods", *Mechanics of Time-Dependent Materials* **8:** 17–37, 2004.
[17] G'Sell, C., Jonas, J. J., "Yield and transient effects during the plastic deformation of solid polymers", *Journal of Materials Science*. Vol. 16, pp. 1956-74. July 1981.
[18] Fung, YCl, Biomechanics Mechanical Properties of Living Tissues, Springer Science, 1993.
[19] Damian O. Craiem, Ricardo L. Armentano, "Arterial viscoelasticity: a fractional derivative model", Proceedings of the 28th IEEE EMBS Annual International Conference, New York City, USA, Aug 30-Sept 3, 2006.
[20] WR Milnor and CD Bertram, "The relation between arterial viscoelasticity and wave propagation in the canine femoral artery in vivo", *Circ. Res.* 1978;43;870-879.
[21] Hideyuki Hasegawa, Hiroshi Kanai, Transcutaneous Measurement of Viscoelasticity of Arterial Wall by Application of Remote Actuation, *IEEE International Ultrasonics, Ferroelectrics, and Frequency Control Joint 50th Anniversary Conference*, 2004.
[22] Nathan Yang, NI Signal Streaming: "Sustaining High-SpeedData Streams on USB", Doc Vers 14, *www.ni.com*,2006.
[23] "PID Theory Explained", National Instruments, http://zone.ni.com/devzone/cda/tut/p/id/3782
[24] Gabriel Elkaim, lecture notes EE 154, lectures #4 & 8, UC Santa Cruz, Winter 2007.
[25] Deepak Doraiswamy, "The Origins of Rheology: A Short Historical Excursion, DuPont iTechnologies, Experimental Station, http://www.rheology.org/sor/publications/Rheology_B/Jan02/Origin_of_Rheology.pdf.
[26] William R. Milnor, Wilmer W. Nichols, "A New Method of Measuring Propagation Coefficients and Characteristic Impedance in Blood Vessels", *Circ. Res.* 1975;36;631-639.
[27] Kim, J., Sholar, G., Kim, S., 2008. "Determination of Accurate Creep Compliance and Relaxation Modulus at a Single Temperature for Viscoelastic Solids," ASCE Journal of Materials in Civil Engineering, **20**(2): 147-156.
[28] Gibson, R.F., Hwang, S.J., Sheppard, C.H., 1990. "Characterization of Creep in Polymer Composites by the Use of Frequency-Time Transformations," Journal of Composite Materials, **24**(4): 441-453.

[29] Rees, David (2006). Basic Engineering Plasticity - An Introduction with Engineering and Manufacturing Applications. Butterworth-Heinemann. ISBN 0750680253. http://books.google.com/?id=4KWbmn_1hcYC.